

# Scalable production of bismuth-based materials for photo/electrochemical applications *via* aerosol-assisted chemical vapour deposition

This thesis is submitted in partial fulfilment for the requirements of the Degree of Doctor of Philosophy.

# Mingyue Wang

Supervised by Prof. Claire J. Carmalt

Department of Chemistry

University College London

20 Gordon Street

WC1H 0AJ

2023

### **Declaration**

I, Mingyue Wang, confirm that the work presented in this thesis is my own. Where information has been derived from other sources, I confirm that this has been indicated in the thesis.

#### **Abstract**

This thesis is concerned with the film fabrication of bismuth-based semiconductors, including phenethylammonium bismuth iodide and bismuth oxyhalides, through aerosol-assisted chemical vapour deposition (AACVD) and the subsequent study of their applications, such as batteries, photoelectrochemical (PEC) water splitting and photocatalysis. Improvement of the films' performance in the relative applications was achieved through the optimization of film structures and morphologies, heterojunction construction and doping.

In Chapter 1, the fundamentals of AACVD and semiconductors is presented for the preliminary understanding of the technique and materials studied in this thesis. In addition, mechanisms and measurements of PEC water splitting and photocatalysis are discussed in order to understand the applications and performance of the investigated semiconductors. Chapter 2 explores the precursor synthesis and film deposition via AACVD of phenethylammonium bismuth iodide which is a low-toxicity alternative to lead-based perovskites. The effects of deposition parameters, annealing conditions and the type of substrates on the physical and chemical properties of the resultant films were studied thoroughly and discussed in this Chapter. In addition, the obtained films were applied successfully as the anode in aqueous Zn<sup>2+</sup> electrolytes. In Chapter 3, the BiOI film deposited via AACVD was combined with a ZnO film to form a double-layer heterojunction for enhanced PEC activity. In both building structures, deposition temperatures and film thickness of the ZnO exhibited a strong influence on the performance of the heterojunctions. The mechanism behind the improved PEC performance and the stability of the obtained heterojunction were investigated in detail. Chapter 4 describes the significant improvement in visible-light photocatalysis of iodide-doped BiOBr films fabricated by AACVD. The modification of film properties such as growth orientations, morphologies and bandgaps induced by doping was analyzed systematically. The reasons behind the improved photocatalytic activity of iodide-doped BiOBr under visible-light irradiation were discussed as well. Chapter 5 provides a conclusion of the work included in this thesis and future outlook.

#### Impact statement

Problems of environmental pollution and energy depletion caused by the human's excessive reliance on fossil fuels are getting worse. Therefore, the utilization of solar energy in various energy and sustainable applications, such as solar cells, water splitting and photocatalysis, has attracted huge attention in recent decades in order to meet the needs of the global population and economic growth in a 'green' way.

Throughout the work in this doctorate, emphasis is placed on the film deposition of bismuth-based semiconductors through aerosol-assisted chemical vapour deposition (AACVD) and investigating the improved performance of these functional films in photo/electrochemical applications.

Looking for non-toxic and stable alternatives of popular lead halide perovskite materials is in high demand, and the successful single-crystal and film preparation of phenethylammonium bismuth iodide in this work provides an attractive option for this. The detailed study on various influence factors of the film deposition in the AACVD process were conducted, which has great reference value for future research on similar techniques and materials. Furthermore, considering the utilization of AACVD and the outstanding performance of the deposited films in electrochemical measurements, this work contributed to solve a long-standing problem, how to achieve the large-scale production of perovskite and derived materials in practical applications.

Hydrogen as a renewable energy source can be generated effectively through photoelectrochemical (PEC) water splitting. However, visible-light activities of many catalysts in PEC water splitting are low, and thus the full utilization of sunlight is limited. Through combining BiOI and ZnO, a heterojunction was formed which showed remarkable visible-light performance in PEC water oxidation. Both BiOI and ZnO are cheap and non-toxic, and the heterojunction in this work was deposited on the conducting substrate in the film form directly, further reducing the complexity of the production process of photoanodes.

Besides constructing heterojunctions, doping is also an effective method to improve the photoactivity of semiconductors. Recently, the market demand of photocatalytic products grew rapidly, especially in building materials. In this thesis, iodide-doped BiOBr films were fabricated successfully by AACVD from cheap and accessible precursors and showed excellent photocatalytic activities under visible-light irradiation. As a result, these iodide-doped BiOBr coatings could be seen as great candidates for the decomposition of organic pollutants in functional constructions, such as *smart* window.

All of the above materials and relative structures were deposited *via* AACVD, which is a feasible, low-cost and scalable technique, so the potential of AACVD in the scale-up production of various bismuth-based semiconductors was revealed. Therefore, this thesis opens a door for the industrialization of these bismuth-based materials in various energy and sustainable applications.

#### **Acknowledgements**

Firstly, I would like to thank my supervisor Professor Claire J. Carmalt for giving me the opportunity to start the PhD study, so that I had a chance to keep working with you 4 more years after completing the master's degree. You gave me so much support in both lab work and everyday life. I learned a lot from you, as a female, a scientist and of course a supervisor. I am really grateful to your continued help in the past 5 years. I also want to thank my second supervisor Professor Chris Blackman. In the first-year progress viva and upgrade viva, I felt that my progress was witnessed by you, and your suggestions on my projects also inspired me.

Next, I would like to thank every people who helped me during my PhD process. Dr. Clara Sanchez-Perez, thank you for being my friend and my lab partner. Because of you, I became more confident and mature to academics and life. Dr. Sanjayan Sathasivam, thank you for everything helped me in the lab. You are nice and smart. I got a lot of valuable suggestions from you. Dr. Andreas Kafizas, thank you so much for the huge help and support, especially in our collaboration project. I really enjoyed working with you in Imperial College London. Dr Raul Quesada-Cabrera, thank you for the help in the lab work and paper writing. Every meeting with you made me happy because of the great sunshine. In addition, I would like to thank Dr. Kristopher Page for managing our lab and help me order chemicals. I would like to thank Dr. Premrudee Promdet, Dr. Faiza Habib, Dr. Joanna Borowiec and Dr Benjamin Moss for offering help in the lab. I would like to thank Dr. Matthew Blunt for the AFM measurements, Mr. Martin Vickers for training me on using XRD instruments and Dr. Steven Firth for training me to use SEM. I also would like to thank University College London and the China Scholarship Council for the joint PhD scholarship.

Finally, I would like to thank my family, my parents, brother, grandparents....., as well as my bestie and Mr. Xin Fang. You've always been there for me. Without your support, I cannot finish my PhD.

## **Table of Contents**

Declara	tion.		2
Abstrac	t		3
Impact	state	ment	4
Acknow	ledge	ements	6
Table o	f Cor	ntents	7
List of F	igure	es	. 11
List of T	able	S	. 20
Abbrevi	ation	S	. 21
Chapte	1:	Introduction	. 23
1.1	Aer	osol-assisted chemical vapour deposition	. 23
1.2	Ser	miconductors	. 24
1.2	.1	Energy bands in semiconductors	. 24
1.2	.2	Direct and indirect bandgap semiconductors	. 27
1.2	.3	Heterojunctions	. 28
1.3	Cha	aracterization techniques	. 29
1.3	.1	Photoluminescence spectroscopy	. 29
1.3	.2	Transient absorption spectroscopy	. 32
1.4	Pho	otoelectrochemical water splitting	. 34
1.4	.1	Mechanism involved in PEC water splitting	. 35
1.4	.2	PEC measurement setup	. 37
1.4	.3	Performance indicators	. 39
1.5	Pho	otocatalysis	. 41
1.5	.1	Mechanism involved in photocatalysis	. 41
1.5	.2	Smart ink photocatalytic test	. 43
1.6	Ref	erence	. 45
Chapte	2:	Phenethylammonium bismuth iodide films	. 53

2.1	Bac	kground	53
2.2	Exp	perimental	57
2.2.	1	Precursor synthesis	57
2.2.	2	Film deposition	60
2.2.	3	Physical characterization	61
2.3	Res	sults and discussions	62
2.3.	1	Crystal structure and film composition	62
2.3.	2	Film morphology	70
2.3.	3	[PEA] <sub>3</sub> [Bi <sub>2</sub> l <sub>9</sub> ] films on TiO <sub>2</sub> /glass and FTO/glass	70
2.3.	4	Vacuum-annealed [PEA]3[Bi2l9] films	73
2.3.	5	Optoelectrical properties and band gap calculations	79
2.3.	6	Stability	83
2.3.	7	Applications	84
2.4	Sur	nmary	85
2.5	Ref	erence	86
Chapter	3:	ZnO/BiOI heterojunctions with enhanced photoelectrochem	ical water
oxidation	n act	ivity	100
3.1	Bac	ckground	100
3.2	Exp	perimental	104
3.2.	1	Film deposition	104
3.2.	2	Physical characterization	105
3.2.	3	Photoelectrochemical measurements	106
3.2.	4	Faradaic efficiency measurements	106
3.2.	5	Theoretical calculations	106
3.3	Res	sults and discussions	107
3.3.	1	GIXRD characterization	107
3.3.	2	XPS analysis	112

	3.3.	3	Film morphology characte	rization			117
3.3.4		4	Optical properties and bar	nd gap calculati	ons		122
	3.3.	5	Photoelectrochemical mea	asurements			125
	3.3.	6	Surface roughness				134
	3.3.	7	Photoluminescence sp	ectroscopy	and	transient	absorption
	spe	ctros	copy				135
	3.3.8		Stability test				140
	3.3.	9	Faradaic efficiency measu	rements			144
	3.3.	10	TiO <sub>2</sub> /BiOI heterostructure.				147
3.	4	Sun	nmary				151
3.	5	Ref	erence				152
Cha	pter	4:	Iodide-doped BiOBr films	with enhance	d photo	ocatalytic ac	tivity under
visib	le-li	ght ir	radiation				164
4.	1	Bac	kground				164
4.	2	Ехр	erimental				167
	4.2.	1	Film deposition				167
	4.2.	2	Smart Rz ink preparation.				167
	4.2.	3	Physical characterization.				167
	4.2.	4	Photocatalytic test				168
	4.2.	5	Photoelectrochemical mea	asurements			169
4.	3	Res	ults and discussions				170
	4.3.	1	GIXRD characterization				170
	4.3.	2	XPS analysis				174
	4.3.	3	Film morphology				180
	4.3.	4	Surface roughness				184
	4.3.	5	Optical properties and bar	nd gap calculati	ons		186
	4.3.	6	Photocatalysis test				190
	4.3.	7	Photoluminescence specti	roscopy			199

4.3.	8 Photoelectrochemical measurements	200
4.4	Summary	204
4.5	Reference	205
Chapter	5: Conclusions and future work	216
Publicat	ions	219

# List of Figures

Figure 1-1. Illustration of AACVD setup. From left to right, the inert gas is used to
transfer the precursor solution (orange) as a mist, which is generated using an
ultrasonic humidifier, into the reactor. A top plate was suspended above the glass
substrate to ensure a laminar flow. The film is deposited on the heated substrate in
the reactor. The deposition temperature is controlled by a temperature controller.
Byproducts and unreacted precursors leave the reactor through the exhaust with the
carrier gas24
Figure 1-2. Band diagram of the intrinsic semiconductor, n-type semiconductor, and
p-type semiconductor26
Figure 1-3. Band diagram of shallow and deep donor (SD and DD) and acceptor (SA
and DA) levels in the semiconductor26
Figure 1-4. Energy band diagram of (a) direct bandgap and (b) indirect bandgap
semiconductors27
Figure 1-5. Schematic diagram of the energy band alignment of type-I, type-II and
type-III heterojunctions29
Figure 1-6. Schematic diagram of a simplified setup for the PL measurement 30
Figure 1-7. Schematic diagram of the principle of PL spectroscopy in semiconductors.
31
Figure 1-8. Schematic diagram of the photon emission process in the (a) direct and
the (b) indirect band gap semiconductors32
Figure 1-9. Schematic diagram of a typical TAS setup33
Figure 1-10. Schematic diagram of the principle of TAS in semiconductors34
Figure 1-11. Schematic diagram of a simplified PEC system with a n-type
semiconductor as the photoanode and a metal as the counter electrode36
Figure 1-12. Schematic diagram of PEC water splitting systems using (a) a
photoanode, (b) a photocathode and (c) photoanode and photocathode37
Figure 1-13. Schematic diagram of a basic PEC measurement setup38
Figure 1-14. Schematic diagram of photocatalysis mechanism in semiconductors 42
Figure 1-15. Proposed reaction scheme of the photocatalyst ink identifying the major
underlying reactions43
Figure 1-16. Structures of the indicator dye, Rz, its initial reduced form Rf, and further
reduced form, <i>HRf</i> , which can be reoxidized to <i>Rf</i> by ambient oxygen44

Figure 2-1. The typical structure of an ABX <sub>3</sub> perovskite	. 54
Figure 2-2. (a) Single crystal and (b) recrystallized single crystal of [PEA] <sub>3</sub> [Bi <sub>2</sub> I <sub>9</sub> ].	(c)
Unit cell of crystal [PEA] <sub>3</sub> [Bi <sub>2</sub> l <sub>9</sub> ] drawn using Diamond®	. 58
Figure 2-3. Scheme of films deposited on (a) glass, (b) TiO <sub>2</sub> /glass and (c) FTO/gla	
Figure 2-4. GIXRD pattern of the TiO <sub>2</sub> thin film on glass	
Figure 2-5. GIXRD patterns of [PEA] <sub>3</sub> [Bi <sub>2</sub> l <sub>9</sub> ] films deposited on TiO <sub>2</sub> /glass at (a) 125 (b) 160 °C and (c) 195 °C	
Figure 2-6. Top-view SEM images of [PEA] <sub>3</sub> [Bi <sub>2</sub> l <sub>9</sub> ] films deposited on TiO <sub>2</sub> /glass at 125 °C, (b) 160 °C and (c) 195 °C	
Figure 2-7. Top-view SEM images of [PEA] <sub>3</sub> [Bi <sub>2</sub> l <sub>9</sub> ] films deposited on TiO <sub>2</sub> /glass fr (a) 0.05 M, (b) 0.1 M and (c) 0.2 M precursor solutions.	
Figure 2-8. GIXRD patterns of [PEA] <sub>3</sub> [Bi <sub>2</sub> I <sub>9</sub> ] films deposited on glass at differ annealing temperatures in N <sub>2</sub>	
Figure 2-9. PXRD patterns of scraped annealed film on glass, calculated from SCX and calculated from literature.	
Figure 2-10. FT-IR spectra of [PEA] <sub>3</sub> [Bi <sub>2</sub> I <sub>9</sub> ] powders scratched from the deposited fill before and after annealing in N <sub>2</sub>	
Figure 2-11. High resolution XPS spectra of (a) C 1s, (b) N 1s, (c) Bi 4f and (d) I from the [PEA] <sub>3</sub> [Bi <sub>2</sub> I <sub>9</sub> ] film on glass annealed at 150 °C in N <sub>2</sub>	l 3d
Figure 2-12. XPS survey spectrum of the [PEA]3[Bi2l9] film on glass annealed at 150 in N2.	) °C
Figure 2-13. EDS analysis of the [PEA] <sub>3</sub> [Bi <sub>2</sub> I <sub>9</sub> ] film on glass annealed at 150 °C in	$N_2$ .
Figure 2-14. Top-view SEM images of [PEA] <sub>3</sub> [Bi <sub>2</sub> I <sub>9</sub> ] films on glass, (a) as deposit annealed in N <sub>2</sub> at (b) 130 °C and (c) 150 °C.	ted,
Figure 2-15. GIXRD patterns of [PEA] <sub>3</sub> [Bi <sub>2</sub> l <sub>9</sub> ] films deposited on TiO <sub>2</sub> /glass at differ annealing temperatures in N <sub>2</sub>	rent
Figure 2-16. GIXRD patterns of [PEA] <sub>3</sub> [Bi <sub>2</sub> l <sub>9</sub> ] films deposited on FTO/glass at differ	
annealing temperatures in N2	. 72
Figure 2-17. Top-view SEM images of [PEA] <sub>3</sub> [Bi <sub>2</sub> I <sub>9</sub> ] films on TiO <sub>2</sub> /glass, (a)	as
deposited, annealed in N <sub>2</sub> at (b) 130 °C and (c) 150 °C	. 73
Figure 2-18. Top-view SEM images of [PEA] <sub>3</sub> [Bi <sub>2</sub> l <sub>9</sub> ] films on FTO/glass, (a)	as
deposited, annealed in N2 at (b) 130 °C and (c) 150 °C	. 73

Figure 2-19. GIXRD patterns of [PEA] <sub>3</sub> [Bi <sub>2</sub> I <sub>9</sub> ] films deposited on glass (red), TiO <sub>2</sub> /glass
(green) and FTO/glass (blue) annealed at 120 °C in the vacuum oven74
Figure 2-20. Top-view SEM images of [PEA] <sub>3</sub> [Bi <sub>2</sub> l <sub>9</sub> ] films on (a) glass, (b) TiO <sub>2</sub> /glass
and (c) FTO/glass annealed at 120 °C in the vacuum oven
Figure 2-21. AFM images of [PEA] <sub>3</sub> [Bi <sub>2</sub> I <sub>9</sub> ] films vacuum-annealed at 120 °C on (a)
glass, (b) TiO <sub>2</sub> /glass and (c) FTO/glass. All images were of a 20 x 20 $\mu m^2$ area 76
Figure 2-22. DMF contact angles on (a) glass, (b) TiO <sub>2</sub> /glass and (c) FTO/glass77
Figure 2-23. Side-view SEM images of [PEA] <sub>3</sub> [Bi <sub>2</sub> l <sub>9</sub> ] films on glass, (a) as deposited,
(b) annealed at 150 °C in $N_2$ and (c) annealed at 120 °C in the vacuum oven 78
Figure 2-24. Side-view SEM images of [PEA] <sub>3</sub> [Bi <sub>2</sub> I <sub>9</sub> ] films on TiO <sub>2</sub> /glass, (a) as
deposited, (b) annealed at 150 $^{\circ}\text{C}$ in N <sub>2</sub> and (c) annealed at 120 $^{\circ}\text{C}$ in the vacuum
oven78
Figure 2-25. Side-view SEM images of [PEA] <sub>3</sub> [Bi <sub>2</sub> I <sub>9</sub> ] films on FTO/glass, (a) as
deposited, (b) annealed at 150 $^{\circ}\text{C}$ in N <sub>2</sub> and (c) annealed at 120 $^{\circ}\text{C}$ in the vacuum
oven78
Figure 2-26. Transmittance spectra of [PEA] <sub>3</sub> [Bi <sub>2</sub> I <sub>9</sub> ] films on glass, as deposited,
annealed at 150 $^{\circ}\text{C}$ in $N_2$ and annealed at 120 $^{\circ}\text{C}$ in the vacuum oven. Optical band
gaps were calculated using a Tauc-plot method 80
Figure 2-27. Transmittance spectra of [PEA] <sub>3</sub> [Bi <sub>2</sub> I <sub>9</sub> ] films on TiO <sub>2</sub> /glass, as deposited,
annealed at 150 $^{\circ}\text{C}$ in $N_2$ and annealed at 120 $^{\circ}\text{C}$ in the vacuum oven. Optical band
gaps were calculated using a Tauc-plot method80
Figure 2-28. Transmittance spectra of [PEA] <sub>3</sub> [Bi <sub>2</sub> l <sub>9</sub> ] films on FTO/glass, as deposited,
annealed at 150 $^{\circ}\text{C}$ in $N_2$ and annealed at 120 $^{\circ}\text{C}$ in the vacuum oven. Optical band
gaps were calculated using a Tauc-plot method81
Figure 2-29. Energy band alignment diagram with respect to the vacuum level of FTO,
TiO <sub>2</sub> and [PEA] <sub>3</sub> [Bi <sub>2</sub> I <sub>9</sub> ] (PEABI). <sup>84</sup>
Figure 2-30. PL spectra of [PEA] <sub>3</sub> [Bi <sub>2</sub> I <sub>9</sub> ] films on (a) glass, (b) TiO <sub>2</sub> /glass and (c)
FTO/glass82
Figure 2-31. Water contact angles on vacuum-annealed (120 °C) [PEA] <sub>3</sub> [Bi <sub>2</sub> l <sub>9</sub> ] films
deposited over (a) glass, (b) TiO <sub>2</sub> /glass and (c) FTO/glass83
Figure 2-32. GIXRD patterns of [PEA] <sub>3</sub> [Bi <sub>2</sub> l <sub>9</sub> ] films vacuum-annealed at 120 °C on
glass, TiO <sub>2</sub> /glass and FTO/glass after 6-month exposure in ambient conditions 84
Figure 2-33. The structure of a complete solar cell device based on the [PEA]3[Bi2l9]
film85

Figure 3-1. AM 1.5 solar spectrum
Figure 3-2. Energy band alignment diagram of TiO2, ZnO, BiOI, BiOBr and BiOC
compared to the potentials of water splitting at pH = 7
Figure 3-3. (a) GIXRD patterns of BiOI films on FTO deposited at 250, 300 and 350 °C
(b) JV curves of BiOI films measured in the dark (dashed lines) and under the action
of light (350 nm, 2.58 mW·cm <sup>-2</sup> ) (solid lines). Samples were irradiated at the
semiconductor-electrolyte interface. The voltage was swept from 0.10 $V_{RHE}$ to 1.60
V <sub>RHE</sub> at a rate of 10 mV·s <sup>-1</sup> 108
Figure 3-4. GIXRD patterns of ZnO, BiOI, BiOI/ZnO and ZnO/BiOI films on FTO, with
all ZnO layers grown from 0.5 g Zn(OAc)2-2H2O at 350 °C. The asterisked peaks were
reflections from FTO substrates110
Figure 3-5. GIXRD patterns of ZnO/BiOI films on FTO, with ZnO deposited from 0.5 g
Zn(OAc) <sub>2</sub> -2H <sub>2</sub> O at 300, 350, 400 and 450 °C111
Figure 3-6. GIXRD patterns of ZnO/BiOI films on FTO, with ZnO deposited from 0.1
0.3, 0.5, 0.7 and 0.9 g Zn(OAc) <sub>2</sub> ·2H <sub>2</sub> O at 350 °C112
Figure 3-7. High resolution XPS spectra of the (a) Zn 2p and (b) O 1s peaks from the
ZnO film on FTO from 0.5 g Zn(OAc) <sub>2</sub> -2H <sub>2</sub> O at 350 °C
Figure 3-8. High resolution XPS spectra of the (a) Bi 4f and (b) I 3d peaks from the
BiOI film on FTO
Figure 3-9. High resolution XPS spectra of the (a) Bi 4f, (b) I 3d, (c) O 1s and (d) Zr
2p peaks from the BiOI/ZnO film on FTO, with the ZnO layer grown from 0.5 g
Zn(OAc) <sub>2</sub> -2H <sub>2</sub> O at 350 °C114
Figure 3-10. High resolution XPS spectra of the (a) Zn 2p, (b) O 1s, (c) Bi and (d)
peaks from the ZnO/BiOI film on FTO, with the ZnO layer grown from 0.5 g
Zn(OAc) <sub>2</sub> -2H <sub>2</sub> O at 350 °C116
Figure 3-11. Composition (%) variation of ZnO/BiOI with the etching time in XPS
including (a) C, O, Zn, Bi and I, and (b) Zn and Bi, with the ZnO layer grown from 0.5
g Zn(OAc) <sub>2</sub> ·2H <sub>2</sub> O at 350 °C117
Figure 3-12. Top-view SEM images of (a) ZnO, (b) BiOI, (c) BiOI/ZnO and (e) ZnO/BiO
films on FTO; side-view SEM images of (d) BiOI/ZnO and (f) ZnO/BiOI films on FTO
with all ZnO layers grown from 0.5 g Zn(OAc) <sub>2</sub> ·2H <sub>2</sub> O at 350 °C
Figure 3-13. Top-view SEM images of ZnO/BiOI films deposited on FTO with ZnC
deposited from 0.5 g Zn(OAc) <sub>2</sub> ·2H <sub>2</sub> O at (a) 300, (b) 400 and (c) 450 °C 121

Figure 3-14. Top-view SEM images of ZnO/BiOI films deposited on FTO with ZnO
deposited from (a) 0.1 g, (b) 0.3 g, (c) 0.7 g and (d) 0.9 g Zn(OAc) <sub>2</sub> -2H <sub>2</sub> O at 350 °C.
121
Figure 3-15. Side-view SEM images of ZnO/BiOI films deposited on FTO with ZnO
deposited from (a) 0.1 g, (b) 0.3 g, (c) 0.7 g and (d) 0.9 g Zn(OAc) <sub>2</sub> ·2H <sub>2</sub> O at 350 °C.
Figure 3-16. (a) UV-Vis transmittance spectra of ZnO, BiOI, BiOI/ZnO and ZnO/BiOI
films deposited on FTO, with all ZnO layers grown from 0.5 g Zn(OAc)2-2H2O at
350 °C; calculated optical band gaps of (b) ZnO and (c) BiOI films
Figure 3-17. UV-Vis transmittance spectra of ZnO/BiOI films deposited on FTO with
ZnO deposited from 0.5 g Zn(OAc) <sub>2</sub> ·2H <sub>2</sub> O at 300, 350, 400 and 450 °C 124
Figure 3-18. UV-Vis transmittance spectra of ZnO/BiOI films deposited on FTO with
ZnO deposited from 0.1 g, 0.3 g, 0.5 g, 0.7 g and 0.9 g Zn(OAc) <sub>2</sub> -2H <sub>2</sub> O at 350 °C.
Figure 3-19. JV curves of ZnO, BiOI, and BiOI/ZnO films measured in the dark (dashed
lines) and under the action of light (1 sun illumination, solid lines), with all ZnO layers
grown from 0.5 g Zn(OAc) <sub>2</sub> ·2H <sub>2</sub> O at 350 °C. Samples were irradiated at the
semiconductor-electrolyte interface. The voltage was swept from 0.10 V <sub>RHE</sub> to 1.60
V <sub>RHE</sub> at a rate of 10 mV⋅s <sup>-1</sup> 127
Figure 3-20. JV curves of ZnO, BiOI, and ZnO/BiOI films measured in the dark (dashed
lines) and under the action of light (350 nm, 2.58 mW·cm <sup>-2</sup> ) (solid lines), with all ZnC
layers grown from 0.5 g Zn(OAc)2-2H2O at 350 °C. Samples were irradiated at the
semiconductor-electrolyte interface. The voltage was swept from 0.10 $V_{\text{RHE}}$ to 1.60
V <sub>RHE</sub> at a rate of 10 mV⋅s <sup>-1</sup> 128
Figure 3-21. JV curves of ZnO/BiOI films in the dark (dashed lines) and under the
action of light (350 nm, 2.58 mW·cm <sup>-2</sup> ) (solid lines), (a) with ZnO deposited from 0.5
g Zn(OAc) <sub>2</sub> ·2H <sub>2</sub> O at 300, 350, 400 and 450 °C; (b) with ZnO deposited from 0.1, 0.3,
0.5, 0.7 and 0.9 g Zn(OAc) <sub>2</sub> -2H <sub>2</sub> O at 350 °C. Samples were irradiated at the
semiconductor-electrolyte interface. The voltage was swept from 0.10 $V_{\text{RHE}}$ to 1.60
V <sub>RHE</sub> at a rate of 10 mV⋅s <sup>-1</sup> 129
Figure 3-22. ABPE curves of ZnO, BiOI, and ZnO/BiOI under the action of light (1 sun
illumination), with all ZnO layers grown from 0.5 g Zn(OAc) <sub>2</sub> ·2H <sub>2</sub> O at 350 °C 130
Figure 3-23. IPCE of ZnO, BiOI, and ZnO/BiOI films, with all ZnO layers grown from
0.5 g Zn(OAc) <sub>2</sub> -2H <sub>2</sub> O at 350 °C131

Figure 3-24. TSPs of (a) BiOI, (b) ZnO and (c) ZnO/BiOI under AM 1.5 solar spectrum
when the applied voltage was held at 1.23 $V_{\text{RHE}}$ , with all ZnO layers grown from 0.5 g
Zn(OAc) <sub>2</sub> ·2H <sub>2</sub> O at 350 °C
Figure 3-25. AFM images of ZnO, BiOI, and ZnO/BiOI films deposited on FTO, with all
ZnO layers grown from 0.5 g Zn(OAc) <sub>2</sub> ·2H <sub>2</sub> O at 350 °C
Figure 3-26. PL spectra of ZnO, BiOI, and ZnO/BiOI, with all ZnO layers grown from
0.5 g Zn(OAc) <sub>2</sub> -2H <sub>2</sub> O at 350 °C. The excitation wavelength was 325 nm
Figure 3-27: Transient absorption decay kinetics of (a) ZnO, (b) BiOI and (c) ZnO/BiOI
films deposited on FTO from 10 µs after the laser pulse until 1 s, measured at select
probe wavelengths from 550 to 1100 nm. The excitation wavelength was 355 nm. The
pulse width was ~6 ns. All ZnO layers were grown from 0.5 g Zn(OAc) <sub>2</sub> ·2H <sub>2</sub> O at 350 °C138
Figure 3-28: Transient absorption spectra of (a) ZnO, (b) BiOI and (c) ZnO/BiOI films
deposited on FTO at select times from 10 µs after the laser pulse until 900 ms,
measured at select probe wavelengths from 550 to 1100 nm. The excitation
wavelength was 355 nm. The pulse width was ~6 ns. All ZnO layers were grown from
0.5 g Zn(OAc) <sub>2</sub> ·2H <sub>2</sub> O at 350 °C139
Figure 3-29: Transient absorption decay kinetics for the ZnO, BiOI and ZnO/BiOI films
deposited on FTO, measured at the probe wavelengths (a) 550 nm and (b) 1100 nm from 10 up after the least pulse until 1 a. The excitation wavelength was 355 nm. The
from 10 µs after the laser pulse until 1 s. The excitation wavelength was 355 nm. The
pulse width was ~6 ns. All ZnO layers were grown from 0.5 g Zn(OAc) <sub>2</sub> -2H <sub>2</sub> O at 350 °C140
Figure 3-30. Stability of ZnO, BiOI, and ZnO/BiOI photoanodes at 1.23 $V_{\text{RHE}}$ , under
the action of light (350 nm, 2.58 mW⋅cm <sup>-2</sup> )141
Figure 3-31. JV curves of (a) ZnO, (b) BiOI and (c) ZnO/BiOI films deposited on FTO
were measured in the dark (dashed lines) and under the action of light (1 sun
illumination, solid lines) before and after the 1.5-hour stability test. The voltage was
swept from 0.10 V <sub>RHE</sub> to 1.60 V <sub>RHE</sub> at a rate of 10 mV·s <sup>-1</sup> 142
Figure 3-32. GIXRD patterns of (a) ZnO, (b) BiOI and (c) ZnO/BiOI deposited on FTO
before and after the 1.5-hour stability test144
Figure 3-33. (a) Photocurrent vs. time plots of the ZnO/BiOI photoanode at a constant
potential of 1.0 V vs. Ag/AgCl. (b) Theoretical O2 yield calculated from photocurrent.
(c) Liner calibration of voltage vs. O2 volume. (d) Experimental O2 yield of ZnO/BiOI.
Grey and red areas correspond to irradiation light off and on respectively 146

Figure 3-34. (a) Photocurrent vs. time plots of the ZnO photoanode at a constar
potential of 1.0 V vs. Ag/AgCl. (b) Theoretical $O_2$ yield calculated from photocurren
c) Liner calibration of voltage vs. $O_2$ volume. (d) Experimental $O_2$ yield of ZnO. Gre
and red areas correspond to irradiation light off and on respectively14
Figure 3-35. GIXRD patterns of TiO <sub>2</sub> , BiOI and TiO <sub>2</sub> /BiOI films deposited on FTO.14
Figure 3-36. JV curves of TiO2, BiOI and TiO2/BiOI films deposited on FTO wer
neasured in the dark (dashed lines) and under the action of light (1 sun illumination
solid lines). The voltage was swept from 0.10 $V_{RHE}$ to 1.60 $V_{RHE}$ at a rate of 10 mV·s $^-$
14
Figure 3-37. IPCE for $TiO_2$ , $BiOI$ , and $TiO_2/BiOI$ films deposited on FTO
igure 4-1. The emission spectra of the 365 nm, 450 nm and 627 nm LED 16
Figure 4-2. (a) GIXRD patterns and (b) enlarged patterns of BiOBr, BiOI and <b>I-BB</b> film
leposited on FTO. The asterisked peaks indicate positions of reflections from the FT0
substrate17
Figure 4-3. Comparison of $c$ values of <b>I-BB</b> samples calculated from GIXRD pattern
and from the Vegard's law17
Figure 4-4. (a) GIXRD patterns and (b) enlarged patterns of BiOBr, BiOI and <b>I-BB</b> film
leposited on glass17
Figure 4-5. High resolution XPS spectra of the (a) Br 3d and (b) O 1s peaks from th
BiOBr film on FTO17
Figure 4-6. High resolution XPS spectra of the (a) Bi 4f, (b) I 3d and (c) O 1s peak
rom the BiOI film on FTO17
Figure 4-7. High resolution XPS spectra of I 3d of all <b>I-BB</b> samples on FTO 17
Figure 4-8. XPS depth profile analysis of I 3d from the <b>I-BB S4</b> on FTO17
Figure 4-9. High resolution XPS spectra of (a) Bi 4f, (b) Br 3d and (c) O 1s from <b>the</b>
BB S4 film grown on FTO17
Figure 4-10. High resolution XPS spectra of Bi 4f from I-BB S4 and BiOBr on FTC
17
Figure 4-11. High resolution XPS spectra of (a) Bi 4f, (b) Br 3d and (c) O 1s from th
-BB S4 film grown on glass17
Figure 4-12. High resolution XPS spectra of I 3d of all I-BB samples on glass 18
Figure 4-13. Top-view SEM and inserted side-view SEM images of BiOBr and BiOI o
TO18

Figure 4-14. Top-view SEM and inserted side-view SEM images of I-BB S1, I-BB S2,
I-BB S3, I-BB S4, I-BB S5, I-BB S6, I-BB S7, I-BB S8 and I-BB S9 on FTO 182
Figure 4-15. Top-view SEM images of BiOBr and BiOI on glass
Figure 4-16. Top-view SEM images of I-BB S1, I-BB S2, I-BB S3, I-BB S4, I-BB S5,
I-BB S6, I-BB S7, I-BB S8 and I-BB S9 on glass
Figure 4-17. AFM images of (a) BiOBr and (b) BiOI films. Both images were of a 5 $\times$ 5
μm square area185
Figure 4-18. AFM images of (a) I-BB S1, (b) I-BB S2, (c) I-BB S3, (d) I-BB S4, (e) I-
BB S5,  (f)  I-BB S6,  (g)  I-BB S7,  (h)  I-BB S8  and (i)  I-BB S9  on FTO.  All images were  S1, S2, S3, S4, S5, S6, S6
of a 5 x 5 µm square area
Figure 4-19. UV-Vis transmittance spectra of BiOBr, BiOI and I-BB films deposited on
FTO
Figure 4-20. Optical band gaps were calculated through the Tauc plot method 189
Figure 4-21. Images of the $Rz$ ink coating on I-BB S5 (upper) and FTO (lower) 192
Figure 4-22. The absorption spectrum (red) of the smart Rz ink coated on blank FTO.
The blue lines illustrate the emission spectra of the 450 nm and 627 nm LED 192
Figure 4-23. Images of the $Rz$ ink coating on FTO, BiOBr, I-BB samples and BiOI
under 450 nm LED irradiation
Figure 4-24. $R_t$ vs. t plots of the $\emph{Rz}$ intelligence ink on BiOBr, BiOI and I-BB films
deposited on FTO under 450 nm LED irradiation
Figure 4-25. Rates of $\it Rz$ conversion (dR <sub>t</sub> /dt) of FTO, BiOBr, I-BB and BiOI films
deposited on FTO under 450 nm LED irradiation
Figure 4-26. Images of the $Rz$ ink test on FTO, BiOBr, I-BB and BiOI films deposited
on FTO under 365 nm LED irradiation
Figure 4-27. $R_t$ vs. $t$ plots of the $\emph{Rz}$ ink test on FTO, BiOBr, I-BB and BiOI films
deposited on FTO under 365 nm LED irradiation
Figure 4-28. Rates of $\it Rz$ conversion (dR <sub>t</sub> /dt) of FTO, BiOBr, I-BB and BiOI films
deposited on FTO under 365 nm LED irradiation
Figure 4-29. Photoluminescence spectra excited at 325 nm of BiOBr, BiOI and I-BB
films deposited on FTO
Figure 4-30. Transient photocurrent response of BiOBr, BiOI and I-BB films deposited
on FTO

Figure 4-31. JV curves of BiOBr and BiOI films on FTO were measured with front-side
illumination (1 sun illumination, solid lines) and in the dark (dashed lines). The voltage
was swept from 0.11 V <sub>RHE</sub> to 1.10 V <sub>RHE</sub> at a rate of 10 mV·s <sup>-1</sup> 202
Figure 4-32. $JV$ curves of <b>I-BB</b> films on FTO were measured with front-side illumination
(1 sun illumination, solid lines) and in the dark (dashed lines). The voltage was swept
from 0.11 V <sub>RHE</sub> to 1.10 V <sub>RHE</sub> at a rate of 10 mV·s <sup>-1</sup>

## **List of Tables**

Table 2-1. Crystallographic data from two single crystal samples 59
Table 2-2. Calculated direct and indirect band gaps of [PEA] <sub>3</sub> [Bi <sub>2</sub> I <sub>9</sub> ] films 81
Table 3-1. Unit cell parameters (a, c), cell volume (V) and average crystallite size of
ZnO, BiOI, BiOI/ZnO and ZnO/BiOI films on FTO, with all ZnO layers grown from 0.5
g precursor at 350 °C
Table 3-2. A summary of the PEC water oxidation performance of selected studies
using ZnO, BiOI and ZnO/BiOI134
Table 4-1. Unit cell parameters (a, c), cell volume (V) and average crystallite size of
BiOBr, BiOI and I-BB films
Table 4-2. Atomic concentration of as-fabricated I-BB films on FTO 176
Table 4-3. Atomic concentration of as-fabricated <b>I-BB</b> films on glass
Table 4-4. Roughness factors of films on FTO calculated from AFM images 186
Table 4-5. Optical band gaps of BiOBr, BiOI and I-BB films deposited on FTO 190

#### **Abbreviations**

AACVD aerosol-assisted chemical vapour deposition

AFM atomic force microscopy

APBE applied bias photo-to-current efficiency

CB conduction band

CBM conduction band minimum

CVD chemical vapour deposition

DMF N',N'-dimethylformamide

EDS energy dispersive spectroscopy

Eg bandgap energy

FE faraday efficiency

FT-IR Fourier transform infrared

FTO fluorine-doped tin oxide

GIXRD grazing incident X-ray diffraction

HLVD high-low vacuum deposition

HRf dihydroresorufin

IPCE incident photon-to-current efficiency

ITO indium tin oxide

MAPI methylammonium lead iodide

MBI methylammonium bismuth iodide

P3HT poly(3-hexylthiophene)

PEAI phenethylammonium iodide

PEC photoelectrochemical

PL photoluminescence

PV photovoltaic

PXRD powder X-ray diffraction

Rf resorufin

RGB red-green-blue

RHE reversible hydrogen electrode

RMS root mean square

Rz resazurin

SED sacrificial electron donor

SEM scanning electron microscope

TAS transient absorption spectroscopy

TSP theoretical solar photocurrent

UV-Vis ultraviolet-visible

VB valence band

VBM valence band maximum

XPS X-ray photoelectron spectroscopy

#### **Chapter 1: Introduction**

#### 1.1 Aerosol-assisted chemical vapour deposition

Aerosol-assisted chemical vapour deposition (AACVD) is a technique utilized for the synthesis and deposition of thin films or coatings on solid substrates. It is a combination of solution-based and vapour deposition processes.<sup>1</sup> Figure 1-1 shows a typical AACVD setup. An AACVD process typically involves the following steps:

- 1. Preparation of precursor solutions: The precursor chemicals are dissolved in suitable solvents to form solutions.
- 2. Generation of aerosol: Aerosol mist containing fine droplets of the precursor solution suspended in a carrier gas is generated using an ultrasonic humidifier.
- 3. Transport: Aerosol mist is transferred into the CVD reactor *via* the carrier gas, such as compressed air, N<sub>2</sub> and Ar, and then delivered to the heated substrate surface
- 4. Film deposition: With the high temperature effect, the solvent evaporates when the precursor solution droplets encounter the heated substrate, and then the solid film composed of desired materials starts to grow on the substrate. The exhaust including the unreacted precursor and by-products is carried out at the end of the reactor with the carrier gas flow.

Through changing parameters such as the kind of solvents, concentration of precursor solutions, substrate temperatures, the flow rate of carrier gases, and deposition time, the morphologies and thickness of deposited films can be modified in the AACVD process.<sup>2</sup> In addition, the kind of carrier gases can be changed easily depending on the requirement of the reaction atmosphere, especially convenient for air- or moisture-sensitive chemicals.

In a traditional CVD process, precursors in vapour phases are introduced directly into the reactor, and then chemical reactions and film deposition occur on the substrate. However, in AACVD, the precursors are dissolved in solvents to form an aerosol, subsequently carried to the substrate surface. Because the AACVD process depends on the solubility but not the volatility of precursors, a wide range of suitable precursors can be chosen in AACVD. Furthermore, AACVD can be performed at atmospheric

pressure, and a less complicated assembled instrument than that in the traditional CVD process is required for AACVD. Therefore, the cost of AACVD is significantly reduced, and it is easier to achieve large-scale film deposition.

Until now, a large number of materials has been synthesized by AACVD, including metals, metal oxides and organic–inorganic hybrid materials, and applied in various fields, such as thin-film solar cells, gas sensors and photocatalysis.<sup>3,4</sup>

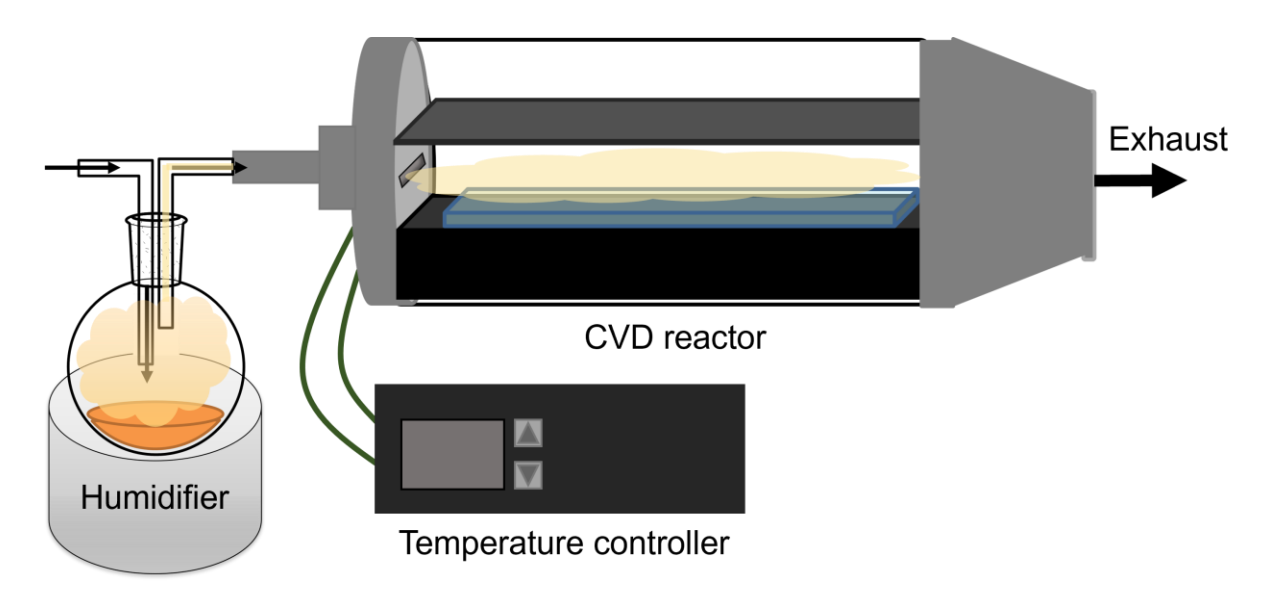


Figure 1-1. Illustration of AACVD setup. From left to right, the inert gas is used to transfer the precursor solution (orange) as a mist, which is generated using an ultrasonic humidifier, into the reactor. A top plate was suspended above the glass substrate to ensure a laminar flow. The film is deposited on the heated substrate in the reactor. The deposition temperature is controlled by a temperature controller. Byproducts and unreacted precursors leave the reactor through the exhaust with the carrier gas.

#### 1.2 Semiconductors

#### 1.2.1 Energy bands in semiconductors

Electrons in an atom occupy orbitals with discrete energy levels in a semiconductor. Due to the interaction among atomic orbitals, these discrete energy level split into a band of levels, and finally a continuous energy band can be formed.<sup>5</sup> At absolute zero, the frontier band occupied by electrons fully is termed as the valence band (VB), while the frontier band which is vacant is termed as the conduction band (CB). The energy

gap separating the VB and CB is the forbidden band. The difference between the top of VB ( $E_v$ ) and the bottom of CB ( $E_c$ ) is the bandgap energy ( $E_g$ ).  $E_g$  of semiconductors are normally in the range of 1 eV to 4 eV. For semiconductors, the Fermi level ( $E_f$ ) is thermodynamically defined as the energy level where the probability to find electrons is 50% at 0K (Figure 1-2).

In a semiconductor, if electrons are thermally excited from the VB to CB, unoccupied states will appear simultaneously in the VB and be regarded as holes. These electrons and holes tend to recombine after radon motions in the lattice. The average time of two continuous processes including the generation and recombination of electron-hole pairs is called the lifetime of these charge carriers. The concentration of electrons (n) in the CB and holes (p) in the VB is given as follows:

$$n = N_C \times e^{\frac{-(E_C - E_f)}{kT}}$$
, with  $N_C = 2 \times (\frac{2\pi m_e^* kT}{h^2})^{\frac{3}{2}}$ 

$$p = N_V \times e^{\frac{-(E_f - E_v)}{kT}}$$
, with  $N_V = 2 \times (\frac{2\pi m_h^* kT}{h^2})^{\frac{3}{2}}$ 

where  $N_C$  and  $N_V$  are the effective density of states for the CB and VB, respectively;  $m_e^*$  and  $m_h^*$  are the effective mass of electrons and holes; k is Boltzmann constant; T is the temperature and h is Planck's constant.<sup>7</sup>

And the conductivity of the material is expressed as:

$$\sigma = ne\mu_e + pe\mu_h$$

where  $\mu_e$  and  $\mu_h$  are the mobility of electrons and holes respectively.<sup>7</sup>

The intrinsic semiconductor is referred to as a semiconductor without impurities or defects. In an intrinsic semiconductor,  $n = p = n_i$  during the generation of charge carriers, where  $n_i$  is the intrinsic carrier concentration.  $E_f$  of an intrinsic semiconductor in equilibrium is in the middle of the band gap approximately.<sup>6</sup>

In practical applications, impurities and defects are often intentionally introduced into materials through doping to obtain semiconductors with desired properties, such as improved conductivity, because intrinsic semiconductors typically possess a low concentration of charge carriers under ambient conditions. These doped materials are called extrinsic semiconductors. Impurities providing electrons to the CB are referred

to as donors, and the resulting semiconductor is called n-type, where electrons are the majority carriers. In this case,  $E_f$  in the semiconductor is closer to  $E_c$ , as shown in Figure 1-2. The p-type semiconductor results from acceptor impurities which contribute holes to the VB, where holes are majority carriers, and  $E_f$  in the semiconductor shifts towards  $E_v$  (Figure 1-2).8 Both donors and acceptors lie in the band gap of the semiconductor (Figure 1-3). If their positions are close to  $E_c$  and  $E_v$  respectively, donors and acceptors are called shallow. Otherwise, they are called deep. Besides foreign dopants, native defects commonly exist as well to influence the performance of semiconductors, such as vacancies, interstitials and antisite defects.

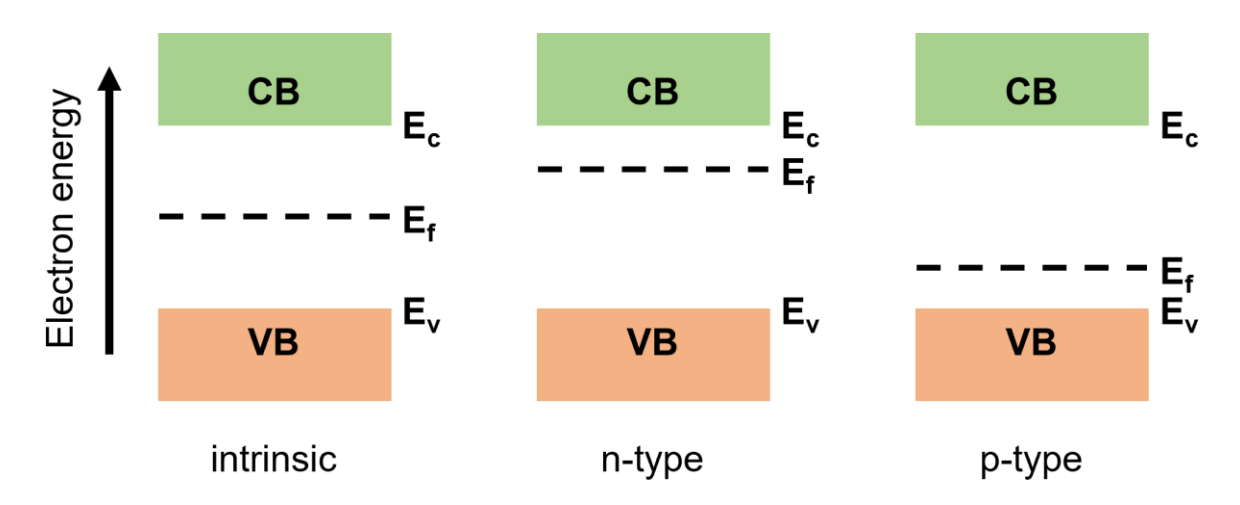


Figure 1-2. Band diagram of the intrinsic semiconductor, n-type semiconductor, and p-type semiconductor.

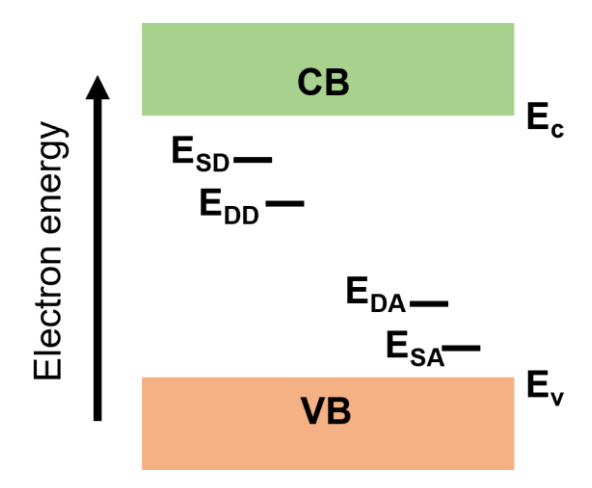


Figure 1-3. Band diagram of shallow and deep donor (SD and DD) and acceptor (SA and DA) levels in the semiconductor.

#### 1.2.2 Direct and indirect bandgap semiconductors

During the process of electron transitions in a semiconductor, both energy and momentum need to be conserved. When the valence band maximum (VBM) and conduction band minimum (CBM) of a semiconducting material are at the same point in the k space, electron transitions are direct, and this kind of materials is termed as a direct bandgap semiconductor (Figure 1-4a). If the VBM and CBM are positioned at different k vectors, electron transitions in the semiconductor from VB to CB require a change in the momentum, so this kind of materials are termed as indirect bandgap semiconductors (Figure 1-4b).<sup>7</sup>

In a fundamental absorption process of a direct bandgap semiconductor, a photon with energy greater than the E<sub>g</sub> is absorbed and then the electron in the filled VB can be excited and transfer to the empty CB. Photons carry little momentum, so electron transitions assisted by photons are vertical. However, in the indirect bandgap semiconductor, the absorption of extra particles, such as phonons, is required due to the momentum conservation. Electron transitions assisted by phonons are typically horizontal. As a result, electron transitions in the indirect bandgap semiconductor are less likely to occur than in the direct bandgap semiconductor.<sup>9</sup>

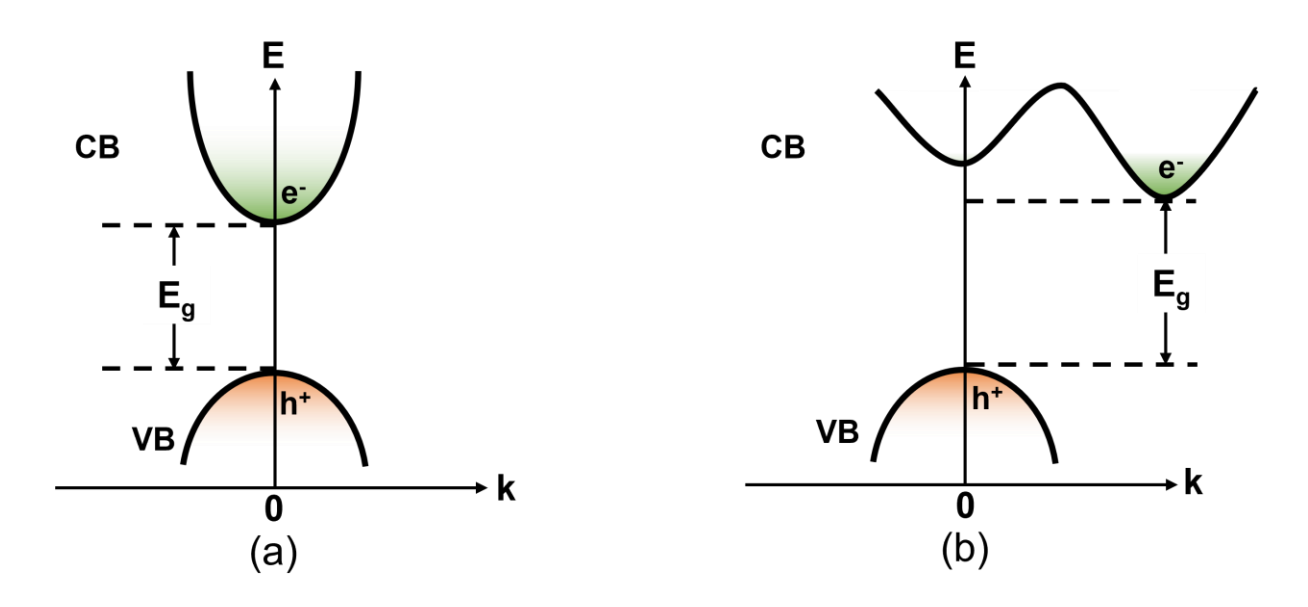


Figure 1-4. Energy band diagram of (a) direct bandgap and (b) indirect bandgap semiconductors.

#### 1.2.3 Heterojunctions

Heterojunctions refer to the junctions formed between two semiconductors with different energy band structures. Heterojunctions dramatically widen the choices for various devices based on semiconductors, such as photocatalysts, diodes and optoelectrical devices. Through the formation of a heterojunction, the transport of charge carriers is able to be controlled. Several conditions need to be satisfied to achieve high-quality heterojunctions, including that the crystal structures, lattice constants and thermal expansion coefficients of the two semiconductors are similar to minimize the mismatch strain and defect formation.<sup>7</sup>

According to the conductivity type of the individual semiconductors, heterojunctions can be divided into isotype heterojunctions constituted by semiconductors with the same conductivity type, such as p-p junctions and n-n junctions, and anisotype heterojunctions constituted by semiconductors with different conductivity types, for example p-n junctions.<sup>7</sup>

In addition, classified by the energy band alignments of the formed heterojunctions, there are three main types of heterojunctions, including type-I heterojunctions with straddling gaps, type-II heterojunctions with staggered gaps and type-III heterojunctions with broken gaps (Figure 1-5).<sup>10</sup> In the type-I heterojunction, the CBM of the semiconductor **A** is higher than that of semiconductor **B** while the VBM is lower, so both electrons and holes transfer from **A** to **B** and finally accumulate in **B**, leading to serious recombination of electrons and holes. However, in the type-II semiconductor, electrons can transfer from semiconductor **B** with the higher CBM to **A** and holes can transfer from semiconductor **A** with the lower VBM to **B**. Thus, the charge carriers are separated effectively in the heterojunction. No charge transport between two semiconductors happens in the type-III heterojunction. Therefore, the type-II heterojunction is the most desired in practical applications.<sup>11,12</sup>

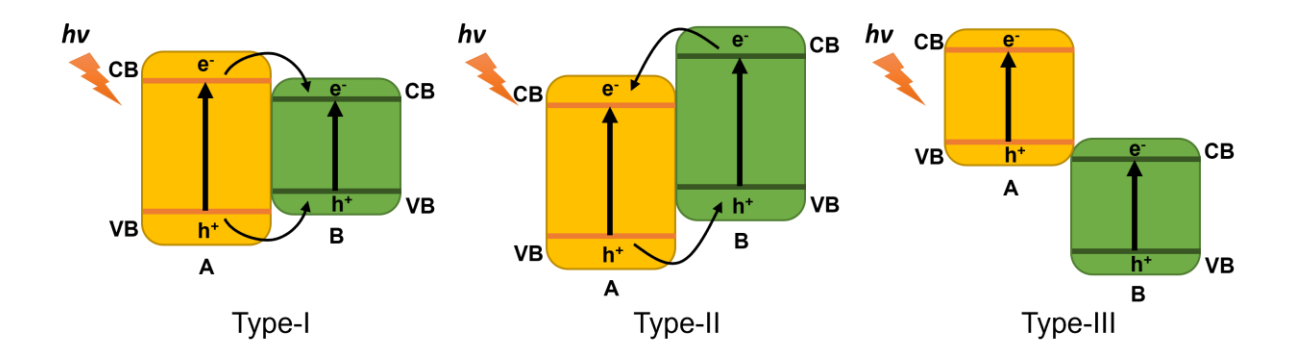


Figure 1-5. Schematic diagram of the energy band alignment of type-II and type-III heterojunctions.

#### 1.3 Characterization techniques

#### 1.3.1 Photoluminescence spectroscopy

Photoluminescence (PL) spectroscopy is a kind of nondestructive and noncontact technique to probe both intrinsic and extrinsic properties of semiconducting materials, such as band structures, charge transfer behaviors, defects and impurities, and so on. Due to its powerful functions and the simple and low-cost setup, the PL measurement has been widely used in both lab and industry until now. A simplified setup for the PL measurement is given in Figure 1-6. The excitation beam with a single wavelength is obtained after the light goes through the filter. Then, the sample is irradiated and excited by the beam. The luminescence produced by the sample can be filtered and detected by the detector. Generally, the detector is positioned at 90° to the light source in order to minimize the amount of the collected scattered light.

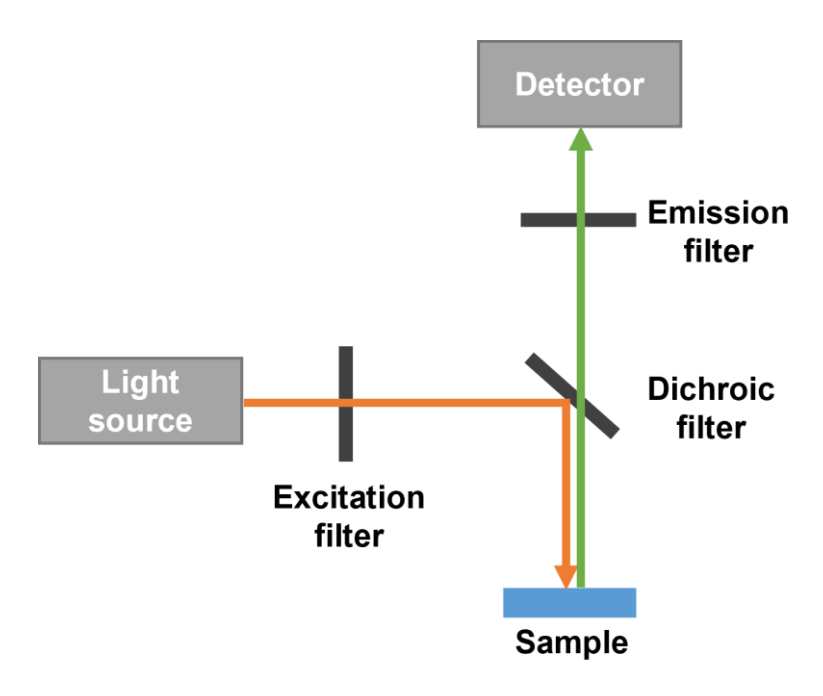


Figure 1-6. Schematic diagram of a simplified setup for the PL measurement.

PL spectroscopy depends on the luminescence phenomenon of semiconducting materials. The diagram illustrating the PL principle is shown in Figure 1-7. When their energy is equal or greater than the band gap energy of the semiconductor, photons from the excitation source can be absorbed by the semiconductor. Electrons in the VB can be excited by these photons with holes left. These electrons stay in the permissible excited states high up in the CB for a very short time (~10<sup>-13</sup> s), and then jump to the bottom of the CB through a non-radiative relaxation process, accompanied by the emission of phonons. 14 If defects and impurities exist in the semiconductor, trap states are also possible to be formed below the CBM. Therefore, electrons will further relax to trap states. Electrons in the CB and trap states tend to go back to the VB at the lower energy level and recombine with holes. If this return process is radiative, luminescence photons will be generated. Through collecting and analysis of these photons, abundant information about the optoelectrical characterizations of the excited semiconductor can be obtained. Furthermore, in the PL measurement, the observation of photons with the energy lower than the bandgap energy of the material is the characteristic of defects. The concentration of defects can even be available through the quantification of PL signals. As a result, PL spectroscopy is a direct and convenient way to determine the defect formation in the study of semiconductors.

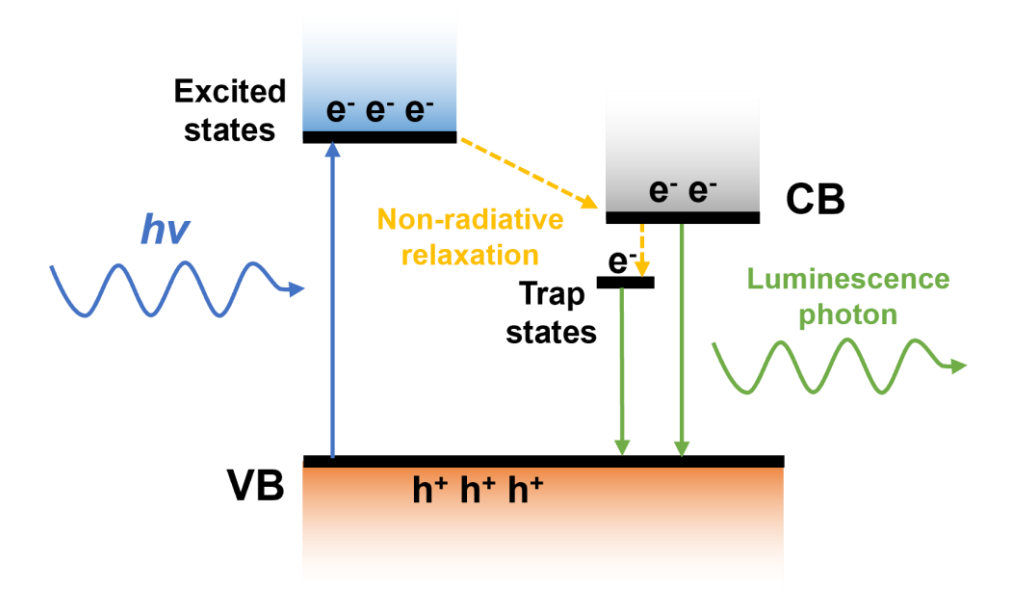


Figure 1-7. Schematic diagram of the principle of PL spectroscopy in semiconductors.

The above detailed PL process is described based on the direct bandgap semiconductors, however the indirect bandgap semiconductors have some differences in the PL process. 13,14 As aforementioned, for the direct bandgap semiconductor, CBM and VBM have the same k vector, so the recombination of electrons and holes can occur directly, with photons emitted. The lifetime of this radiative process is short (10<sup>-8</sup>–10<sup>-9</sup>). However, in the indirect bandgap semiconductor, the points of CBM and VBM are different in the Brillouin zone (Figure 1-8b). The electron and hole must be in the same **k** vector before the recombination. Therefore, in the luminescence process, a phonon has to be absorbed or emitted for the conversation of the momentum.<sup>14</sup> The emission of both phonon and photon makes this recombination transition a second-order process which is less probable than the direct recombination. For example, the possibility of the radiative transition happening in the direct bandgap semiconductor, InSb, is 10<sup>5</sup> times higher than that of silicon with the indirect band gap. In addition, the lifetime of the excited electrons in the indirect bandgap semiconductor is 106-108 times longer than that of the direct bandgap semiconductor.13

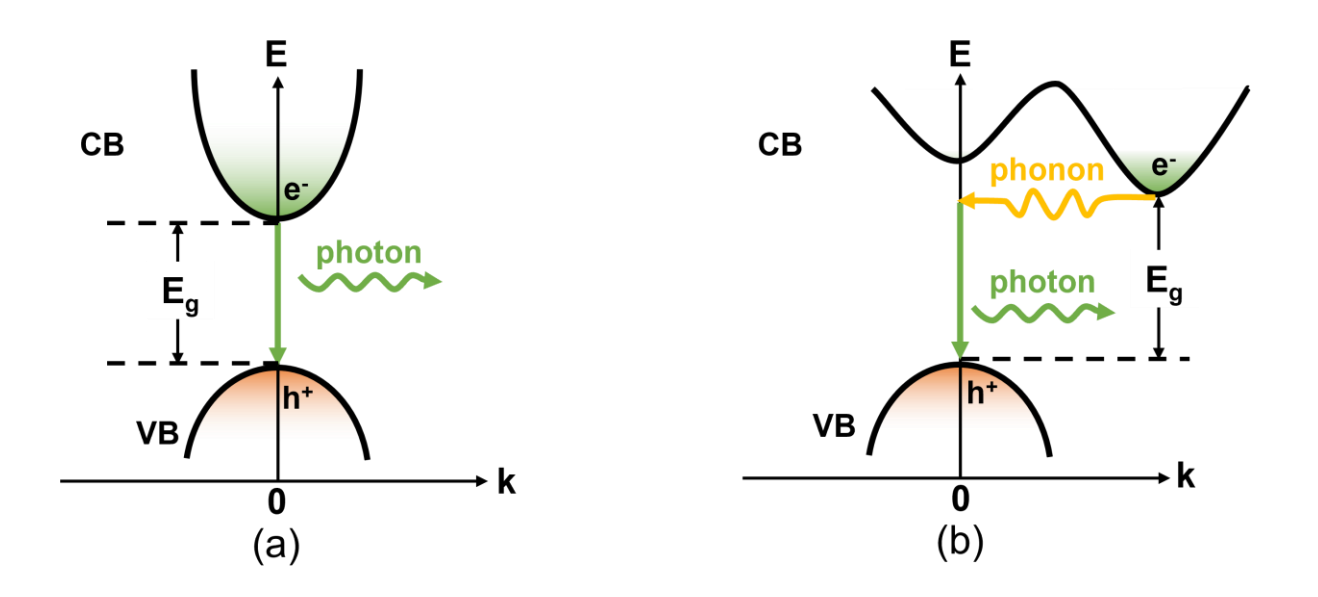


Figure 1-8. Schematic diagram of the photon emission process in the (a) direct and the (b) indirect band gap semiconductors.

PL spectroscopy has found widespread applications in various fields. <sup>15</sup> It is widely employed to investigate the surface processes in photocatalysis due to the inherent correlation between photocatalytic activities and PL signals, providing a lot of information about defects, band structures, and photochemical properties of semiconducting materials. <sup>16</sup> In addition, PL spectroscopy is a useful technique for the confirmation of the quantum confinement in nanocrystals. <sup>17</sup> PL measurement is able to be carried out *in situ*. Therefore, the dynamics of charge transport, defect formation and intermediates during reactions can be investigated *operando*. <sup>18–20</sup> Furthermore, the interfaces between two solid semiconductors, semiconducting materials and liquid, semiconducting materials and gas can all be characterized by PL spectroscopy as well. <sup>21–23</sup>

#### 1.3.2 Transient absorption spectroscopy

Transient absorption spectroscopy (TAS) is a pump-probe spectroscopic technique which has been widely used to study the dynamics of photogenerated charge carriers in semiconductors. A typical setup of TAS is shown in Figure 1-9.<sup>24</sup> Firstly, the measured sample is excited by a pulse of light with a specific wavelength, typically in the form of a laser. After a short delay, the sample is irradiated by the light from a lamp going through a series of lenses, which is known as the probe light. A long-pass filter will be used if the photoexcitation of the sample can be caused by this probe light. The

probe light is normally in the visible and near-infrared range. The transmitted probe light is detected by a photodetector after passing a monochromator. The difference in absorption before (ground state) and after (excited state) the laser ( $\Delta A$ ) will be measured. In addition, through changing the delay time between the excitation pulse and probe light, the  $\Delta A$  could be profiled as a function of the time and wavelength finally,<sup>25</sup> where the information about the excited states or transient species can be collected and analysed.

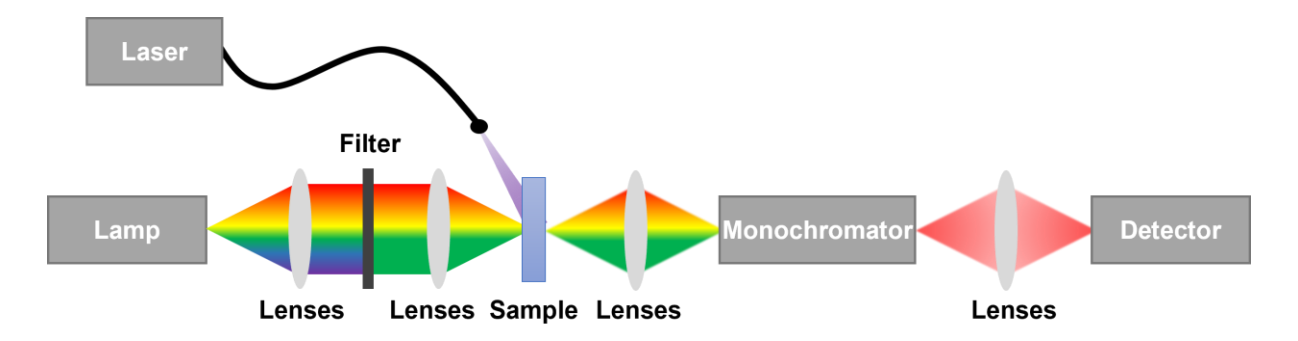


Figure 1-9. Schematic diagram of a typical TAS setup.

The simplified principle of TAS in semiconductors is illustrated in Figure 1-10. Generally, three main processes contribute to the transient absorption spectrum. The first process is ground state bleach. After numerous electrons in the semiconductor are excited from VB to CB by the laser pulse, the charge carriers at the ground state are less. As a result, the ground state absorption of the excited sample is weaker than that in the pre-excited, leading to negative bleach signals observed within the wavelength range of the ground state absorption in the spectrum. The second process is stimulated emission. The excited electrons in CB tend to jump back to VB with lower energy, and this process is often companied with the energy emission. The photon generated from the stimulated emission is in the same direction as the probe light, and thus both are collected by the detector. The detected increased light intensity leads to negative signals. The third process is excited state absorption. Due to the existence of defects and vacancies in the semiconducting material, the trap states can be formed between VB and CB. Therefore, the electron transition can occur in specific wavelength regions from the trap states to CB in a higher energy level, and the probe light at these wavelengths will be absorbed. Thus, positive signals in the spectrum are observed.25

TAS can be measured in either ultrafast (fs to ns) or slower (ms to s) timescales. Processes such as nongeminate and geminate recombination (recombination happening prior to the separation of charge carriers) are able to be detected in ultrafast timescales.<sup>26,27</sup> In addition, electrons or holes can be detected individually in TAS by using scavengers, <sup>28</sup> and the photocatalytic kinetics can also be determined in diverse fields through the selective study of electrons and holes in TAS, such as photocatalytic oxidation of adsorbed alcohols, 29 deoxygenation 30 and water oxidation. 31 The separation of photogenerated electrons and holes in the heterojunction can be monitored as well.<sup>32</sup> Furthermore, TAS has been widely utilized to study the charge carrier dynamics in the PEC water oxidation process.<sup>33,34</sup> it is worth mentioning that because the principle of TAS is to detect changes in light transmission passing through the tested samples, besides radiative processes, nonradiative processes are also able to be observed directly, which cannot be achieved by PL spectroscopy.<sup>25</sup> Based on plenty of research, it can be concluded that TAS plays a great role in studying the separation, transfer and recombination of photogenerated charge carriers in semiconducting materials.<sup>24</sup>

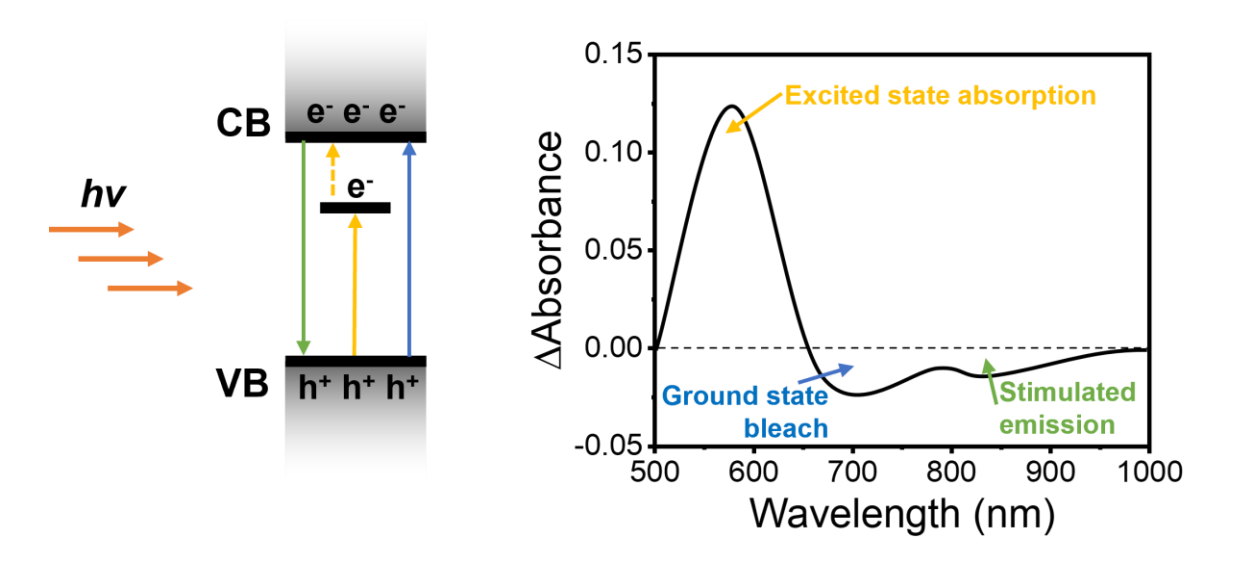


Figure 1-10. Schematic diagram of the principle of TAS in semiconductors.

#### 1.4 Photoelectrochemical water splitting

In recent decades, there has been an increasing awareness about fossil fuel depletion and serious environmental pollution resulting from the use of fossil fuels. In 2020, the global human energy consumption increased to  $5 \times 10^{20}$  joules,<sup>35</sup> and this number

continues to grow. Every year,  $3 \times 10^{24}$  joules of energy from the Sun can reach to the Earth, which is nearly  $10^4$  times the current energy demand. Therefore, taking full advantage of such a huge amount of solar energy could solve the issues around energy shortage effectively. Compared with gasoline, hydrogen has around 4 times higher mass energy density. In addition, it can be consumed directly or in other ways, like combustion engines and fuel cells. Hydrogen is also storable and transportable. More importantly, there are no pollutants produced during the consumption of hydrogen, so carbon emission can be reduced significantly. As a kind of versatile and clean fuel, hydrogen is going to play a crucial part in the sustainable development of society. Since the first report about PEC water oxidation on a  $TiO_2$  photoelectrode in 1970s,  $^{36}$  PEC water splitting has been investigated extensively and regarded as a promising approach to convert solar energy into usable fuels, such as hydrogen and oxygen. In theory, n-type semiconductors can be used as photoanodes for water oxidation, and p-type semiconductors can be used as photocathodes in PEC water splitting for water reduction.

#### 1.4.1 Mechanism involved in PEC water splitting

In the view of thermodynamics, water splitting is an unfavorable reaction with the Gibbs free energy ( $\Delta G$ ) of +237.2 kJ·mol<sup>-1</sup>. According to the equation:

$$\Delta G = -nFE$$

where n is the number of moles of electrons transferred and F = 96500 C·mol<sup>-1</sup>, it can be obtained that the redox potential of water splitting is 1.23 V<sub>NHE</sub> at 298K and neutral pH.<sup>37</sup> Therefore, energy is necessary to drive this reaction, provided by both light and electricity in PEC water splitting.

The mechanism of PEC water splitting based on the n-type semiconductor is illustrated in Figure 1-11. When the semiconducting photoanode contacts with the electrolyte, electron transfer happens between them to achieve the equilibrium of the Fermi level of the semiconductor and the redox potential of the electrolyte, which leads to the band bending and the formation of space charge region. Three main steps are involved in the PEC water splitting process. The first step is the light absorption by the photoanode. The n-type semiconductor can absorb the incident photons with the energy (hv) larger than its band gap energy ( $E_g$ ), in which electrons are excited to CB with holes left in

VB. Under irradiation, electrons and holes with non-equilibrium populations are generated, whose electrochemical potential can be described as electron quasi-Fermi level ( $E_{f,n}$ ) and hole quasi-Fermi level ( $E_{f,n}$ ) individually. The electron potential of the counter electrode equals to  $E_{f,n}$ . Secondly, charge carriers are separated and transported. Photogenerated holes accumulate on the photoanode surface, while electrons are transported to the metal counter electrode through the external circuit. However, these charge carriers are also possible to recombine in the bulk or on the surface. Finally, redox reactions occur on the surface of electrodes. For the photoanode, the VBM level has to be more positive than the  $O_2/H_2O$  potential (1.23  $V_{NHE}$ ) to allow the water oxidation. In the whole process, energy is consumed when photogenerated holes go through the space charge region and electrons are transported to the counter electrode through the circuit. Therefore, extra overpotential needs to be applied to compensate for these energy losses.<sup>39</sup>

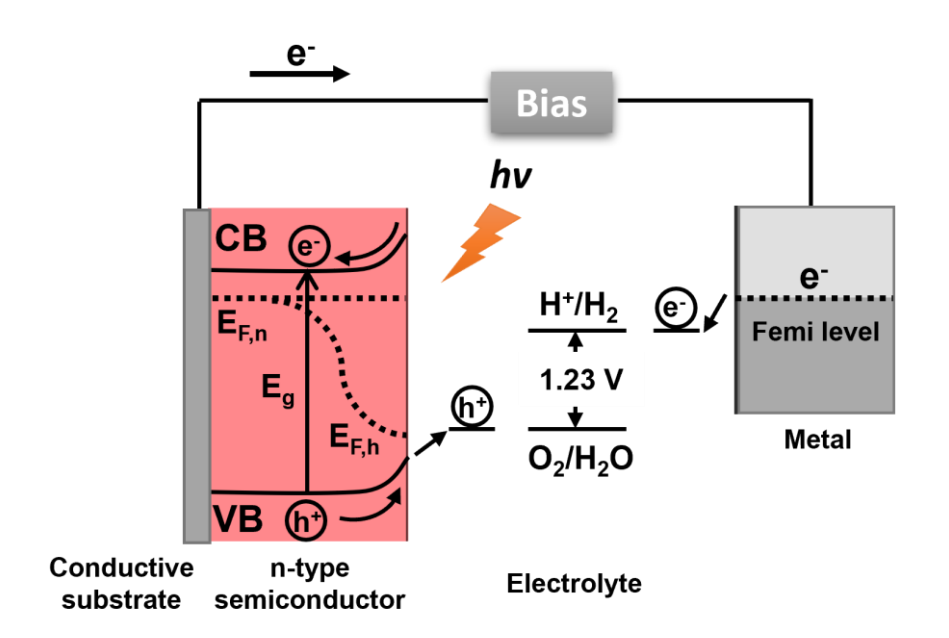


Figure 1-11. Schematic diagram of a simplified PEC system with a n-type semiconductor as the photoanode and a metal as the counter electrode.

For above PEC water splitting in a neutral electrolyte, specific reactions happen on different electrodes. On the photoanode, the oxygen evolution reaction (OER) can be driven by the holes, which can be explained as follows:

$$H_2O + 2h^+ \rightarrow 1/2O_2 + 2H^+$$

At the same time, with the effect of electrons, the hydrogen evolution reaction (HER) can occur on the counter electrode, which is:

$$2H^+ + 2e^- \rightarrow H_2$$

Therefore, the overall reaction involved in the PEC water splitting is:

$$2H_2O \rightarrow O_2 + 2H_2$$

Typically, besides the photoanode-counter electrode cell (Figure 1-12a) mentioned above, there are two other kinds of PEC water splitting configurations, including the photocathode-counter electrode cell, with the p-type semiconductor as the photocathode (Figure 1-12b), and photoanode-photocathode tandem cell (Figure 1-12c).<sup>38</sup>

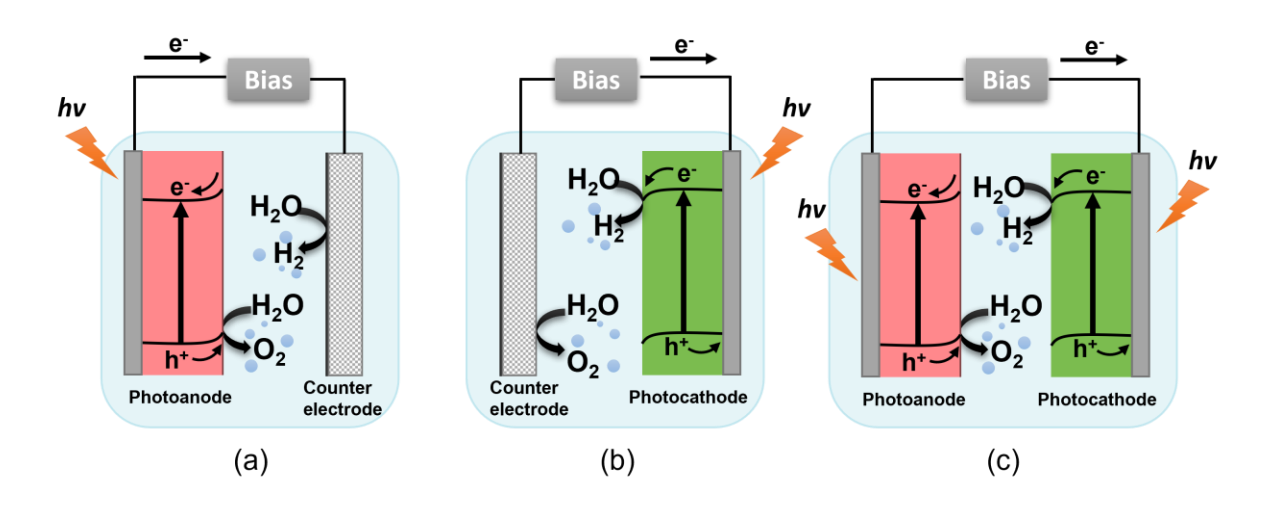


Figure 1-12. Schematic diagram of PEC water splitting systems using (a) a photoanode, (b) a photocathode and (c) photoanode and photocathode.

## 1.4.2 PEC measurement setup

Based on the introduced mechanism, it can be seen that the photoelectrode is the most crucial part in PEC water splitting and searching for semiconducting photoelectrodes with better performance is the main objective in relative studies. There are several requirements of semiconducting materials for PEC water splitting. Firstly, semiconductors need to have narrow band gaps for a great light absorption capacity. In addition, the band gap energy must be larger than 1.23 eV and the band positions have to be suitable to drive redox reactions in water splitting. Secondly, efficient separation and transportation of photogenerated electrons and

holes are necessary for highly active photoelectrodes. Thirdly, materials used as photoelectrodes should be stable and robust enough to stand the long-term use in various environments. Finally, for practical applications and industrialization, these materials should be cheap and non-toxic. Several n-type semiconducting materials with earth-abundant elements, such as BiVO<sub>4</sub>,<sup>41</sup> Fe<sub>2</sub>O<sub>3</sub>,<sup>42</sup> and WO<sub>3</sub>,<sup>43</sup> have shown great potentials as photoanodes. In addition, for photocathodes, Cu-based metal oxides have been investigated widely.<sup>44</sup>

A basic measurement setup for PEC water splitting, is shown in Figure 1-13, which consists of a light source, a PEC cell, a potentiostat and a computer. A Xe lamp equipped with filters, or a monochromator is often used as the light source for the sunlight simulation or to produce monochromatic light. PEC reactions are typically performed in an enclosed reactor with a flat optical window. A three-electrode system is used to measure the activity of the photoelectrode, where the n-type semiconductor works as the photoanode while the p-type semiconductor as the photocathode. This system is composed of a working electrode (photoelectrode), reference electrode (such as Ag/AgCl electrode) and counter electrode (such as platinum mesh) immersed in an electrolyte, and a potentiostat is used to control the applied voltage on the working electrode with respect to the reference electrode. Finally, the currents under illumination and in the dark are recorded and plotted as a function of the potential or time.

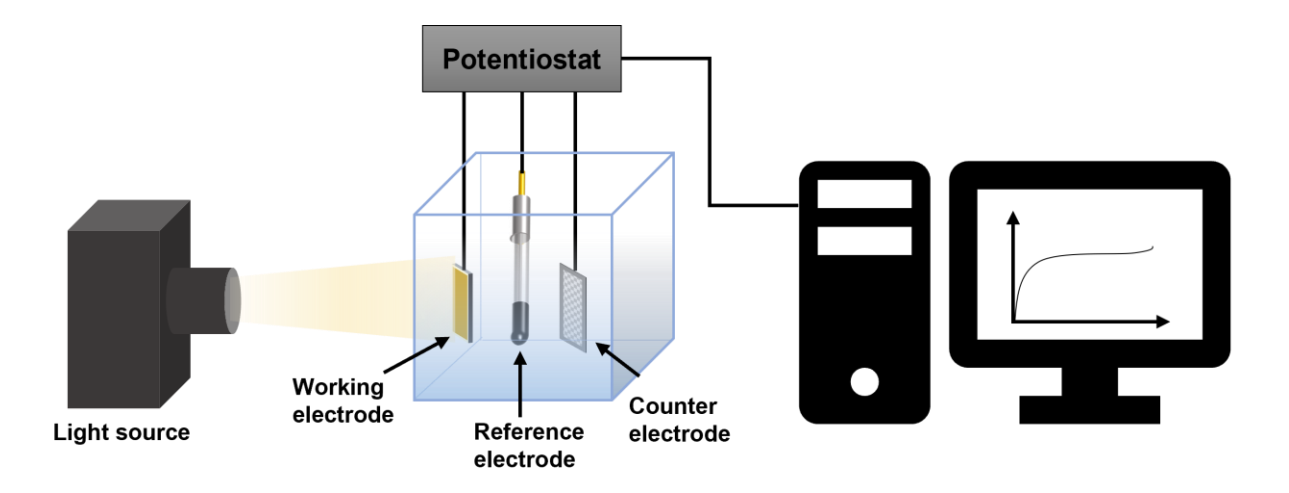


Figure 1-13. Schematic diagram of a basic PEC measurement setup.

### 1.4.3 Performance indicators

In order to quantify and compare the PEC performance of various semiconductors, some key indicators are identified and introduced as follows.

# 1.4.3.1 Current density-voltage curve

Photocurrent density is the most common value collected in the PEC measurement. Through sweeping the applied voltage (*V*), the current density (*J*) is recorded and plotted as a *JV* curve. Firstly, the measurement is proceeded in the dark, and normally no photocurrent can be observed. Then, the PEC measurement under irradiation is conducted in the same voltage range, where positive or negative photocurrents can be generated from the photoanode or photocathode respectively.<sup>38</sup> In *JV* curves, the onset potential at which the photocurrent start to be observed, and the photocurrent at the thermodynamic potential of water oxidation (1.23 V<sub>NHE</sub>) for the photoanode or water reduction (0 V<sub>NHE</sub>) for the photocathode can be obtained.

The applied voltage in *JV* curves is typically reported against the reversible hydrogen electrode (RHE), converted by the Nernst equation:

$$V_{RHE} = V_{app(RE)} + 0.05916 \text{ pH} + V_{RE}^{\emptyset}$$

where  $V_{app(RE)}$  is the applied potential versus the reference electrode (RE), pH is the electrolyte pH and  $V_{RE}^{\emptyset}$  is the standard potential of RE.

### 1.4.3.2 Incident photon-to-current efficiency

Incident photon-to-current efficiency (IPCE) is identified as the proportion of incident photons utilized to produce the photocurrent density within a specific wavelength range.<sup>40</sup> In the IPCE measurement, the photoelectrode is irradiated by monochromatic light at a constant voltage.

The IPCE can be calculated using the following equation:

IPCE (%) = 
$$(I \times 1239.8)/(P_{mono} \times \lambda) \times 100$$

where J is the photocurrent density, 1239.8 is from multiplying Planck's constant (4.14  $\times$  10<sup>-15</sup> eV·Hz<sup>-1</sup>) and the speed of light (3.0  $\times$  10<sup>8</sup> m·s<sup>-1</sup>),  $P_{mono}$  is the light power, and  $\lambda$  is the wavelength of the monochromate light.

## 1.4.3.3 Applied bias photon-to-current efficiency

The electrical energy from the external voltage applied to the PEC system should be subtracted to evaluate the performance of photoelectrodes. Thus, the applied bias photon-to-current efficiency (ABPE) is frequently used and calculated from the equation:

ABPE (%) = 
$$J \times (1.23 \text{ V}_{RHE} - \text{V}_{app}) / \text{Plight} \times 100$$

Where *J* is the photocurrent density, V<sub>app</sub> is the applied voltage vs. RHE, and P<sub>light</sub> is the power density of the light source.<sup>45</sup>

# 1.4.3.4 Theoretical solar photocurrent

Due to the unavoidable mismatch between the artificial light source and real sunlight, the theoretical solar photocurrent (TSP) is used to compare the performance of photoelectrodes under AM 1.5 G sunlight, which can be calculated by multiplying the IPCE with the AM 1.5 solar spectrum, then converted into the photocurrent density:

$$TSP = \int_{3000nm}^{280nm} IPCE \times AM \ 1.5 \ (photon \cdot cm^{-2}) \times 1000/1C$$

Where 1C is  $6.241 \times 10^{18}$  electrons per second.<sup>46</sup>

### 1.4.3.5 Faradaic efficiency

Faradaic efficiency is the value to quantify the fraction of the measured photocurrent which is generated from PEC water splitting reactions but not photocorrosion or other undesired reactions occurring on the photoelectrode. Faradaic efficiency can be obtained from dividing the measured amount of oxygen or hydrogen by the predicted amount calculated from the measured photocurrent, which is explained by the equation:

$$\eta \ (\%) = \frac{N_{Measured}}{\frac{J \times A}{n \times F}} \times 100$$

where N<sub>measured</sub> is the molar flux of measured oxygen or hydrogen, *J* is the photocurrent density, A is the photoelectrode area, F is Faraday constant (96485 C⋅mol<sup>-1</sup>), and n is the electron stoichiometry, which is 4 for the water oxidation reaction and 2 for water reduction.<sup>40</sup>

## 1.5 Photocatalysis

In order to meet the huge demand of the population increase and economic development in last decades, industrial and agricultural activities have achieved the rapid growth. However, the serious environmental pollution also came worldwide at a cost, with poor air and water qualities, and the destruction to ecosystems. Therefore, while challenging, it is of great importance to find effective ways to remove toxic pollutants from industrial wastewater and exhaust gas.<sup>47</sup> So far, numerous physical and chemical treatments have been put forward, such as physical adsorption, chemical adsorption, electrochemical treatments and photocatalysis.<sup>48–53</sup> Among them, photocatalysis has gained great attention because of its potential in the field of pollution remediation. In the photocatalysis process, the sunlight could be used to initiate chemical reactions of various pollutants with the effect of photocatalysts, and then the toxic organic compounds can be degraded into smaller and less harmful molecules or even decomposed completely.<sup>54</sup> As a result, photocatalysis is both an economic and eco-friendly method to solve environmental concerns.

# 1.5.1 Mechanism involved in photocatalysis

The basic principles of the photocatalysis process in semiconductors are summarized by the schematic diagram in Figure 1-14. When the semiconductor, as the photocatalyst, is irradiated by a light source with the energy equal or higher than its E<sub>g</sub>, it will be excited by absorbed photons and then generate electron-hole pairs (e<sup>-</sup>-h<sup>+</sup>). These photogenerated e<sup>-</sup>-h<sup>+</sup> will separate, and transfer to the surface of the semiconductor to initiate reduction and oxidation reactions respectively. <sup>55</sup> However, some e<sup>-</sup> and h<sup>+</sup> will recombine at the surface or in the bulk. During the recombination process, the energy can be released in the form of photons (radiative recombination) or phonons (nonradiative recombination). <sup>56</sup>

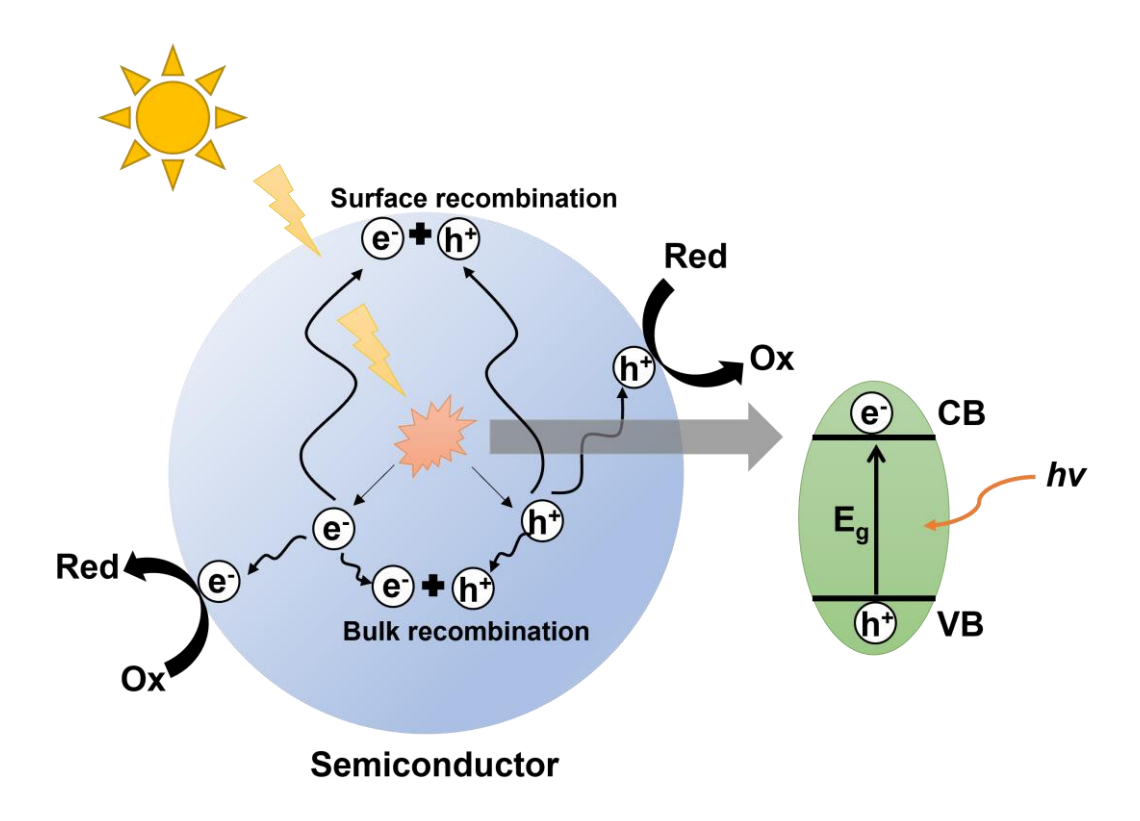


Figure 1-14. Schematic diagram of photocatalysis mechanism in semiconductors.

There are three critical steps in the photocatalytic process based on the above analysis of the mechanism, including solar light harvesting, separation and transportation of charge carriers, and photocatalytic redox reactions.<sup>57</sup> Therefore, the intrinsic properties of photocatalysts have significant influence on the photocatalytic efficiency, and semiconductors with narrower band gaps, lower charge carrier effective masses and more active sites are more desirable in photocatalysis.

Challenges still remain for photocatalysis although it has shown great potential in environmental applications. The underlying mechanisms of photocatalysis vary with kinds of pollutants and photocatalysts. The investigation of more efficient and cheaper photocatalysts and their scale-up production are also ongoing. Furthermore, by-products and environmental impacts of photocatalytic processes should be considered for the overall sustainability. Many traditional semiconducting materials, such as silicon and various metal oxides (TiO<sub>2</sub>, ZnO, Fe<sub>2</sub>O<sub>3</sub>, WO<sub>3</sub> and Cu<sub>2</sub>O), have been utilized in diverse photocatalytic applications, such as water splitting, CO<sub>2</sub> reduction and organic pollutants degradation, and photocatalytic activities of these materials continue to be improved through structural control, doping and building heterojunctions.<sup>50</sup>

## 1.5.2 Smart ink photocatalytic test

Organic dyes such as Rhodamine B, methyl orange and methylene blue have been widely used as indicators of the photocatalytic activity in photocatalytic measurements. However, their decomposition rate is normally slow (>1 hour), and UV-Vis spectroscopy is necessary to monitor the photocatalytic progress, 58 leading to high cost of time, labour and equipment. Furthermore, the popular testing routes based on these dyes are specially designed for powder samples, which is not suitable in the photocatalytic measurement of films.<sup>59</sup> Recently, a standard smart ink, which is an aqueous hydroxyethyl-cellulose solution containing the redox dye resazurin (Rz) and the sacrificial electron donor glycerol was reported to probe the photocatalytic performance of semiconductors, especially semiconducting films. 60 This photocatalyst ink operates through a photo-reductive mechanism (Figure 1-15). Holes generated through the photoexcitation of the photocatalytic film can react irreversibly with the sacrificial electron donor (SED), such as glycerol, whereas the blue Rz dye can be reduced irreversibly to the pink resorufin (Rf) by photogenerated electrons, and also possibly to the further bleached form, dihydroresorufin (HRf), which can be reoxidized to Rf by ambient oxygen. 61 Structures of the indicator dye Rz, its initial reduced form Rf and the second reduced form HRf are shown in Figure 1-16. In this process, the colour change rate of the Rz ink (even on the second timescale for highly active films), which is positively related to the photocatalytic activity of semiconductors, is significantly faster than that of traditional photooxidative dyes.<sup>62</sup> In addition, the photoreductive degradation assessment of the Rz ink is able to be analysed quantitatively by red-green-blue (RGB) values of digital images taken by cameras, where no expensive instruments and techniques are needed.<sup>63</sup>

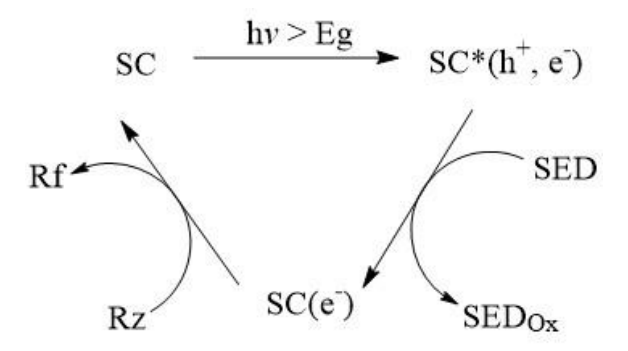


Figure 1-15. Proposed reaction scheme of the photocatalyst ink identifying the major underlying reactions.

Figure 1-16. Structures of the indicator dye, *Rz*, its initial reduced form *Rf*, and further reduced form, *HRf*, which can be reoxidized to *Rf* by ambient oxygen.

Work in this thesis focuses on the film deposition of non-toxic bismuth-based semiconducting materials, including the rarely reported phenethylammonium bismuth iodide and widely studied bismuth oxyhalides. Furthermore, the optimized films based on these materials are investigated in various sustainable applications, such as PEC water splitting and photocatalysis, with attractive performance through morphological control, doping and the construction of heterojunctions. Different from existing research, the preparation and optimization of bismuth-based materials are processed in the film form directly in this thesis, and no extra treatment of films is required for further applications. In addition, due to the utilization of AACVD, the film deposition of above materials is possible to be scaled up. As a result of the described work, great progress of bismuth-based semiconductor coating has been made towards practical applications.

#### 1.6 Reference

- (1) Knapp, C. E.; Carmalt, C. J. Solution Based CVD of Main Group Materials. *Chem Soc Rev* **2016**, *45* (4), 1036–1064. https://doi.org/10.1039/C5CS00651A.
- (2) Marchand, P.; Hassan, I. A.; Parkin, I. P.; Carmalt, C. J. Aerosol-Assisted Delivery of Precursors for Chemical Vapour Deposition: Expanding the Scope of CVD for Materials Fabrication. *Dalt Trans* **2013**, *42* (26), 9406–9422. https://doi.org/10.1039/c3dt50607j.
- (3) Wang, M.; Carmalt, C. J. Film Fabrication of Perovskites and Their Derivatives for Photovoltaic Applications via Chemical Deposition. *ACS Appl Energy Mater* **2022**, *5* (5), 5434–5448. https://doi.org/10.1021/acsaem.1c02612.
- (4) Hou, X.; Choy, K. L. Processing and Applications of Aerosol-Assisted Chemical Vapor Deposition. *Chem Vap Depos* **2006**, *12* (10), 583–596. https://doi.org/10.1002/CVDE.200600033.
- (5) Neamen, D. A. Semiconductor Physics and Devices, Basic Principles; 2012.
- (6) Krishnan Rajeshwar. Fundamentals of Semiconductor Electrochemistry and Photoelectrochemistry. In *Encyclopedia of Electrochemistry*; Wiley, 2002. https://doi.org/10.1002/9783527610426.bard060001.
- (7) Mathematics, A. *Semiconductor Materials*; Microdevices; Kluwer Academic Publishers: Boston, 2003. https://doi.org/10.1007/b105378.
- (8) van de Krol, R. Photoelectrochemical Measurements. In *Springer Handbook of Electrochemical Energy*; Springer Berlin Heidelberg: Berlin, Heidelberg, 2012; pp 69–117. https://doi.org/10.1007/978-1-4614-1380-6\_3.
- (9) Pierret, R. F.; Neudeck, G. W. Modular Series on Solid State Devices VI. Advanced Semiconductor Fundamentals; 1989.
- (10) Low, J.; Yu, J.; Jaroniec, M.; Wageh, S.; Al-Ghamdi, A. A. Heterojunction Photocatalysts. *Adv Mater* **2017**, *29* (20), 1601694. https://doi.org/10.1002/ADMA.201601694.

- (11) Moniz, S. J. A.; Shevlin, S. A.; Martin, D. J.; Guo, Z.-X.; Tang, J. Visible-Light Driven Heterojunction Photocatalysts for Water Splitting a Critical Review. *Energy Environ Sci* **2015**, *8* (3), 731–759. https://doi.org/10.1039/C4EE03271C.
- (12) Li, S.; Xu, W.; Meng, L.; Tian, W.; Li, L. Recent Progress on Semiconductor Heterojunction-Based Photoanodes for Photoelectrochemical Water Splitting. *Small Science* **2022**, *2* (5), 2100112. https://doi.org/10.1002/smsc.202100112.
- (13) Perkowitz, S. Optical Characterization of Semiconductors: Infrared, Raman, and Photoluminescence Spectroscopy; Academic Press, 1993.
- (14) Moore, E. A.; Smart, L. E. Optical Properties of Solids. In *Solid State Chemistry*; CRC Press, 2016; pp 344–369. https://doi.org/10.1201/b12047-14.
- (15) Erbe, A.; Nayak, S.; Chen, Y.-H.; Niu, F.; Pander, M.; Tecklenburg, S.; Toparli, C. How to Probe Structure, Kinetics, and Dynamics at Complex Interfaces In Situ and Operando by Optical Spectroscopy. In *Encyclopedia of Interfacial Chemistry*; Elsevier, 2018; pp 199–219. https://doi.org/10.1016/B978-0-12-409547-2.14061-2.
- (16) Liqiang, J.; Yichun, Q.; Baiqi, W.; Shudan, L.; Baojiang, J.; Libin, Y.; Wei, F.; Honggang, F.; Jiazhong, S. Review of Photoluminescence Performance of Nano-Sized Semiconductor Materials and Its Relationships with Photocatalytic Activity. *Solar Energy Materials and Solar Cells* **2006**, *90* (12), 1773–1787. https://doi.org/10.1016/j.solmat.2005.11.007.
- (17) Ledoux, G.; Gong, J.; Huisken, F.; Guillois, O.; Reynaud, C. Photoluminescence of Size-Separated Silicon Nanocrystals: Confirmation of Quantum Confinement. *Appl Phys Lett* **2002**, *80* (25), 4834–4836. https://doi.org/10.1063/1.1485302.
- (18) Nakamura, R.; Nakato, Y. Primary Intermediates of Oxygen Photoevolution Reaction on TiO<sub>2</sub> (Rutile) Particles, Revealed by in Situ FTIR Absorption and Photoluminescence Measurements. *J Am Chem Soc* **2004**, *126* (4), 1290–1298. https://doi.org/10.1021/ja0388764.
- (19) Sarfraz, A.; Posner, R.; Bashir, A.; Topalov, A.; Mayrhofer, K. J. J.; Lill, K.; Erbe, A. Effect of Polarisation Mimicking Cathodic Electrodeposition Coating on Industrially

- Relevant Metal Substrates with ZrO<sub>2</sub> -Based Conversion Coatings. *ChemElectroChem* **2016**, *3* (9), 1415–1421. https://doi.org/10.1002/celc.201600216.
- (20) Deng, X.; Wen, X.; Zheng, J.; Young, T.; Lau, C. F. J.; Kim, J.; Green, M.; Huang, S.; Ho-Baillie, A. Dynamic Study of the Light Soaking Effect on Perovskite Solar Cells by In-Situ Photoluminescence Microscopy. *Nano Energy* **2018**, *46*, 356–364. https://doi.org/10.1016/J.NANOEN.2018.02.024.
- (21) Chazalviel, J. N. Experimental Techniques for the Study of the Semiconductor—Electrolyte Interface. *Electrochim Acta* **1988**, 33 (4), 461–476. https://doi.org/10.1016/0013-4686(88)80163-4.
- (22) Meyer, G. J.; Lisensky, G. C.; Ellis, A. B. Evidence for Adduct Formation at the Semiconductor-Gas Interface. Photoluminescent Properties of Cadmium Selenide in the Presence of Amines. *J Am Chem Soc* **1988**, *110* (15), 4914–4918. https://doi.org/10.1021/ja00223a007.
- (23) Gfroerer, T. H. Photoluminescence in Analysis of Surfaces and Interfaces. *Encyclopedia of Analytical Chemistry* **2006**. https://doi.org/10.1002/9780470027318.A2510.
- (24) Kafizas, A.; Godin, R.; Durrant, J. R. Charge Carrier Dynamics in Metal Oxide Photoelectrodes for Water Oxidation. In *Semiconductors and Semimetals*; Elsevier, 2017; Vol. 97, pp 3–46. https://doi.org/10.1016/bs.semsem.2017.02.002.
- (25) Berera, R.; van Grondelle, R.; Kennis, J. T. M. Ultrafast Transient Absorption Spectroscopy: Principles and Application to Photosynthetic Systems. *Photosynth Res* **2009**, *101* (2–3), 105–118. https://doi.org/10.1007/s11120-009-9454-y.
- (26) Pendlebury, S. R.; Wang, X.; Le Formal, F.; Cornuz, M.; Kafizas, A.; Tilley, S. D.; Grätzel, M.; Durrant, J. R. Ultrafast Charge Carrier Recombination and Trapping in Hematite Photoanodes under Applied Bias. *J Am Chem Soc* **2014**, *136* (28), 9854–9857. https://doi.org/10.1021/ja504473e.
- (27) Sachs, M.; Pastor, E.; Kafizas, A.; Durrant, J. R. Evaluation of Surface State Mediated Charge Recombination in Anatase and Rutile TiO<sub>2</sub>. *J Phys Chem Lett* **2016**, 7 (19), 3742–3746. https://doi.org/10.1021/acs.jpclett.6b01501.

- (28) Wang, X.; Kafizas, A.; Li, X.; Moniz, S. J. A.; Reardon, P. J. T.; Tang, J.; Parkin, I. P.; Durrant, J. R. Transient Absorption Spectroscopy of Anatase and Rutile: The Impact of Morphology and Phase on Photocatalytic Activity. *J Phys Chem C* **2015**, *119* (19), 10439–10447. https://doi.org/10.1021/acs.jpcc.5b01858.
- (29) Tamaki, Y.; Furube, A.; Murai, M.; Hara, K.; Katoh, R.; Tachiya, M. Direct Observation of Reactive Trapped Holes in TiO<sub>2</sub> Undergoing Photocatalytic Oxidation of Adsorbed Alcohols: Evaluation of the Reaction Rates and Yields. *J Am Chem Soc* **2006**, *128* (2), 416–417. https://doi.org/10.1021/ja055866p.
- (30) Xiao-e, L.; Green, A. N. M.; Haque, S. A.; Mills, A.; Durrant, J. R. Light-Driven Oxygen Scavenging by Titania/Polymer Nanocomposite Films. *J Photochem Photobiol A Chem* **2004**, *162* (2–3), 253–259. https://doi.org/10.1016/j.nainr.2003.08.010.
- (31) Zhang, M.; De Respinis, M.; Frei, H. Time-Resolved Observations of Water Oxidation Intermediates on a Cobalt Oxide Nanoparticle Catalyst. *Nat Chem* **2014**, *6* (4), 362–367. https://doi.org/10.1038/nchem.1874.
- (32) Kafizas, A.; Wang, X.; Pendlebury, S. R.; Barnes, P.; Ling, M.; Sotelo-Vazquez, C.; Quesada-Cabrera, R.; Li, C.; Parkin, I. P.; Durrant, J. R. Where Do Photogenerated Holes Go in Anatase:Rutile TiO 2? A Transient Absorption Spectroscopy Study of Charge Transfer and Lifetime. *J Phys Chem A* **2016**, *120* (5), 715–723. https://doi.org/10.1021/acs.jpca.5b11567.
- (33) Selim, S.; Francàs, L.; García-Tecedor, M.; Corby, S.; Blackman, C.; Gimenez, S.; Durrant, J. R.; Kafizas, A. WO<sub>3</sub>/BiVO<sub>4</sub>: Impact of Charge Separation at the Timescale of Water Oxidation. *Chem Sci* **2019**, *10* (9), 2643–2652. https://doi.org/10.1039/c8sc04679d.
- (34) Li, Y.; Wu, Q.; Chen, Y.; Zhang, R.; Li, C.; Zhang, K.; Li, M.; Lin, Y.; Wang, D.; Zou, X.; Xie, T. Interface Engineering Z-Scheme Ti-Fe<sub>2</sub>O<sub>3</sub>/In<sub>2</sub>O<sub>3</sub> Photoanode for Highly Efficient Photoelectrochemical Water Splitting. *Appl Catal B* **2021**, *290*, 120058. https://doi.org/10.1016/J.APCATB.2021.120058.

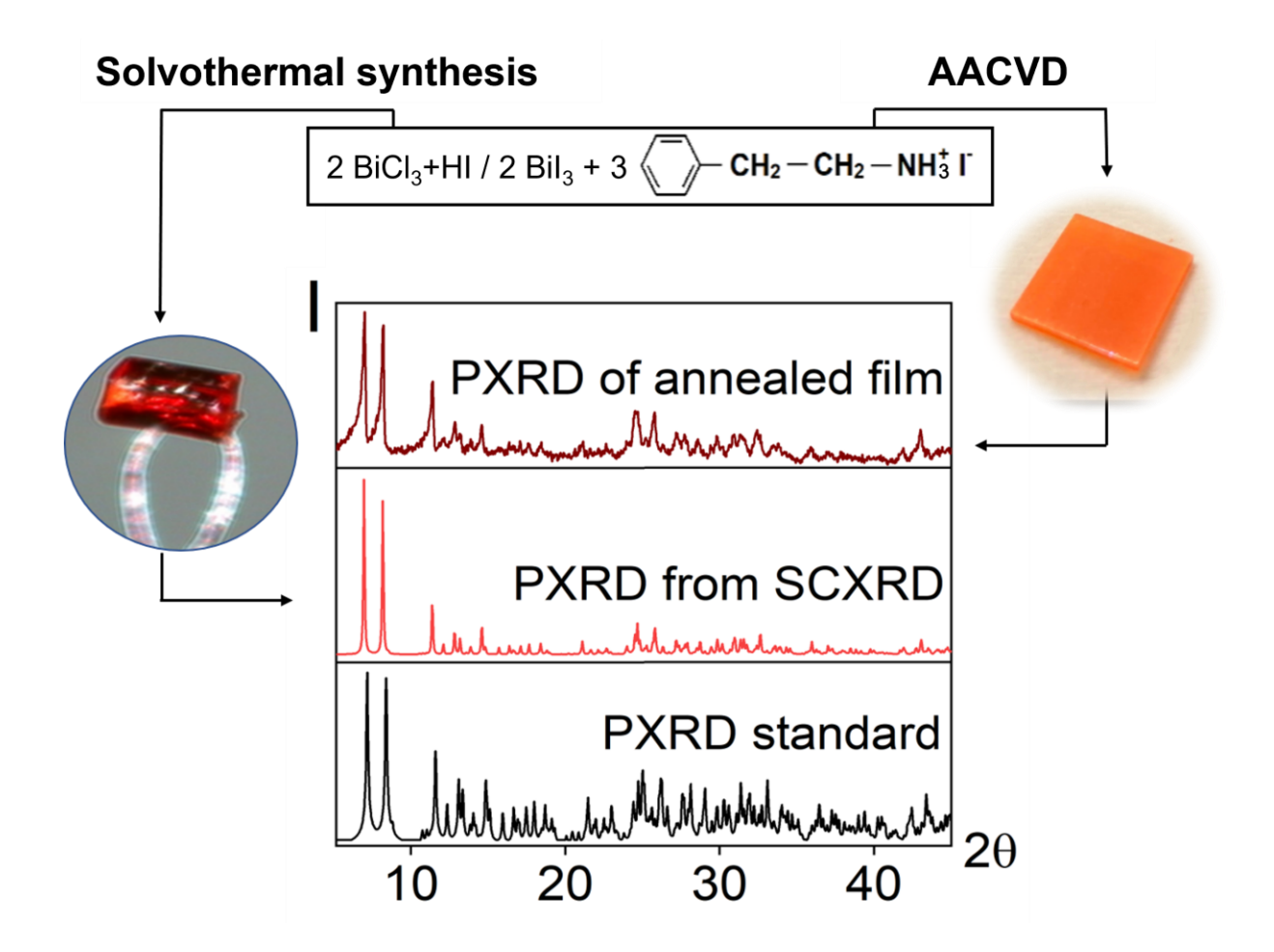
- (35) Statistical Review of World Energy | Energy economics | Home. https://www.bp.com/en/global/corporate/energy-economics/statistical-review-of-world-energy.html#tab\_sr-2021 (accessed 2023-07-02).
- (36) Fujishima, A.; Honda, K. Electrochemical Photolysis of Water at a Semiconductor Electrode. *Nature* **1972**, *238* (5358), 37–38. https://doi.org/10.1038/238037a0.
- (37) Walter, M. G.; Warren, E. L.; McKone, J. R.; Boettcher, S. W.; Mi, Q.; Santori, E. A.; Lewis, N. S. Solar Water Splitting Cells. *Chem Rev* **2010**, *110* (11), 6446–6473. https://doi.org/10.1021/cr1002326.
- (38) Hisatomi, T.; Kubota, J.; Domen, K. Recent Advances in Semiconductors for Photocatalytic and Photoelectrochemical Water Splitting. *Chem Soc Rev* **2014**, *4*3 (22), 7520–7535. https://doi.org/10.1039/c3cs60378d.
- (39) Jiang, C.; Moniz, S. J. A.; Wang, A.; Zhang, T.; Tang, J. Photoelectrochemical Devices for Solar Water Splitting Materials and Challenges. *Chem Soc Rev* **2017**, *46* (15), 4645–4660. https://doi.org/10.1039/C6CS00306K.
- (40) Moss, B.; Babacan, O.; Kafizas, A.; Hankin, A. A Review of Inorganic Photoelectrode Developments and Reactor Scale-Up Challenges for Solar Hydrogen Production. *Adv Energy Mater* **2021**, *11* (13), 2003286. https://doi.org/10.1002/aenm.202003286.
- (41) Kim, J. H.; Lee, J. S. Elaborately Modified BiVO 4 Photoanodes for Solar Water Splitting. *Adv Mater* **2019**, *31* (20), 1806938. https://doi.org/10.1002/adma.201806938.
- (42) Li, J.; Chen, H.; Triana, C. A.; Patzke, G. R. Hematite Photoanodes for Water Oxidation: Electronic Transitions, Carrier Dynamics, and Surface Energetics. *Angew Chemie Int Ed* **2021**, *60* (34), 18380–18396. https://doi.org/10.1002/anie.202101783.
- (43) Zheng, G.; Wang, J.; Liu, H.; Murugadoss, V.; Zu, G.; Che, H.; Lai, C.; Li, H.; Ding, T.; Gao, Q.; Guo, Z. Tungsten Oxide Nanostructures and Nanocomposites for Photoelectrochemical Water Splitting. *Nanoscale* **2019**, *11* (41), 18968–18994. https://doi.org/10.1039/C9NR03474A.

- (44) Li, C.; He, J.; Xiao, Y.; Li, Y.; Delaunay, J. J. Earth-Abundant Cu-Based Metal Oxide Photocathodes for Photoelectrochemical Water Splitting. *Energy Environ Sci* **2020**, *13* (10), 3269–3306. https://doi.org/10.1039/D0EE02397C.
- (45) Chen, Z.; Jaramillo, T. F.; Deutsch, T. G.; Kleiman-Shwarsctein, A.; Forman, A. J.; Gaillard, N.; Garland, R.; Takanabe, K.; Heske, C.; Sunkara, M.; McFarland, E. W.; Domen, K.; Miller, E. L.; Turner, J. A.; Dinh, H. N. Accelerating Materials Development for Photoelectrochemical Hydrogen Production: Standards for Methods, Definitions, and Reporting Protocols. *J Mater Res* **2010**, *25* (1), 3–16. https://doi.org/10.1557/JMR.2010.0020.
- (46) Kafizas, A.; Xing, X.; Selim, S.; Mesa, C. A.; Ma, Y.; Burgess, C.; McLachlan, M. A.; Durrant, J. R. Ultra-Thin Al<sub>2</sub>O<sub>3</sub> Coatings on BiVO<sub>4</sub> Photoanodes: Impact on Performance and Charge Carrier Dynamics. *Catal Today* **2019**, *321*–*322*, 59–66. https://doi.org/10.1016/j.cattod.2017.11.014.
- (47) Arumugam, M.; Choi, M. Y. Recent Progress on Bismuth Oxyiodide (BiOI) Photocatalyst for Environmental Remediation. *J Ind Eng Chem* **2020**, *81*, 237–268. https://doi.org/10.1016/j.jiec.2019.09.013.
- (48) He, X.; Deng, F.; Shen, T.; Yang, L.; Chen, D.; Luo, J.; Luo, X.; Min, X.; Wang, F. Exceptional Adsorption of Arsenic by Zirconium Metal-Organic Frameworks: Engineering Exploration and Mechanism Insight. *J Colloid Interface Sci* **2019**, *539*, 223–234. https://doi.org/10.1016/j.jcis.2018.12.065.
- (49) Luo, X.; Wang, C.; Wang, L.; Deng, F.; Luo, S.; Tu, X.; Au, C. Nanocomposites of Graphene Oxide-Hydrated Zirconium Oxide for Simultaneous Removal of As(III) and As(V) from Water. *Chem Eng J* **2013**, *220*, 98–106. https://doi.org/10.1016/j.cej.2013.01.017.
- (50) Yang, X.; Wang, D. Photocatalysis: From Fundamental Principles to Materials and Applications. *ACS Appl Energy Mater* **2018**, *1* (12), 6657–6693. https://doi.org/10.1021/acsaem.8b01345.
- (51) Xia, M.; Chen, Z.; Li, Y.; Li, C.; Ahmad, N. M.; Cheema, W. A.; Zhu, S. Removal of Hg(II) in Aqueous Solutions through Physical and Chemical Adsorption Principles. *RSC Adv* **2019**, *9* (36), 20941–20953. https://doi.org/10.1039/C9RA01924C.

- (52) Zhang, H.; Hu, X.; Li, T.; Zhang, Y.; Xu, H.; Sun, Y.; Gu, X.; Gu, C.; Luo, J.; Gao, B. MIL Series of Metal Organic Frameworks (MOFs) as Novel Adsorbents for Heavy Metals in Water: A Review. *J Hazard Mater* **2022**, *429*, 128271. https://doi.org/10.1016/j.jhazmat.2022.128271.
- (53) Alkhadra, M. A.; Su, X.; Suss, M. E.; Tian, H.; Guyes, E. N.; Shocron, A. N.; Conforti, K. M.; de Souza, J. P.; Kim, N.; Tedesco, M.; Khoiruddin, K.; Wenten, I. G.; Santiago, J. G.; Hatton, T. A.; Bazant, M. Z. Electrochemical Methods for Water Purification, Ion Separations, and Energy Conversion. *Chem Rev* **2022**, *122* (16), 13547–13635. https://doi.org/10.1021/acs.chemrev.1c00396.
- (54) Wang, Z.; Chen, M.; Huang, D.; Zeng, G.; Xu, P.; Zhou, C.; Lai, C.; Wang, H.; Cheng, M.; Wang, W. Multiply Structural Optimized Strategies for Bismuth Oxyhalide Photocatalysis and Their Environmental Application. *Chem Eng J* **2019**, *374*, 1025–1045. https://doi.org/10.1016/j.cej.2019.06.018.
- (55) Schneider, J.; Matsuoka, M.; Takeuchi, M.; Zhang, J.; Horiuchi, Y.; Anpo, M.; Bahnemann, D. W. Understanding TiO<sub>2</sub> Photocatalysis: Mechanisms and Materials. *Chem Rev* **2014**, *114* (19), 9919–9986. https://doi.org/10.1021/cr5001892.
- (56) Zhu, S.; Wang, D. Photocatalysis: Basic Principles, Diverse Forms of Implementations and Emerging Scientific Opportunities. *Adv Energy Mater* **2017**, *7* (23), 1700841. https://doi.org/10.1002/AENM.201700841.
- (57) Jin, X.; Ye, L.; Xie, H.; Chen, G. Bismuth-Rich Bismuth Oxyhalides for Environmental and Energy Photocatalysis. *Coord Chem Rev* **2017**, *349*, 84–101. https://doi.org/10.1016/j.ccr.2017.08.010.
- (58) Cheng, H.; Huang, B.; Dai, Y. Engineering BiOX (X = Cl, Br, I) Nanostructures for Highly Efficient Photocatalytic Applications. *Nanoscale* **2014**, *6* (4), 2009. https://doi.org/10.1039/c3nr05529a.
- (59) Alansi, A. M.; Qahtan, T. F.; Saleh, T. A. Solar-Driven Fixation of Bismuth Oxyhalides on Reduced Graphene Oxide for Efficient Sunlight-Responsive Immobilized Photocatalytic Systems. *Adv Mater Interfaces* **2021**, *8* (3), 2001463. https://doi.org/10.1002/admi.202001463.

- (60) Mills, A.; Wang, J.; Lee, S. K.; Simonsen, M. An Intelligence Ink for Photocatalytic Films. *Chem Commun* **2005**, *21*, 2721–2723. https://doi.org/10.1039/b501131k.
- (61) Mills, A.; Wang, J.; McGrady, M. Method of Rapid Assessment of Photocatalytic Activities of Self-Cleaning Films. *J Phys Chem B* **2006**, *110* (37), 18324–18331. https://doi.org/10.1021/jp063577x.
- (62) Kafizas, A.; Mills, A.; Parkin, I. P. A Comprehensive Aerosol Spray Method for the Rapid Photocatalytic Grid Area Analysis of Semiconductor Photocatalyst Thin Films. *Anal Chim Acta* **2010**, *663* (1), 69–76. https://doi.org/10.1016/j.aca.2010.01.022.
- (63) Kafizas, A.; Adriaens, D.; Mills, A.; Parkin, I. P. Simple Method for the Rapid Simultaneous Screening of Photocatalytic Activity over Multiple Positions of Self-Cleaning Films. *Phys Chem Chem Phys* **2009**, *11* (37), 8367. https://doi.org/10.1039/b905222d.

Chapter 2: Phenethylammonium bismuth iodide films



### 2.1 Background

Halide perovskite materials have gained much attention in recent decades because of their unique properties and simple solution synthesis, especially in the field of perovskite solar cells.<sup>1</sup> In general, halide perovskites represent the crystal structure with the chemical formula ABX<sub>3</sub>, where A is an organic (such as methylammonium and formamidinium)<sup>2–4</sup> or metal cation (such as caesium and silver),<sup>3,5</sup> B is a metal cation (such as lead, bismuth and tin)<sup>2,6,7</sup> and X is a halide anion. In the three-dimensional structure, the A cation is in the cuboctahedra space formed by corner-sharing BX<sub>6</sub> octahedra (Figure 2-1).<sup>8</sup> In addition to the three-dimensional corner-sharing BX<sub>6</sub> octahedra, due to the difference in cations or anions, there are many variants of the halide perovskite structures with lower dimensions, such as the two-dimensional corner-sharing layer structure,<sup>9–11</sup> the one-dimensional edge-sharing chain structure<sup>12,13</sup> and zero-dimensional face-sharing octahedra.<sup>14,15</sup> Halide perovskites exist in various crystal phases, including cubic, tetragonal and orthorhombic.<sup>7,16,17</sup>

Changes of A, B or X ions are all possible to result in different crystal phases. The phase transition can also happen for the same material under different external conditions. The crystal symmetry of perovskites would be lower with decreased temperatures. For example, the phase transition from cubic to tetragonal and finally to orthorhombic methylammonium lead iodide (MAPI) takes place at 330 K and 160 K.<sup>16</sup> Similar conditions were observed in tin-based analogues as well.<sup>7</sup>

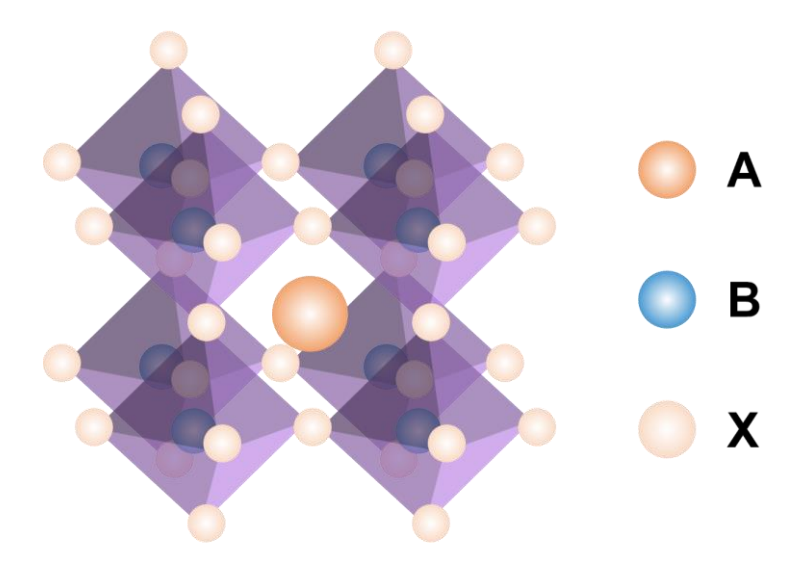


Figure 2-1. The typical structure of an ABX<sub>3</sub> perovskite.

Halide perovskites and their derivatives have desired band gaps for the transition process of light-excited electrons. In addition, their band gaps are tunable through changing organic, metal or halide ions. Furthermore, they also possess some unique properties, such as defect-tolerance, <sup>18</sup> long-range electron-hole diffusion lengths, <sup>19</sup> well-balanced charge transfer <sup>20</sup> and high optical absorption coefficient, <sup>1</sup> leading to their outstanding performance in optoelectrical applications.

Since 2009, when MAPI was first used as the absorber layer in the solar cell, interest in hybrid halide perovskites has increased.<sup>2</sup> Until now, the power conversion efficiencies (PCE) of perovskite solar cells have increased from 3.8% to latest 25.7%,<sup>2,21</sup> comparable to the efficiency of solar cells based on industrially produced single crystalline silicon,<sup>22</sup> and the cost of perovskite solar cells is much lower than that of the silicon solar cell.<sup>4</sup> Furthermore, halide perovskites and their derivatives have been applied in many other fields, such as photosensor,<sup>23</sup> light-emitting diodes<sup>24</sup> and energy storage devices.<sup>25</sup>

Nowadays, the most developed perovskites in optoelectrical applications are lead-based materials due to their outstanding performance in devices.<sup>2</sup> Nevertheless, lead-based perovskites suffer from intrinsic disadvantages such as instability in ambient conditions, toxicity of lead and current-voltage hysteresis in optoelectrical devices.<sup>26</sup> For example, MAPI can easily decompose into Pb(0), PbI<sub>2</sub> and MAI under a moist atmosphere, especially at the grain boundaries.<sup>27</sup> Furthermore, as a kind of structurally soft materials, hybrid lead halide perovskites are susceptible to external perturbations, such as increased temperatures,<sup>27,28</sup> impeding their practical applications. As a result, it is necessary to find lead-free alternatives which are environmentally friendly, stable and highly efficient in devices.

In fact, many kinds of metals have been studied as replacements of lead in the perovskite structure. Group 14 elements (Sn and Ge),29 Group 15 elements (Sb and Bi),<sup>30,31</sup> and transition metals (Cu)<sup>32</sup> have been reported to replace lead in perovskite structures. However, Sn- and Ge-based materials have poor stability although they show comparable device efficiencies to lead halide perovskites.<sup>29</sup> Organocopper halide perovskites are stable in ambient atmosphere, but they show thermal instability and low PCEs in solar cells.<sup>32</sup> For Sb, its toxicity is still nonnegligible. Thus, Bi is one of the most promising alternatives for Pb based materials. Bi has a similar electron configuration and ionic radius to Pb, so structures of bismuth halide perovskites are similar to those based on Pb.1 Besides the non-toxic nature, bismuth halide perovskites and derived materials have been reported to be much more stable towards degradation than Pb-based ones. They also have tunable band gaps and good solution processability like lead halide perovskites. 30,33-35 Therefore, a variety of bismuth halide perovskites and derived materials have been investigated, such as methylammonium bismuth iodide (MBI), and notable progress has been made in recent decades.<sup>36–38</sup>

In addition to common photovoltaic (PV) applications, bismuth halide perovskites and derived materials can be applied in photocatalysis and photosensors as well.<sup>39,40</sup> Compared with lead-based ones, the stability against heat, humidity and light exposure of devices with bismuth halide materials is improved significantly, while PCEs are far less.<sup>41–43</sup> The main reasons for such low efficiencies are the high carrier recombination rate due to numerous morphological flaws of deposited films, and slow

carrier transport across interfaces in devices resulting from the fast crystallization process of bismuth halide films.<sup>15</sup>

Beside metal elements, different organic ligands in perovskite structures have been studied to increase the stability of the materials. Perovskites composed of highly hygroscopic alkylammonium ligands, such as MA+, are prone to decompose irreversibly in humid environments, deteriorating their performance in devices. 27,44 Therefore, larger organic ligands have been introduced to yield more stable materials, for example the phenethylammonium cation (PEA+), and perovskites with lower dimensions were obtained due to the larger ion radii of the organic ligands. 9–11,45,46 The hydrophobic nature of PEA+ with a benzene ring is helpful in improving the moisture resistance of perovskites. 46 In addition, the thermal stability of perovskites with larger cations can be improved due to the suppressed ion movement. 46–48 Furthermore, films with preferential orientation, less defects and pinholes can be obtained in the presence of PEA+.11 Recently, the single crystal and thin film of [PEA]3[Bi2l9] were prepared successfully through slow evaporation and spin-coating methods respectively, showing a uniform film morphology and great stability. 15

Perovskite films in devices can be easily prepared by solution processes, such as spin coating. However, as one of the most popular ways to fabricate perovskite thin films, spin coating can only be utilized with a small range of precursors, and inert atmosphere is required in most cases, so the glovebox is often used. However, films would crystallize quickly in the glovebox, leading to poor film morphologies and device performance. In addition, two-step spin coating or using anti-solvent are common ways to improve film morphologies, which makes spin coating harder to be applied in the large-scale. 5,49,50 In order to obtain uniform films with less defects and better crystallization, solvent-free methods like high-low vacuum deposition (HLVD) were investigated.<sup>30</sup> Although homogeneous films with larger crystal grains were deposited and the efficiency of devices was increased significantly due to slower crystallization process, HLVD is costly and non-scalable as well. Therefore, low-cost and scalable thin film deposition methods for the industrialization of optoelectrical devices based on perovskites are in high demand, where aerosol assisted chemical vapor deposition (AACVD) came into sight and has been applied in the preparation of perovskite films. 51-54 However, only lead-based perovskite films were prepared by AACVD, and

there was no detailed study of their characterizations and the influence of substrates on deposited films.

In this research project, a lead-free perovskite-derived material, phenethylammonium bismuth iodide ([PEA]3[Bi2l9]), was prepared in the form of orange films with good coverage across the substrate *via* AACVD. [PEA]3[Bi2l9] films with good stability in ambient atmosphere were deposited successfully on three kinds of substrates, including glass, TiO2/glass and FTO/glass. Compositional, morphological and optoelectrical characterizations were carried out to investigate the influence of substrates and annealing conditions on film properties, which would be a great reference for future study about films of perovskites and derived materials prepared by AACVD.

## 2.2 Experimental

## 2.2.1 Precursor synthesis

Phenethylammonium iodide (PEAI) (>98%) and nitromethane were purchased from Sigma-Aldrich. BiCl<sub>3</sub> (>98%) was purchased from Alfa Aesar. HI (57 wt%) was purchased from MERCK. All of these reagents were used without further treatment.

Two methods were used to synthesize the single crystal. BiCl<sub>3</sub> (0.315 g, 1.00 mmol) and PEAI (0.170 g, 0.75 mmol) were dissolved in 12 mL methanol respectively. Then, 5 mL HI (57 wt%) was added into the mixed solution and allowed to stir at room temperature for 15 min. The final solution was transferred into in a 50 mL Teflon-lined stainless-steel autoclave, which was placed in a furnace at 140 °C for 24 hours. Orange needle-shaped crystals were obtained after cooling down to room temperature (Figure 2-2a). The obtained crystals were washed with ethanol several times and dried in air. Due to the poor diffraction of needle-like crystals, a small number of crystals were redissolved in nitromethane, and the solution was filtered to obtain a dark red solution. Good quality and strongly diffracting red block-type [PEA]<sub>3</sub>[Bi<sub>2</sub>I<sub>9</sub>] crystals were formed after about one week at room temperature (Figure 2-2b) and the unit cell (Figure 2-2c) was elucidated from SCXRD data.

As shown in Figure 2-2c, for each face-sharing octahedron, Bi is located in the center while iodide ions are on the corner of the octahedron. At the same time, PEA cations surround each isolated [Bi<sub>2</sub>I<sub>9</sub>]<sup>3-</sup> complex. The PXRD pattern of [PEA]<sub>3</sub>[Bi<sub>2</sub>I<sub>9</sub>] was

calculated from the SCXRD data in Mercury® to match phases and evaluate the existence of preferential orientations in following investigation. Crystallographic data of [PEA]<sub>3</sub>[Bi<sub>2</sub>I<sub>9</sub>] single crystals are shown in

Table 2-1. In addition, the bond distance of bridging Bi–I bonds (3.197 - 3.292 Å) is longer than that of terminal bonds (2.913 - 2.987 Å), which is in accord with structures in the literature. The angles of I(terminal)–Bi–I(bridging) range from 85.79° to 174.85°, while Bi–I(bridging)–Bi range from 82.90° to 84.11°. These angle values are also close to those reported. The angles of I(terminal)–Bi–I(bridging)–Bi range from 82.90° to 84.11°.

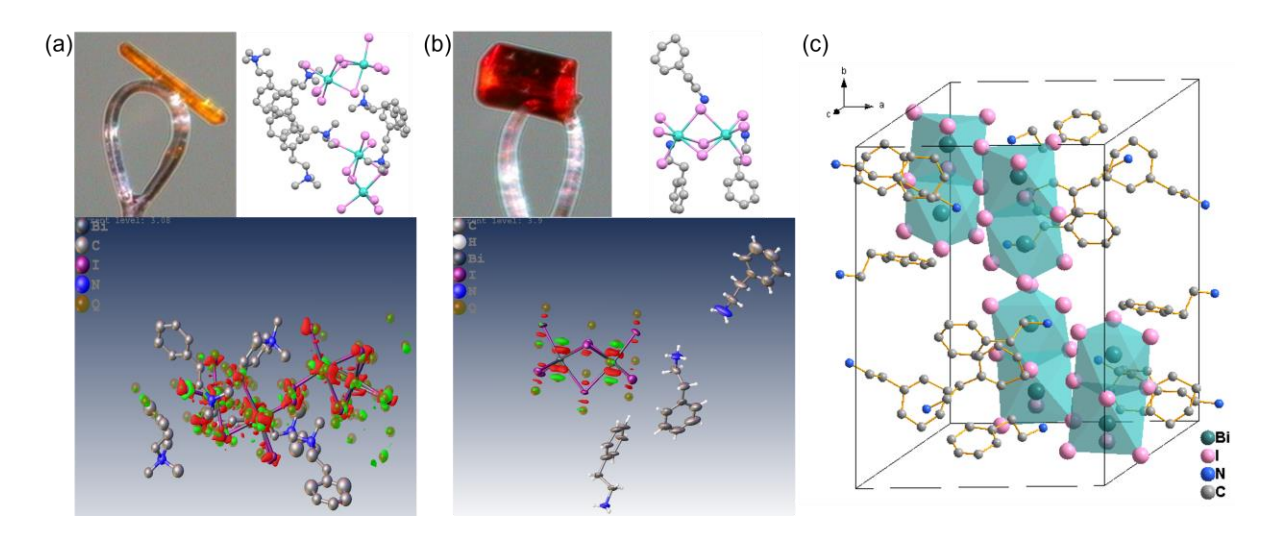


Figure 2-2. (a) Single crystal and (b) recrystallized single crystal of [PEA]<sub>3</sub>[Bi<sub>2</sub>I<sub>9</sub>]. (c) Unit cell of crystal [PEA]<sub>3</sub>[Bi<sub>2</sub>I<sub>9</sub>] drawn using Diamond®.

It is worth mentioning that in the asymmetric unit of [PEA]<sub>3</sub>[Bi<sub>2</sub>I<sub>9</sub>] (solvothermal) there are two [Bi<sub>2</sub>I<sub>9</sub>] anions and six PEA cations (Figure 2-2a), while the asymmetric unit of the recrystallized one contains one [Bi<sub>2</sub>I<sub>9</sub>] anion and three PEA cations (Figure 2-2b). Therefore, the empirical formula of the former structure is double of the latter. The difference in crystal structures is also evident from the unit cell dimensions, where the unit cell dimension of the recrystallized crystal is half of [PEA]<sub>3</sub>[Bi<sub>2</sub>I<sub>9</sub>] (solvothermal) (

Table 2-1). Furthermore, in

Table 2-1, diffraction peaks are large for both cases. As seen from the electron density map, for [PEA]<sub>3</sub>[Bi<sub>2</sub>I<sub>9</sub>] (solvothermal), the maximum peak is located near the Bi ion (Figure 2-2a). This unresolved peak could be an absorption peak which is common with heavy metal complexes, because heavy metal ions tend to absorb X-ray

radiations. The deepest hole is also observed between the maximum peak and the Bi ion. Similarly, the largest peak is located in the Bi ion for the recrystallized crystal structure (Figure 2-2b). This disorder peak hasn't been possible to resolve. The R value would be increased eventually if the disorder is solved through the introduction of several restrains and constrains, so we left the peaks unsolved.

Table 2-1. Crystallographic data from two single crystal samples.

	[PEA] <sub>3</sub> [Bi <sub>2</sub> I <sub>9</sub> ] (solvothermal)	[PEA] <sub>3</sub> [Bi <sub>2</sub> I <sub>9</sub> ]
Empirical formula	$C_{48}H_{72}Bi_4I_{18}N_6$	$C_{24}H_{36}Bi_2I_9N_3$
Formula weight	3854.24	1926.59
Temperature/K	151(2)	293(2)
Crystal system	monoclinic	monoclinic
Space group	P2 <sub>1</sub> /c	P2₁/n
a/Å	34.6046(5)	14.6383(3)
b/Å	10.00170(10)	20.7493(3)
c/Å	34.3474(5)	15.9278(3)
α/°	90	90
β/°	117.351(2)	113.193(2)
γ/°	90	90
Volume/Å <sup>3</sup>	10558.8(3)	4446.85(15)
Z	4	4
Pcalc/g cm <sup>-3</sup>	2.425	2.873
μ/mm <sup>-1</sup>	54.370	64.549
F (000)	6756.0	3364.0
Radiation	CuK <sub>α</sub> (λ = 1.54184 Å)	CuK <sub>α</sub> (λ = 1.54184 Å)
$2\theta$ range for data	7.5 to 167.5	7.0 to 145.5
Reflections collected	160612	31856
Independent reflections	21304 [Rint = 0.2774]	8715 [Rint = 0.1255]
Goodness-of-fit on F <sup>2</sup>	1.096	1.073
Final R indexes [I>=2σ (I)]	$R_1 = 0.1265$ , $wR_2 = 0.3152$	$R_1 = 0.1009$ , $wR_2 = 0.2550$
Final R indexes [all data]	$R_1 = 0.1606$ , $wR_2 = 0.3809$	$R_1 = 0.1108$ , $wR_2 = 0.2762$
Largest diff. peak/hole/eÅ-3	5.64/-5.88	8.03/-7.34

 $R_1 = (\sum ||Fo| - |Fc||/\sum |Fo|), WR_2 = [\sum (w(F_O^2 - F_C^2)^2) /\sum (w|F_O^2|^2)]^{1/2}$ 

## 2.2.2 Film deposition

Bismuth triiodide (Bil<sub>3</sub>) (>99%) and titanium(IV) ethoxide (Ti(OEt)<sub>4</sub>) were purchased from Sigma-Aldrich. Toluene (99.8%) was purchased from Fisher Scientific. Nitrogen (99.99%) was obtained from BOC. All of these reagents were used without further treatment. *N'*,*N'*-dimethylformamide (DMF) was purchased from VMR chemicals, and then was degassed and dehydrated using Schlenk line and molecular sieves 3 Å (Sigma-Aldrich). The glass and fluorine-doped tin oxide (FTO) substrates used in AACVD were supplied by Pilkington® NSG. 50 nm SiO<sub>2</sub> layer was coated on 3 mm thick soda lime float glass. The barrier layer of the glass substrate is to prevent ion migration from the underlying glass.

The AACVD set-up was assembled according to the literature.<sup>51</sup> All substrates in the size of 13 cm  $\times$  4.5 cm  $\times$  0.3 cm were washed successively by deionized water, acetone and isopropanol respectively and dried in the oven at 60 °C before starting film deposition. A top plate was suspended 0.5 cm above the glass substrate to ensure a laminar flow.

**TiO<sub>2</sub> thin film deposition.** Ti(OEt)<sub>4</sub> (0.46 mL, 2.2 mmol) was dissolved in toluene (20 mL) to form the precursor solution. The N<sub>2</sub> flow rate was kept at 1.0 L·min<sup>-1</sup>. The glass substrate was kept at 450 °C. The deposition time was 20 mins. The substrate was cooled down under N<sub>2</sub> flow after the deposition. TiO<sub>2</sub> thin films deposited on glass was used as the substrate for the further [PEA]<sub>3</sub>[Bi<sub>2</sub>I<sub>9</sub>] film deposition.

[PEA]₃[Bi₂I₃] film deposition. Bil₃ (1180 mg, 2 mmol) and PEAI (748 mg, 3 mmol) were dissolved in DMF (5 mL) under N₂ atmosphere. The mixed solution was treated ultrasonically for 1 hour. Films were deposited on glass, TiO₂/glass and FTO/glass respectively (Figure 2-3). For glass and FTO/glass substrates, the deposition of [PEA]₃[Bi₂I₃] films was achieved using the precursors in DMF directly. For the film deposition on the TiO₂/glass substrate, an extra step to deposit a TiO₂ thin film on the glass was required before depositing the [PEA]₃[Bi₂I₃] film. All substrates were kept at 125 °C during deposition for 45 mins, and the N₂ flow rate was kept at 0.8 L·min⁻¹. After the deposition, substrates were cooled down to room temperature under N₂ flow. The deposited films were then annealed in the CVD reactor with N₂ flow or in the vacuum oven for 30 mins.

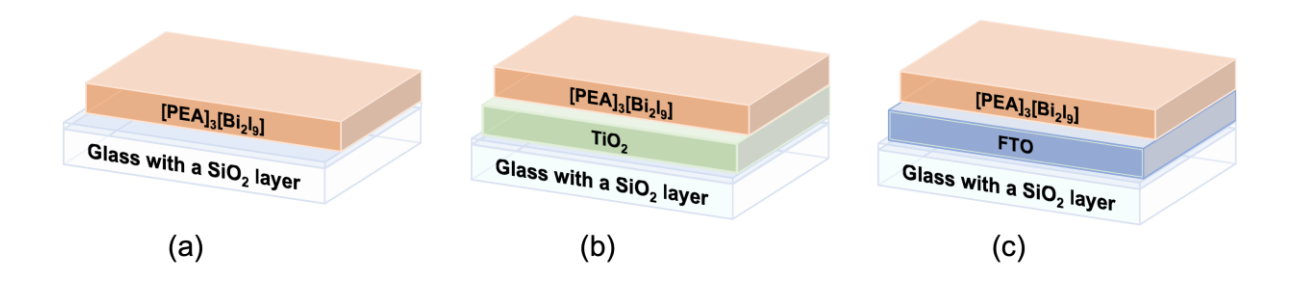


Figure 2-3. Scheme of films deposited on (a) glass, (b) TiO<sub>2</sub>/glass and (c) FTO/glass.

# 2.2.3 Physical characterization

Data points of single crystal X-ray diffraction (SCXRD) were collected by a SuperNova Atlas (Dual) diffractometer using Cu K $\alpha$  radiation ( $\lambda$  = 1.5418 Å). Crystals with suitable sizes and structures were selected under microscope prior to the measurement and mounted on a nylon loop. Powder X-ray diffraction (PXRD) patterns were obtained by a STOE SEIFERT diffractometer with detected angular range of  $2^{\circ}$  <  $2\theta$  <  $45^{\circ}$  with a Mo X-ray radiation source ( $\lambda = 0.7107 \text{ Å}$ ). Gradient-incident X-ray diffraction (GIXRD) patterns were obtained using a Bruker-Axs D8 diffractometer with parallel beam optics and a PSD LynxEye silicon strip detector. A detected angular range is  $4^{\circ} < 2\theta < 45^{\circ}$ and counted at 0.5 s per step (0.05° for each step). This instrument used monochromatic Cu  $K_{\alpha 1}$  radiation ( $\lambda = 1.5406 \text{ Å}$ ) at 40 kV with 30 mA emission current, and the incident beam angle was set to 1°. The FT-IR spectrum was measured in the range of 4000-400 nm<sup>-1</sup> using a Bruker Alpha-T ATR-FTIR Fourier Transform Infrared Spectrometer. Film morphologies were investigated by a JEOL JSM-6301F field emission scanning electron microscope (SEM) and energy dispersive spectroscopy (EDS). All samples were sputtered with a thin layer of gold to improve the surface electrical conductivity in order to avoid charging effects. X-ray photoelectron spectroscopy (XPS) was performed by a Thermo Scientific K-alpha photoelectron spectrometer using monochromatic Al-Ka radiation. Survey scans were collected in the range 0-1100 eV (binding energy) at a pass energy of 160 eV. XPS data was processed using CasaXPS® software, and all peak positions were calibrated to adventitious carbon (284.8 eV). UV-Vis measurements were conducted using a spectrometer (Shimadzu UV-2700, Shimadzu Corporation, NAKAGYO-KU KYOTO, Japan), and transmission/reflectance spectra were recorded in the 300-1100 nm range. Photoluminescence (PL) (Renishaw 1000) spectroscopy at room temperature was obtained for studying optical properties of films using a He-Cd laser (325 nm).

Water and solvent contact angle were measured with an optical contact angle meter (FTA 1000) with a 5 µL liquid droplet under ambient environment. Every sample was tested three times at different positions for statistical comparison.

#### 2.3 Results and discussions

# 2.3.1 Crystal structure and film composition

The GIXRD pattern of the TiO<sub>2</sub> thin film deposited on glass matched perfectly with the calculated anatase XRD pattern (*PDF 21-1272*) (Figure 2-4), showing that TiO<sub>2</sub>/glass was prepared successfully as the substrate for the next film deposition.

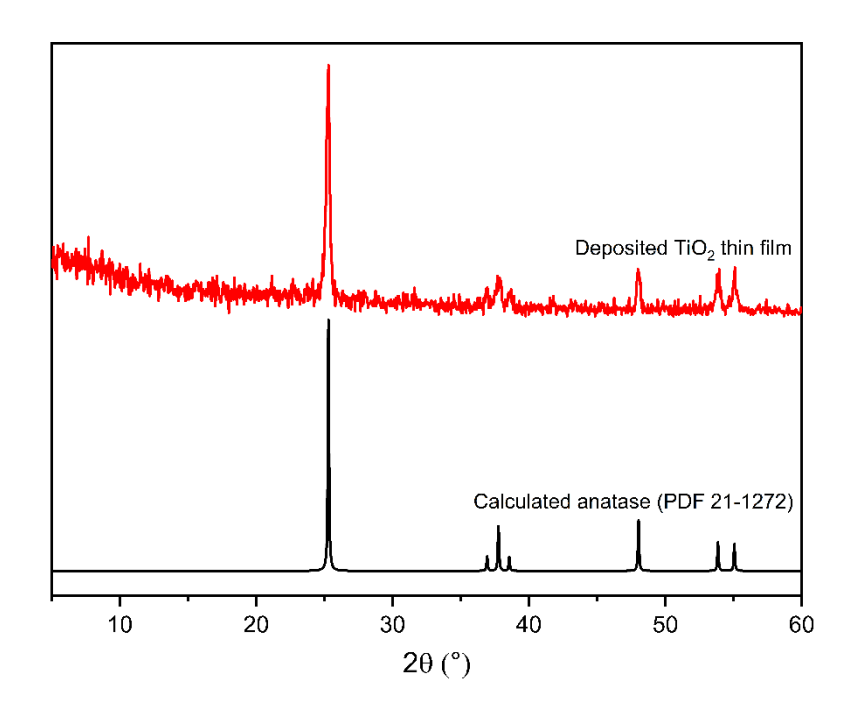


Figure 2-4. GIXRD pattern of the TiO<sub>2</sub> thin film on glass.

The single crystal of [PEA]<sub>3</sub>[Bi<sub>2</sub>I<sub>9</sub>] was synthesized first due to its novelty and the lack of available information of the crystal structure, and then the PXRD pattern of [PEA]<sub>3</sub>[Bi<sub>2</sub>I<sub>9</sub>] calculated from single crystal data was used as the standard to compare with the PXRD and GIXRD patterns of the deposited films. In the progress of this project, research about the single crystal of [PEA]<sub>3</sub>[Bi<sub>2</sub>I<sub>9</sub>] was published, and the crystal structure of the prepared crystal in this work was in good accordance with that in the literature.<sup>15</sup> The crystal structure of [PEA]<sub>3</sub>[Bi<sub>2</sub>I<sub>9</sub>] obtained in this work is shown in Figure 2-2c.

In the investigation of the film deposition *via* AACVD, various deposition temperatures and concentrations of precursor solutions were used. It was found that the solvent (DMF) of the precursor solution could not evaporate completely in the film deposition process at low deposition temperatures (125 °C and 160 °C) because of its high boiling point (153 °C). Some DMF remained in the deposited films, leading to a peak shift in the GIXRD patterns (Figure 2-5). Due to the thermal instability of the organic ligand (PEA+), a higher temperature (195 °C) would lead to the decomposition of [PEA]<sub>3</sub>[Bi<sub>2</sub>I<sub>9</sub>] (Figure 2-5). In the SEM images, the formation of powdery films was observed in films deposited above 125 °C (Figure 2-6).

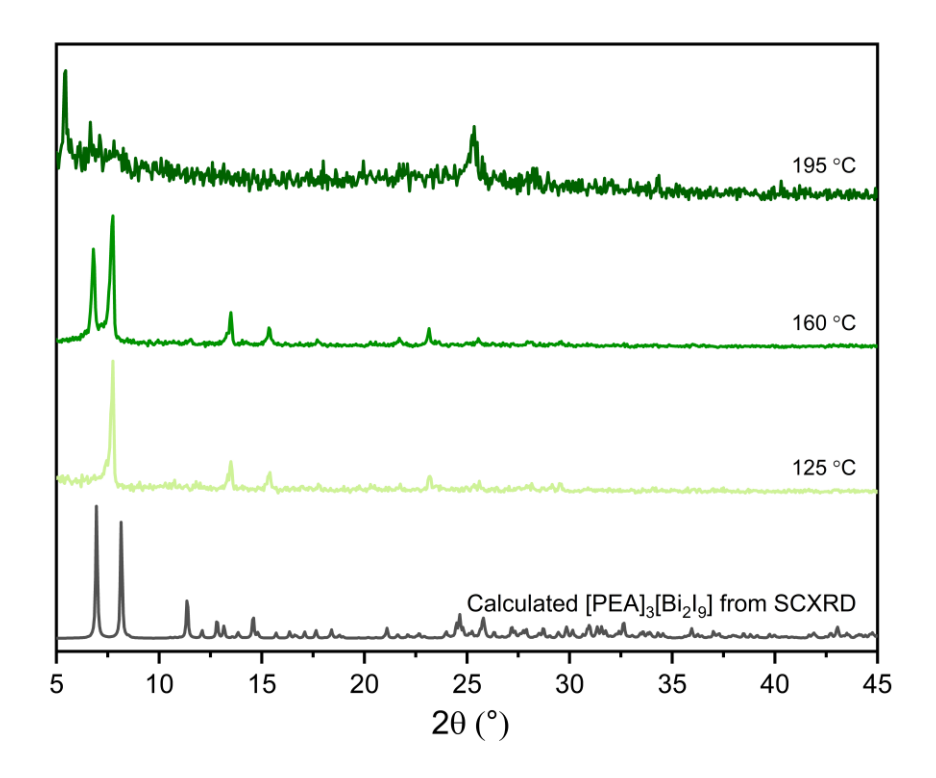


Figure 2-5. GIXRD patterns of [PEA] $_3$ [Bi $_2$ I $_9$ ] films deposited on TiO $_2$ /glass at (a) 125 °C, (b) 160 °C and (c) 195 °C.

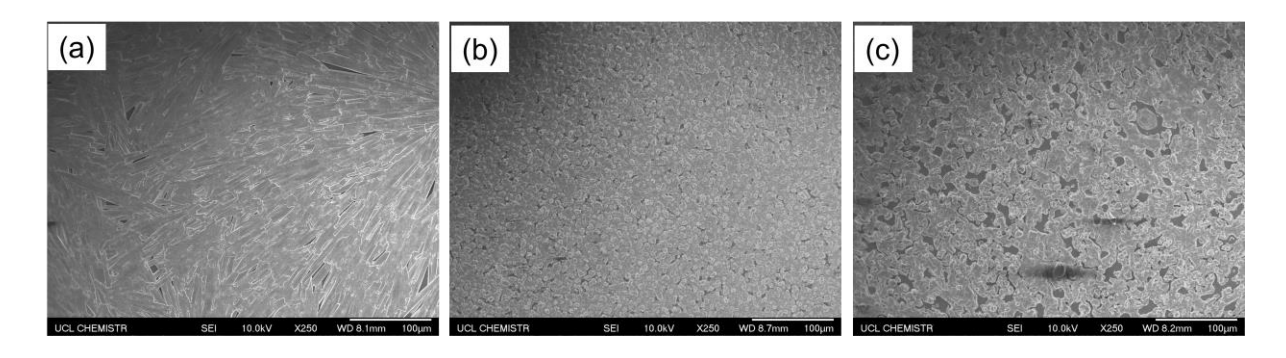


Figure 2-6. Top-view SEM images of [PEA]<sub>3</sub>[Bi<sub>2</sub>l<sub>9</sub>] films deposited on TiO<sub>2</sub>/glass at (a) 125 °C, (b) 160 °C and (c) 195 °C.

In addition, the coverage of films over substrates varied a lot with changing the concentrations of precursor solutions. From top-view SEM images, a significant difference in morphologies of films deposited from 0.05 M, 0.1 M and 0.2 M precursor solutions was observed (Figure 2-7). Films with poor coverage were deposited from 0.05 M and 0.1 M precursor solutions, until the solution concentration increased to 0.2 M, then a well-covered film was obtained. Therefore, based on the above investigation, all films were deposited at 125 °C with 0.2 M precursor solutions to obtain films with desired compositions and morphologies in the following study. It was necessary to anneal the films further to remove the remaining DMF.

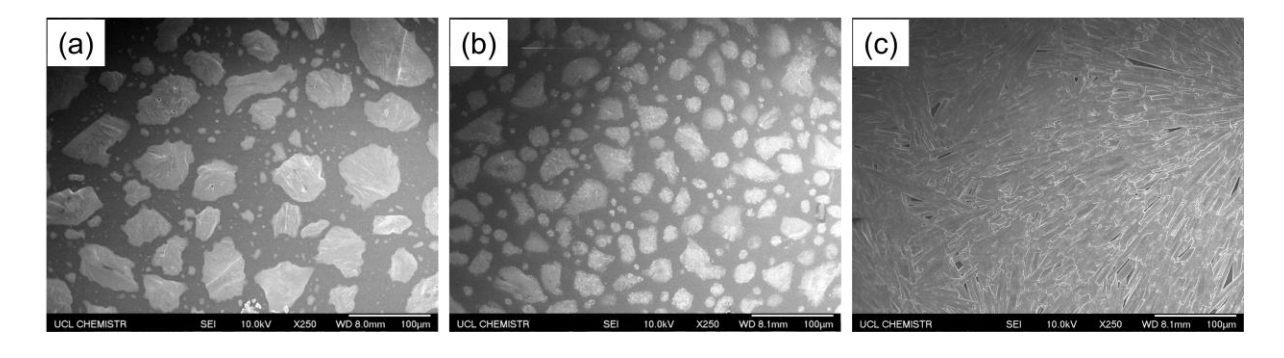


Figure 2-7. Top-view SEM images of [PEA]<sub>3</sub>[Bi<sub>2</sub>I<sub>9</sub>] films deposited on TiO<sub>2</sub>/glass from (a) 0.05 M, (b) 0.1 M and (c) 0.2 M precursor solutions.

First, [PEA]<sub>3</sub>[Bi<sub>2</sub>I<sub>9</sub>] films were deposited on glass *via* AACVD. Because the deposition temperature was set at 125 °C, DMF in the film was not able to evaporate completely. It was observed that, compared with the calculated XRD patterns, diffraction peaks of the as-deposited film shifted slightly toward lower angles, which resulted from the expansion of the unit cell because of the co-crystallized DMF molecules (Figure 2-8).<sup>56</sup> Therefore, films were annealed in the CVD reactor under N<sub>2</sub> flow. Different annealing

temperatures including 110 °C, 130 °C and 150 °C were investigated. For deposited [PEA] $_3$ [Bi $_2$ I $_9$ ] films on glass, with the increase of annealing temperatures, two strong peaks at 6.9° and 8.1° appeared while the peak at 7.7° disappeared gradually. In addition, the positions of the other peaks matched better with the XRD pattern calculated from the single crystal data at higher annealing temperatures, indicating that the effect of the remaining DMF on the diffraction peak positions of the [PEA] $_3$ [Bi $_2$ I $_9$ ] films was reducing (Figure 2-8). When the annealing temperature was increased to 150 °C, the deposited film showed an identical GIXRD pattern to the single crystal [PEA] $_3$ [Bi $_2$ I $_9$ ]. In addition, the deposited film showed preferential growth orientation in the (10 $\overline{1}$ ) and (11 $\overline{1}$ ) planes.

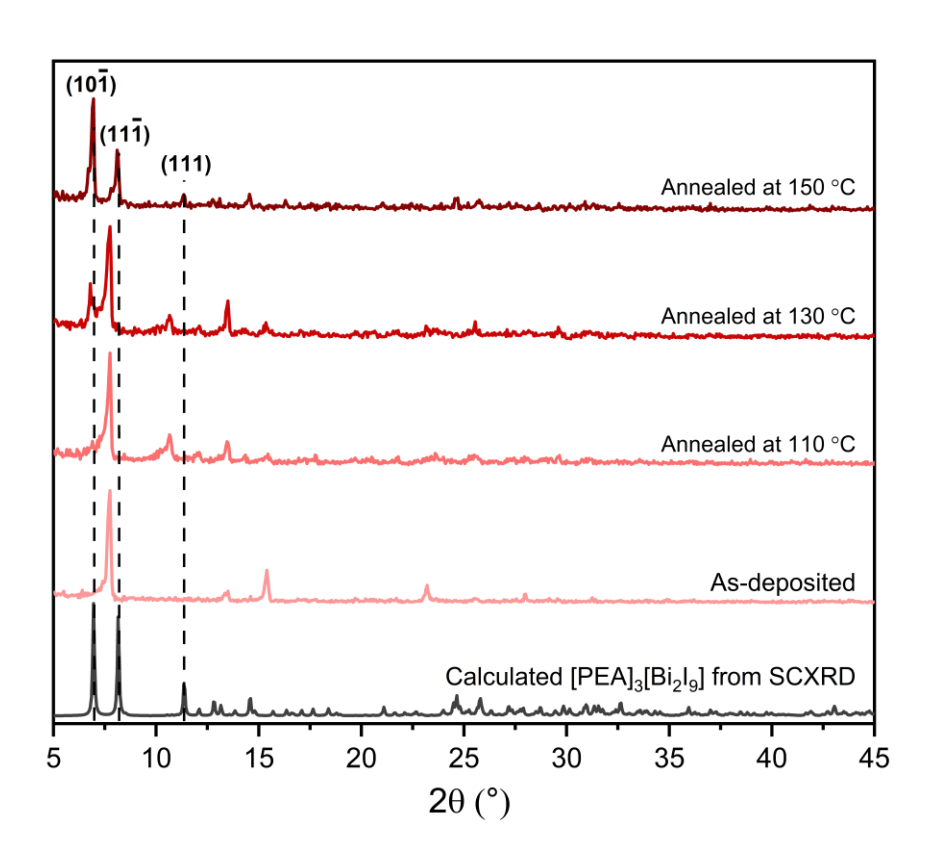


Figure 2-8. GIXRD patterns of [PEA]<sub>3</sub>[Bi<sub>2</sub>I<sub>9</sub>] films deposited on glass at different annealing temperatures in N<sub>2</sub>.

For a more accurate comparison without the disturbance of the preferential growth, the PXRD pattern of the annealed film was obtained as well through testing the powder sample scratched from deposited films. It was observed that the PXRD pattern

matched perfectly with both calculated XRD patterns from this work and literature, <sup>15</sup> showing that pure phase [PEA]<sub>3</sub>[Bi<sub>2</sub>I<sub>9</sub>] films were deposited successfully *via* AACVD (Figure 2-9).

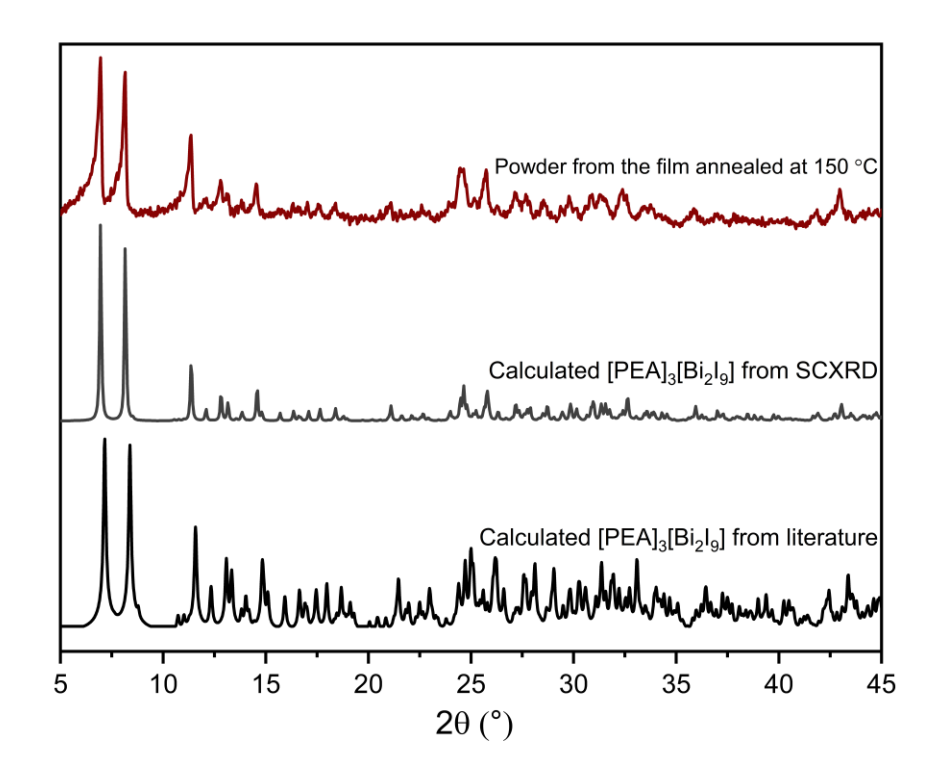


Figure 2-9. PXRD patterns of scraped annealed film on glass, calculated from SCXRD and calculated from literature.

In addition, the FT-IR spectra were obtained through testing the scratched powder samples. Through comparing with the spectrum of the annealed film, two extra peaks in the spectrum of the as-deposited film were observed at 1640 cm<sup>-1</sup> (C=O stretch) and 663 cm<sup>-1</sup> (O=C-N bend), showing the existence of DMF.<sup>57</sup> A wide band in the range of 3200–2500 cm<sup>-1</sup>, corresponding to the O-H stretch, was detected in both samples, which was likely due to moisture absorption since samples were kept in air for a long time (Figure 2-10).<sup>58</sup> Therefore, it can be concluded that through annealing films at 150 °C in N<sub>2</sub> for 30 mins, co-crystallized DMF molecules were able to be removed completely from the deposited [PEA]<sub>3</sub>[Bi<sub>2</sub>I<sub>9</sub>] films.

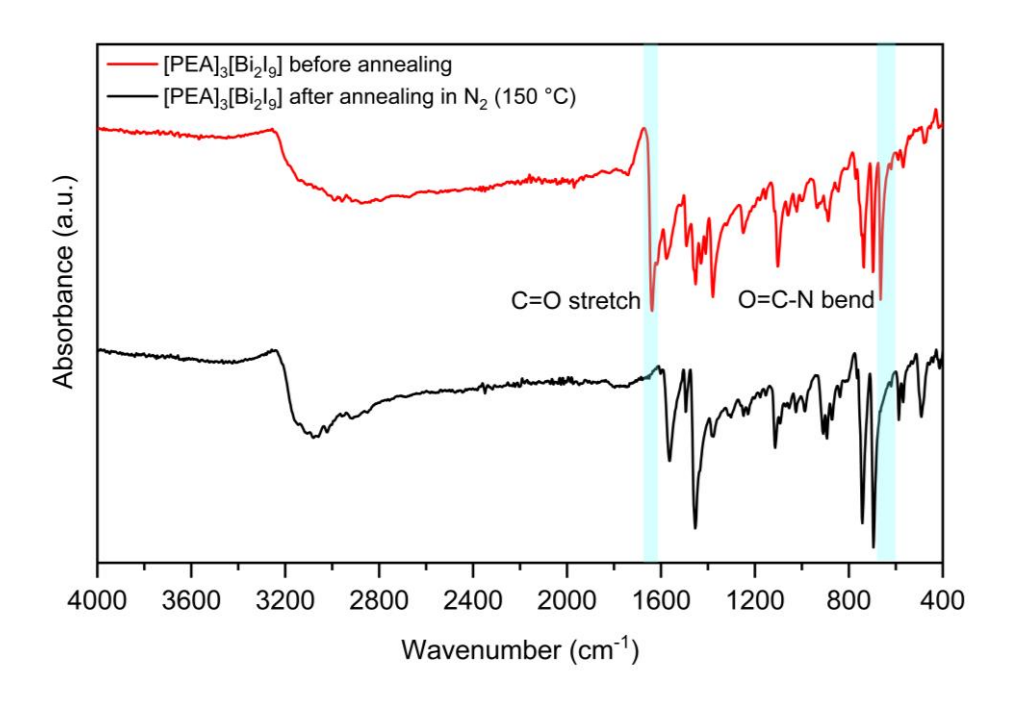


Figure 2-10. FT-IR spectra of [PEA]<sub>3</sub>[Bi<sub>2</sub>I<sub>9</sub>] powders scratched from the deposited films before and after annealing in N<sub>2</sub>.

The composition and oxidation state of elements in the annealed [PEA]<sub>3</sub>[Bi<sub>2</sub>I<sub>9</sub>] film were characterized through XPS. High resolution XPS spectra for C 1s, N 1s, Bi 4f and I 3d are shown in Figure 2-11. The C 1s spectrum was best fitted with two peaks at 284.8 eV and 286.1 eV, corresponding to the existence of 2 types of carbon atoms in phenethylammonium cation, C-C and C-N, respectively (Figure 2-11a). 9,59,60 In addition, a weak and broad peak area corresponding to the  $\pi - \pi$  bond of benzene ring in the cation was also observed. The N 1s spectrum showed 2 components (Figure 2-11b). The peak at 402.4 eV could be assigned to the nitrogen in the organic ligand, and the other at 400.7 eV was likely to be attributed to the decomposition of the organic ligand. 61,62 Similar N 1s spectra with two peaks were also reported in the study of MAPI films due to the decomposition of methylammonium ligand into CH<sub>3</sub>NH<sub>2</sub>.<sup>52</sup> Although CH<sub>3</sub>NH<sub>2</sub> is in gas form, it is still possible to be absorbed by the film surface and then detected in XPS measurements. In Figure 2-11c, peaks for Bi<sup>3+</sup>  $4f_{7/2}$  (159.5 eV) and  $4f_{5/2}$  (164.8 eV) were observed. The splitting between these bands was about 5.3 eV, indicating that bismuth was present in its normal Bi3+ state.62 In addition, shoulder peaks centred at 157.8 eV and 163.1 eV originated from the existence of metallic bismuth (Bi<sup>0</sup>), due to the photoreduction under incident X-rays and the likely decomposition of [PEA]<sub>3</sub>[Bi<sub>2</sub>I<sub>9</sub>] and BiI<sub>3</sub>. This is often shown in XPS measurements of bismuth-based perovskite materials.<sup>43,63</sup> The signal in the I 3d spectrum produced I 3d<sub>5/2</sub> and I 3d<sub>3/2</sub> peaks centered at 619.8 eV and 631.3 eV, respectively, which can be attributed to the characteristic signals of I<sup>-</sup> (Figure 2-11d).<sup>61</sup>

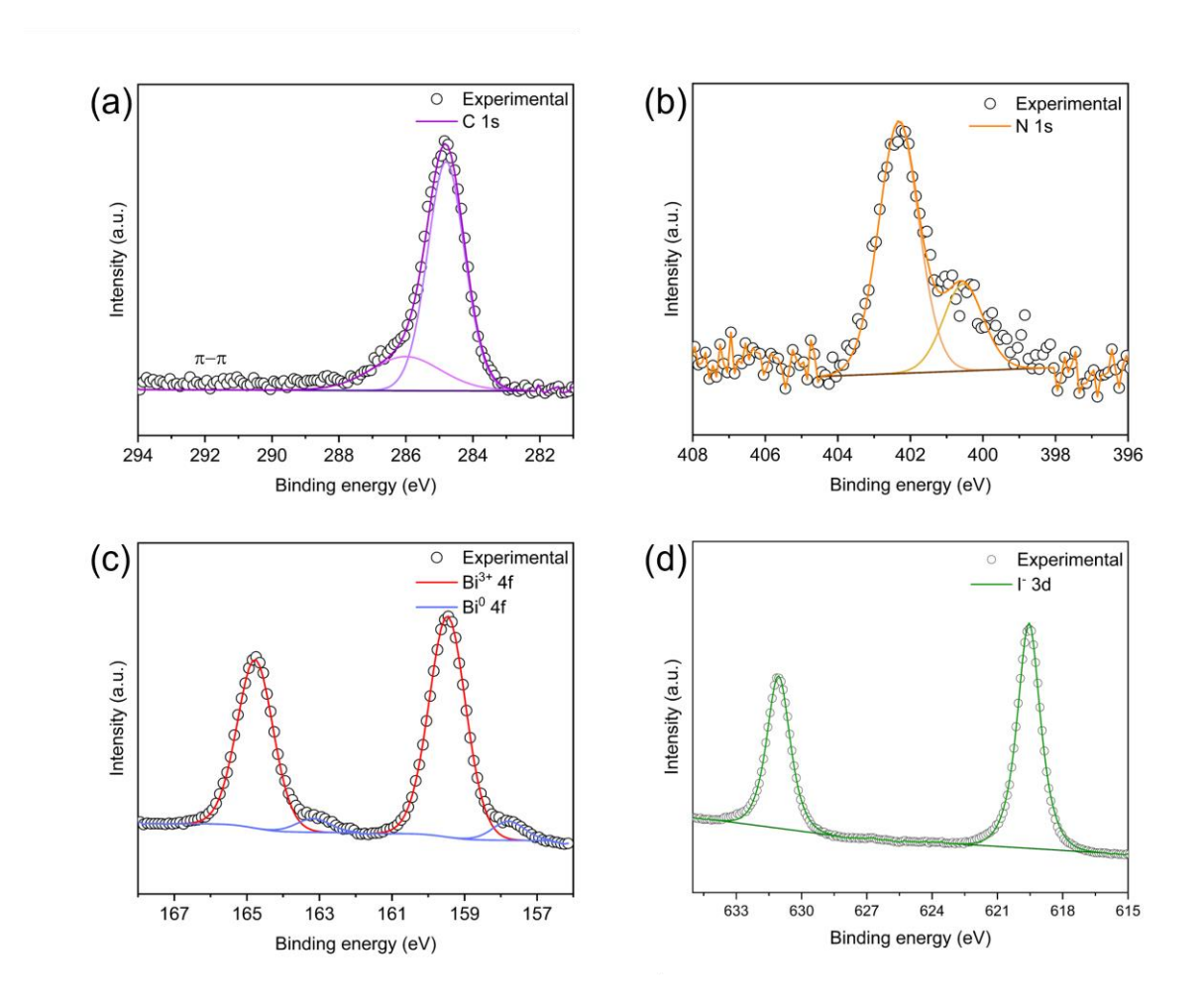


Figure 2-11. High resolution XPS spectra of (a) C 1s, (b) N 1s, (c) Bi 4f and (d) I 3d from the [PEA]<sub>3</sub>[Bi<sub>2</sub>I<sub>9</sub>] film on glass annealed at 150 °C in N<sub>2</sub>.

Furthermore, in the survey spectrum of the [PEA]<sub>3</sub>[Bi<sub>2</sub>I<sub>9</sub>] film, the O and Si elements were detected as well (Figure 2-12). These peaks originated from the silica coated barrier glass substrate, which was exposed in XPS measurements due to the incomplete coverage of the [PEA]<sub>3</sub>[Bi<sub>2</sub>I<sub>9</sub>] film over the glass substrate, which was also observed in the SEM images (Figure 2-14). The peak positions for oxygen (532.7 eV) and Si (103.2 eV) were consistent with the values of SiO<sub>2</sub> in the NIST database.<sup>62</sup>

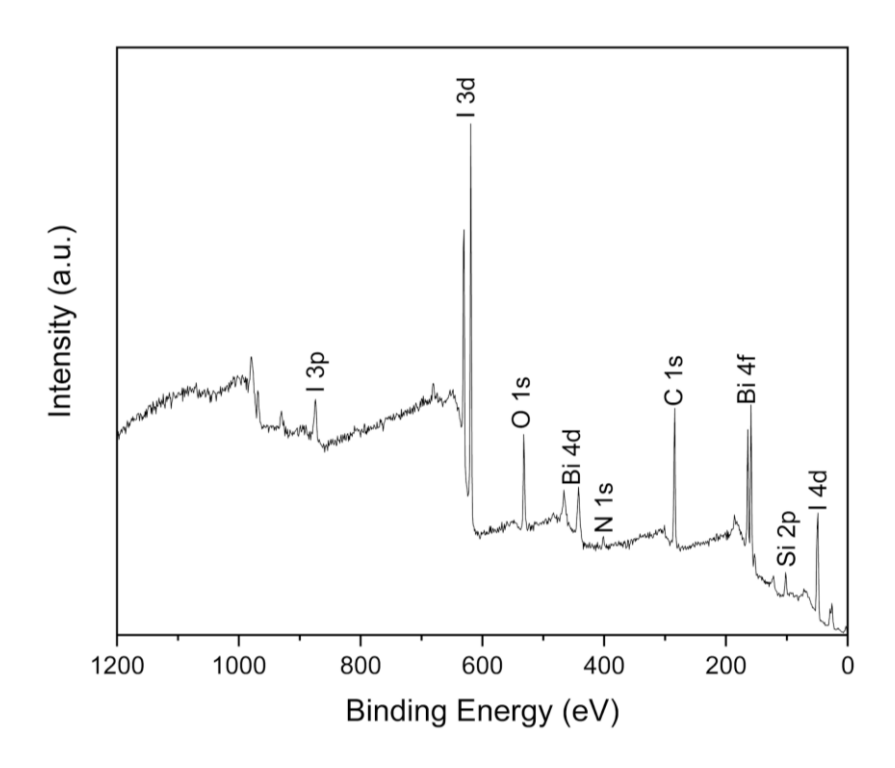


Figure 2-12. XPS survey spectrum of the [PEA] $_3$ [Bi $_2$ I $_9$ ] film on glass annealed at 150 °C in N $_2$ .

The elemental composition and atomic ratio of the film annealed at 150 °C in N<sub>2</sub> were determined through EDS. Peaks of prominent elements, including C, Bi and I, were all observed in the spectrum (Figure 2-13). The atom percentage of Bi and I in the spectrum was around 4.4, which is close to the calculated value of [PEA]<sub>3</sub>[Bi<sub>2</sub>I<sub>9</sub>], 4.5.

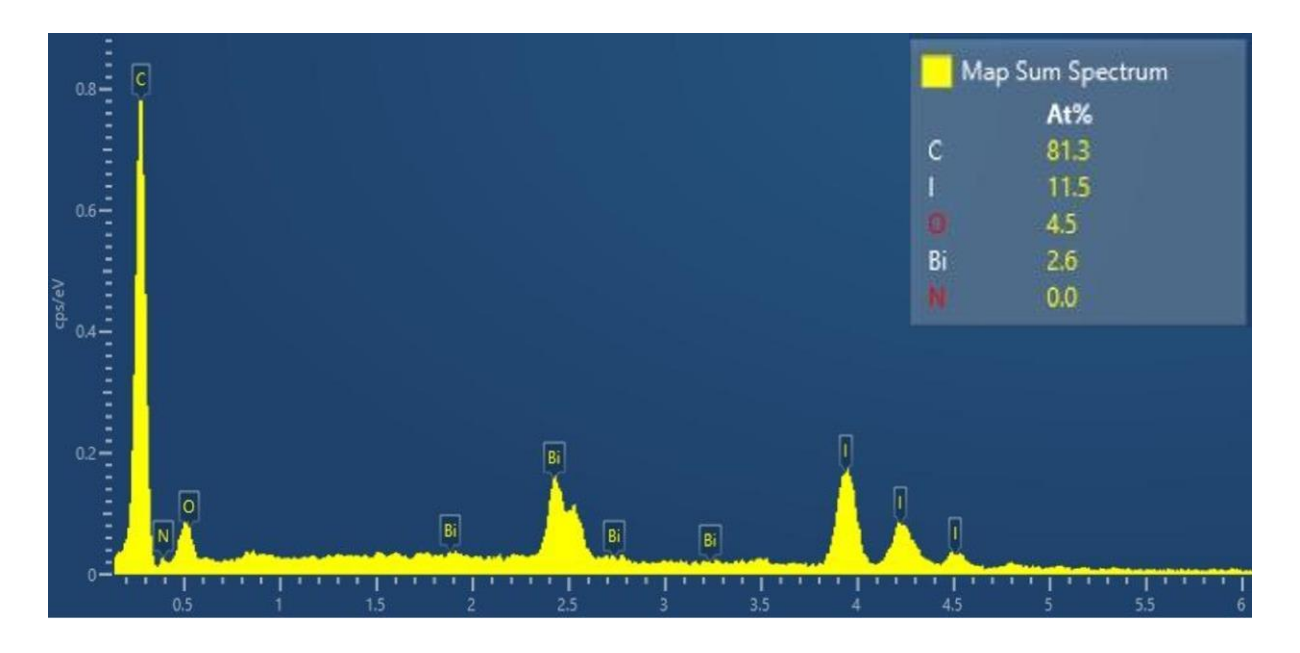


Figure 2-13. EDS analysis of the [PEA]<sub>3</sub>[Bi<sub>2</sub>I<sub>9</sub>] film on glass annealed at 150 °C in N<sub>2</sub>.

## 2.3.2 Film morphology

Top-view SEM was performed to study morphologies of deposited [PEA]<sub>3</sub>[Bi<sub>2</sub>I<sub>9</sub>] films on glass. All deposited films were powdery and showed poor adhesion to the glass substrate. Film grains were in the size of 5–10 µm (Figure 2-14). It can be observed that the grain size decreased with the increased annealing temperatures. This decrease in the grain size could be attributed to the loss of the remaining DMF in the [PEA]<sub>3</sub>[Bi<sub>2</sub>I<sub>9</sub>] films. Although annealing at 150 °C could completely remove the cocrystallized DMF, films with desired morphologies were unable to be obtained on the glass substrate.

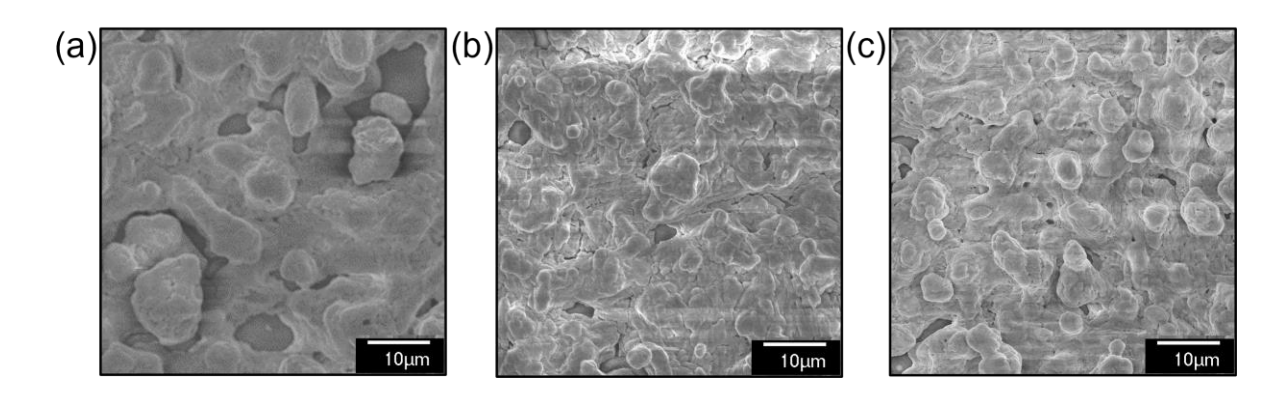


Figure 2-14. Top-view SEM images of [PEA]<sub>3</sub>[Bi<sub>2</sub>I<sub>9</sub>] films on glass, (a) as deposited, annealed in N<sub>2</sub> at (b) 130 °C and (c) 150 °C.

## 2.3.3 [PEA]<sub>3</sub>[Bi<sub>2</sub>l<sub>9</sub>] films on TiO<sub>2</sub>/glass and FTO/glass

In order to address the problem of powdery films deposited on amorphous glass, TiO<sub>2</sub>/glass or FTO/glass were utilized as substrates with crystalline surfaces. This is of interest since TiO<sub>2</sub>, as a kind of *n*-type semiconductor, can form a heterojunction when contacting with [PEA]<sub>3</sub>[Bi<sub>2</sub>l<sub>9</sub>],<sup>64</sup> which shows great potential in various applications, such as photocatalysis.<sup>65</sup> In addition, FTO, a kind of transparent conducting oxide, is widely used as the substrate in the film deposition process to explore the photoelectrochemical applications of films.<sup>66</sup> Many works about perovskites and derived materials deposited on conducting FTO for PV devices have been reported as well.<sup>25,67,68</sup> Therefore, through depositing [PEA]<sub>3</sub>[Bi<sub>2</sub>l<sub>9</sub>] on TiO<sub>2</sub>/glass and FTO/glass, more applications of [PEA]<sub>3</sub>[Bi<sub>2</sub>l<sub>9</sub>] films can be investigated.

[PEA]<sub>3</sub>[Bi<sub>2</sub>l<sub>9</sub>] films annealed at different temperatures on TiO<sub>2</sub>/glass and FTO/glass were also investigated. In the GIXRD patterns (Figure 2-15 and Figure 2-16), two

strong peaks in the range of 5–10° appeared, while the peak between them disappeared gradually, and DMF in the films was removed completely through annealing at 150 °C for 30 min. These transition trends of peaks were similar to that of films on glass. Among films annealed at 150 °C on three kinds of substrates, the [PEA] $_3$ [Bi $_2$ I $_9$ ] film deposited on FTO/glass had the highest degree of preferential growth orientation in the (10 $\overline{1}$ ) plane (20 = 6.9°), followed by the film on TiO $_2$ /glass. Therefore, it can be determined that the kind of substrates has an effect on the preferential orientation of the film growth.

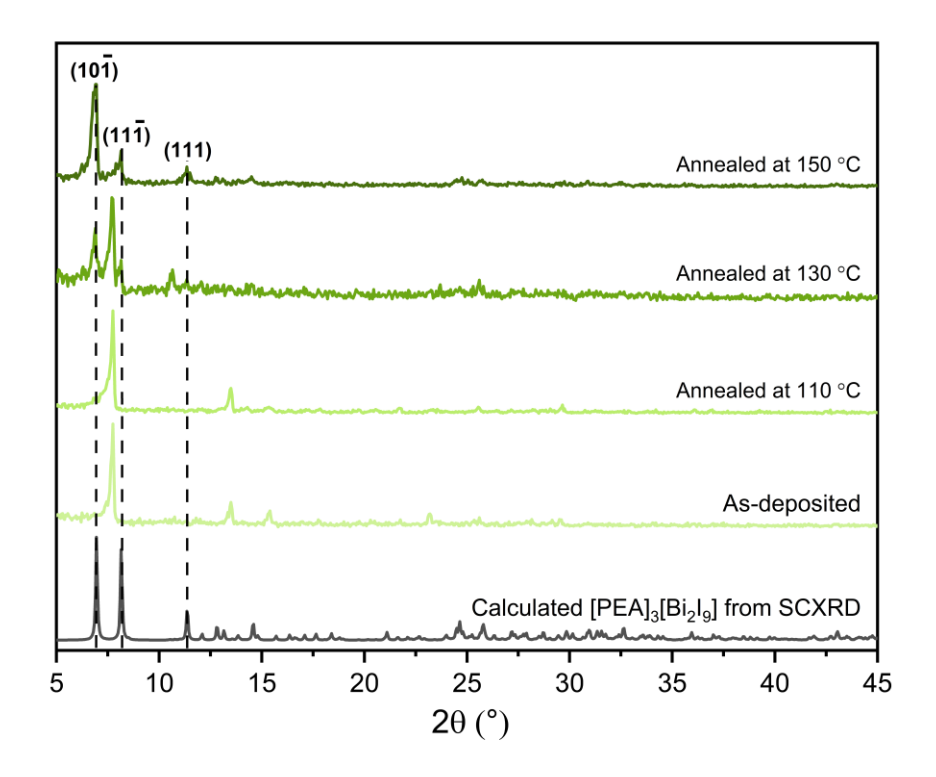


Figure 2-15. GIXRD patterns of [PEA] $_3$ [Bi $_2$ I $_9$ ] films deposited on TiO $_2$ /glass at different annealing temperatures in N $_2$ .

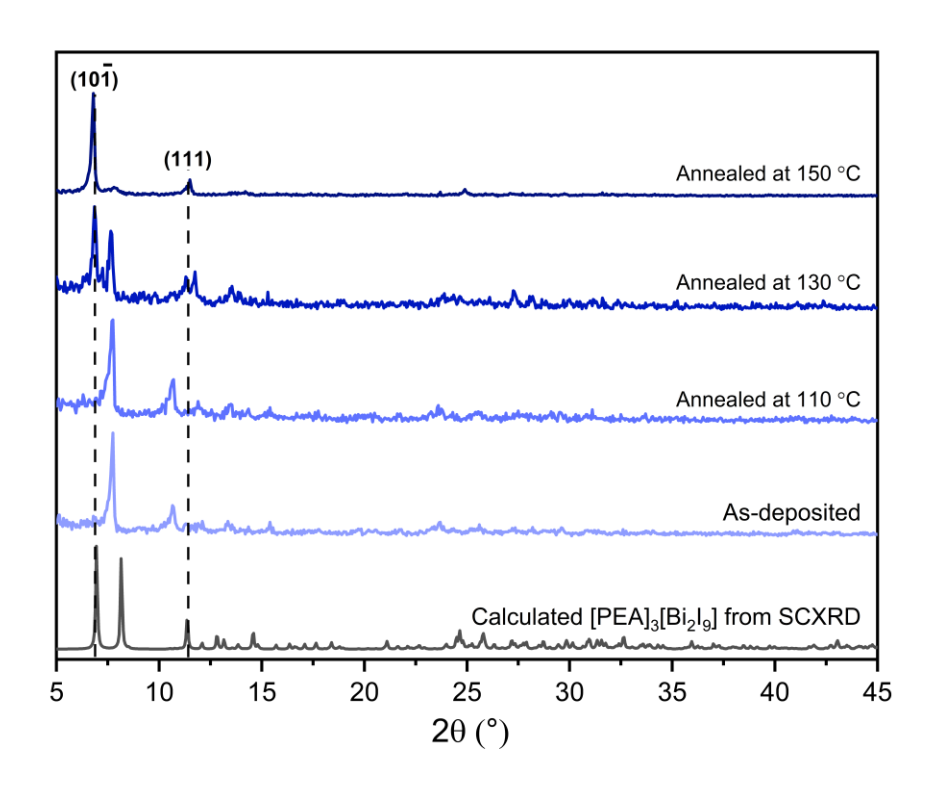


Figure 2-16. GIXRD patterns of [PEA]<sub>3</sub>[Bi<sub>2</sub>l<sub>9</sub>] films deposited on FTO/glass at different annealing temperatures in N<sub>2</sub>.

The morphologies of the [PEA]3[Bi2l9] films on TiO2/glass and on FTO/glass were dramatically different from films on glass. Films on TiO2/glass exhibited large and flat particles ( $5 \times 60$ – $100 \,\mu$ m) (Figure 2-17a), and film grains on FTO/glass were small and block-shaped ( $2 \times 2 \,\mu$ m) (Figure 2-18a). For films on TiO2/glass, different annealing temperatures led to various film morphologies. The as-deposited film and the film annealed at 130 °C showed obvious crystallization and compact growth (Figure 2-17a, b). However, the film annealed at 150 °C was in a less desired powder form (Figure 2-17c). This trend was shown in the macro-scale, which could be seen easily by the naked eye. In addition, compact and crystallized film morphologies, which were observed in as-deposited films and films annealed at 130 °C on FTO/glass, could not be seen in the film annealed at 150 °C (Figure 2-18c). Annealing films at 150 °C in N2 allowed the growth of film surfaces with high energy, leading to the particle agglomeration (5–10  $\mu$ m) and roughened surface independent of the kind of substrates (Figure 2-17c and Figure 2-18c). As observed for films on glass, the decrease of grain size also occurred for films on TiO2/glass and FTO/glass after

annealing. The [PEA]<sub>3</sub>[Bi<sub>2</sub>I<sub>9</sub>] films on TiO<sub>2</sub>/glass and FTO/glass annealed at 150 °C could be wiped off easily from the substrates, while as-deposited films and films annealed at 130 °C were much better adhered. However, annealing at 130 °C cannot 100% remove the DMF from the film. As a result, films with ideal composition and morphologies are unable to be obtained by just changing substrates and increasing the annealing temperatures.

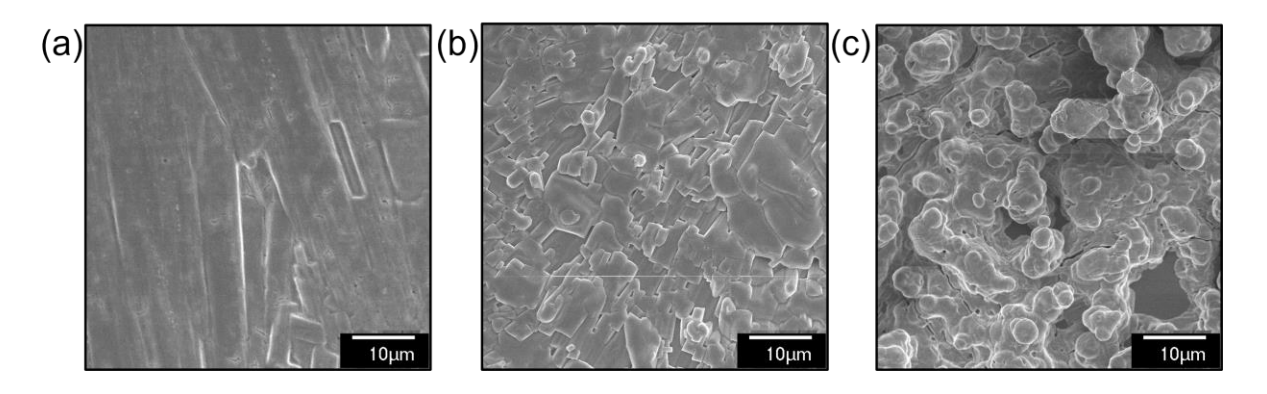


Figure 2-17. Top-view SEM images of [PEA] $_3$ [Bi $_2$ I $_9$ ] films on TiO $_2$ /glass, (a) as deposited, annealed in N $_2$  at (b) 130 °C and (c) 150 °C.

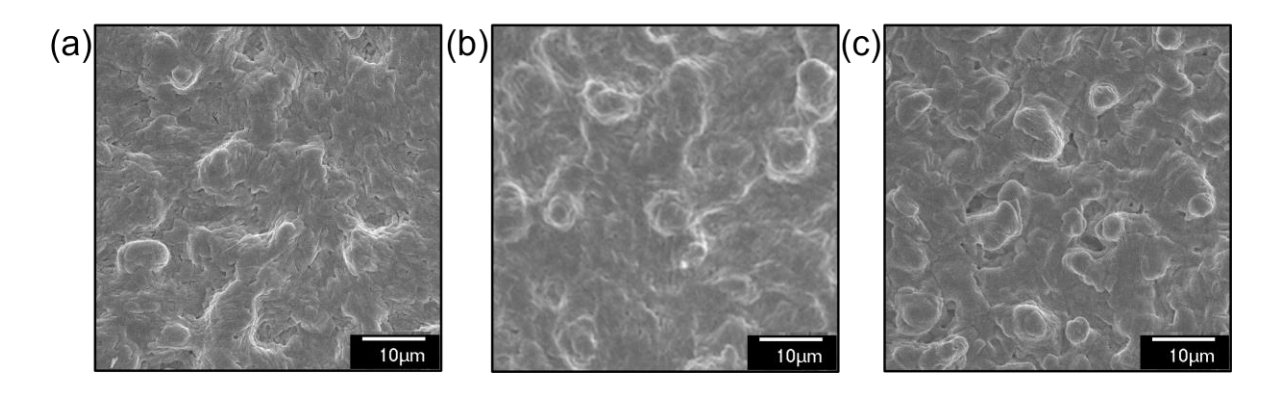


Figure 2-18. Top-view SEM images of [PEA]<sub>3</sub>[Bi<sub>2</sub>l<sub>9</sub>] films on FTO/glass, (a) as deposited, annealed in N<sub>2</sub> at (b) 130 °C and (c) 150 °C.

# 2.3.4 Vacuum-annealed [PEA]<sub>3</sub>[Bi<sub>2</sub>l<sub>9</sub>] films

In order to obtain [PEA]<sub>3</sub>[Bi<sub>2</sub>I<sub>9</sub>] films with no DMF and desired morphologies and adhesion, a vacuum oven was used to replace the CVD reactor for the film annealing. The reason is that the effect of vacuum environment can help DMF evaporate from the film at a lower temperature compared to under atmospheric conditions. After annealing at 120 °C for 30 min in the vacuum oven, GIXRD patterns of films on glass, TiO<sub>2</sub>/glass and FTO/glass all matched well with the calculated pattern from SCXRD

(Figure 2-19), demonstrating that the residual DMF was removed completely. It is worth mentioning that an obvious preferential growth orientation in the  $(10\bar{1})$  plane could be seen in all three samples, and the degree of preferential orientation was in the order of the film deposition on glass < TiO<sub>2</sub>/glass < FTO/glass, with the  $(11\bar{1})$  peak intensity decreasing gradually. A similar condition was observed in [PEA]<sub>3</sub>[Bi<sub>2</sub>I<sub>9</sub>] films annealed at 150 °C in the CVD reactor as well (Figure 2-8, Figure 2-15 and Figure 2-16). This indicated that the film showed less preferential to grow in the direction of *b*-axis in the substrate plane. The preferential growth orientation is typically beneficial to the deposition of films with compact, uniform and smooth surfaces.<sup>69</sup>

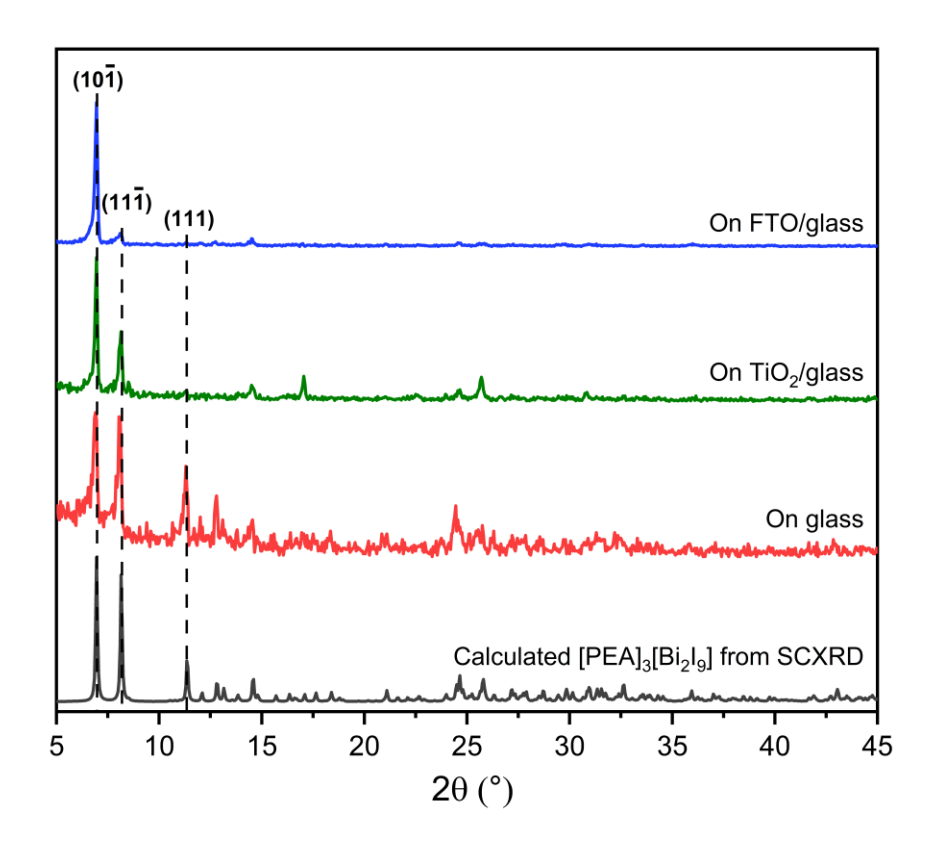


Figure 2-19. GIXRD patterns of [PEA]<sub>3</sub>[Bi<sub>2</sub>l<sub>9</sub>] films deposited on glass (red), TiO<sub>2</sub>/glass (green) and FTO/glass (blue) annealed at 120 °C in the vacuum oven.

In the top-view SEM images (Figure 2-20), it was observed that due to the lower annealing temperature in the vacuum oven than that used in the CVD reactor, the [PEA]<sub>3</sub>[Bi<sub>2</sub>I<sub>9</sub>] films still maintained a good crystallization after DMF removal, and showed good coverage over substrates, especially TiO<sub>2</sub>/glass and FTO/glass.

Rectangular crystals with flat surfaces constituted the [PEA]<sub>3</sub>[Bi<sub>2</sub>I<sub>9</sub>] films on TiO<sub>2</sub>/glass and FTO/glass. Considering both GIXRD patterns and top-view SEM images, it is worth mentioning that while all films showed preferential growth orientation in the ( $10\overline{1}$ ) plane, only films without detected perpendicular (111) reflection ( $2\theta = 11.4^{\circ}$ ) were composed of flat crystallites with shallow surfaces observed in SEM (Figure 2-15, Figure 2-17a, Figure 2-19 and Figure 2-20b, c).

Compared with films annealed in the CVD reactor, films annealed in the vacuum oven presented closer morphologies to those of as-deposited films, while some cracks appeared on the film surfaces. These cracks are likely resulted from the fast evaporation of DMF under vacuum. Furthermore, it was observed that film grains did not shrink after vacuum-annealing, different from films annealed in the CVD reactor. It was reported that perovskite films with large grains showed better performance in solar cell devices, because the grain boundary could be reduced for larger grains, leading to less defects.<sup>70</sup> Therefore, the charge recombination, which hinders the device efficiency, was decreased.<sup>43</sup>

The vacuum-annealed film on FTO/glass underwent sintering to form a compact film, and was the smoothest among films on the three kinds of substrates, where the RMS roughness of the [PEA] $_3$ [Bi $_2$ I $_9$ ] films on glass, TiO $_2$ /glass and FTO/glass, obtained from AFM measurements, were 0.467 µm, 0.265 µm and 0.128 µm respectively (Figure 2-21). The vacuum-annealed film on FTO/glass also has the lowest RMS roughness than other reported perovskite films deposited *via* AACVD. $^{53}$  This surface characteristic was indicated in side-view SEM images as well (Figure 2-25c). The vacuum-annealed film on FTO/glass, with as large as 4 × 20 µm crystals, showed minimized grain boundaries and a less cracked surface (Figure 2-20c), and its high degree of preferential orientation in the (10 $\overline{1}$ ) plane is accordance with the observed shallow surface features.

Furthermore, similar to films annealed in the CVD reactor, vacuum-annealed [PEA]<sub>3</sub>[Bi<sub>2</sub>I<sub>9</sub>] films on TiO<sub>2</sub>/glass and FTO/glass were less powdery and better adhered than the film on amorphous glass (Figure 2-20). This further demonstrated that with the benefits of the crystalline substrates, the [PEA]<sub>3</sub>[Bi<sub>2</sub>I<sub>9</sub>] film was able to grow with a higher degree of preferential orientation and process better crystallization. The variation in morphological features of [PEA]<sub>3</sub>[Bi<sub>2</sub>I<sub>9</sub>] films on different substrates

resulted from the difference in chemical compatibility, lattice match and crystalline surface of glass, TiO<sub>2</sub>/glass and FTO/glass.<sup>71</sup>

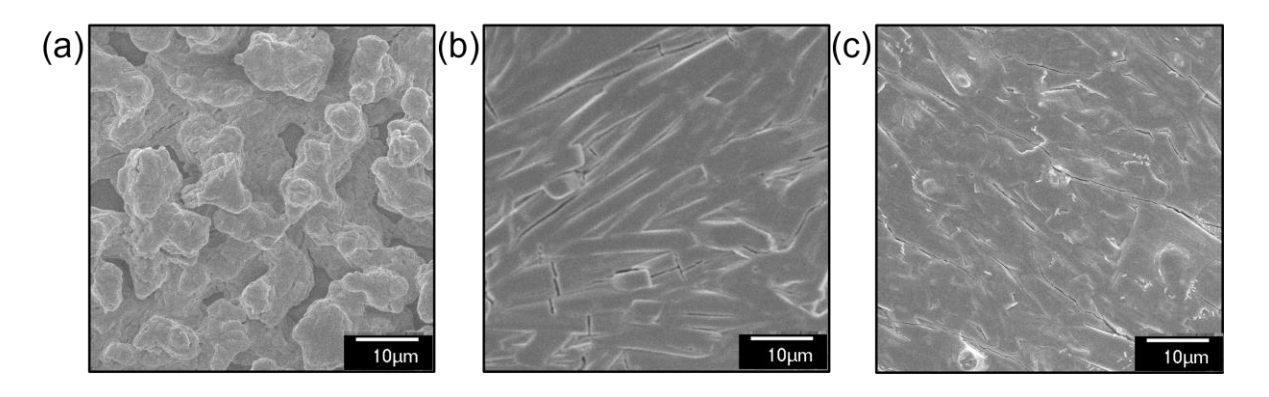


Figure 2-20. Top-view SEM images of [PEA]<sub>3</sub>[Bi<sub>2</sub>I<sub>9</sub>] films on (a) glass, (b) TiO<sub>2</sub>/glass and (c) FTO/glass annealed at 120 °C in the vacuum oven.

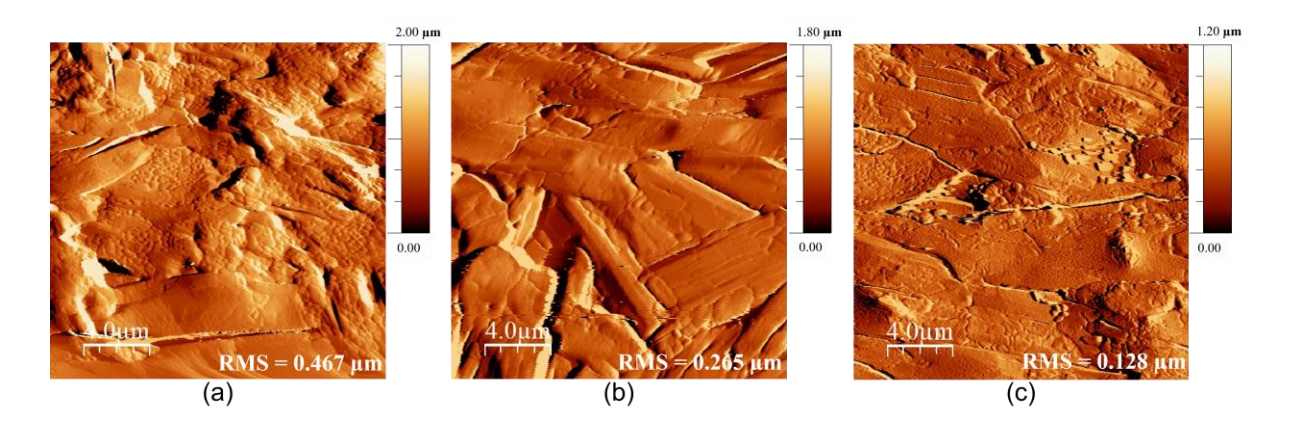


Figure 2-21. AFM images of [PEA]<sub>3</sub>[Bi<sub>2</sub>I<sub>9</sub>] films vacuum-annealed at 120 °C on (a) glass, (b) TiO<sub>2</sub>/glass and (c) FTO/glass. All images were of a 20 x 20 μm<sup>2</sup> area.

To investigate the reason for the varied degree of preferential orientation in films deposited on different substrates, the contact angle test was performed on the three kinds of substrates (Figure 2-22). Based on the intrinsic properties of AACVD, the interaction between precursor solution droplets and the substrate during the deposition process is one of the most important factors influencing the film growth. Because the contact angle between the precursor solution and the substrate is largely determined by the polarity of the solvent, DMF was used in the contact angle test. It can be seen from the images that the contact angles of DMF on glass, TiO<sub>2</sub>/glass and FTO/glass were 45.8°, 23.4° and 12.9° respectively. The lowest contact angle on FTO/float glass means the best hydrophilicity of DMF. It has been reported that the nucleation energy barrier in the film growth process would be less if the contact angle between the

solution and the substrate is lower.<sup>72</sup> Therefore, compared with glass and TiO<sub>2</sub>/glass, FTO/glass is more favorable to the nucleation and growth of [PEA]<sub>3</sub>[Bi<sub>2</sub>I<sub>9</sub>] films as the substrate when DMF is used as the solvent of the precursor solution. The results of the contact angle test also gave a reason for the highest degree of preferential orientation in films on FTO/glass.<sup>73</sup>

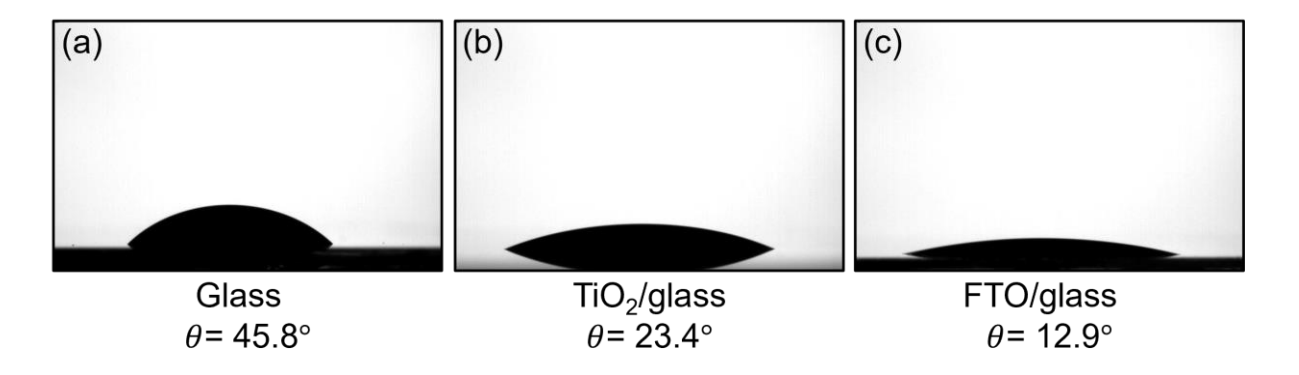


Figure 2-22. DMF contact angles on (a) glass, (b) TiO<sub>2</sub>/glass and (c) FTO/glass.

From side-view SEM images, [PEA]<sub>3</sub>[Bi<sub>2</sub>I<sub>9</sub>] films deposited on different substrates showed similar thickness in the range of 5–8 µm (Figure 2-23, Figure 2-24 and Figure 2-25). A thin layer of TiO<sub>2</sub> with a thickness around 150 nm can be seen clearly between the glass and the [PEA]<sub>3</sub>[Bi<sub>2</sub>I<sub>9</sub>] film (Figure 2-24), reconfirming the successful deposition of TiO<sub>2</sub>. It can also be observed that the film thickness was affected slightly by the annealing treatment in all cases. In addition, for vacuum-annealed films on TiO<sub>2</sub>/glass and FTO/glass, crystalline, uniform and compact film features were unaffected compared with as-deposited films (Figure 2-24c and Figure 2-25c). This further proved that films with desired morphologies could be obtained by using crystalline substrates and vacuum-annealing at 120 °C. The film fabricated *via* AACVD in this work is much thicker than the spin-coated film of a similar bismuth halide material (~600 nm).<sup>74</sup> Different mechanisms of the crystal growth in AACVD and spin-coating processes could explain this variation in the film thickness,<sup>75</sup> as well as the grain size and preferential orientation.<sup>15</sup>

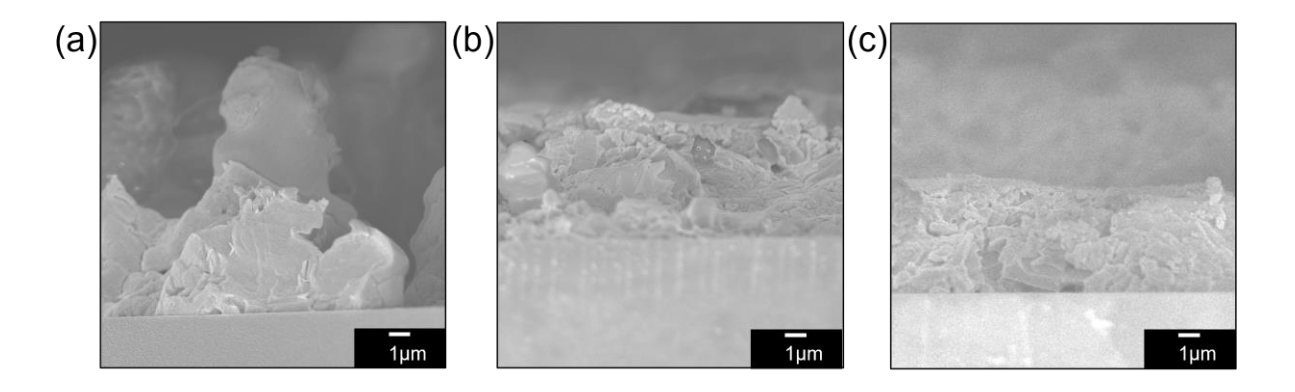


Figure 2-23. Side-view SEM images of [PEA]<sub>3</sub>[Bi<sub>2</sub>I<sub>9</sub>] films on glass, (a) as deposited, (b) annealed at 150 °C in N<sub>2</sub> and (c) annealed at 120 °C in the vacuum oven.

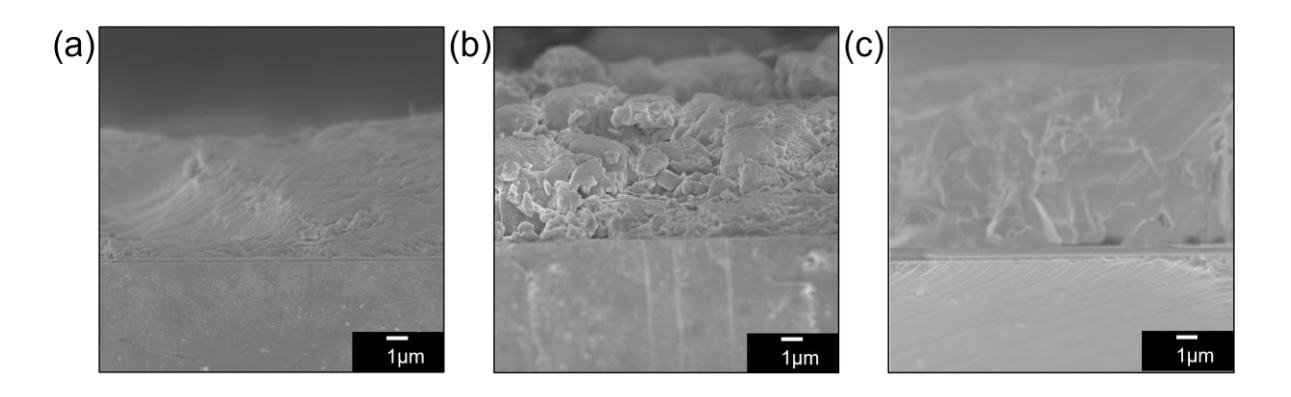


Figure 2-24. Side-view SEM images of [PEA] $_3$ [Bi $_2$ I $_9$ ] films on TiO $_2$ /glass, (a) as deposited, (b) annealed at 150 °C in N $_2$  and (c) annealed at 120 °C in the vacuum oven.

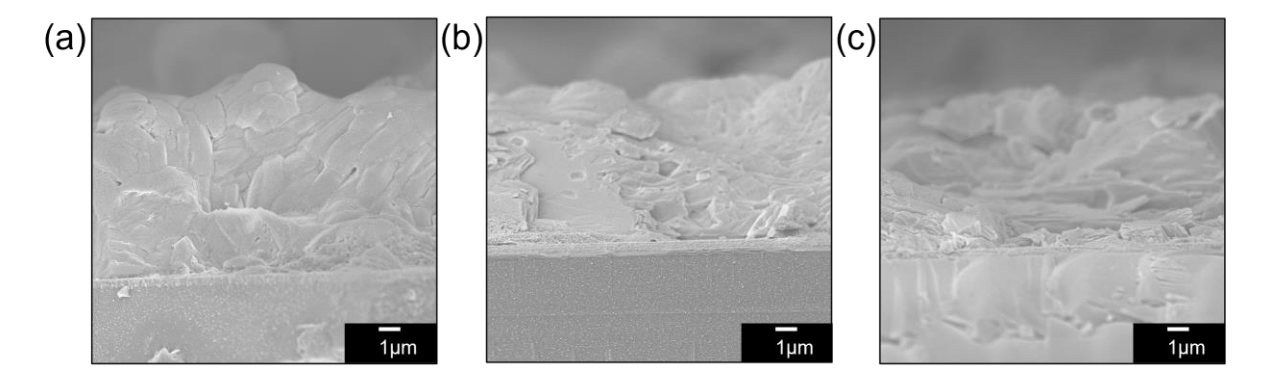


Figure 2-25. Side-view SEM images of [PEA] $_3$ [Bi $_2$ I $_9$ ] films on FTO/glass, (a) as deposited, (b) annealed at 150 °C in N $_2$  and (c) annealed at 120 °C in the vacuum oven.

## 2.3.5 Optoelectrical properties and band gap calculations

Optoelectrical properties of the [PEA]3[Bizl9] films fabricated *via* AACVD were studied by the UV-Vis spectroscopy, and the optical band gaps of films were obtained using Tauc-plot method. In order to investigate the influence of annealing conditions and kinds of substrates on the film properties, the as-deposited [PEA]3[Bizl9] films, films annealed at 150 °C in N2 and films vacuum-annealed at 120 °C were characterized. As determined in the side-view SEM images, the [PEA]3[Bizl9] films were very thick. According to the Beer-Lambert law, a thicker film is less likely to transmit light. As a result, the transmittance of all [PEA]3[Bizl9] films in this work were lower than 60%, which is far less than spin-coated films (around 90%). All [PEA]3[Bizl9] films deposited on three substrates exhibited a reddish orange colour and absorbed light within 500–600 nm (Figure 2-26, Figure 2-27 and Figure 2-28). In addition, there was no significant influence of annealing conditions on the transmittance spectra of films on the three substrates. Due to the incomplete coverage of films on glass, an extra absorbance peak from the glass substrate appeared at 350 nm (Figure 2-26). However, this peak did not affect the analysis of spectra or the calculation of band gaps.

Both direct and indirect band gaps of films were calculated, and values are summarized in Table 2-2. The band gaps of films on TiO<sub>2</sub>/glass and FTO/glass were the same, while films on glass had smaller band gaps regardless of direct or indirect band gaps. Because the thickness of all films were similar, film thickness should not be the reason for the different band gaps. The indirect band gap of films on TiO<sub>2</sub>/glass and FTO/glass was 2.17 eV, which is close to the reported value of the spin-coated [PEA]<sub>3</sub>[Bi<sub>2</sub>I<sub>9</sub>] film on FTO (2.23 eV).<sup>15</sup> Nevertheless, the indirect band gap of films on glass was 2.05 eV. This difference in band gaps of films on different substrates was reported in methylammonium bismuth iodide as well, while no possible reasons were discussed.<sup>3,61,77-80</sup> The band bending between perovskites and semiconducting substrates such as TiO<sub>2</sub> and FTO has been reported.<sup>81,82</sup> In addition, according to energy band levels of materials, the band alignment between [PEA]<sub>3</sub>[Bi<sub>2</sub>I<sub>9</sub>] and TiO<sub>2</sub> or FTO can lead to the band bending in theory, and influence the work function of materials (Figure 2-29). Therefore, both direct and indirect band gaps calculated from transmittance spectra of films on TiO<sub>2</sub>/glass and FTO/glass were larger than those of films on glass. 83 The indirect band gap of films on glass, 2.05 eV, should be the intrinsic

band gap of [PEA]<sub>3</sub>[Bi<sub>2</sub>I<sub>9</sub>]. This value is also accordance with that from the DFT calculation.<sup>15</sup>

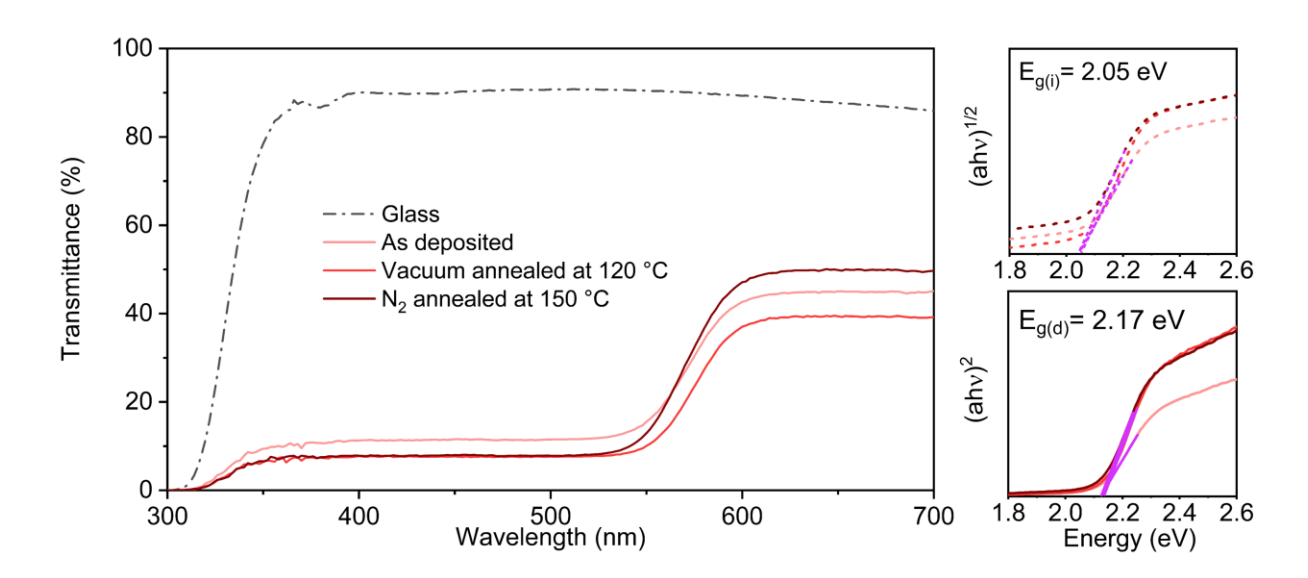


Figure 2-26. Transmittance spectra of [PEA] $_3$ [Bi $_2$ I $_9$ ] films on glass, as deposited, annealed at 150 °C in N $_2$  and annealed at 120 °C in the vacuum oven. Optical band gaps were calculated using a Tauc-plot method.

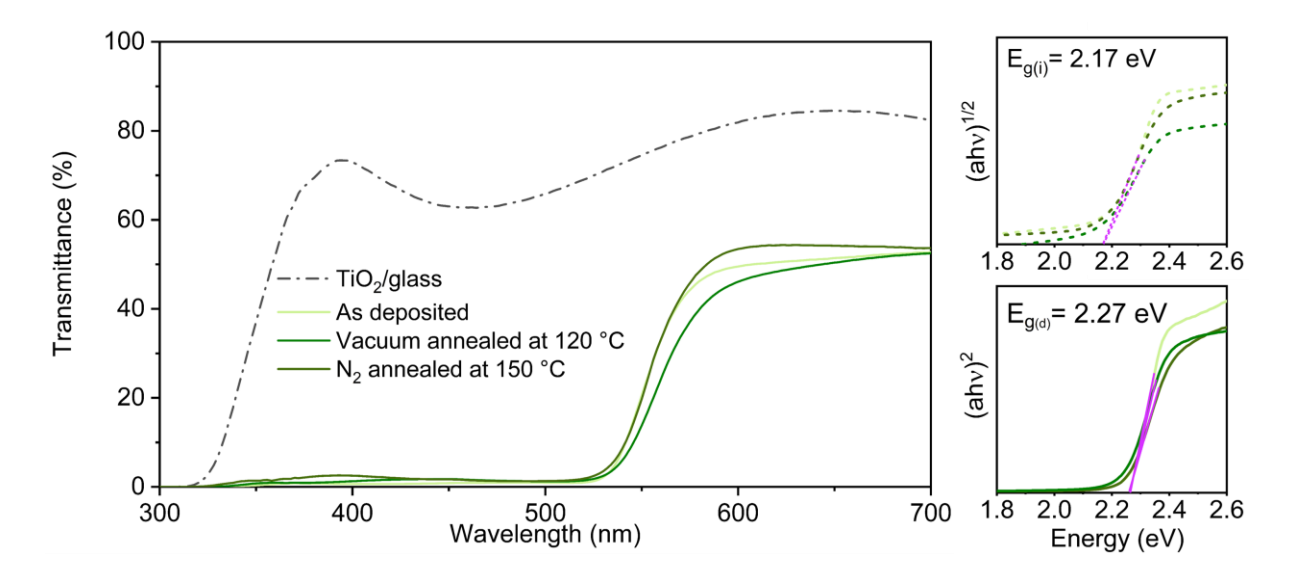


Figure 2-27. Transmittance spectra of [PEA]<sub>3</sub>[Bi<sub>2</sub>I<sub>9</sub>] films on TiO<sub>2</sub>/glass, as deposited, annealed at 150 °C in N<sub>2</sub> and annealed at 120 °C in the vacuum oven. Optical band gaps were calculated using a Tauc-plot method.

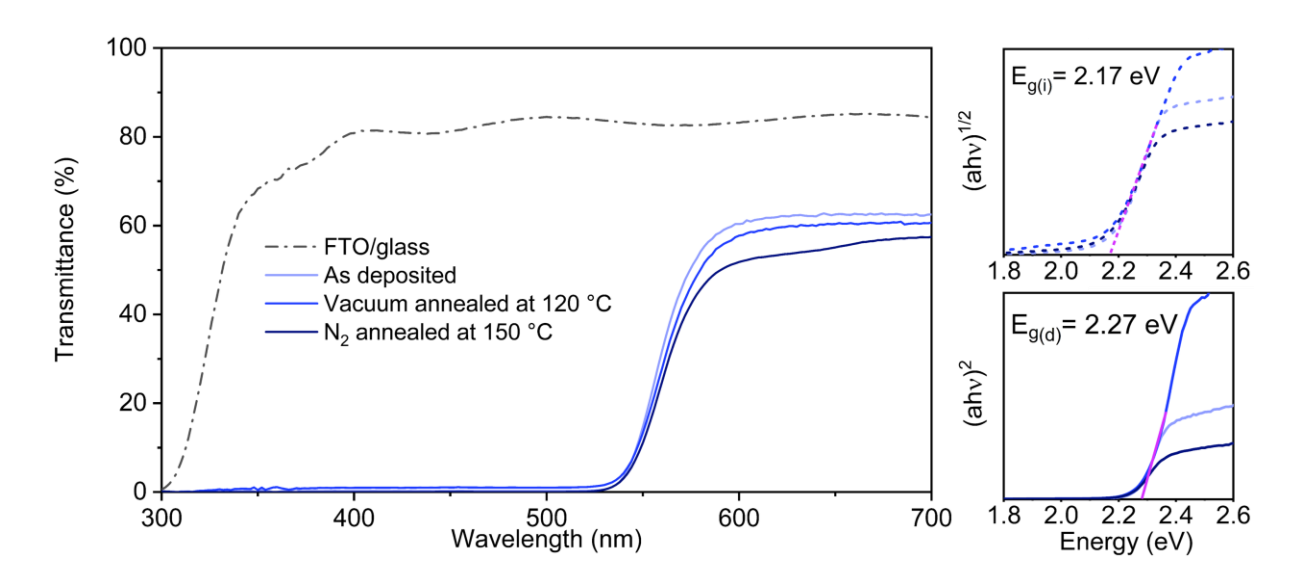


Figure 2-28. Transmittance spectra of [PEA]<sub>3</sub>[Bi<sub>2</sub>I<sub>9</sub>] films on FTO/glass, as deposited, annealed at 150 °C in N<sub>2</sub> and annealed at 120 °C in the vacuum oven. Optical band gaps were calculated using a Tauc-plot method.

Table 2-2. Calculated direct and indirect band gaps of [PEA]<sub>3</sub>[Bi<sub>2</sub>l<sub>9</sub>] films.

[PEA] <sub>3</sub> [Bi <sub>2</sub> l <sub>9</sub> ]	On glass	On TiO <sub>2</sub> /glass	On FTO/glass
Direct band gap (eV)	2.17	2.27	2.27
Indirect band gap (eV)	2.05	2.17	2.17

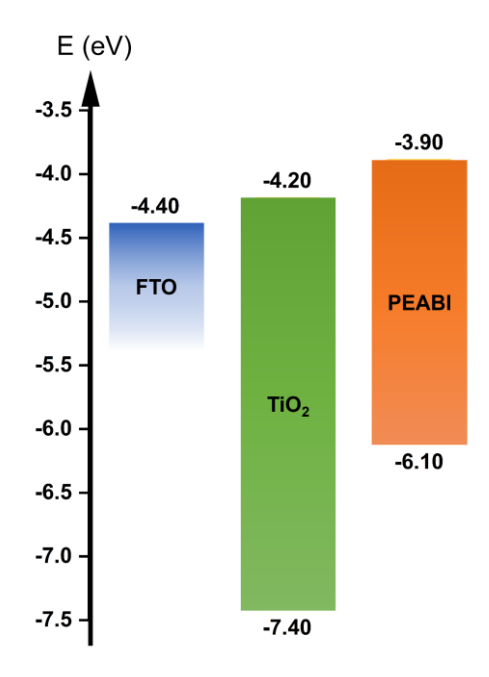


Figure 2-29. Energy band alignment diagram with respect to the vacuum level of FTO, TiO<sub>2</sub> and [PEA]<sub>3</sub>[Bi<sub>2</sub>I<sub>9</sub>] (PEABI).<sup>84</sup>

To further determine the band gap of [PEA]<sub>3</sub>[Bi<sub>2</sub>I<sub>9</sub>] without interference factors, PL spectroscopy was carried out. PL is a surface technique, so no band bending effect should be detected in PL testing.<sup>85</sup> Low-dimensional perovskite-derived materials with indirect band gaps typically generate weak PL, so low intensities in Figure 2-30 are expected. It is interesting that PL peaks of all measured films were observed at the same wavelength (~600 nm), and excitation binding energies of [PEA]<sub>3</sub>[Bi<sub>2</sub>I<sub>9</sub>] films were estimated from PL spectra, which were the same as the indirect band gap of films on glass.

A PL peak at ~600 nm and two bands (around 525 nm and 658 nm) were observed in the PL spectra of all films (Figure 2-30). Similar bands were also observed in the PL spectra of MAPI treated by PEAI.<sup>86</sup> Two-dimensional perovskites have been reported to present multiple PL peaks because of the existence of secondary phases.<sup>87,88</sup> Furthermore, based on the combined analysis of GIXPD patterns, SEM images and PL spectra, it was found that the contribution of each emission band had a correlation with the preferential orientation. The [PEA]<sub>3</sub>[Bi<sub>2</sub>I<sub>9</sub>] films composed of crystallites with flat surfaces showed stronger 525 nm emission, where the preferential orientation in the (111) plane was not detected in GIXRD. The influence of the crystal orientation on PL was also reported in MAPI.<sup>89</sup> These emissions are possibly resulting from the surface trap-mediated recombination, and the variation of the surface trap population can lead to different PL intensities.<sup>59,90</sup>

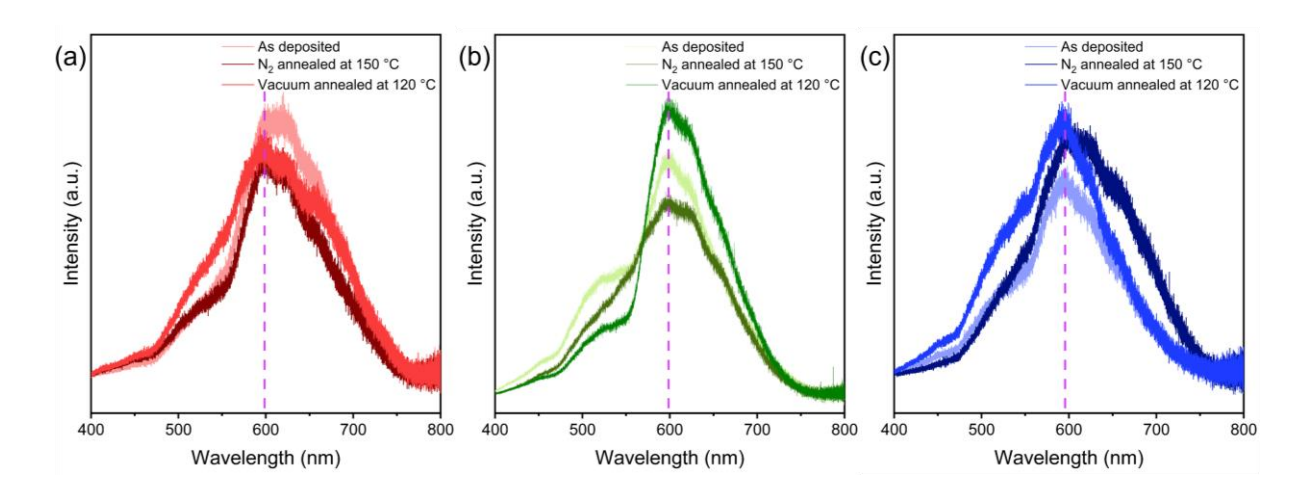


Figure 2-30. PL spectra of [PEA]<sub>3</sub>[Bi<sub>2</sub>l<sub>9</sub>] films on (a) glass, (b) TiO<sub>2</sub>/glass and (c) FTO/glass.

## 2.3.6 Stability

Measuring the water contact angle is a common way to study the wettability of a solid surface. Because films annealed in the vacuum oven showed the best morphologies, water contact angles were collected for vacuum-annealed [PEA]<sub>3</sub>[Bi<sub>2</sub>I<sub>9</sub>] films on three kinds of substrates (Figure 2-31). Compared with other 3D or PEAI-treated 2D/3D lead halide perovskite films,  $^{60,91,92}$  larger water contact angles on all [PEA]<sub>3</sub>[Bi<sub>2</sub>I<sub>9</sub>] films prepared *via* AACVD in this work demonstrated the improved water repellency of films, with contact angles of 72.9°, 73.2° and 75.4° for films on glass, TiO<sub>2</sub>/glass and FTO/glass respectively. Using Neumann's equation:  $\cos(\theta) = -1 + 2(\gamma_{SV}/\gamma_{LV})^{1/2} \times \exp(-\beta(\gamma_{LV}-\gamma_{SV})^2)$ ,  $^{93,94}$  the surface free energy, also known as solid surface tension, can be calculated from the water contact angle, which is 37.3 mJ·m<sup>-2</sup> for the [PEA]<sub>3</sub>[Bi<sub>2</sub>I<sub>9</sub>] film on FTO. This surface free energy is significantly lower than the reported energies of 3D perovskite films,  $^{60,94}$  implying a better moisture resistance of [PEA]<sub>3</sub>[Bi<sub>2</sub>I<sub>9</sub>] films.

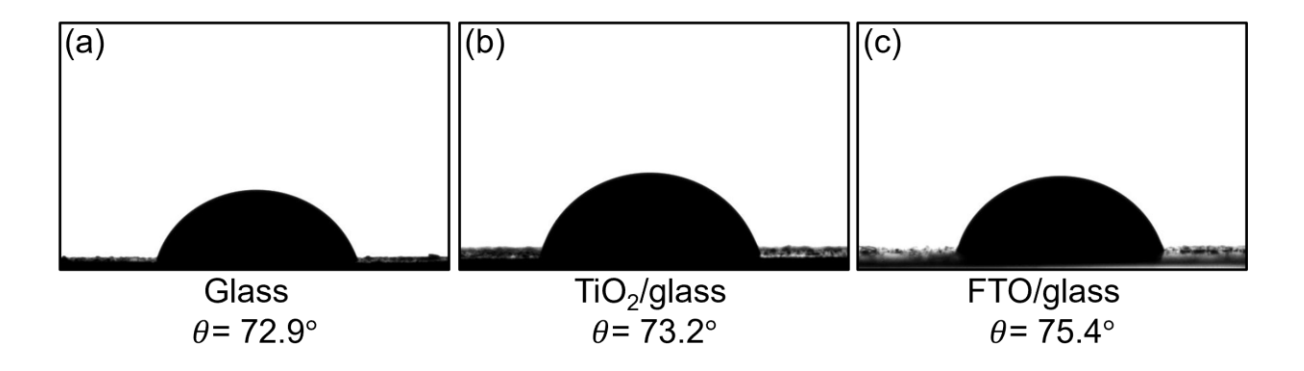


Figure 2-31. Water contact angles on vacuum-annealed (120 °C) [PEA]<sub>3</sub>[Bi<sub>2</sub>I<sub>9</sub>] films deposited over (a) glass, (b) TiO<sub>2</sub>/glass and (c) FTO/glass.

Films in this work were stored in air up to 6 months, after which no extra peaks originated from the degradation or oxidation of [PEA]<sub>3</sub>[Bi<sub>2</sub>I<sub>9</sub>] were observed in GIXRD patterns (Figure 2-32), indicating that [PEA]<sub>3</sub>[Bi<sub>2</sub>I<sub>9</sub>] films fabricated *via* AACVD have a remarkable ambient stability. Therefore, relative devices based on these films would likely have an increased longevity in a moist environment due to their improved water repellency, which shows their great potential in water-based devices for energy applications.

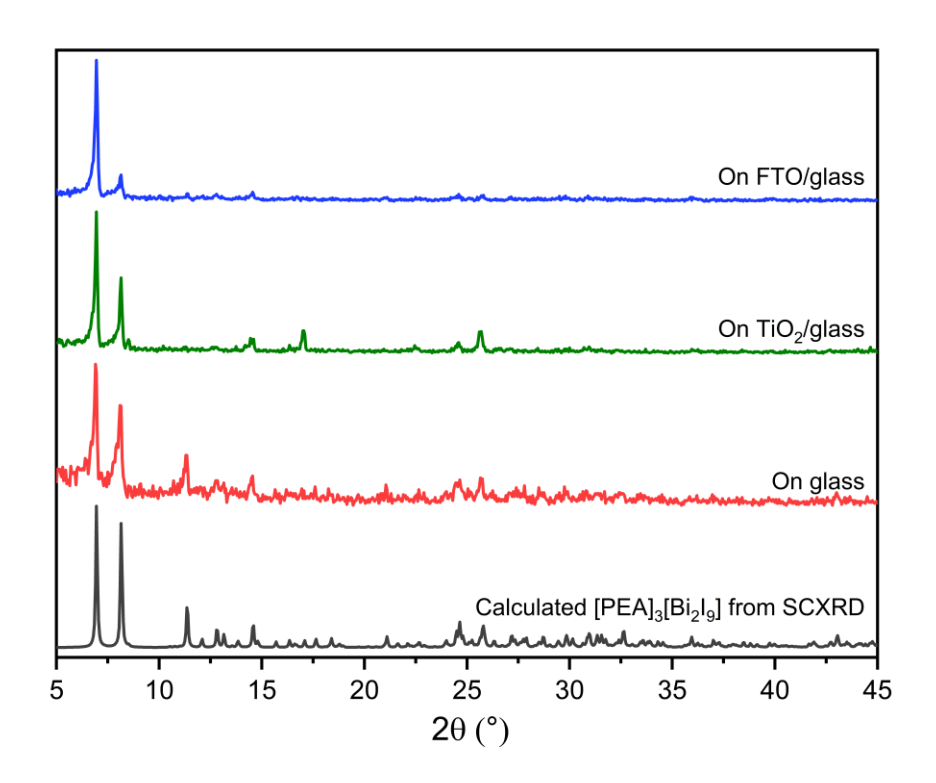


Figure 2-32. GIXRD patterns of [PEA]<sub>3</sub>[Bi<sub>2</sub>l<sub>9</sub>] films vacuum-annealed at 120 °C on glass, TiO<sub>2</sub>/glass and FTO/glass after 6-month exposure in ambient conditions.

## 2.3.7 Applications

Complete solar cells were attempted to be fabricated based on [PEA]<sub>3</sub>[Bi<sub>2</sub>I<sub>9</sub>] films

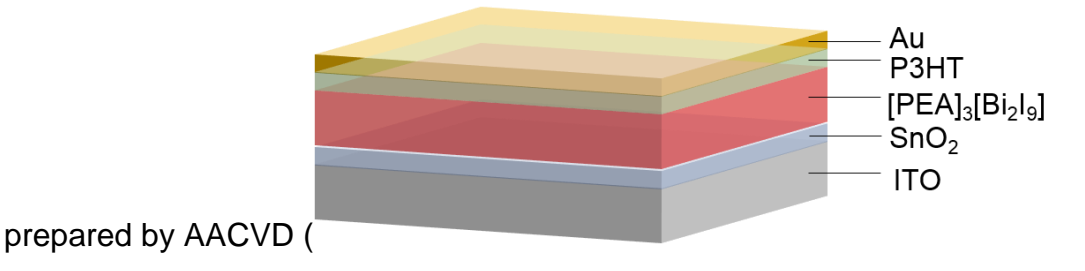


Figure 2-33). However, none of these devices showed attractive performance. There are two possible reasons for the failure of these solar cells. Firstly, there are too many pinholes in the [PEA] $_3$ [Bi $_2$ I $_9$ ] films, and cracks shown in top-view SEM images would also affect the performance of devices. Secondly, [PEA] $_3$ [Bi $_2$ I $_9$ ] films prepared by AACVD were too thick. Typically, the thickness of active perovskite layers in solar cells is less than 1  $\mu$ m. However, the thickness of films in this work was around 5  $\mu$ m. Thick films would increase the possibility of charge recombination, hindering the device

efficiency. Similar problems also appeared in other perovskite films fabricated by AACVD.<sup>53</sup> Therefore, future work needs to be done to deposit thinner [PEA]<sub>3</sub>[Bi<sub>2</sub>I<sub>9</sub>] films with uniform and smooth morphologies *via* AACVD through optimizing precursors and deposition parameters.

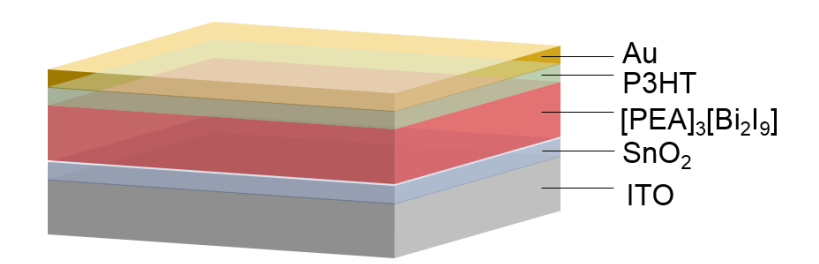


Figure 2-33. The structure of a complete solar cell device based on the [PEA]<sub>3</sub>[Bi<sub>2</sub>l<sub>9</sub>] film.

Besides perovskite solar cells, [PEA]<sub>3</sub>[Bi<sub>2</sub>I<sub>9</sub>] films were also attempted to be applied in photocatalysis. However, no photocatalytic activity was observed. In the photocatalytic test, the resazurin ink was used as the indicator. Due to the hydrophobic surface of [PEA]<sub>3</sub>[Bi<sub>2</sub>I<sub>9</sub>] films, the ink could not attach to the film surface, and no reaction occurred between the film and the ink.

However, a collaboration project with Hellenic Mediterranean University in Greece was carried out to explore the electrochemical properties of AACVD-grown [PEA] $_3$ [Bi $_2$ I $_9$ ] films. In this project, the [PEA] $_3$ [Bi $_2$ I $_9$ ] film deposited on FTO was used as the anode in aqueous Zn $^{2+}$  electrolytes.

The [PEA]₃[Bi₂l₃] anode showed a great electrochemical stability within the electrochemical window from −0.5 V to +1.5 V, and the reservable phase transition of Zn²+ intercalation/deintercalation was observed in the anode. In the 1 M ZnSO₄·7H₂O electrolyte, the [PEA]₃[Bi₂l₃] film on FTO showed a specific capacity of 220 mAh⋅g⁻¹ at 0.4 A⋅g⁻¹. Furthermore, it presented the stable crystal structure and capacity retention of almost 100% after 50 continuous scans.<sup>95</sup> This project demonstrated the potential of [PEA]₃[Bi₂l₃] films fabricated by AACVD in the battery field and provided a reference for the large-scale production of electrodes.

#### 2.4 Summary

In conclusion, a hybrid lead-free halide perovskite-derived material, [PEA]<sub>3</sub>[Bi<sub>2</sub>I<sub>9</sub>], was deposited successfully on different substrates, such as glass, TiO<sub>2</sub>/glass and FTO/glass via AACVD, and the deposition and annealing conditions of the [PEA]<sub>3</sub>[Bi<sub>2</sub>I<sub>9</sub>] film were optimized. Crystal structures, compositions and morphologies were investigated for all films, showing the influence of substrates and annealing conditions on the bulk properties of films. Powdery films were deposited on amorphous glass, but with the support of crystalline substrates like TiO2 and FTO, uniform and compact films of [PEA]<sub>3</sub>[Bi<sub>2</sub>I<sub>9</sub>] were obtained. Films exhibited a thickness of 5-8 µm and preferential orientation when deposited on crystalline substrates, especially FTO/glass. Films with desired compositions and morphologies were finally fabricated by using crystalline substrates and vacuum-annealing at 120 °C. Optoelectrical properties of films were studied by transmittance spectroscopy and PL spectroscopy. The optical band gap of the [PEA]<sub>3</sub>[Bi<sub>2</sub>I<sub>9</sub>] films was 2.05 eV. Band bending occurred between [PEA]<sub>3</sub>[Bi<sub>2</sub>I<sub>9</sub>] films and semiconducting substrates, leading to the variation of experimental band gaps. Due to the existence of the hydrophobic PEA+ ligand, the remarkable humidity resistance of films was demonstrated in water contact angle test, mild preparation and storage environment. Ultimately, this work highlights a scalable and inexpensive method, AACVD, to fabricate films of a novel stable perovskitederived material with tunable morphologies on different substrates, as well as showing the potential of these films in various energy applications.

#### 2.5 Reference

- (1) Jena, A. K.; Kulkarni, A.; Miyasaka, T. Halide Perovskite Photovoltaics: Background, Status, and Future Prospects. *Chem Rev* **2019**, *119*, 3036–3103. https://doi.org/10.1021/acs.chemrev.8b00539.
- (2) Kojima, A.; Teshima, K.; Shirai, Y.; Miyasaka, T. Organometal Halide Perovskites as Visible-Light Sensitizers for Photovoltaic Cells. *J Am Chem Soc* **2009**, 131 (17), 6050–6051. https://doi.org/10.1021/ja809598r.
- (3) Park, B. W.; Philippe, B.; Zhang, X.; Rensmo, H.; Boschloo, G.; Johansson, E. M. J. Bismuth Based Hybrid Perovskites A3Bi2I9 (A: Methylammonium or Cesium) for Solar Cell Application. *Adv Mater* **2015**, *27* (43), 6806–6813. https://doi.org/10.1002/adma.201501978.

- (4) Min, H.; Kim, M.; Lee, S. U.; Kim, H.; Kim, G.; Choi, K.; Lee, J. H.; Seok, S. II. Efficient, Stable Solar Cells by Using Inherent Bandgap of a-Phase Formamidinium Lead lodide. *Science* **2019**, *366* (6466), 749–753. https://doi.org/10.1126/science.aay7044.
- (5) Hu, W.; He, X.; Fang, Z.; Lian, W.; Shang, Y.; Li, X.; Zhou, W.; Zhang, M.; Chen, T.; Lu, Y.; Zhang, L.; Ding, L.; Yang, S. Bulk Heterojunction Gifts Bismuth-Based Lead-Free Perovskite Solar Cells with Record Efficiency. *Nano Energy* **2020**, *68*, 104362. https://doi.org/10.1016/j.nanoen.2019.104362.
- (6) Goforth, A. M.; Tershansy, M. A.; Smith, M. D.; Peterson, L. R.; Kelley, J. G.; DeBenedetti, W. J. I.; Zur Loye, H. C. Structural Diversity and Thermochromic Properties of Iodobismuthate Materials Containing D-Metal Coordination Cations: Observation of a High Symmetry [Bi<sub>3</sub>I<sub>11</sub>]<sup>2-</sup> Anion and of Isolated I<sup>-</sup> Anions. *J Am Chem Soc* **2011**, *133* (3), 603–612. https://doi.org/10.1021/ja108278j.
- (7) Stoumpos, C. C.; Malliakas, C. D.; Kanatzidis, M. G. Semiconducting Tin and Lead Iodide Perovskites with Organic Cations: Phase Transitions, High Mobilities, and near-Infrared Photoluminescent Properties. *Inorg Chem* **2013**, *52* (15), 9019–9038. https://doi.org/10.1021/ic401215x.
- (8) Solar, P.; Review, C. A.; Sani, F. Advancement on Lead-Free Organic-Inorganic Halide. *Materials* **2018**, *11*, 1008. https://doi.org/10.3390/ma11061008.
- (9) Jiang, Q.; Zhao, Y.; Zhang, X.; Yang, X.; Chen, Y.; Chu, Z.; Ye, Q.; Li, X.; Yin, Z.; You, J. Surface Passivation of Perovskite Film for Efficient Solar Cells. *Nat Photonics* **2019**, *13* (7), 460–466. https://doi.org/10.1038/s41566-019-0398-2.
- (10) Straus, D. B.; Hurtado Parra, S.; Iotov, N.; Zhao, Q.; Gau, M. R.; Carroll, P. J.; Kikkawa, J. M.; Kagan, C. R. Tailoring Hot Exciton Dynamics in 2D Hybrid Perovskites through Cation Modification. *ACS Nano* **2020**, *14*, 3621–3629. https://doi.org/10.1021/acsnano.0c00037.
- (11) Bouduban, M. E. F.; Queloz, V. I. E.; Caselli, V. M.; Cho, K. T.; Kirmani, A. R.; Paek, S.; Roldan-Carmona, C.; Richter, L. J.; Moser, J. E.; Savenije, T. J.; Nazeeruddin, M. K.; Grancini, G. Crystal Orientation Drives the Interface Physics at

- Two/Three-Dimensional Hybrid Perovskites. *J Phys Chem Lett* **2019**, *10* (19), 5713–5720. https://doi.org/10.1021/acs.jpclett.9b02224.
- (12) Liu, B.; Xu, L.; Guo, G. C.; Huang, J. S. Three Inorganic-Organic Hybrids of Bismuth(III) Iodide Complexes Containing Substituted 1,2,4-Triazole Organic Components with Charaterizations of Diffuse Reflectance Spectra. *J Solid State Chem* **2006**, *179* (6), 1611–1617. https://doi.org/10.1016/j.jssc.2006.02.011.
- (13) Li, T.; Wang, Q.; Nichol, G. S.; Morrison, C. A.; Han, H.; Hu, Y.; Robertson, N. Extending Lead-Free Hybrid Photovoltaic Materials to New Structures: Thiazolium, Aminothiazolium and Imidazolium Iodobismuthates. *Dalt Trans* **2018**, *47* (20), 7050–7058. https://doi.org/10.1039/c8dt00864g.
- (14) Węcławik, M.; Gągor, A.; Jakubas, R.; Piecha-Bisiorek, A.; Medycki, W.; Baran, J.; Zieliński, P.; Gałązka, M. Structure-Property Relationships in Hybrid (C<sub>3</sub>H<sub>5</sub>N<sub>2</sub>)<sub>3</sub>[Sb<sub>2</sub>l<sub>9</sub>] and (C<sub>3</sub>H<sub>5</sub>N<sub>2</sub>)<sub>3</sub>[Bi<sub>2</sub>l<sub>9</sub>] Isomorphs. *Inorg Chem Front* **2016**, 3 (10), 1306–1316. https://doi.org/10.1039/c6qi00260a.
- (15) Ghasemi, M.; Lyu, M.; Roknuzzaman, M.; Yun, J.-H.; Hao, M.; He, D.; Bai, Y.; Chen, P.; Bernhardt, P. V.; Ostrikov, K. (Ken); Wang, L. Phenethylammonium Bismuth Halides: From Single Crystals to Bulky-Organic Cation Promoted Thin-Film Deposition for Potential Optoelectronic Applications. *J Mater Chem A* **2019**, *7* (36), 20733–20741. https://doi.org/10.1039/C9TA07454F.
- (16) Poglitsch, A.; Weber, D. Dynamic Disorder in Methylammoniumtrihalogenoplumbates (II) Observed by Millimeter-Wave Spectroscopy. *J Chem Phys* **1987**. https://doi.org/10.1063/1.453467.
- (17) Park, B.; Philippe, B.; Jain, S. M.; Zhang, X.; Edvinsson, T.; Rensmo, H.; Zietz, B.; Boschloo, G. Chemical Engineering of Methylammonium Lead Iodide/Bromide Perovskites: Tuning of Opto-Electronic Properties and Photovoltaic Performance. *J Mater Chem A* **2015**, *3* (43), 21760–21771. https://doi.org/10.1039/C5TA05470B.
- (18) Ball, J. M.; Petrozza, A. Defects in Perovskite-Halides and Their Effects in Solar Cells. *Nat Energy* **2016**, *1* (11). https://doi.org/10.1038/nenergy.2016.149.

- (19) Xing, G.; Mathews, N.; Lim, S. S.; Lam, Y. M.; Mhaisalkar, S.; Sum, T. C. Long-Range Balanced Electron- and Hole-Transport Lengths in Organic-Inorganic CH<sub>3</sub>NH<sub>3</sub>Pbl<sub>3</sub>. *Science* **2013**, *342* (6156), 344–347.
- (20) Miyata, A.; Mitioglu, A.; Plochocka, P.; Portugall, O.; Wang, J. T.; Stranks, S. D.; Snaith, H. J.; Nicholas, R. J. Organic Inorganic Tri-Halide Perovskites. *Nat Phys* **2015**, *11*, 582–587. https://doi.org/10.1038/NPHYS3357.
- (21) Park, J.; Kim, J.; Yun, H. S.; Paik, M. J.; Noh, E.; Mun, H. J.; Kim, M. G.; Shin, T. J.; Seok, S. II. Controlled Growth of Perovskite Layers with Volatile Alkylammonium Chlorides. *Nature* **2023**, *616* (7958), 724–730. https://doi.org/10.1038/s41586-023-05825-y.
- (22) Zhang, L.; Wang, K.; Zou, B. Bismuth Halide Perovskite-Like Materials: Current Opportunities and Challenges. *ChemSusChem* **2019**, *12*, 1612–1630. https://doi.org/10.1002/cssc.201802930.
- (23) Liu, Y.; Zhang, Y.; Yang, Z.; Ye, H.; Feng, J.; Xu, Z.; Zhang, X.; Munir, R.; Liu, J.; Zuo, P.; Li, Q.; Hu, M.; Meng, L.; Wang, K.; Smilgies, D. M.; Zhao, G.; Xu, H.; Yang, Z.; Amassian, A.; Li, J.; Zhao, K.; Liu, S. F. Multi-Inch Single-Crystalline Perovskite Membrane for High-Detectivity Flexible Photosensors. *Nat Commun* **2018**, *9*, 5302. https://doi.org/10.1038/s41467-018-07440-2.
- (24) Lee, J. W.; Choi, Y. J.; Yang, J. M.; Ham, S.; Jeon, S. K.; Lee, J. Y.; Song, Y. H.; Ji, E. K.; Yoon, D. H.; Seo, S.; Shin, H.; Han, G. S.; Jung, H. S.; Kim, D.; Park, N. G. In-Situ Formed Type i Nanocrystalline Perovskite Film for Highly Efficient Light-Emitting Diode. *ACS Nano* **2017**, *11* (3), 3311–3319. https://doi.org/10.1021/acsnano.7b00608.
- (25) Ahmad, S.; George, C.; Beesley, D. J.; Baumberg, J. J.; De Volder, M. Photo-Rechargeable Organo-Halide Perovskite Batteries. *Nano Lett* **2018**, *18* (3), 1856–1862. https://doi.org/10.1021/acs.nanolett.7b05153.
- (26) Habisreutinger, S. N.; Noel, N. K.; Snaith, H. J. Hysteresis Index: A Figure without Merit for Quantifying Hysteresis in Perovskite Solar Cells. *ACS Energy Lett* **2018**, 3 (10), 2472–2476. https://doi.org/10.1021/acsenergylett.8b01627.

- (27) Conings, B.; Drijkoningen, J.; Gauquelin, N.; Babayigit, A.; D'Haen, J.; D'Olieslaeger, L.; Ethirajan, A.; Verbeeck, J.; Manca, J.; Mosconi, E.; De Angelis, F.; Boyen, H. G. Intrinsic Thermal Instability of Methylammonium Lead Trihalide Perovskite. *Adv Energy Mater* **2015**, *5* (15), 1–8. https://doi.org/10.1002/aenm.201500477.
- (28) Frost, J. M.; Butler, K. T.; Walsh, A. Molecular Ferroelectric Contributions to Anomalous Hysteresis in Hybrid Perovskite Solar Cells. *APL Mater* **2014**, *2*, 081506. https://doi.org/10.1063/1.4890246.
- (29) Ito, N.; Kamarudin, M. A.; Hirotani, D.; Zhang, Y.; Shen, Q.; Ogomi, Y.; Iikubo, S.; Minemoto, T.; Yoshino, K.; Hayase, S. Mixed Sn-Ge Perovskite for Enhanced Perovskite Solar Cell Performance in Air. *J Phys Chem Lett* **2018**, *9* (7), 1682–1688. https://doi.org/10.1021/acs.jpclett.8b00275.
- (30) Zhang, Z.; Li, X.; Xia, X.; Wang, Z.; Huang, Z.; Lei, B.; Gao, Y. High-Quality (CH3NH3)3Bi2I9 Film-Based Solar Cells: Pushing Efficiency up to 1.64%. *J Phys Chem Lett* **2017**, 8 (17), 4300–4307. https://doi.org/10.1021/acs.jpclett.7b01952.
- (31) Hebig, J. C.; Kühn, I.; Flohre, J.; Kirchartz, T. Optoelectronic Properties of (CH3NH3)3Sb2I9 Thin Films for Photovoltaic Applications. *ACS Energy Lett* **2016**, *1* (1), 309–314. https://doi.org/10.1021/acsenergylett.6b00170.
- (32) Li, X.; Zhong, X.; Hu, Y.; Li, B.; Sheng, Y.; Zhang, Y.; Weng, C.; Feng, M.; Han, H.; Wang, J. Organic–Inorganic Copper(II)-Based Material: A Low-Toxic, Highly Stable Light Absorber for Photovoltaic Application. *J Phys Chem Lett* **2017**, *8* (8), 1804–1809. https://doi.org/10.1021/acs.jpclett.7b00086.
- (33) Wu, C.; Zhang, Q.; Liu, G.; Zhang, Z.; Wang, D.; Qu, B.; Chen, Z.; Xiao, L. From Pb to Bi: A Promising Family of Pb-Free Optoelectronic Materials and Devices. *Adv Energy Mater* **2019**, *1902496*, 1–30. https://doi.org/10.1002/aenm.201902496.
- (34) Lehner, A. J.; Fabini, D. H.; Evans, H. A.; Hébert, C. A.; Smock, S. R.; Hu, J.; Wang, H.; Zwanziger, J. W.; Chabinyc, M. L.; Seshadri, R. Crystal and Electronic Structures of Complex Bismuth Iodides A<sub>3</sub>Bi<sub>2</sub>I<sub>9</sub>(A = K, Rb, Cs) Related to Perovskite: Aiding the Rational Design of Photovoltaics. *Chemistry of Materials* **2015**, *27* (20), 7137–7148. https://doi.org/10.1021/acs.chemmater.5b03147.

- (35) Singh, T.; Kulkarni, A.; Ikegami, M.; Miyasaka, T. Effect of Electron Transporting Layer on Bismuth-Based Lead-Free Perovskite (CH<sub>3</sub>NH<sub>3</sub>)<sub>3</sub>Bi<sub>2</sub>I<sub>9</sub> for Photovoltaic Applications. *ACS Appl Mater Interfaces* **2016**, *8* (23), 14542–14547. https://doi.org/10.1021/acsami.6b02843.
- (36) Bresolin, B.; Ben, S.; Sillanpää, M. Methylammonium Iodo Bismuthate Perovskite (CH<sub>3</sub>NH<sub>3</sub>)<sub>3</sub>Bi<sub>2</sub>I<sub>9</sub> as New Effective Visible Light-Responsive Photocatalyst for Degradation of Environment Pollutants. *J Photochem Photobiol A Chem* **2019**, 376 (March), 116–126. https://doi.org/10.1016/j.jphotochem.2019.03.009.
- (37) Eckhardt, K.; Bon, V.; Grothe, J.; Wisser, F. M.; Kaskel, S. Crystallographic Insights into (CH<sub>3</sub>NH<sub>3</sub>)<sub>3</sub>(Bi<sub>2</sub>I<sub>9</sub>): A New Lead-Free Hybrid Organic–Inorganic Material as a Potential Absorber for Photovoltaics. *Chem Commun* **2016**, *52*, 3058–3060. https://doi.org/10.1039/c5cc10455f.
- (38) Okano, T.; Suzuki, Y. Gas-Assisted Coating of Bi-Based (CH<sub>3</sub>NH<sub>3</sub>)<sub>3</sub>Bi<sub>2</sub>l<sub>9</sub> Active Layer in Perovskite Solar Cells. *Mater Lett* **2017**, *191*, 77–79. https://doi.org/10.1016/j.matlet.2017.01.047.
- (39) Eckhardt, K.; Pérez, N.; Rasche, B.; Zeugner, A.; Grothe, J.; Doert, T.; Nielsch, K.; Kaskel, S. A Photosensor Based on Lead-Free Perovskite-like Methyl-Ammonium Bismuth Iodide. *Sens Actuators A Phys* **2019**, *291*, 75–79. https://doi.org/10.1016/j.sna.2019.03.031.
- (40) Dai, Y.; Poidevin, C.; Ochoa-Hernández, C.; Auer, A. A.; Tüysüz, H. A Supported Bismuth Halide Perovskite Photocatalyst for Selective Aliphatic and Aromatic C–H Bond Activation. *Angew Chemie Int Ed* **2020**, *59* (14), 5788–5796. https://doi.org/10.1002/anie.201915034.
- (41) Ahmad, K.; Ansari, S. N.; Natarajan, K.; Mobin, S. M. A (CH<sub>3</sub>NH<sub>3</sub>)<sub>3</sub>Bi<sub>2</sub>I<sub>9</sub> Perovskite Based on a Two-Step Deposition Method: Lead-Free, Highly Stable, and with Enhanced Photovoltaic Performance. *ChemElectroChem* **2019**, *6* (4), 1192–1198. https://doi.org/10.1002/celc.201801322.
- (42) Bryant, D.; Aristidou, N.; Pont, S.; Sanchez-Molina, I.; Chotchunangatchaval, T.; Wheeler, S.; Durrant, J. R.; Haque, S. A. Light and Oxygen Induced Degradation Limits the Operational Stability of Methylammonium Lead Triiodide Perovskite Solar

- Cells. *Energy Environ Sci* **2016**, 9 (5), 1655–1660. https://doi.org/10.1039/C6EE00409A.
- (43) Jain, S. M.; Phuyal, D.; Davies, M. L.; Li, M.; Philippe, B.; De Castro, C.; Qiu, Z.; Kim, J.; Watson, T.; Tsoi, W. C.; Karis, O.; Rensmo, H.; Boschloo, G.; Edvinsson, T.; Durrant, J. R. An Effective Approach of Vapour Assisted Morphological Tailoring for Reducing Metal Defect Sites in Lead-Free, (CH<sub>3</sub>NH<sub>3</sub>)<sub>3</sub>Bi<sub>2</sub>l<sub>9</sub> Bismuth-Based Perovskite Solar Cells for Improved Performance and Long-Term Stability. *Nano Energy* **2018**, *49*, 614–624. https://doi.org/10.1016/j.nanoen.2018.05.003.
- (44) Yang, J.; Siempelkamp, B. D.; Liu, D.; Kelly, T. L. Investigation of CH<sub>3</sub>NH<sub>3</sub>PbI<sub>3</sub> degradation Rates and Mechanisms in Controlled Humidity Environments Using in Situ Techniques. *ACS Nano* **2015**, *9* (2), 1955–1963. https://doi.org/10.1021/nn506864k.
- (45) Niu, T.; Lu, J.; Jia, X.; Xu, Z.; Tang, M. C.; Barrit, D.; Yuan, N.; Ding, J.; Zhang, X.; Fan, Y.; Luo, T.; Zhang, Y.; Smilgies, D. M.; Liu, Z.; Amassian, A.; Jin, S.; Zhao, K.; Liu, S. Interfacial Engineering at the 2D/3D Heterojunction for High-Performance Perovskite Solar Cells. *Nano Lett* **2019**, *19* (10), 7181–7190. https://doi.org/10.1021/acs.nanolett.9b02781.
- (46) Schlipf, J.; Hu, Y.; Pratap, S.; Bießmann, L.; Hohn, N.; Porcar, L.; Bein, T.; Docampo, P.; Müller-Buschbaum, P. Shedding Light on the Moisture Stability of 3D/2D Hybrid Perovskite Heterojunction Thin Films. *ACS Appl Energy Mater* **2019**, *2* (2), 1011–1018. https://doi.org/10.1021/acsaem.9b00005.
- (47) Lin, Y.; Bai, Y.; Fang, Y.; Wang, Q.; Deng, Y.; Huang, J. Suppressed Ion Migration in Low-Dimensional Perovskites. *ACS Energy Letters*. 2017. https://doi.org/10.1021/acsenergylett.7b00442.
- (48) Lin, Y.; Bai, Y.; Fang, Y.; Chen, Z.; Yang, S.; Zheng, X.; Tang, S.; Liu, Y.; Zhao, J.; Huang, J. Enhanced Thermal Stability in Perovskite Solar Cells by Assembling 2D/3D Stacking Structures. *J Phys Chem Lett* **2018**, *9*, 654–658. https://doi.org/10.1021/acs.jpclett.7b02679.
- (49) Li, F.; Fan, H.; Wang, P.; Li, X.; Song, Y.; Jiang, K.-J. Improved Film Morphology of (CH<sub>3</sub>NH<sub>3</sub>)<sub>3</sub>Bi<sub>2</sub>I<sub>9</sub> via Cation Displacement Approach for Lead-Free

- Perovskite Solar Cells. *J Mater Sci* **2019**, *54* (14), 10371–10378. https://doi.org/10.1007/s10853-019-03582-w.
- (50) Dunlap-Shohl, W. A.; Zhou, Y.; Padture, N. P.; Mitzi, D. B. Synthetic Approaches for Halide Perovskite Thin Films. *Chem Rev* **2019**, *119* (5), 3193–3295. https://doi.org/10.1021/acs.chemrev.8b00318.
- (51) Bhachu, D. S.; Scanlon, D. O.; Saban, E. J.; Bronstein, H.; Parkin, I. P.; Carmalt, C. J.; Palgrave, R. G. Scalable Route to CH<sub>3</sub>NH<sub>3</sub>Pbl<sub>3</sub> Perovskite Thin Films by Aerosol Assisted Chemical Vapour Deposition. *J Mater Chem A* **2015**, *3* (17), 9071–9073. https://doi.org/10.1039/c4ta05522e.
- (52) Ke, C. R.; Lewis, D. J.; Walton, A. S.; Chen, Q.; Spencer, B. F.; Mokhtar, M. Z.; Compean-Gonzalez, C. L.; O'Brien, P.; Thomas, A. G.; Flavell, W. R. Air-Stable Methylammonium Lead Iodide Perovskite Thin Films Fabricated via Aerosol-Assisted Chemical Vapor Deposition from a Pseudohalide Pb(SCN)<sub>2</sub> Precursor. *ACS Appl Energy Mater* **2019**, *2* (8), 6012–6022. https://doi.org/10.1021/acsaem.9b01124.
- (53) Ratnasingham, S. R.; Mohan, L.; Daboczi, M.; Degousée, T.; Binions, R.; Fenwick, O.; Kim, J.-S.; McLachlan, M. A.; Briscoe, J. Novel Scalable Aerosol-Assisted CVD Route for Perovskite Solar Cells. *Mater Adv* **2021**, *2* (5), 1606–1612. https://doi.org/10.1039/D0MA00906G.
- (54) Balderas-Aguilar, J. U.; Falcony-Guajardo, C.; Velázquez-Nevárez, G. A.; González-Pérez, V.; Martínez-Guerra, E.; Aguirre-Tostado, F. S. Luminescence and Structural Characteristics of Lead Halide Perovskite Films Deposited In Situ by a Versatile Multisource Aerosol Assisted Chemical Vapor Deposition (AACVD) Method. *Adv Mater Technol* **2022**, *7* (5), 2100657. https://doi.org/10.1002/admt.202100657.
- (55) Sathasivam, S.; Bhachu, D. S.; Lu, Y.; Chadwick, N.; Althabaiti, S. A.; Alyoubi, A. O.; Basahel, S. N.; Carmalt, C. J.; Parkin, I. P. Tungsten Doped TiO<sub>2</sub> with Enhanced Photocatalytic and Optoelectrical Properties via Aerosol Assisted Chemical Vapor Deposition. *Sci Rep* **2015**, *5* (1), 10952. https://doi.org/10.1038/srep10952.
- (56) Petrov, A. A.; Sokolova, I. P.; Belich, N. A.; Peters, G. S.; Dorovatovskii, P. V.; Zubavichus, Y. V.; Khrustalev, V. N.; Petrov, A. V.; Grätzel, M.; Goodilin, E. A.; Tarasov, A. B. Crystal Structure of DMF-Intermediate Phases Uncovers the Link

- Between CH<sub>3</sub>NH<sub>3</sub>PbI<sub>3</sub> Morphology and Precursor Stoichiometry. *J Phys Chem C* **2017**, 121 (38), 20739–20743. https://doi.org/10.1021/acs.jpcc.7b08468.
- (57) V. Venkata Chalapathi; Ramiah, K. V. Normal VIBRATIONS OF N, N-DIMETHYLFORMAMIDE AND N, N-DIMETHYLACETAMIDE. *Proc. Ind. Ar Sci., A* **1968**, *91*, 109–121.
- (58) Shastri, A.; Das, A. K.; Krishnakumar, S.; Singh, P. J.; Raja Sekhar, B. N. Spectroscopy of N, N -Dimethylformamide in the VUV and IR Regions: Experimental and Computational Studies. *J Chem Phys* **2017**, *147*, 224305. https://doi.org/10.1063/1.5006126.
- (59) Zhou, L.; Lin, Z.; Ning, Z.; Li, T.; Guo, X.; Ma, J.; Su, J.; Zhang, C.; Zhang, J.; Liu, S.; Chang, J.; Hao, Y. Highly Efficient and Stable Planar Perovskite Solar Cells with Modulated Diffusion Passivation Toward High Power Conversion Efficiency and Ultrahigh Fill Factor. *Solar RRL* **2019**, *3* (11), 1–10. https://doi.org/10.1002/solr.201900293.
- (60) Zhu, H.; Liu, Y.; Eickemeyer, F. T.; Pan, L.; Ren, D.; Ruiz-Preciado, M. A.; Carlsen, B.; Yang, B.; Dong, X.; Wang, Z.; Liu, H.; Wang, S.; Zakeeruddin, S. M.; Hagfeldt, A.; Dar, M. I.; Li, X.; Grätzel, M. Tailored Amphiphilic Molecular Mitigators for Stable Perovskite Solar Cells with 23.5% Efficiency. *Adv Mater* **2020**, 32 (12). https://doi.org/10.1002/adma.201907757.
- (61) Lyu, M.; Yun, J. H.; Cai, M.; Jiao, Y.; Bernhardt, P. V.; Zhang, M.; Wang, Q.; Du, A.; Wang, H.; Liu, G.; Wang, L. Organic–Inorganic Bismuth (III)-Based Material: A Lead-Free, Air-Stable and Solution-Processable Light-Absorber beyond Organolead Perovskites. *Nano Res* **2016**, *9* (3), 692–702. https://doi.org/10.1007/s12274-015-0948-y.
- (62) Alexander V. Naumkin, Anna Kraut-Vass, Stephen W. Gaarenstroom, and C. J. P. NIST X-Ray Photoelectron Spectroscopy Database. *Measurement Services Division of the National Institute of Standards and Technology (NIST)* **2012**, *20899* (20), 20899. https://doi.org/10.18434/T4T88K.
- (63) Lindblad, R.; Bi, D.; Park, B.-W.; Oscarsson, J.; Gorgoi, M.; Siegbahn, H.; Odelius, M.; Johansson, E. M. J.; Rensmo, H. Electronic Structure of

- TiO2/CH3NH3Pbl3 Perovskite Solar Cell Interfaces. *J Phys Chem Lett* **2014**, *5* (4), 648–653. https://doi.org/10.1021/jz402749f.
- (64) Marchioro, A.; Teuscher, J.; Friedrich, D.; Kunst, M.; Van De Krol, R.; Moehl, T.; Grätzel, M.; Moser, J. E. Unravelling the Mechanism of Photoinduced Charge Transfer Processes in Lead Iodide Perovskite Solar Cells. *Nat Photonics* **2014**, *8*, 250–255. https://doi.org/10.1038/nphoton.2013.374.
- (65) Bresolin, B. M.; Balayeva, N. O.; Granone, L. I.; Dillert, R.; Bahnemann, D. W.; Sillanpää, M. Anchoring Lead-Free Halide Cs<sub>3</sub>Bi<sub>2</sub>I<sub>9</sub> Perovskite on UV100–TiO<sub>2</sub> for Enhanced Photocatalytic Performance. *Sol Energy Mater and Sol Cells* **2020**, *204* (July 2019), 1–11. https://doi.org/10.1016/j.solmat.2019.110214.
- (66) van de Krol, R. Photoelectrochemical Measurements. In *Springer Handbook of Electrochemical Energy*; Springer Berlin Heidelberg: Berlin, Heidelberg, 2012; pp 69–117. https://doi.org/10.1007/978-1-4614-1380-6\_3.
- (67) Beilsten-Edmands, J.; Eperon, G. E.; Johnson, R. D.; Snaith, H. J.; Radaelli, P. G. Non-Ferroelectric Nature of the Conductance Hysteresis in CH<sub>3</sub>NH<sub>3</sub>Pbl<sub>3</sub> Perovskite-Based Photovoltaic Devices. *Appl Phys Lett* **2015**, *106* (17), 173502. https://doi.org/10.1063/1.4919109.
- (68) Popoola, I.; Gondal, M.; Oloore, L.; Popoola, A.; AlGhamdi, J. Fabrication of Organometallic Halide Perovskite Electrochemical Supercapacitors Utilizing Quasi-Solid-State Electrolytes for Energy Storage Devices. *Electrochim Acta* **2020**, 332, 135536. https://doi.org/10.1016/j.electacta.2019.135536.
- (69) Oesinghaus, L.; Schlipf, J.; Giesbrecht, N.; Song, L.; Hu, Y.; Bein, T.; Docampo, P.; Müller-Buschbaum, P. Toward Tailored Film Morphologies: The Origin of Crystal Orientation in Hybrid Perovskite Thin Films. *Adv Mater Interfaces* **2016**, 3 (19), 1600403. https://doi.org/10.1002/ADMI.201600403.
- (70) Liang, Z.; Zhang, S.; Xu, X.; Wang, N.; Wang, J.; Wang, X.; Bi, Z.; Xu, G.; Yuan, N.; Ding, J. A Large Grain Size Perovskite Thin Film with a Dense Structure for Planar Heterojunction Solar Cells via Spray Deposition under Ambient Conditions. *RSC Adv* **2015**, *5*, 60562–60569. https://doi.org/10.1039/c5ra09110a.

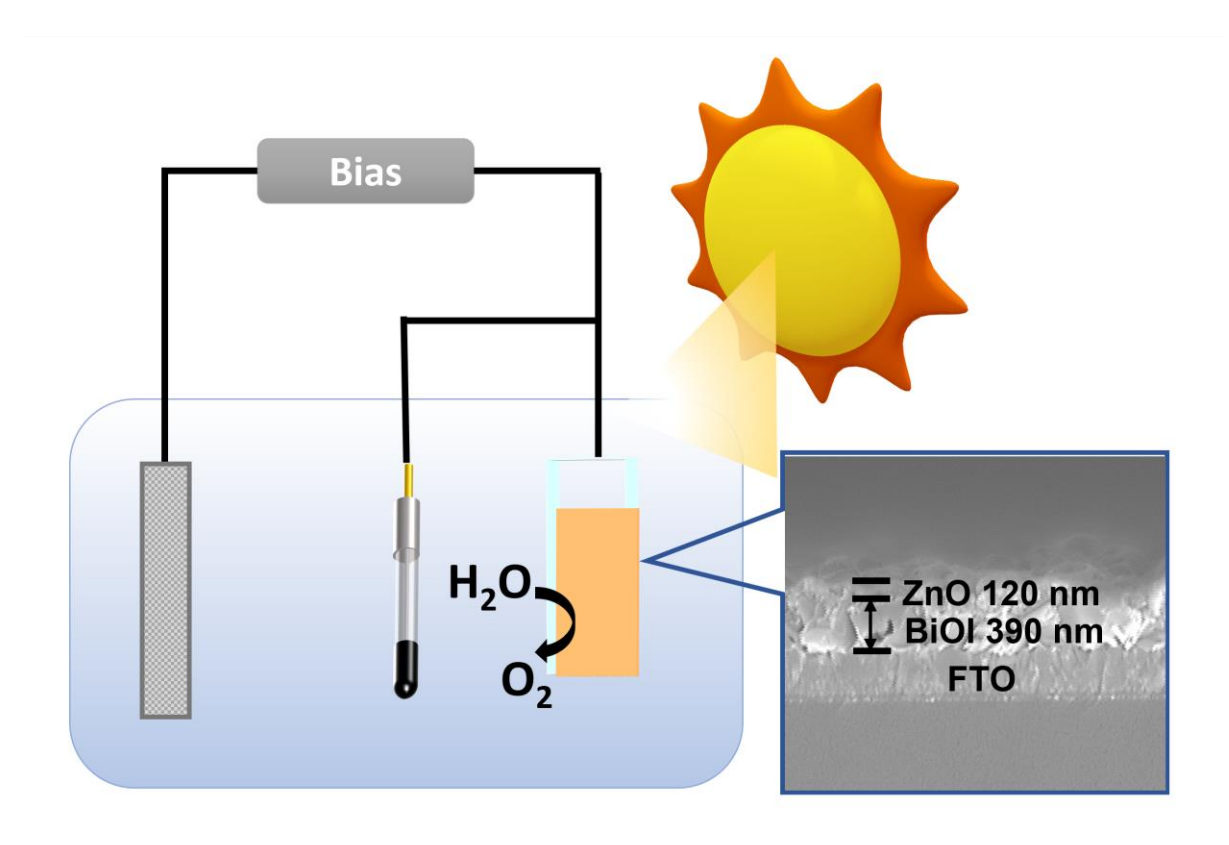
- (71) Phillips, J. M. Substrate Selection for Thin-Film Graft. *MRS Bull* **1995**, *20* (4), 35–39. https://doi.org/10.1557/S0883769400044651.
- (72) Salim, T.; Sun, S.; Abe, Y.; Krishna, A.; Grimsdale, A. C.; Lam, Y. M. Perovskite-Based Solar Cells: Impact of Morphology and Device Architecture on Device Performance. *J Mater Chem A* **2015**, 3 (17), 8943–8969. https://doi.org/10.1039/c4ta05226a.
- (73) Song, Y.; Wu, Y.; Jiang, Y.; Yang, H.; Jiang, Y. Polymers and Solvent-Induced Polymorphic Selection and Preferential Orientation of Pyrazinamide Crystal. *Cryst Growth Des* **2020**, *20* (1), 352–361. https://doi.org/10.1021/acs.cgd.9b01287.
- (74) Zhang, X.; Wu, G.; Gu, Z.; Guo, B.; Liu, W.; Yang, S.; Ye, T.; Chen, C.; Tu, W.; Chen, H. Active-Layer Evolution and Efficiency Improvement of (CH<sub>3</sub>NH<sub>3</sub>)<sub>3</sub>Bi<sub>2</sub>I<sub>9</sub>-Based Solar Cell on TiO<sub>2</sub>-Deposited ITO Substrate. *Nano Res* **2016**, *9* (10), 2921–2930. https://doi.org/10.1007/s12274-016-1177-8.
- (75) Marchand, P.; Hassan, I. A.; Parkin, I. P.; Carmalt, C. J. Aerosol-Assisted Delivery of Precursors for Chemical Vapour Deposition: Expanding the Scope of CVD for Materials Fabrication. *Dalt Trans* **2013**, *42* (26), 9406–9422. https://doi.org/10.1039/c3dt50607j.
- (76) Viezbicke, B. D.; Patel, S.; Davis, B. E.; Birnie, D. P. Evaluation of the Tauc Method for Optical Absorption Edge Determination: ZnO Thin Films as a Model System. *Phys Status Solidi B Basic Res* **2015**, *252* (8), 1700–1710. https://doi.org/10.1002/pssb.201552007.
- (77) Hoye, R. L. Z.; Brandt, R. E.; Osherov, A.; Stevanovic, V.; Stranks, S. D.; Wilson, M. W. B.; Kim, H.; Akey, A. J.; Perkins, J. D.; Kurchin, R. C.; Poindexter, J. R.; Wang, E. N.; Bawendi, M. G.; Bulovic, V.; Buonassisi, T. Methylammonium Bismuth Iodide as a Lead-Free, Stable Hybrid Organic-Inorganic Solar Absorber. *Chem A Eur J* **2016**, *22* (8), 2605–2610. https://doi.org/10.1002/chem.201505055.
- (78) Mali, S. S.; Kim, H.; Kim, D. H.; Kook Hong, C. Anti-Solvent Assisted Crystallization Processed Methylammonium Bismuth Iodide Cuboids towards Highly Stable Lead-Free Perovskite Solar Cells. *ChemistrySelect* **2017**, *2* (4), 1578–1585. https://doi.org/10.1002/slct.201700025.

- (79) Chen, X.; Myung, Y.; Thind, A.; Gao, Z.; Yin, B.; Shen, M.; Cho, S. B.; Cheng, P.; Sadtler, B.; Mishra, R.; Banerjee, P. Atmospheric Pressure Chemical Vapor Deposition of Methylammonium Bismuth Iodide Thin Films. *J Mater Chem A* **2017**, *5* (47), 24728–24739. https://doi.org/10.1039/c7ta06578g.
- (80) Huang, J.; Gu, Z.; Zhang, X.; Wu, G.; Chen, H. Lead-Free (CH<sub>3</sub>NH<sub>3</sub>)<sub>3</sub>Bi<sub>2</sub>I<sub>9</sub> Perovskite Solar Cells with Fluorinated PDI Films as Organic Electron Transport Layer. *J Alloys Compd* **2018**, *767*, 870–876. https://doi.org/10.1016/j.jallcom.2018.07.185.
- (81) Akbari, A.; Hashemi, J.; Mosconi, E.; De Angelis, F.; Hakala, M. First Principles Modelling of Perovskite Solar Cells Based on TiO<sub>2</sub> and Al<sub>2</sub>O<sub>3</sub>: Stability and Interfacial Electronic Structure. *J Mater Chem A* **2017**, *5* (5), 2339–2345. https://doi.org/10.1039/C6TA08874K.
- (82) Huang, S.; Dong, Q.; Shi, Y.; Duan, L.; Wang, L. RbF Modified FTO Electrode Enable Energy-Level Matching for Efficient Electron Transport Layer-Free Perovskite Solar Cells. *Chem Eng J* **2020**, 394, 125024. https://doi.org/10.1016/J.CEJ.2020.125024.
- (83) Olthof, S. Research Update: The Electronic Structure of Hybrid Perovskite Layers and Their Energetic Alignment in Devices. *APL Mater* **2016**, *4* (9), 091502. https://doi.org/10.1063/1.4960112.
- (84) Haque, M. A.; Sheikh, A. D.; Guan, X.; Wu, T. Metal Oxides as Efficient Charge Transporters in Perovskite Solar Cells. *Adv Energy Mater* **2017**, *7* (20), 1–23. https://doi.org/10.1002/aenm.201602803.
- (85) PERKOWITZ, S. Optical Theory for Semiconductor Characterization. In *Optical Characterization of Semiconductors*; Elsevier, 1993; pp 7–16. https://doi.org/10.1016/B978-0-12-550770-7.50007-2.
- (86) Zhang, Y.; Zhang, Y.; Jang, S.; Jang, S.; Hwang, I. W.; Jung, Y. K.; Lee, B. R.; Kim, J. H.; Kim, K. H.; Park, S. H.; Park, S. H. Bilateral Interface Engineering for Efficient and Stable Perovskite Solar Cells Using Phenylethylammonium Iodide. *ACS Appl Mater Interfaces* **2020**, *12* (22), 24827–24836. https://doi.org/10.1021/acsami.0c05632.

- (87) Lv, Y.; Shi, Y.; Song, X.; Liu, J.; Wang, M.; Wang, S.; Feng, Y.; Jin, S.; Hao, C. Bromine Doping as an Efficient Strategy to Reduce the Interfacial Defects in Hybrid Two-Dimensional/Three-Dimensional Stacking Perovskite Solar Cells. *ACS Appl Mater Interfaces* **2018**, *10* (37), 31755–31764. https://doi.org/10.1021/acsami.8b09461.
- (88) Wang, J.; Leng, J.; Liu, J.; He, S.; Wang, Y.; Wu, K.; Jin, S. Engineered Directional Charge Flow in Mixed Two-Dimensional Perovskites Enabled by Facile Cation-Exchange. *J Phys Chem C* **2017**, *121* (39), 21281–21289. https://doi.org/10.1021/acs.jpcc.7b08535.
- (89) Muscarella, L. A.; Hutter, E. M.; Sanchez, S.; Dieleman, C. D.; Savenije, T. J.; Hagfeldt, A.; Saliba, M.; Ehrler, B. Crystal Orientation and Grain Size: Do They Determine Optoelectronic Properties of MAPbl<sub>3</sub> Perovskite? *J Phys Chem Lett* **2019**, 10 (20), 6010–6018. https://doi.org/10.1021/acs.jpclett.9b02757.
- (90) Christians, J. A.; Miranda Herrera, P. A.; Kamat, P. V. Transformation of the Excited State and Photovoltaic Efficiency of CH<sub>3</sub>NH<sub>3</sub>Pbl<sub>3</sub> Perovskite upon Controlled Exposure to Humidified Air. *J Am Chem Soc* **2015**, *137* (4), 1530–1538. https://doi.org/10.1021/ja511132a.
- (91) Li, S.; Hu, L.; Zhang, C.; Wu, Y.; Liu, Y.; Sun, Q.; Cui, Y.; Hao, Y.; Wu, Y. In Situ Growth of a 2D/3D Mixed Perovskite Interface Layer by Seed-Mediated and Solvent-Assisted Ostwald Ripening for Stable and Efficient Photovoltaics. *J Mater Chem C* **2020**, *8* (7), 2425–2435. https://doi.org/10.1039/C9TC05212G.
- (92) Amratisha, K.; Ponchai, J.; Kaewurai, P.; Pansa-ngat, P.; Pinsuwan, K.; Kumnorkaew, P.; Ruankham, P.; Kanjanaboos, P. Layer-by-Layer Spray Coating of a Stacked Perovskite Absorber for Perovskite Solar Cells with Better Performance and Stability under a Humid Environment. *Opt Mater Express* **2020**, *10* (7), 1497. https://doi.org/10.1364/OME.391546.
- (93) Matuana, L. M.; Balatinecz, J. J.; Park, C. B. Effect of Surface Properties on the Adhesion between PVC and Wood Veneer Laminates. *Polym Eng Sci* **1998**, *38* (5), 765–773. https://doi.org/10.1002/pen.10242.

- (94) Liu, Y.; Akin, S.; Pan, L.; Uchida, R.; Arora, N.; Milić, J. V.; Hinderhofer, A.; Schreiber, F.; Uhl, A. R.; Zakeeruddin, S. M.; Hagfeldt, A.; Ibrahim Dar, M.; Grätzel, M. Ultrahydrophobic 3D/2D Fluoroarene Bilayer-Based Water-Resistant Perovskite Solar Cells with Efficiencies Exceeding 22%. *Sci Adv* **2019**, *5* (6), 1–9. https://doi.org/10.1126/sciadv.aaw2543.
- (95) Daskalakis, S.; Wang, M.; Carmalt, C. J.; Vernardou, D. Electrochemical Investigation of Phenethylammonium Bismuth Iodide as Anode in Aqueous Zn<sup>2+</sup> Electrolytes. *Nanomaterials* **2021**, *11* (3), 1–8. https://doi.org/10.3390/nano11030656.

Chapter 3: ZnO/BiOI heterojunctions with enhanced photoelectrochemical water oxidation activity



#### 3.1 Background

Nowadays, due to increasingly serious issues of energy shortage and environmental pollution derived from the use of fossil fuels, photoelectrochemical (PEC) water splitting has become a research hotspot as a promising way to produce hydrogen and oxygen by utilizing solar energy. PEC water splitting based on the Honda-Fujishima effect was first reported in the 1970s, where a  $TiO_2$  electrode was used to catalyze the water oxidation process, and until now  $TiO_2$  has become a heavily studied material in this field. However, owing to the wide band gap ( $\geq 3.0 \text{ eV}$ ),  $TiO_2$  can only absorb UV light, which only accounts for 4% of the whole solar spectrum (Figure 3-1). Therefore, its practical applications are greatly restricted and numerous research has been done to find semiconductors with the a greater ability of visible light harvesting in PEC water splitting. Bismuth oxyhalides, BiOX (where X = CI, Br and I), have attracted attention because of their potential photocatalytic activities within the wavelength range of visible light.

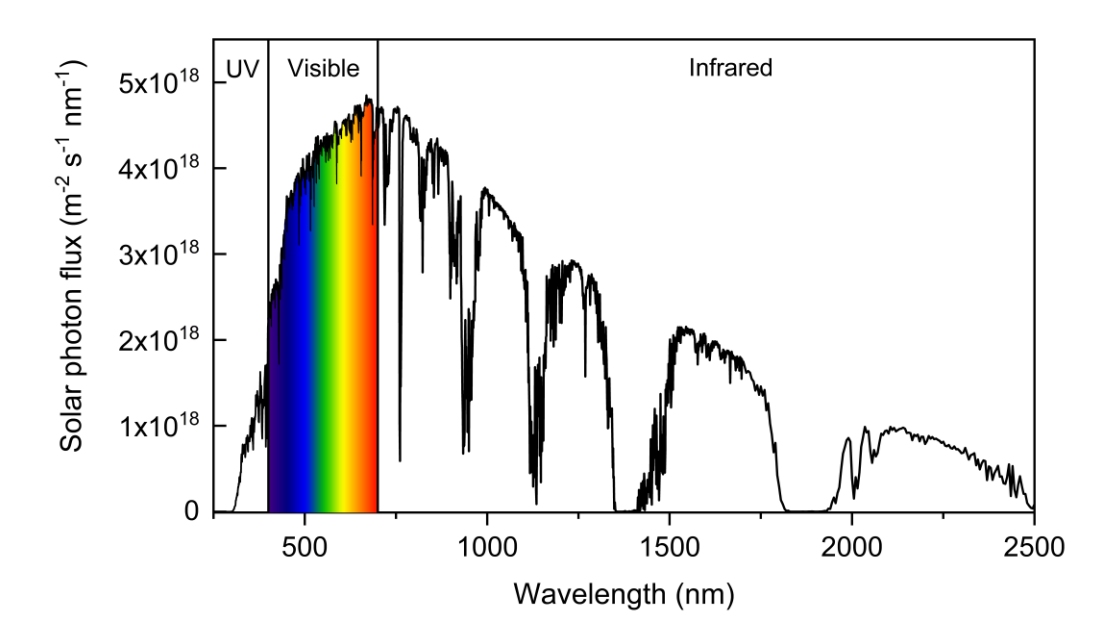


Figure 3-1. AM 1.5 solar spectrum.

The [Bi<sub>2</sub>O<sub>2</sub>]<sup>2+</sup> layers sandwiched between double X<sup>-</sup> slabs constitute the tetragonal crystal structure of BiOX.<sup>4</sup> An internal electric field could be generated by this layered structure, which benefits the charge separation and limits the recombination of electrons and holes.<sup>5</sup> Among all BiOX, the band gap of BiOI is the narrowest (~1.8 eV), and BiOI has showed excellent photocatalytic and PEC activities under visible light irradiation.<sup>6,7</sup> In addition, the indirect band gap of BiOI further hinders the charge recombination,<sup>8,9</sup> and the flat transition position in the bandgap structure of BiOI also facilitates the transition process of charge carriers.<sup>9</sup>

The size and morphology of BiOI can influence its properties significantly, and the conductivity type of BiOI is also tunable. In addition to the most studied p-type BiOI, n-type BiOI utilizing various preparation methods has gradually gained interest and shown notable photocatalytic activities.7,10-14 To date, BiOI powders with many been prepared. 5,14-16 micro/nanostructures from 1D to 3D have hydro/solvothermal methods are the most used. Furthermore, in order to avoid the problems associated with handling photocatalyst suspensions and reclamation, <sup>17</sup> thin films of BiOI have been fabricated by various methods as well, such as electrochemical deposition, 18,19 spray pyrolysis deposition, 11 successive ionic layer adsorption and reaction, 13,20 chemical vapour transport 21 and aerosol-assisted chemical vapour deposition (AACVD).7,22 In addition, an n-type BiOI film composed of

uniform nanoplatelets has been reported to be deposited *via* AACVD, showing the great potential in PEC water splitting as the photoanode.<sup>7</sup>

Various strategies have been applied for further enhancement of the photocatalytic and PEC activity of BiOI. For example, through doping BiOI with metallic elements like Fe, Zn and In, the photocatalytic activity can be improved by the generated crystal defects and modified electronic structures.<sup>23–25</sup> Alternatively, the heterojunction construction of BiOI and other semiconductors can be utilized for performance improvement. Through combining two semiconducting materials with suitable band alignment, excited electrons can transfer from the semiconductor with a lower conduction band minimum (CBM) into the other one, benefiting the separation of photogenerated electron–hole pairs across the solid-solid heterogeneous interface and thus improve the PEC performance significantly.<sup>19,26</sup> A number of heterostructures have been investigated by coupling BiOI with different materials, such as reduced graphene oxide,<sup>12</sup> g-C<sub>3</sub>N<sub>4</sub>,<sup>27</sup> TiO<sub>2</sub>,<sup>19,28,29</sup> ZnO,<sup>30</sup> Bi<sub>2</sub>O<sub>3</sub> <sup>31</sup> and BiVO<sub>4</sub>.<sup>32</sup> All of these heterojunctions presented enhanced performance in PEC applications, such as water splitting.

Besides TiO<sub>2</sub>, ZnO is also a widely investigated n-type semiconductor. Its low toxicity, great stability and electron mobility all make it attractive in PEC applications.33 In addition, ZnO can easily and cheaply grow into various morphologies with appropriate dimensions.<sup>33</sup> Although having a similar wide band gap to TiO<sub>2</sub>, ZnO has a more favorable band structure for fabricating a heterojunction with BiOI than TiO2 (Figure 3-2).<sup>34</sup> If combined with BiOI to form a heterojunction, ZnO with the wide band gap of ~3.3 eV is able to be activated by UV light while allow the visible light to go through and be used by BiOI,35 which can increase the utilization of incident solar light in practical PEC applications. Unfortunately, until now, the heterojunction of ZnO and BiOI has mostly been studied for the photocatalytic degradation of organic pollutants, 36-39 with little investigation of their PEC applications and comprehensive characterizations.<sup>30</sup> Furthermore, the hydro/solvothermal method is the most common way to prepare the ZnO and BiOI heterojunction in the powder form. Therefore, in order to be used as the photoelectrode in PEC water splitting, extra steps are necessary to make powders into films, leading to the increased cost and complicated fabrication process.

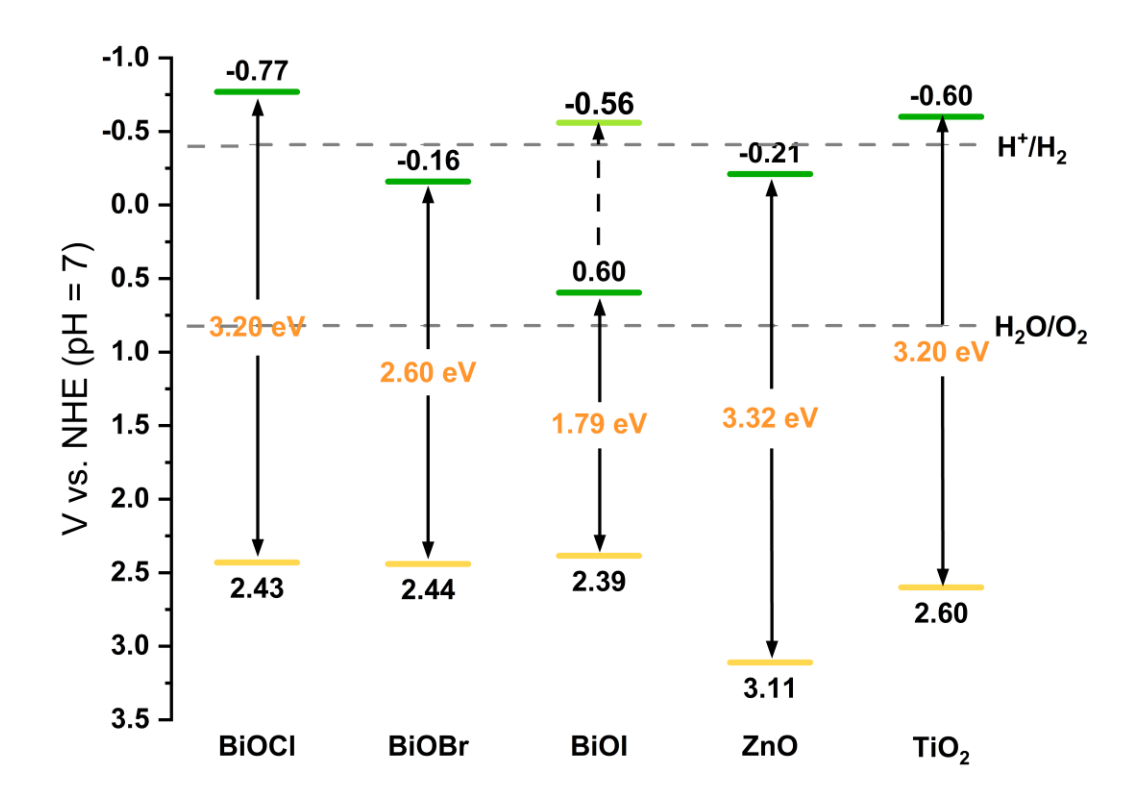


Figure 3-2. Energy band alignment diagram of  $TiO_2$ , ZnO, BiOI, BiOBr and BiOCI compared to the potentials of water splitting at pH = 7.

In this study, heterojunctions with the bilayer structure composed of ZnO and BiOI were fabricated *via* AACVD for the first time, which is a feasible, scalable and cheap film deposition technique. BiOI/ZnO and ZnO/BiOI heterojunctions, where either BiOI or ZnO was present at the surface of the coatings, respectively, were deposited on FTO. The composition, morphologies and optoelectrical properties of the obtained films were investigated. In addition, the activities in PEC water oxidation of the heterojunctions and parent materials were tested, where no obvious improvement was shown for the BiOI/ZnO heterojunction compared with parent materials. However, the ZnO/BiOI heterojunction exhibited a dramatic increase in the PEC performance with the theoretical solar photocurrent of 0.271 mA·cm<sup>-2</sup>. Transmittance spectroscopy, photoluminescence (PL) spectroscopy and transient absorption spectroscopy (TAS) analysis determined that due to the formation of the ZnO/BiOI heterostructure, the visible light activity and the separation of photogenerated charge carriers were increased, leading to significantly improved PEC performance compared to single-

layer ZnO and BiOI films. In addition, the effect of deposition temperatures and thickness of the top ZnO film in the ZnO/BiOI heterojunction was also investigated.

## 3.2 Experimental

## 3.2.1 Film deposition

**BiOI thin film** *via* **AACVD.** BiOI thin films were deposited as reported.<sup>7</sup> 1 mmol Bil<sub>3</sub> (0.5897 g, Sigma-Aldrich) was dissolved in 25 mL anhydrous DMF to form the precursor solution after stirring 30 mins. Compressed air was used as the carrier gas with a flow rate of 1.0 L·min<sup>-1</sup>. The FTO substrate (NSG TEC 15, 15 cm × 4.5 cm) was kept at 300 °C during deposition time (60 mins) and was subsequently left to cool down to room temperature.

**ZnO thin film** *via* **AACVD.** 0.5 g Zn(OAc)<sub>2</sub>·2H<sub>2</sub>O (2.28 mmol, Alfa Aesar) was dissolved in 25 mL methanol to form the precursor solution after stirring 20 mins. Compressed air was used as the carrier gas for all depositions, with a flow rate of 1.0 L·min<sup>-1</sup>. At 350 °C, ZnO films were deposited on FTO substrates (NSG TEC 15, 15 cm× 4.5 cm) over 25 mins, and then the substrates were cooled down to room temperature.

For the BiOI/ZnO heterojunction, the ZnO film was deposited on the FTO substrate first followed by the deposition of the BiOI film. For the ZnO/BiOI heterojunction, the BiOI film was deposited on the FTO substrate firstly. After that, as well as at 350 °C, the ZnO film was deposited on top of the BiOI film at 300, 400 and 450 °C. The obtained heterojunctions will be referred to as **ZnO-300** °C/BiOI, **ZnO-400** °C/BiOI and **ZnO-450** °C/BiOI respectively. In addition to 0.5 g Zn(OAc)<sub>2</sub>·2H<sub>2</sub>O, precursor solutions with 0.1, 0.3, 0.7 and 0.9 g Zn(OAc)<sub>2</sub>·2H<sub>2</sub>O were used in the film deposition at 350 °C to obtain top ZnO films with various thickness. The obtained heterojunctions will be referred to as **ZnO-0.1/BiOI**, **ZnO-0.3/BiOI**, **ZnO-0.7/BiOI** and **ZnO-0.9/BiOI** respectively.

**TiO<sub>2</sub> thin film via AACVD.** 0.6 g titanium isopropoxide (2.19 mmol, Sigma-Aldrich) was dissolved in 10 mL toluene and then ultrasonicated 4 mins to form the precursor solution. Compressed air was used as the carrier gas for all depositions, with a flow rate of 1.0 L·min<sup>-1</sup>. At 350 °C, TiO<sub>2</sub> films were deposited on FTO substrates (NSG TEC

15, 15 cm×4.5 cm) for 20 mins, and then the substrates were cooled down to room temperature.

For the TiO<sub>2</sub>/BiOI heterojunction, the BiOI film was deposited on the FTO substrate first followed by the deposition of the TiO<sub>2</sub> film.

#### 3.2.2 Physical characterization

Grazing incident X-ray diffraction (GIXRD) patterns were collected over 5-60° (0.05° and 0.5 s per point) using a Panalytical Empyrean diffractometer. This instrument used monochromatic Cu  $K_{\alpha 1}$  radiation ( $\lambda = 1.5406 \text{ Å}$ ) at 40 kV with 40 mA emission current, and the incident beam angle was set to 1°. Film morphologies were studied using a JEOL JSM-7600 field emission scanning electron microscope (SEM). UV-Vis spectroscopy was measured using a Shimadzu UV-2700 spectrometer, and transmission spectra were recorded in the 300–1000 nm range. X-ray photoelectron spectroscopy (XPS) was performed using a Thermo Scientific K-alpha spectrometer with monochromated Al  $K_{\alpha 1}$  radiation (8.3418 Å), and a dual beam charge compensation system. Survey scans were collected in the range of 0-1200 eV at a pass energy of 50 eV. XPS depth profiling was carried out by bombarding the films with Ar<sup>+</sup> ion beam for 1350 s to etch the surface. All peak positions were calibrated to adventitious carbon (284.8 eV) and plotted using CasaXPS® software. Photoluminescence (PL) spectra were obtained by a Horiba Fluorolog Fluorometer at room temperature to investigate the optical properties of films. The surface roughness of films was characterized by atomic force microscopy (AFM) on a Keysight 5600LS scanning probe microscope taken at a scale of  $5 \times 5 \mu m^2$ . TAS was measured from ms to s timescale in the transmission mode. A Nd:YAG laser (OPOTEK Opolette 355 II, ~6 ns pulse width) was used as the excitation source, generating 355 nm UV light from the third harmonic (~0.60 mJ.cm<sup>-2</sup> per pulse, with a pulse rate of 0.5 Hz). The light went through the photocatalyst layer and then towards the FTO substrate. The probe light was generated from a 100 W Bentham IL1 quartz halogen lamp. Long pass filters (Comar Instruments) were positioned between the lamp and the sample to minimize the short wavelength irradiation. Transient changes in transmission through the sample were collected using a length lens (2" diameter, 2" focal) and relayed to an Oriel Cornerstone 130 monochromator and measured between 550 and 1100 nm. Time-resolved changes in transmission were detected through a Si photodiode (Hamamatsu S3071) and then converted to absorption. After going through an Costronics amplifier box, data at times faster than 3.6 ms was recorded using an oscilloscope (Tektronics DPO3012). Data at times slower than 3.6 ms was recorded on a National Instrument DAQ card (NI USB-6251). Each kinetic trace was acquired from the average of 200 laser pulses. Acquisitions were triggered by a Thorlabs DET10A photodiode from the laser scatter. Data was processed by a homebuilt software written in Labview. Measurements were done under ambient condition.

#### 3.2.3 Photoelectrochemical measurements

All PEC measurements were carried out in a three-electrode configuration with a quartz window (0.5 cm²). The electrolyte was 0.5 M Na<sub>2</sub>SO<sub>4</sub> aqueous solution (pH = 6.6). The as-fabricated film, Pt mesh and Ag/AgCl/saturated-KCl (0.197 V<sub>NHE</sub> at 25 °C; Metrohm) were used as the working, counter and reference electrode, respectively. Both current density vs. applied voltage (*JV*) curves and IPCE were measured using an ozone-free xenon lamp (75 W, Hamamatsu) coupled with a monochromator (OBB-2001, Photon Technology International). The light intensity was measured using an optical power meter (PM 100, Thorlabs) coupled with a power sensor (S120UV, Thorlabs). An Autolab potentiostat (PGSTAT12 with an FRA2 module) was used to apply voltage and measure currents.

# 3.2.4 Faradaic efficiency measurements

An O<sub>2</sub> microsensor (Unisense, O<sub>2</sub> + UniAmp Multi Channel amplifier) enclosed in a needle was equilibrated in air and then pressed through a rubber septum into a quartz cuvette containing the sample in a 3-electrode configuration with an Ag/AgCl reference and Pt as a counter. 1.60 V<sub>RHE</sub> was applied, and the sample was illuminated with 4 mW of light from a 365 nm LED. The change in voltage read across the sensor was measured and converted to an O<sub>2</sub> signal by injecting known quantities of oxygen.

#### 3.2.5 Theoretical calculations

The applied voltage in our JV curves were reported against RHE ( $V_{RHE}$ ), converted by the Nernst equation:

$$V_{RHE} = V_{Ag/AgCl} + 0.05916 \text{ pH} + V_{Ag/AgCl}^{\phi}$$
 (1)

where  $V_{{\rm Ag}/AgCl}$  is the applied potential versus the Ag/AgCl reference electrode, pH is the electrolyte pH and  $V_{{\rm Ag}/AgCl}^{\emptyset}$  is the standard reference potential (0.197 V<sub>NHE</sub> at 25 °C).

The incident photon-to-current efficiency (IPCE) was calculated using the following equation:

IPCE (%) = 
$$(I \times 1239.8)/(P_{mono} \times \lambda) \times 100$$
 (2)

where J is the photocurrent density,  $P_{mono}$  is the power, and  $\lambda$  is the wavelength of the monochromate light.

The theoretical solar photocurrent (TSP) was calculated by multiplying the IPCE with the AM 1.5 solar spectrum, then converting this into the photocurrent density:

TSP (mA·cm<sup>-2</sup>) = 
$$\int_{3000nm}^{280nm} IPCE \times AM \ 1.5 \ (photon·cm-2) \times 1000/1C$$
 (3)

Where 1*C* is  $6.241 \times 10^{18}$  electrons per second.

The applied bias photo-to-current efficiency (ABPE) of ZnO, BiOI and ZnO/BiOI was calculated from the equation:<sup>40</sup>

ABPE (%) = 
$$J \times (1.23 \text{ V}_{RHE} - \text{V}_{app}) / P_{light} \times 100$$
 (4)

Where J is the photocurrent density,  $V_{app}$  is the applied voltage vs. RHE, and  $P_{light}$  is the power density of the light source.

#### 3.3 Results and discussions

#### 3.3.1 GIXRD characterization

In order to further improve the PEC performance of the BiOI film fabricated by AACVD, bilayer heterojunctions with different structures, such as ZnO/BiOI and BiOI/ZnO, were developed on FTO substrates. BiOI films with an orange colour and excellent coverage were deposited at 300 °C from the reaction of BiI<sub>3</sub> in DMF with compressed air as the carrier gas in the AACVD process. Through the comparison among BiOI films deposited at different temperatures, it can be found that the BiOI film deposited at 300 °C presented the highest degree of (110) preferential orientation (Figure 3-3a). Furthermore, in Figure 3-3b, **BiOI-300** °C showed a better PEC activity than **BiOI-**

**250** °C and **BiOI-350** °C while all of them showed extremely low photocurrent densities. Therefore, in the following study, all BiOI films were deposited at 300 °C in AACVD processes. Highly transparent ZnO films were obtained from Zn(OAc)<sub>2</sub>·2H<sub>2</sub>O in methanol under compressed air flow *via* AACVD at 350 °C, and the reason of choosing 350 °C as the deposition temperature of ZnO will be discussed later. Both ZnO/BiOI and BiOI/ZnO heterojunctions were obtained from individual depositions of each layer from precursor solutions of BiI<sub>3</sub> in DMF or Zn(OAc)<sub>2</sub>·2H<sub>2</sub>O in methanol *via* AACVD as described in the experimental section. Both heterojunctions were orange in appearance. In addition, for the ZnO/BiOI heterojunction, the influence of deposition temperature and film thickness of the top ZnO layer was studied as well.

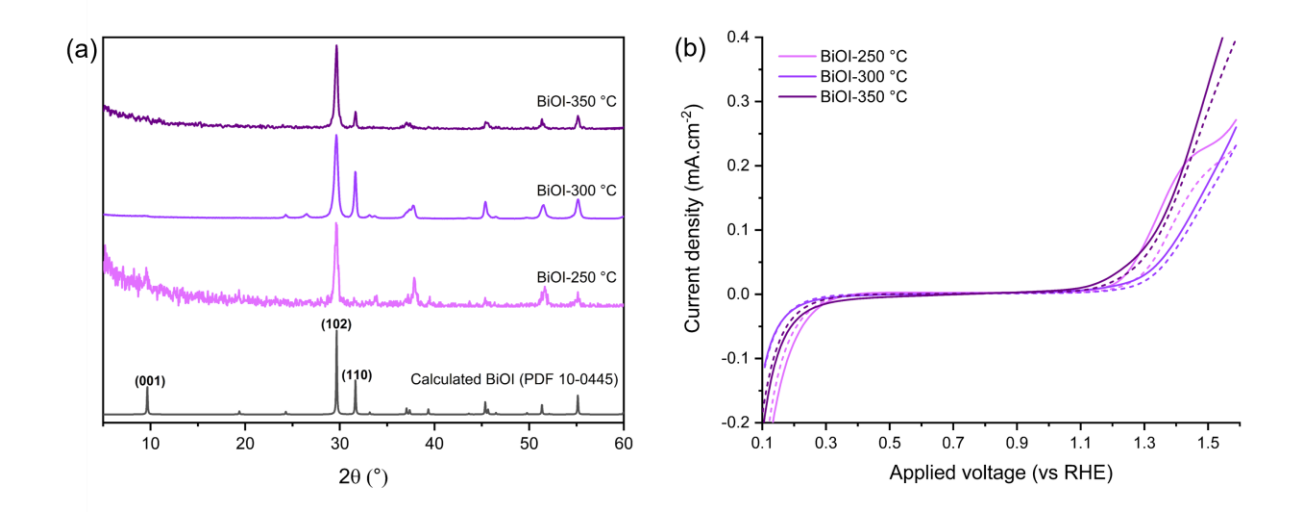


Figure 3-3. (a) GIXRD patterns of BiOI films on FTO deposited at 250, 300 and 350 °C. (b) JV curves of BiOI films measured in the dark (dashed lines) and under the action of light (350 nm, 2.58 mW·cm<sup>-2</sup>) (solid lines). Samples were irradiated at the semiconductor-electrolyte interface. The voltage was swept from 0.10 V<sub>RHE</sub> to 1.60 V<sub>RHE</sub> at a rate of 10 mV·s<sup>-1</sup>.

The composition and crystallographic structures of the deposited films, including ZnO, BiOI and heterojunctions, were identified by GIXRD (Figure 3-4), where ZnO films were grown from 0.5 g Zn(OAc)<sub>2</sub>·2H<sub>2</sub>O at 350 °C. Both single-layer ZnO and BiOI films on FTO showed pure phases and polycrystalline patterns in good agreement with hexagonal ZnO (*PDF 89-0511*) and tetragonal BiOI (*PDF 10-0445*), respectively. While peaks from BiOI and ZnO overlap at ~31.7°, characteristic peaks at 34.4°, 36.3° and 56.6° from ZnO and peaks at 29.6°, 45.4° and 55.1° from BiOI matched well.

It was found that the BiOI film deposited *via* AACVD in this work displayed the preferential growth orientation of (102) and (110), consistent with the reported BiOI film deposited by spray pyrolysis,<sup>11</sup> while different from the other reported AACVD with the BiOI film showing preferred (001) orientation.<sup>7</sup> The possible reason of this variation was that anhydrous DMF was used herein but not in the reference, as the water content in the solvent utilised in AACVD could have an effect on the film growth.<sup>41</sup> Compared with (001) facets, the exposed (110) facets of BiOI has a higher charge transfer efficiency and oxygen adsorption capacity, which is favorable to relative photocatalytic and PEC behaviors.<sup>42,43</sup> Furthermore, it has been found that the inplane direction, such as (110), of BiOI has better charge carrier mobilities.<sup>44,45</sup> As a result, it is reasonable to expect that the charge extraction could be improved through contacting the ZnO layer with the BiOI layer with (110) preferential growth orientation in the heterojunction.

Only peaks from the abovementioned ZnO and BiOI phases were observed for bilayer heterojunctions in the GIXRD patterns, meaning that for both heterojunctions with different structures, no decomposition or unexpected oxidation happened during the deposition process of the second layer. In addition, the XRD data was used to determine the unit cell parameters, cell volumes and average crystallite size of deposited films (Table 3-1). Similar unit cell parameters and cell volumes were obtained from the ZnO and BiOI films, and heterojunctions indicating that little or even no ion diffusion happened between two layers in both ZnO/BiOI and BiOI/ZnO heterojunctions.

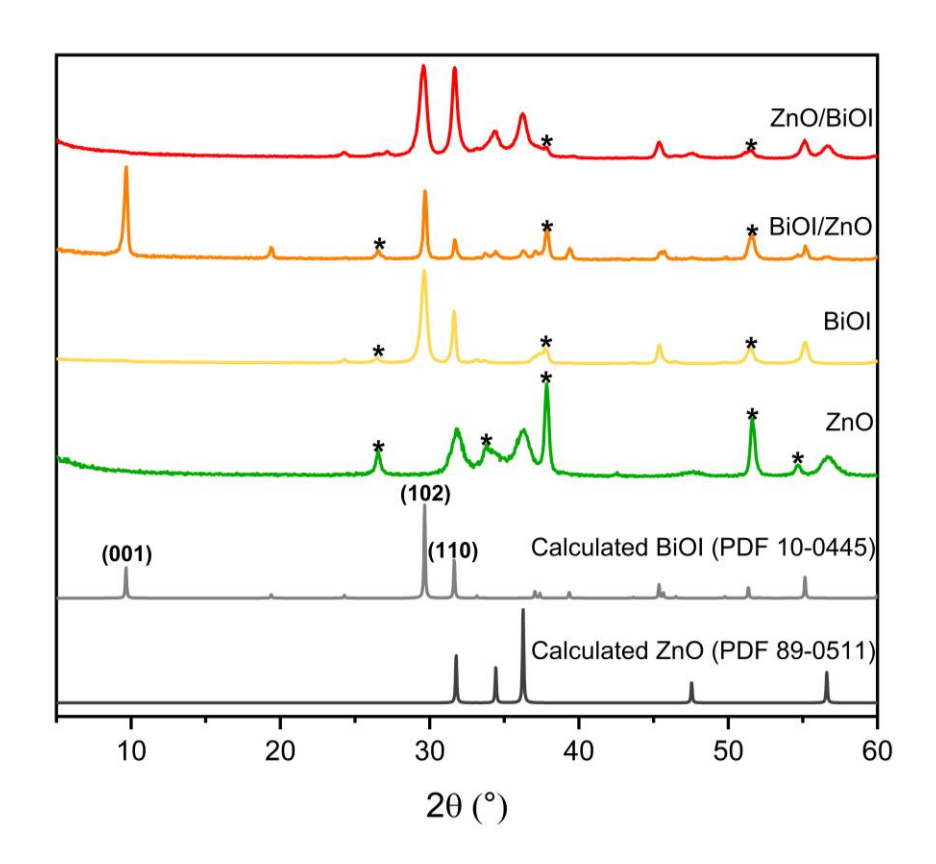


Figure 3-4. GIXRD patterns of ZnO, BiOI, BiOI/ZnO and ZnO/BiOI films on FTO, with all ZnO layers grown from 0.5 g Zn(OAc)<sub>2</sub>·2H<sub>2</sub>O at 350 °C. The asterisked peaks were reflections from FTO substrates.

Table 3-1. Unit cell parameters (a, c), cell volume (V) and average crystallite size of ZnO, BiOI, BiOI/ZnO and ZnO/BiOI films on FTO, with all ZnO layers grown from 0.5 g precursor at 350 °C.

Films		a [Å]	c [Å]	V [ų]	Average crystallite size (Å)	
ZnO standard		3.249	5.205 47.6		-	
BiOI standard		3.994	9.149	145.9	-	
ZnO		3.248 (1)	5.205 (7)	47.56 (7)	139 (4)	
BiOI		3.996 (1)	9.148 (8)	146.10 (14)	178 (4)	
BiOI/ZnO	ZnO	3.251 (6)	5.191 (13)	47.51 (17)	231 (4)	
	BiOI	3.995 (2)	9.149 (3)	146.03 (11)	214 (4)	
ZnO/BiOI	ZnO	3.251 (3)	5.199 (7)	47.58 (9) 159 (4)		
	BiOI	3.997 (1)	9.148 (15)	146.14 (25)	163 (9)	

Different temperatures (300–450 °C) and amounts of the Zn(OAc)<sub>2</sub>-2H<sub>2</sub>O precursor (0.1–0.9 g) were used in the deposition process to obtain ZnO films with different

properties and thickness on the BiOI layers for the optimization of the PEC performance of the ZnO/BiOI heterojunction and to study the influence of the top ZnO film on the heterojunction. First, the amount of Zn(OAc) $_2$ -2H $_2$ O was kept unchanged at 0.5 g. With increasing deposition temperatures from 300 °C to 400° C, the peaks from ZnO grew more intense and sharper, meaning the ZnO films with improved crystallinity were deposited (Figure 3-5). However, it is worth noting that at 400 °C, the characteristic peak at 29.6° from BiOI became broader and asymmetric, indicating that the bottom BiOI film started to decompose. After the deposition temperature was increased to 450° C, the BiOI film was completely decomposed into β-Bi $_2$ O $_3$ , where only peaks from tetragonal β-Bi $_2$ O $_3$  phases but not BiOI were observed. This result was consistent with the reported thermal stability of BiOI.<sup>31</sup>

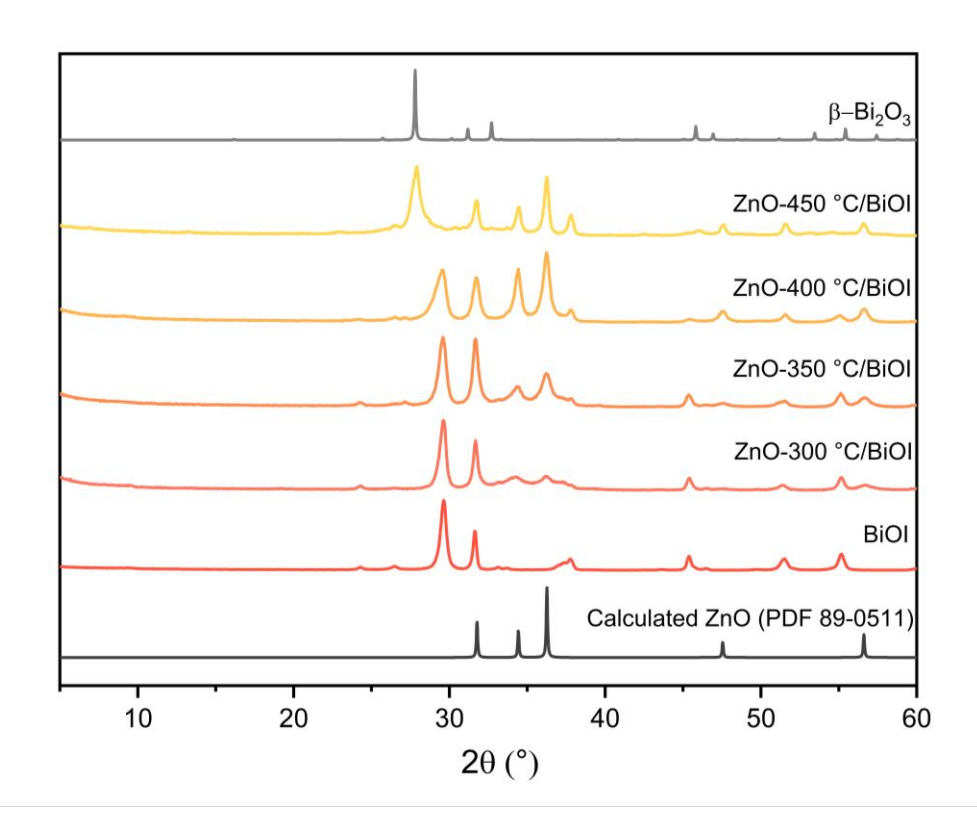


Figure 3-5. GIXRD patterns of ZnO/BiOI films on FTO, with ZnO deposited from 0.5 g Zn(OAc)<sub>2</sub>·2H<sub>2</sub>O at 300, 350, 400 and 450 °C.

Furthermore, the top ZnO films with different thickness were deposited through utilizing different amounts of the precursor in AACVD. Considering the decomposition of BiOI above 400 °C discussed above, the deposition temperature of ZnO films was kept at 350 °C. It could be seen clearly that the characteristic peaks of ZnO at 34.4° and 36.2° showed increased intensity with more Zn(OAc)<sub>2</sub>·2H<sub>2</sub>O used (Figure 3-6). In

addition, the relative peak intensity between the BiOI and ZnO phases also indicated the gradual thickness increase of the top ZnO films. In all samples, there was no visible change for peaks from BiOI, so the film thickness of ZnO did not affect the composition and crystallographic structure of the bottom BiOI layer.

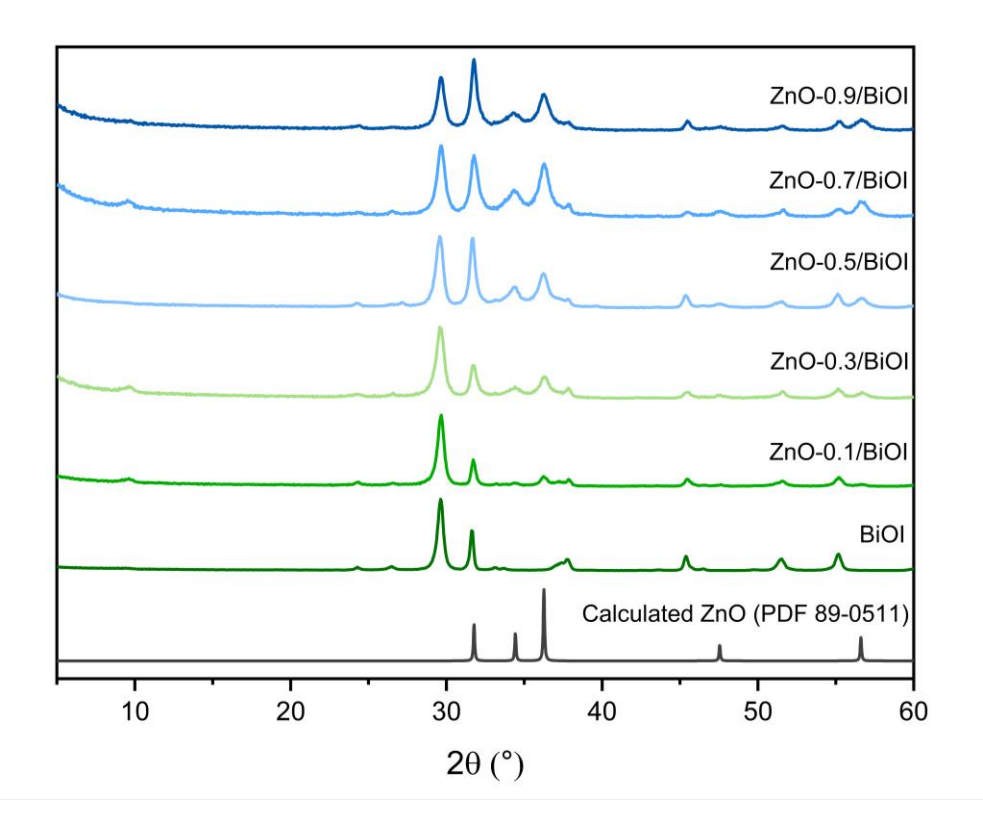


Figure 3-6. GIXRD patterns of ZnO/BiOI films on FTO, with ZnO deposited from 0.1, 0.3, 0.5, 0.7 and 0.9 g Zn(OAc)<sub>2</sub>·2H<sub>2</sub>O at 350 °C.

## 3.3.2 XPS analysis

High resolution XPS was utilized to study the surface composition of the deposited ZnO and BiOI films (Figure 3-7 and Figure 3-8). $^{46-49}$  For the ZnO film deposited from 0.5 g Zn(OAc)<sub>2</sub>·2H<sub>2</sub>O at 350 °C, two peaks at 1021.0 eV and 1044.2 eV were observed in the Zn 2p spectra (Figure 3-7a), which were comparable to the reported Zn<sup>2+</sup> in ZnO. $^{50}$  The O 1s profile could be fitted to two peaks (Figure 3-7b), where the peak at 530.0 eV corresponded to the Zn-O bonds of ZnO, and the peak at 531.5 eV was attributed to the oxygen adsorbed on the film surface. $^{51,52}$  Two components were found in the Bi 4f spectra of the BiOI film (Figure 3-8a). The primary one was fitted to Bi<sup>3+</sup> (Bi  $^{47/2}$  = 158.8 eV and Bi  $^{46/2}$  = 164.1 eV) in BiOI and the minor one was fitted to Bi<sup>0</sup> (Bi  $^{46/2}$  = 157.3 eV and Bi  $^{46/2}$  = 162.6 eV). $^{38}$  The observation of metallic Bi could be

explained by the fact that BiOI is not stable under incident X-rays during XPS measurements, which could result in the photoreduction of Bi<sup>3+</sup>, which has been reported previously in various XPS analysis of Bi-based materials.<sup>7,38</sup> The I 3d spectra was best fitted to two peaks (619.0 eV and 630.5 eV), matching well with those in BiOI (Figure 3-8b).<sup>38</sup>

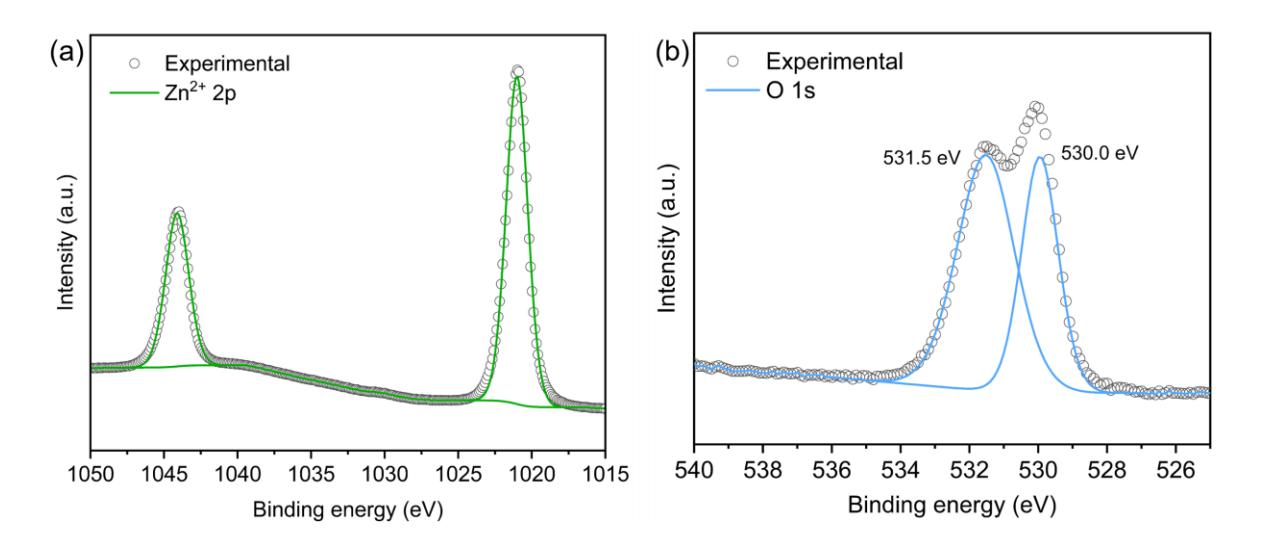


Figure 3-7. High resolution XPS spectra of the (a) Zn 2p and (b) O 1s peaks from the ZnO film on FTO from 0.5 g Zn(OAc)<sub>2</sub>·2H<sub>2</sub>O at 350 °C.

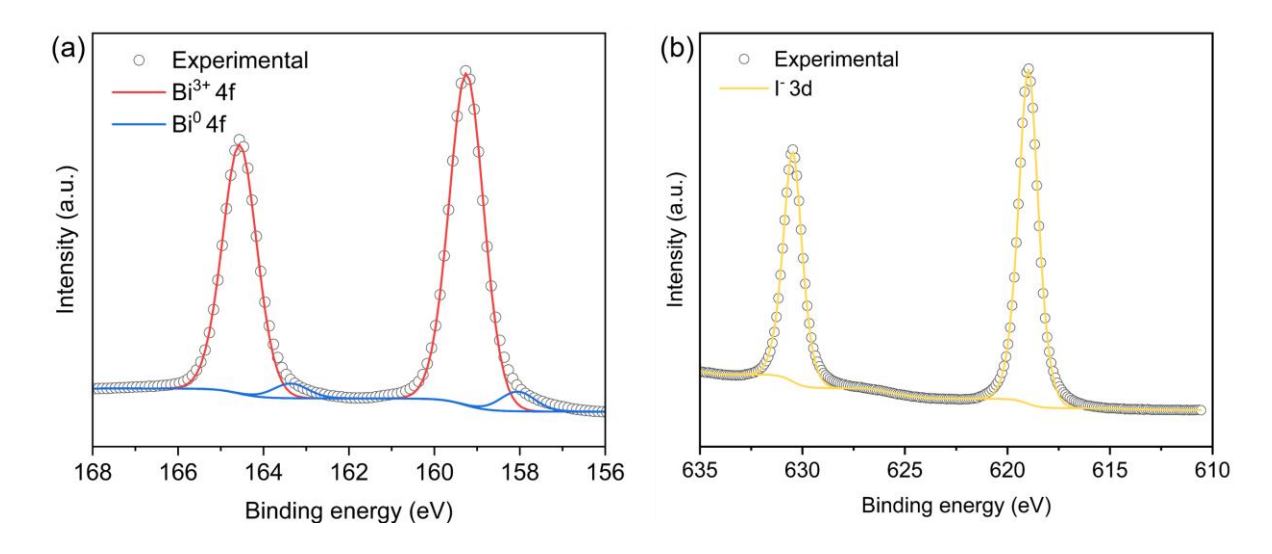


Figure 3-8. High resolution XPS spectra of the (a) Bi 4f and (b) I 3d peaks from the BiOI film on FTO.

For the BiOI/ZnO heterojunction, the Bi 4f spectra were best fitted to 2 components including Bi<sup>3+</sup> and Bi<sup>0</sup>, which was consistent with those of the single-layer BiOI as discussed above (Figure 3-9a). Two strong peaks at 618.6 eV and 630.1 eV were

attributed to I 3d<sub>5/2</sub> and I 3d<sub>3/2</sub>, corresponding to the characteristic signals of I<sup>-</sup> in the top BiOI film (Figure 3-9b).<sup>38</sup> Due to the incomplete coverage of the BiOI film, in addition to the O 1s signal from absorbed oxygen (531.7 eV), two other peaks at 529.4 eV and 530.1 eV were observed in the O 1s spectra, corresponding to the Bi-O bonds in [Bi<sub>2</sub>O<sub>2</sub>] and the Zn-O bonds of ZnO respectively (Figure 3-9c).<sup>52,53</sup> Furthermore, Zn<sup>2+</sup> in ZnO was also observed in XPS spectra for the BiOI/ZnO heterojunction (Figure 3-9d).

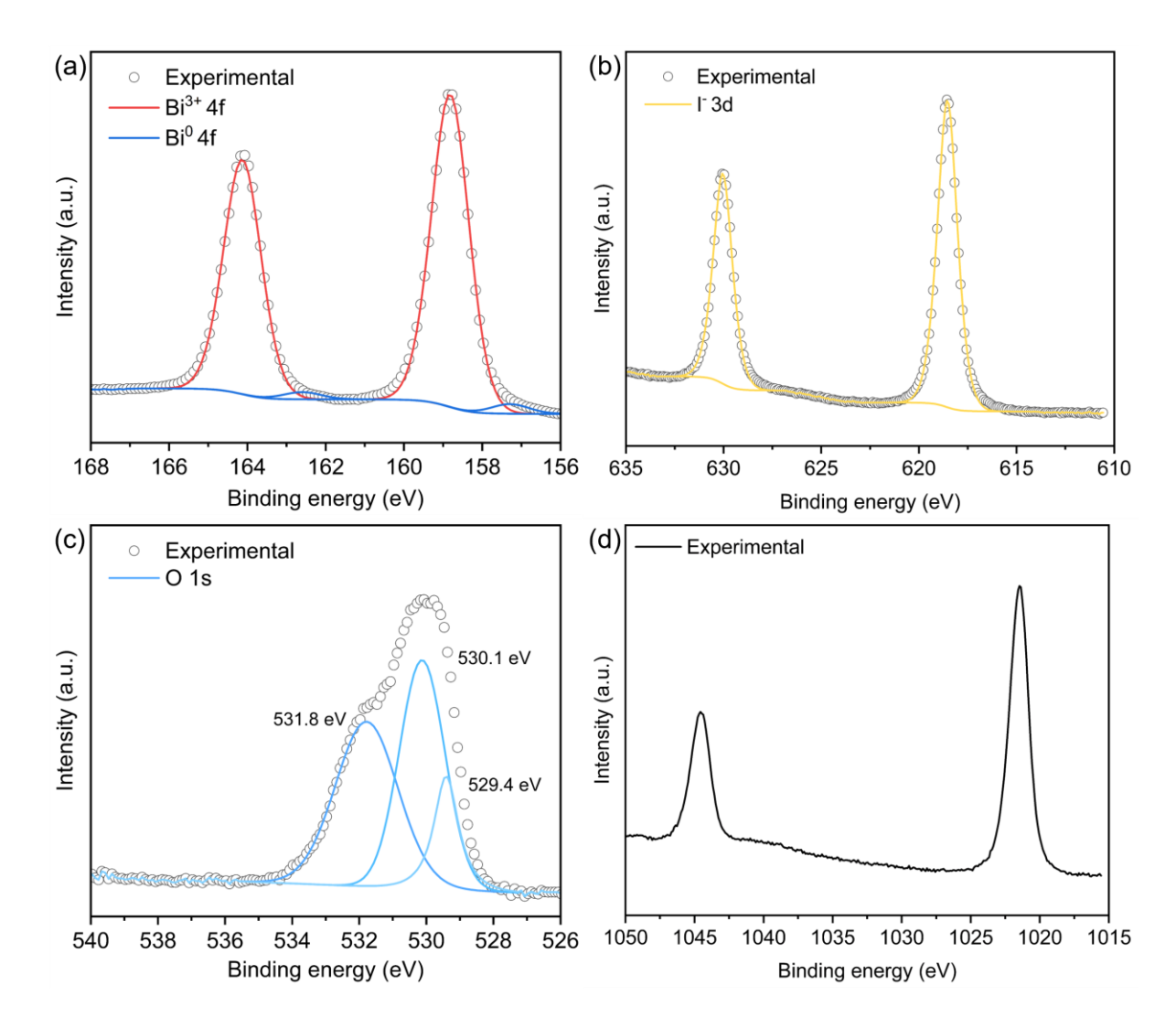


Figure 3-9. High resolution XPS spectra of the (a) Bi 4f, (b) I 3d, (c) O 1s and (d) Zn 2p peaks from the BiOI/ZnO film on FTO, with the ZnO layer grown from 0.5 g Zn(OAc)<sub>2</sub>·2H<sub>2</sub>O at 350 °C.

In the ZnO/BiOI heterojunction, two peaks were observed at the binding energy of 1021.0 eV and 1044.2 eV representing the Zn  $2p_{3/2}$  and Zn  $2p_{1/2}$  environments respectively, indicating the presence of ZnO in the heterojunction (Figure 3-10a).<sup>50</sup>

Contrary to the BiOl/ZnO heterojunction, deconvolution of O 1s signal of the ZnO/BiOl heterojunction was best fitted with only 2 peaks at 530.0 eV and 531.5 eV, attributed to ZnO and surface absorbed oxygen (Figure 3-10b), $^{51,52}$  showing the excellent coverage of the top ZnO layer. Weak signals were also found in the XPS spectra of Bi and I elements, (Figure 3-10c, d). However, considering that such weak signals might not be convincing enough to prove the existence of BiOl, depth profiling XPS was used to support to the study of the elemental composition in the ZnO/BiOl heterojunction with depth (Figure 3-11). Firstly, only Zn 2p and O 1s signals from the top ZnO were observed in depth profiling within the etching time of 0 – 450 s. After 450 s etching, Bi 4f and I 3d signals started to appear. It could be seen that the elemental composition ratio of Bi:Zn increased gradually with longer etching time, demonstrating the bilayer structure of the ZnO/BiOl heterojunction and the presence of the bottom BiOl film (Figure 3-11b).

For both BiOI/ZnO and ZnO/BiOI heterojunctions, all elements in the XPS analysis, such as Zn, O, Bi and I, were in good agreement with the core level XPS of the single-layer ZnO and BiOI films. Therefore, it supported the conclusion that building the bilayer heterojunction would not affect the elemental composition and relative chemical states of each layer in this work.

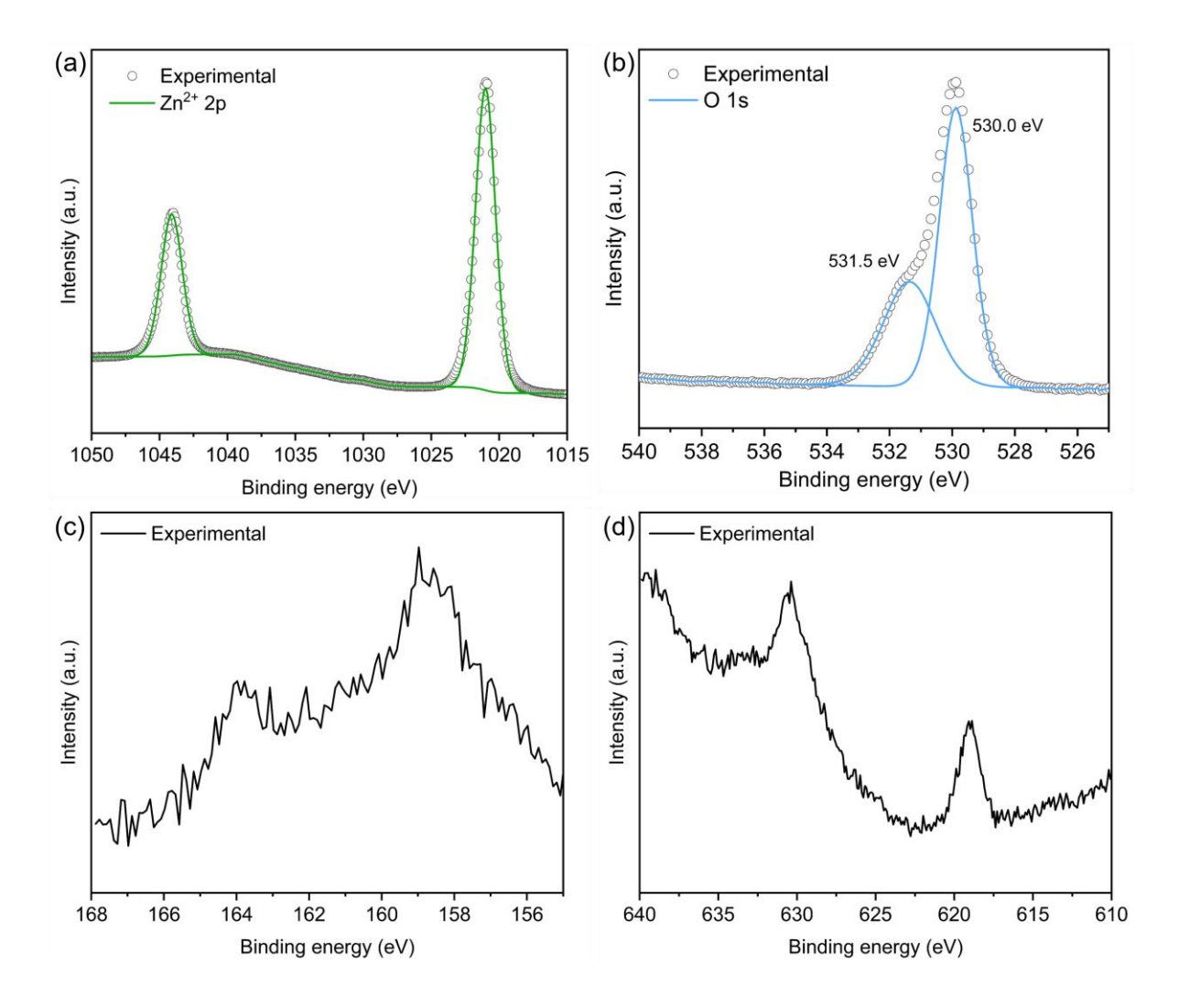


Figure 3-10. High resolution XPS spectra of the (a) Zn 2p, (b) O 1s, (c) Bi and (d) I peaks from the ZnO/BiOI film on FTO, with the ZnO layer grown from 0.5 g  $Zn(OAc)_2 \cdot 2H_2O$  at 350 °C.

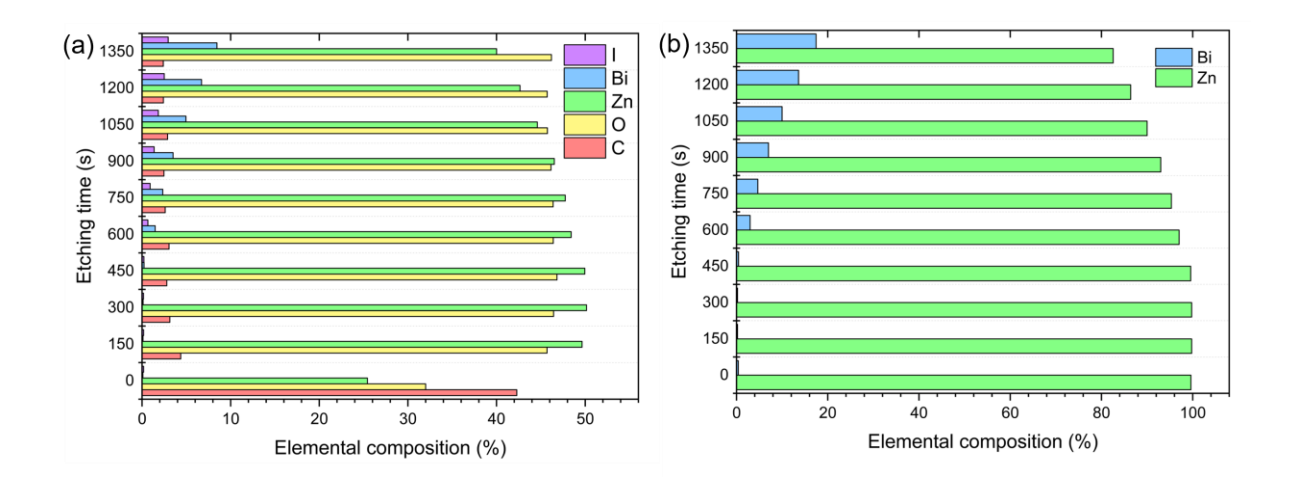


Figure 3-11. Composition (%) variation of ZnO/BiOI with the etching time in XPS, including (a) C, O, Zn, Bi and I, and (b) Zn and Bi, with the ZnO layer grown from 0.5 g Zn(OAc)<sub>2</sub>·2H<sub>2</sub>O at 350 °C.

# 3.3.3 Film morphology characterization

After the determination of the film composition, morphologies of the deposited films were studied by SEM from both top and side views. Top-down and cross-sectional SEM images of ZnO, BiOI, BiOI/ZnO and ZnO/BiOI are shown in Figure 3-12, where all ZnO were deposited from 0.5 g Zn(OAc)<sub>2</sub>·2H<sub>2</sub>O at 350 °C. The ZnO film was composed of round crystals which were packed tightly slightly protruded from the FTO substrate, which were 200 – 300 nm in diameter (Figure 3-12a). This kind of morphology has been reported many times for AACVD-ZnO films.<sup>54,55</sup> Uniform and dense square nanoplatelets whose edge sizes varied from 500 to 900 nm were found in the BiOI film (Figure 3-12b), and previous studies of BiOI films deposited on FTO also reported similar shapes of particles.<sup>7,11,21</sup>

The BiOI/ZnO heterojunction showed a similar surface morphology to the BiOI film, but more scattering nanoplatelets led to the observation of the bottom ZnO layer in the top-view SEM image (Figure 3-12c). This incomplete coverage of the BiOI layer was also mentioned in the XPS analysis of the BiOI/ZnO heterojunction. Unlike the close surface morphologies between the top layer in BiOI/ZnO and the single-layer BiOI film, the top ZnO layer in the ZnO/BiOI heterostructure displayed a variation in the surface morphology compared with the ZnO film. Rather than round ones, the ZnO particles in the ZnO/BiOI heterojunction grew larger and less densely packed rods were formed (Figure 3-12e). The double-layer structures were able to be seen clearly in side-view

SEM images for both BiOI/ZnO and ZnO/BiOI heterojunctions (Figure 3-12d, f). Due to the partial coverage of the top BiOI layer, the BiOI/ZnO film showed an uneven cross section and the thickness of BiOI and ZnO films was around 300 nm and 100 nm respectively. On the contrary, the side-view morphology of the ZnO/BiOI heterojunction was denser and more consistent over the image range, where the ZnO and BiOI layers were around 120 nm and 390 nm thick individually. No dramatic difference in the film thickness were observed due to the different structures of heterojunctions.

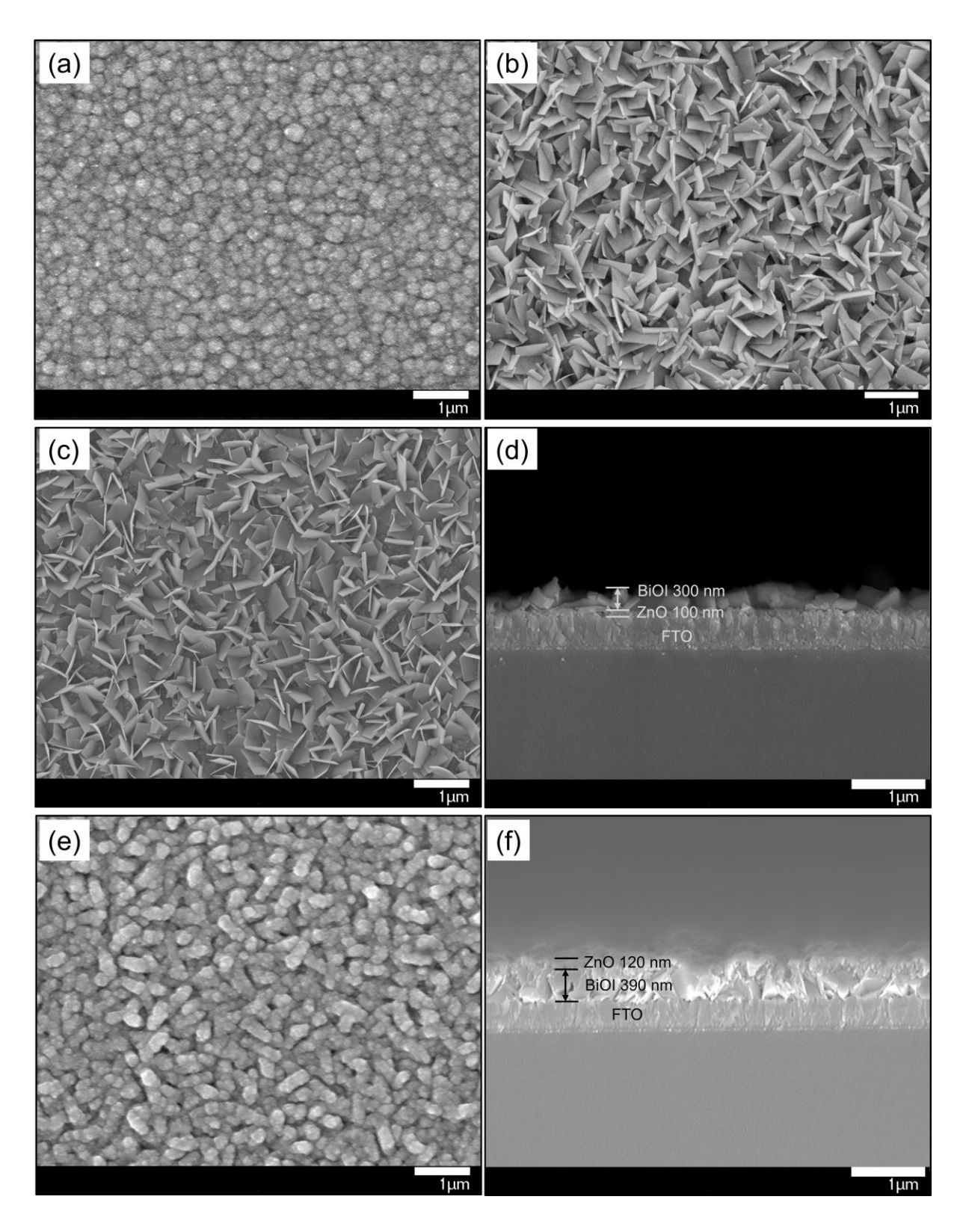


Figure 3-12. Top-view SEM images of (a) ZnO, (b) BiOI, (c) BiOI/ZnO and (e) ZnO/BiOI films on FTO; side-view SEM images of (d) BiOI/ZnO and (f) ZnO/BiOI films on FTO, with all ZnO layers grown from 0.5 g Zn(OAc)<sub>2</sub>·2H<sub>2</sub>O at 350 °C.

As mentioned before, the ZnO/BiOI heterojunctions with the top ZnO layers deposited at various temperatures and precursor amounts were obtained. Therefore, the effect of the deposition temperature and the precursor amount on the film morphology was studied by SEM. In Figure 3-13, it is shown how the particle size of ZnO decreased with increasing the deposition temperature, resulting in a rougher surface. Within the temperature range of 300–400 °C, the top ZnO film could lay over the bottom BiOI film completely. However, due to the thermal decomposition of BiOI into Bi<sub>2</sub>O<sub>3</sub> at 450 °C, particles of **ZnO-450** °C/BiOI were aggregated, and it was hard to distinguish ZnO and BiOI (Figure 3-13c), which was consistent with the analysis from GIXRD patterns (Figure 3-5).

Through increasing the precursor amount used in the ZnO film deposition, significant variation of the surface morphology was observed in the ZnO/BiOI heterojunction (Figure 3-14). When only 0.1 g Zn(OAc)<sub>2</sub>·2H<sub>2</sub>O was used, the BiOI nanoplatelets were dotted with ZnO nanoparticles. With increasing the precursor amount, ZnO particles covered the bottom layer gradually, and completely featured the surface morphology of the intrinsic ZnO film in the end when using 0.9 g of precursor. Interestingly, it was found that the ZnO layer grew along the nanoplatelet edge of the bottom BiOI film, leading to the formation of rod-shaped particles. This growing trend also explained the different surface morphology of the ZnO/BiOI heterojunction from that of the single-layer ZnO film observed in Figure 3-12. Furthermore, through increasing the amount of Zn(OAc)<sub>2</sub>·2H<sub>2</sub>O precursor from 0.1 g to 0.9 g, the thickness variation of the top ZnO films in ZnO/BiOI heterojunctions was displayed clearly in the side-view SEM images (Figure 3-15). It can be seen that the film thickness increased from ~20 nm to ~260 nm, proving that the film thickness of ZnO in the heterojunction could be controlled effectively by adjusting the precursor amount used in the AACVD process.

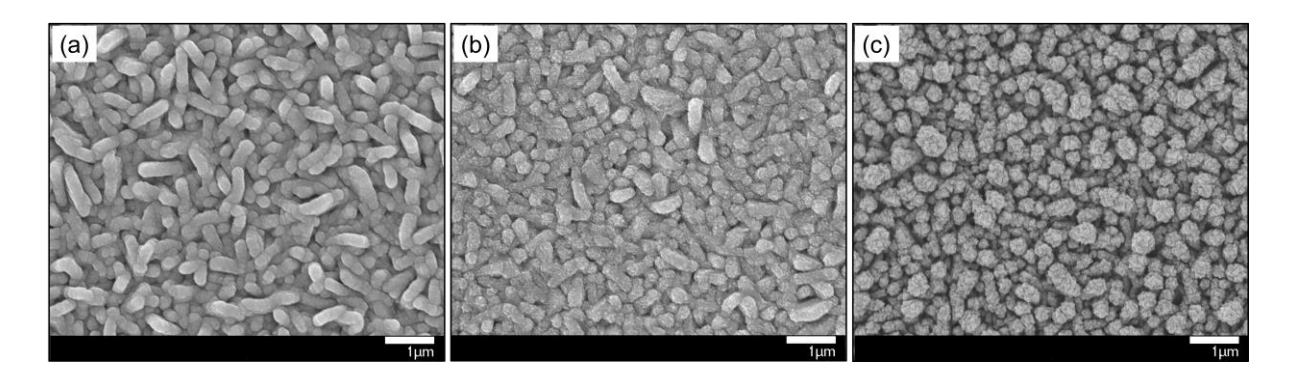


Figure 3-13. Top-view SEM images of ZnO/BiOI films deposited on FTO with ZnO deposited from 0.5 g Zn(OAc)<sub>2</sub>·2H<sub>2</sub>O at (a) 300, (b) 400 and (c) 450 °C.

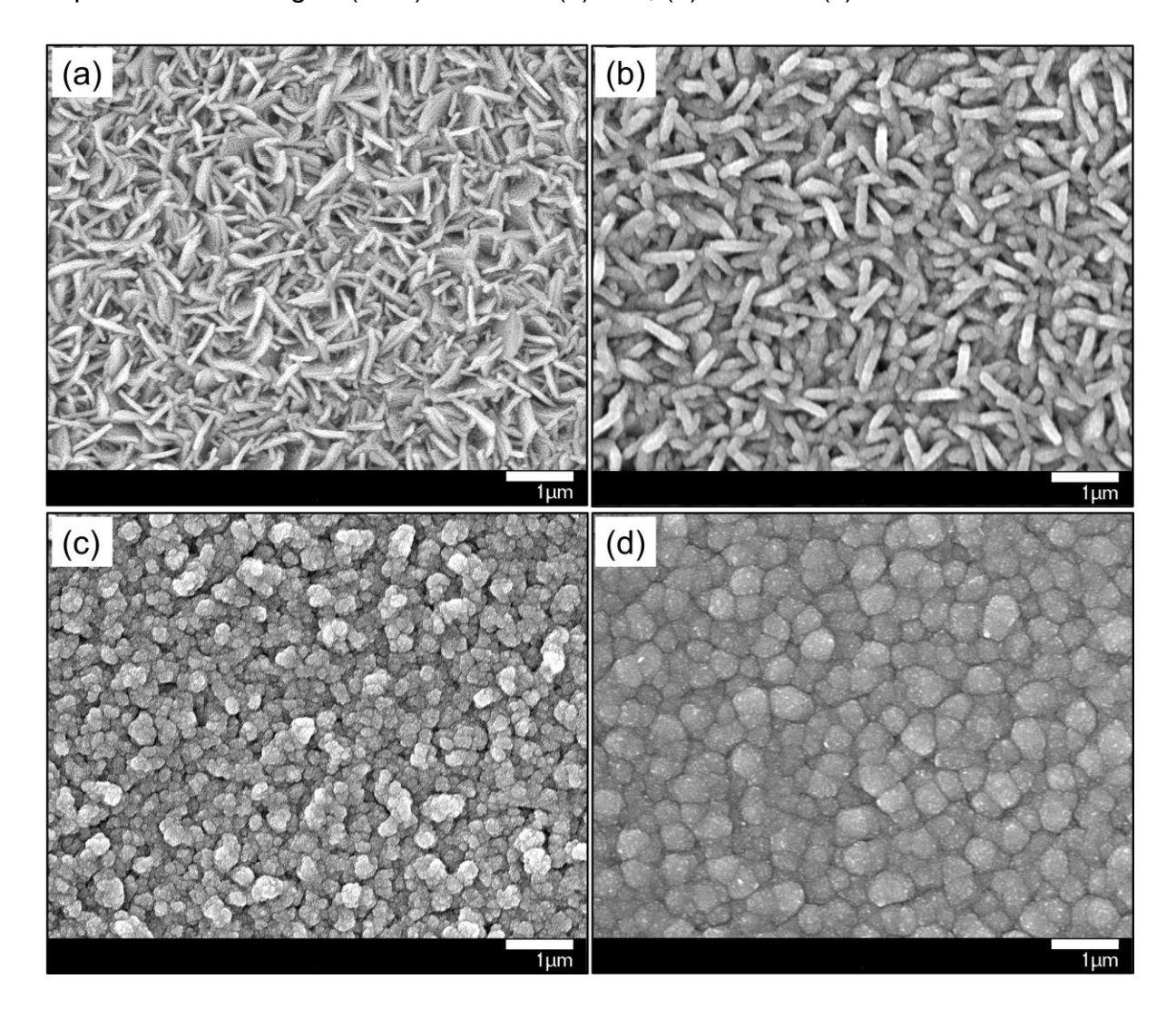


Figure 3-14. Top-view SEM images of ZnO/BiOI films deposited on FTO with ZnO deposited from (a) 0.1 g, (b) 0.3 g, (c) 0.7 g and (d) 0.9 g Zn(OAc)<sub>2</sub>·2H<sub>2</sub>O at 350 °C.

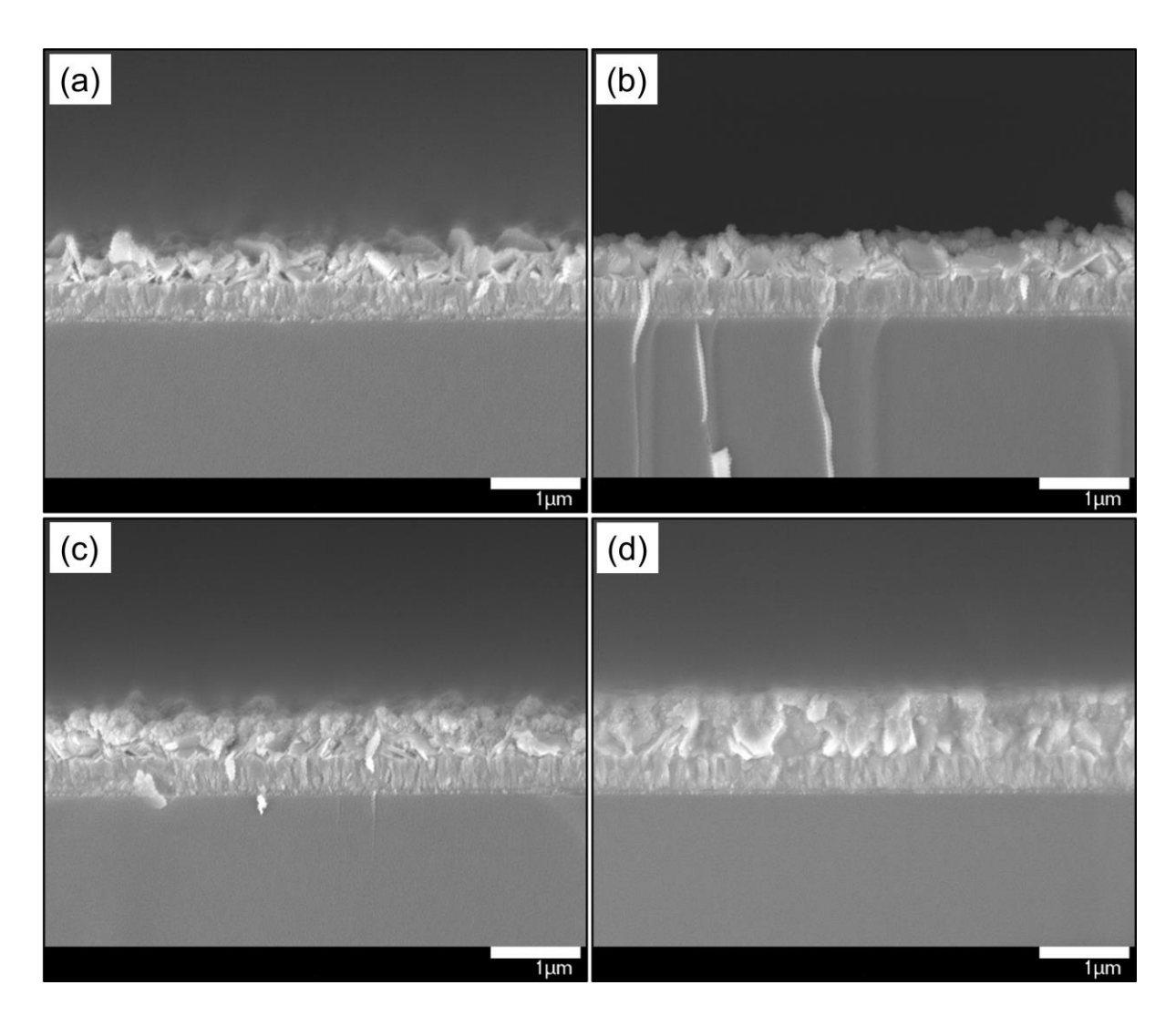


Figure 3-15. Side-view SEM images of ZnO/BiOI films deposited on FTO with ZnO deposited from (a) 0.1 g, (b) 0.3 g, (c) 0.7 g and (d) 0.9 g Zn(OAc)<sub>2</sub>·2H<sub>2</sub>O at 350 °C.

## 3.3.4 Optical properties and band gap calculations

The optical properties of single-layer films and heterojunctions were investigated using UV-Vis transmittance spectroscopy, where all ZnO films were deposited from 0.5 g Zn(OAc)<sub>2</sub>·2H<sub>2</sub>O at 350 °C (Figure 3-16a). Like reported previously,<sup>56</sup> a high degree of visible light transmission (around 80%) was also shown in the spectrum of the ZnO film deposited *via* AACVD herein, and an intense band edge existed at ~375 nm. In addition, the optical band gaps of ZnO were further calculated from the spectrum (Figure 3-16b). Due to the direct characteristic for the semiconductor type of ZnO, n=2 was used in the Tauc-plot method.<sup>57</sup> It was determined that the direct band gap of the ZnO was 3.32 eV, which was in accordance with the reported value in literature.<sup>56</sup> Caused by its wide band gap, ZnO can only be activated by UV light, which is one of

the main factors limiting the practical PEC applications of ZnO. In contrast, the BiOI film had a much lower visible light transmittance with an absorption peak at around 600 nm. Considering its indirect band gap nature, n=1/2 was used in the band gap calculation of BiOI by the Tauc-plot method (Figure 3-16c). The BiOI film on FTO had an indirect band gap of 1.79 eV, consistent with other literature.<sup>7,21</sup>

Because of the incomplete coverage of the top BiOI layer in the BiOI/ZnO heterojunction discussed above, two band edges at ~375 nm (from the ZnO layer) and ~620 nm (from the BiOI layer) were observed in the transmittance spectrum of the BiOI/ZnO heterojunction. However, this situation did not happen for the ZnO/BiOI heterojunction. The UV-Vis transmittance spectrum of ZnO/BiOI was similar to that of the single-layer BiOI film, with a slight blue shift of the absorption edge. This indicated that the ZnO/BiOI heterojunction could absorb a wide range of incident light from UV to yellow visible light. As a result, compared with ZnO alone, the ZnO/BiOI heterojunction has a significantly improved visible light harvesting capacity, which is beneficial to its PEC performance.

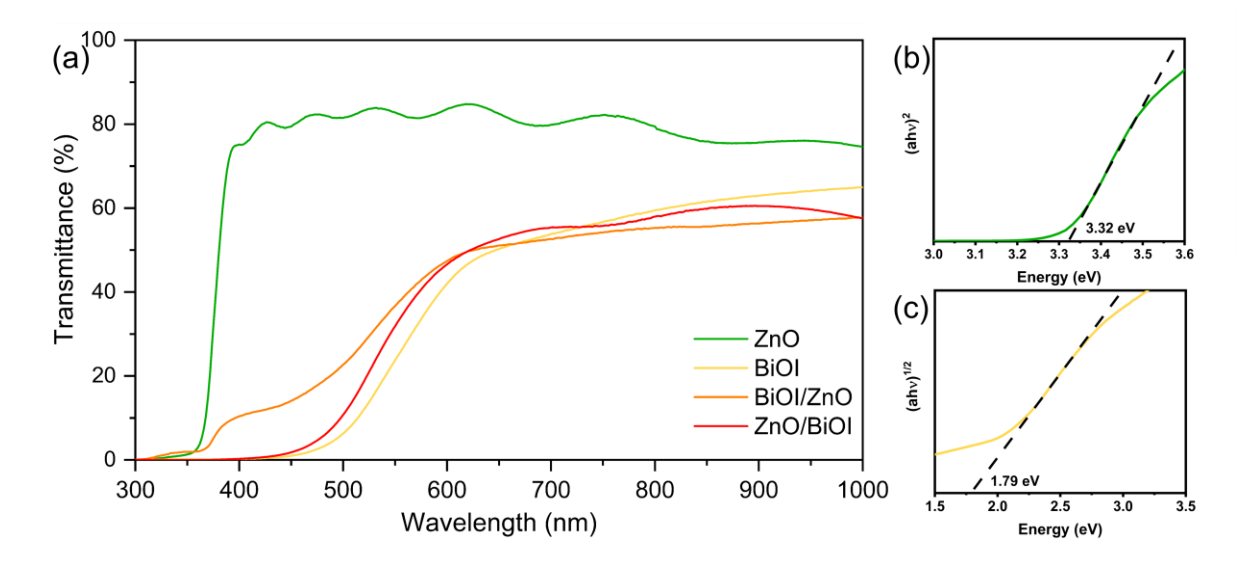


Figure 3-16. (a) UV-Vis transmittance spectra of ZnO, BiOI, BiOI/ZnO and ZnO/BiOI films deposited on FTO, with all ZnO layers grown from 0.5 g Zn(OAc)<sub>2</sub>·2H<sub>2</sub>O at 350 °C; calculated optical band gaps of (b) ZnO and (c) BiOI films.

Based on the ZnO/BiOI heterojunction, the influence of deposition temperatures of the top ZnO layer on the optical properties was studied first. For the series of heterojunctions with ZnO layers deposited at different temperatures, a remarkable blue shift of absorption edges was observed in the UV-Vis spectra (Figure 3-17). As

analyzed from the GIXRD patterns (Figure 3-5), the bottom BiOI layer in the heterojunction decomposed gradually with increasing the deposition temperature of ZnO from 300 °C to 450 °C, corresponding to the colour change of the heterojunctions from orange to pale yellow.

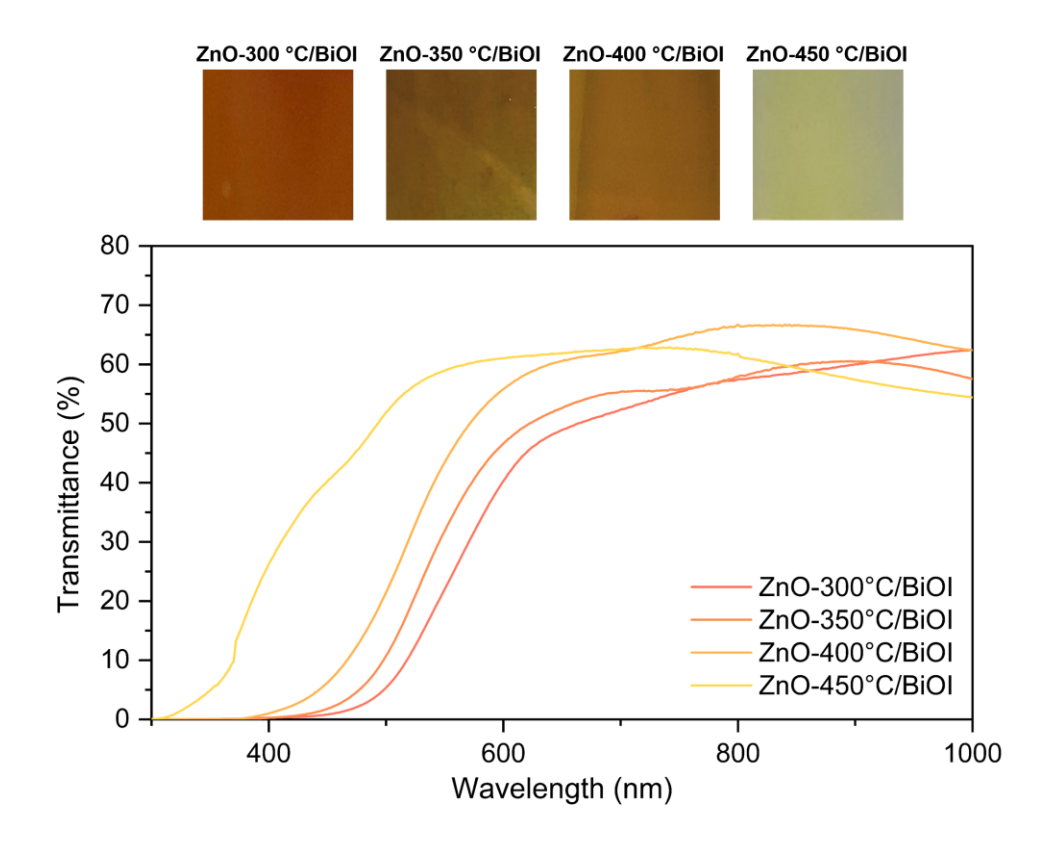


Figure 3-17. UV-Vis transmittance spectra of ZnO/BiOI films deposited on FTO with ZnO deposited from 0.5 g Zn(OAc)<sub>2</sub>·2H<sub>2</sub>O at 300, 350, 400 and 450 °C.

A slight variation of band edges was observed in the series of ZnO/BiOI heterojunctions with the increase of ZnO film thickness, which was in the range of experimental error (Figure 3-18). In addition, with increasing the precursor amount, interference fringes started to appear within the visible-light range of the transmittance spectra, which was also observed in the single-layer ZnO film (Figure 3-16a). It is worth noting that the amplitude of interference fringes was enhanced gradually with thickening the ZnO film, indicating that the film surface became smoother, which was also observed in top-view SEM images (Figure 3-14).<sup>58</sup>

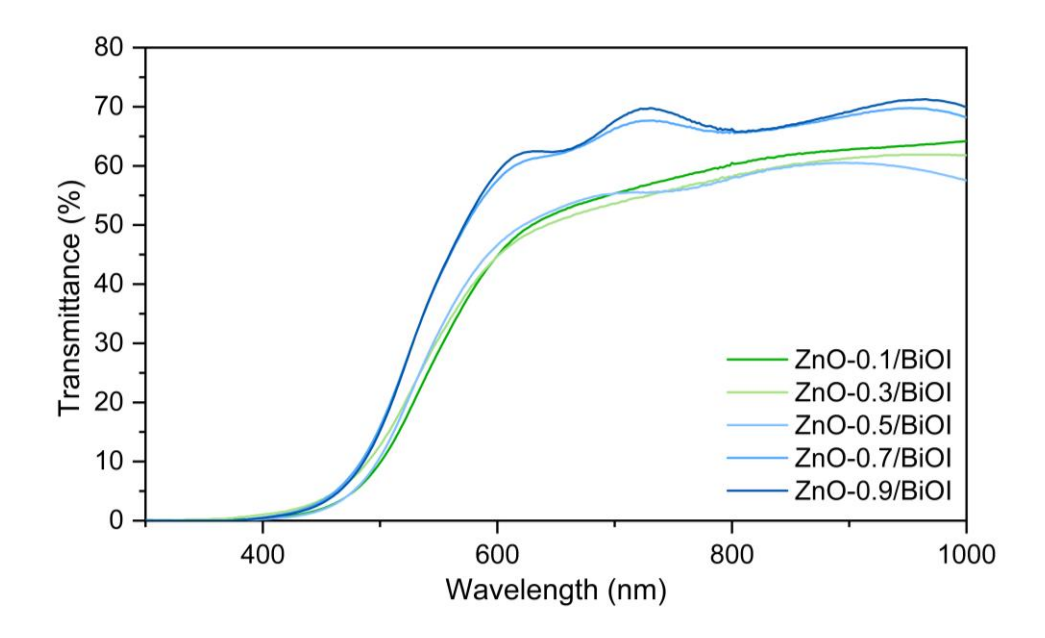


Figure 3-18. UV-Vis transmittance spectra of ZnO/BiOI films deposited on FTO with ZnO deposited from 0.1 g, 0.3 g, 0.5 g, 0.7 g and 0.9 g Zn(OAc)<sub>2</sub>·2H<sub>2</sub>O at 350 °C.

## 3.3.5 Photoelectrochemical measurements

In order to investigate the potential of the prepared heterojunctions in PEC water splitting, JV curves were collected first. All films were tested in the neutral electrolyte, 0.5M Na<sub>2</sub>SO<sub>4</sub> solution. With sweeping the voltage from 0.10 V<sub>RHE</sub> to 1.60 V<sub>RHE</sub>, JV curves were obtained in the dark and under light irradiation. There was no measurable current observed in dark. Electrocatalytic water oxidation happened for all samples after around 1.23 V<sub>RHE</sub> in dark due to the voltage being higher than the redox potential of O<sub>2</sub>/H<sub>2</sub>O<sub>.59</sub> As a result, the current density of all tested samples at 1.10 V<sub>RHE</sub> was picked for the comparison.

The preparation method could easily influence the conductivity type of BiOI.<sup>10,11</sup> It has been reported that n-type BiOI films were deposited successfully *via* AACVD.<sup>7</sup> In this work, due to the similar AACVD fabrication procedure, n-type BiOI was obtained as well. The anodic photocurrent of the as-fabricated BiOI film observed in the *JV* curves also proved its n-type conductivity (Figure 3-19). However, due to the fast recombination of photogenerated charge carriers and slow charge transfer,<sup>60</sup> the BiOI film showed a low photocurrent density of 0.02 mA·cm<sup>-2</sup> at 1.10 V<sub>RHE</sub> under 1 sun illumination as expected. In addition, the BiOI film showed an onset potential of around 0.60 V<sub>RHE</sub>. In contrast, the AACVD-ZnO film exhibited a much higher photocurrent

(0.37 mA·cm<sup>-2</sup> at 1.10 V<sub>RHE</sub>). Interestingly, the PEC performance of the BiOI/ZnO heterojunction was not improved much compared with the single-layer BiOI film, and was worse than that of the single-layer ZnO film, with a photocurrent of 0.057 mA·cm<sup>-2</sup> at 1.10 V<sub>RHE</sub>. However, the onset potentials of ZnO and the BiOI/ZnO heterojunction were close ( $\sim$ 0.30 V<sub>RHE</sub>).

Several reasons could explain this slight improvement. Firstly, as found in XPS and SEM characterizations, the coverage of BiOI in the BiOI/ZnO heterojunction was incomplete (Figure 3-9 and Figure 3-12). Therefore, the bottom ZnO layer cannot fully contact with BiOI to form the heterojunction, leading to a limited enhancement in the PEC activity. In addition, the light capture ability of the heterojunction might also be impaired. Secondly, because ZnO can only utilize UV light which would be absorbed by the top BiOI layer when the heterojunction was irradiated, almost no photocurrent was able to be generated in the ZnO film. However, the close onset potentials of ZnO and the BiOI/ZnO heterojunction indicated that a part of the photocurrent was generated by the ZnO layer in the heterojunction due to the poor coverage of the top BiOI film. Furthermore, it has been reported that there would be a layer of bismuth hydroxide formed on the BiOI film surface when the film is exposed to aqueous solutions. This hydroxide layer could act as an insulting layer inhibiting the transfer of charge carriers.<sup>11</sup> As a result, based on all these limitations, such a low photocurrent density was observed for the BiOI/ZnO film.

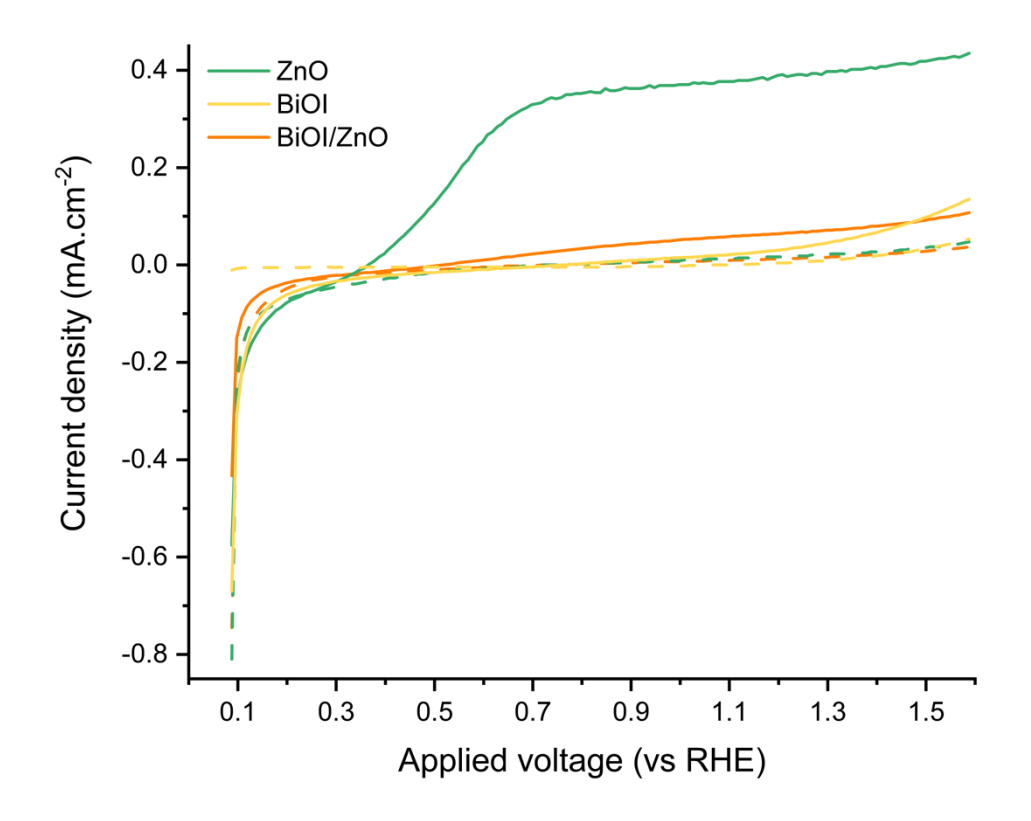


Figure 3-19. JV curves of ZnO, BiOI, and BiOI/ZnO films measured in the dark (dashed lines) and under the action of light (1 sun illumination, solid lines), with all ZnO layers grown from 0.5 g Zn(OAc)<sub>2</sub>·2H<sub>2</sub>O at 350 °C. Samples were irradiated at the semiconductor–electrolyte interface. The voltage was swept from 0.10 V<sub>RHE</sub> to 1.60 V<sub>RHE</sub> at a rate of 10 mV·s<sup>-1</sup>.

Besides BiOI/ZnO, the *JV* curves of the ZnO/BiOI heterojunction and its parent materials were measured as well (Figure 3-20). Significantly different from what was observed in the BiOI/ZnO heterojunction, the PEC performance of the ZnO/BiOI heterojunction showed a large improvement. The photocurrent density of the BiOI film (0.004 mA·cm<sup>-2</sup> at 1.10 V<sub>RHE</sub>) was negligible compared with the ZnO film and the ZnO/BiOI heterojunction, with an onset potential for PEC water oxidation of ~0.60 V<sub>RHE</sub>. For the single-layer ZnO film, the *JV* curve under illumination reached a plateau, corresponding to 0.1 mA·cm<sup>-2</sup>, from 0.60 V<sub>RHE</sub>. However, the photocurrent density of the ZnO/BiOI heterojunction kept rising within the applied voltage range and reached to 0.27 mA·cm<sup>-2</sup> at 1.10 V<sub>RHE</sub>, which was nearly 3 times and 68 times higher than that of the single-layer ZnO and BiOI films respectively. Based on the *JV* curves, these indicated that the construction of the ZnO/BiOI heterojunction was effective in the

enhancement of the PEC activity, and the PEC performance would be dramatically different in the built heterojunctions with diverse layer structures.

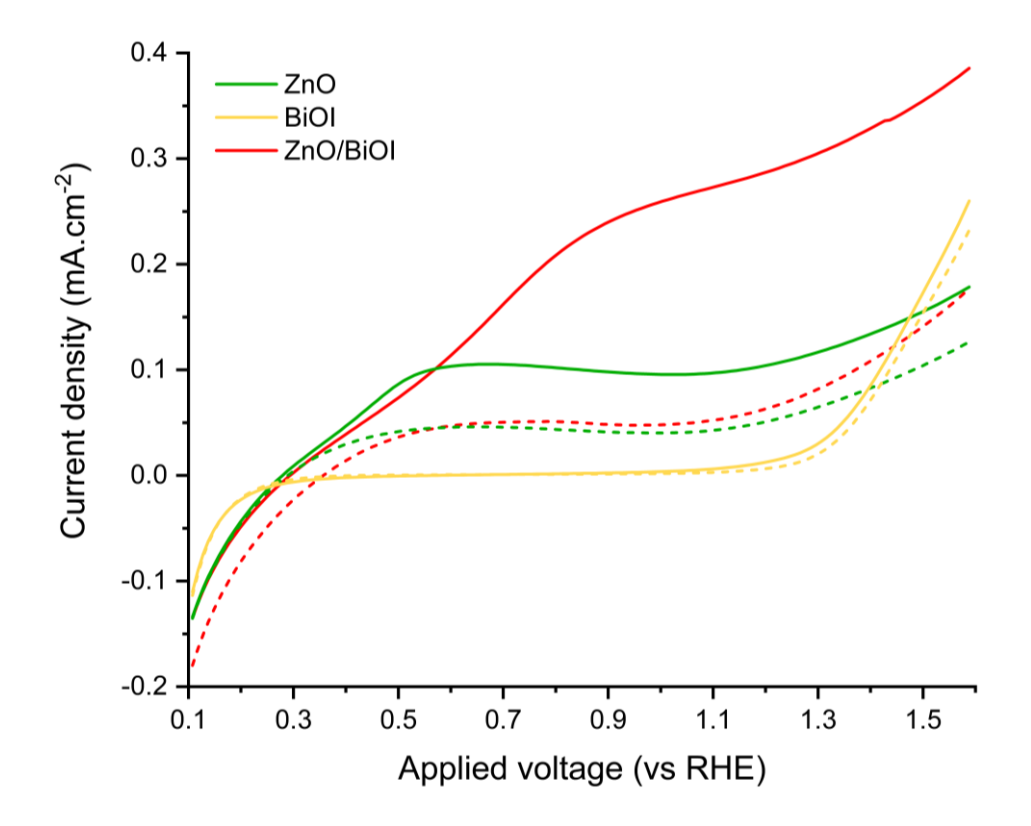


Figure 3-20. *JV* curves of ZnO, BiOI, and ZnO/BiOI films measured in the dark (dashed lines) and under the action of light (350 nm, 2.58 mW·cm<sup>-2</sup>) (solid lines), with all ZnO layers grown from 0.5 g Zn(OAc)<sub>2</sub>·2H<sub>2</sub>O at 350 °C. Samples were irradiated at the semiconductor–electrolyte interface. The voltage was swept from 0.10 V<sub>RHE</sub> to 1.60 V<sub>RHE</sub> at a rate of 10 mV·s<sup>-1</sup>.

Due to its remarkably enhanced PEC activity, the ZnO/BiOI heterojunction was studied in more detail. First, the influence of the deposition temperature of the top ZnO layer on the PEC water oxidation function was investigated (Figure 3-21a). A significant increase in the photocurrent density was observed in the heterojunction with ZnO deposited at 350 °C compared with that at 300 °C. This increase could be the result of better crystallinity of ZnO, which was proved in the GIXRD patterns (Figure 3-5). The low degree of crystallinity usually exists in films grown at low temperatures, which is detrimental to their PEC performance.<sup>61</sup> However, the photocurrent density of the heterojunction did not keep increasing with higher deposition temperatures of ZnO but dropped dramatically once above 400 °C, because the lower BiOI film started to

decompose as determined in the GIXRD patterns (Figure 3-5). The onset potentials of heterojunctions also varied a lot due to the change in composition.

Furthermore, the *JV* curves of ZnO/BiOI heterojunctions with various ZnO film thickness were measured (Figure 3-21b). In the range of the precursor amount from 0.1 g to 0.5 g, corresponding to the ZnO film thickness from 20 nm to 120 nm, the photocurrent density of the heterojunction rose gradually with thickening the ZnO film. When the film thickness was larger than 120 nm, a decrease in the photocurrent was found. There was no great change in the onset potentials of samples observed. The photocurrent value is determined by the number of photogenerated electrons and holes in semiconductors. Initially, the thicker ZnO film is favorable to the incident light absorption in UV range,<sup>62</sup> so that more electrons and holes could be generated. Nevertheless, further increase in the film thickness might limit the transfer of electrons and holes from the bulk to the surface of the ZnO layer where the PEC reaction happens, and then aggravate the charge recombination. As a result, the photocurrent density was decreased.<sup>63</sup>

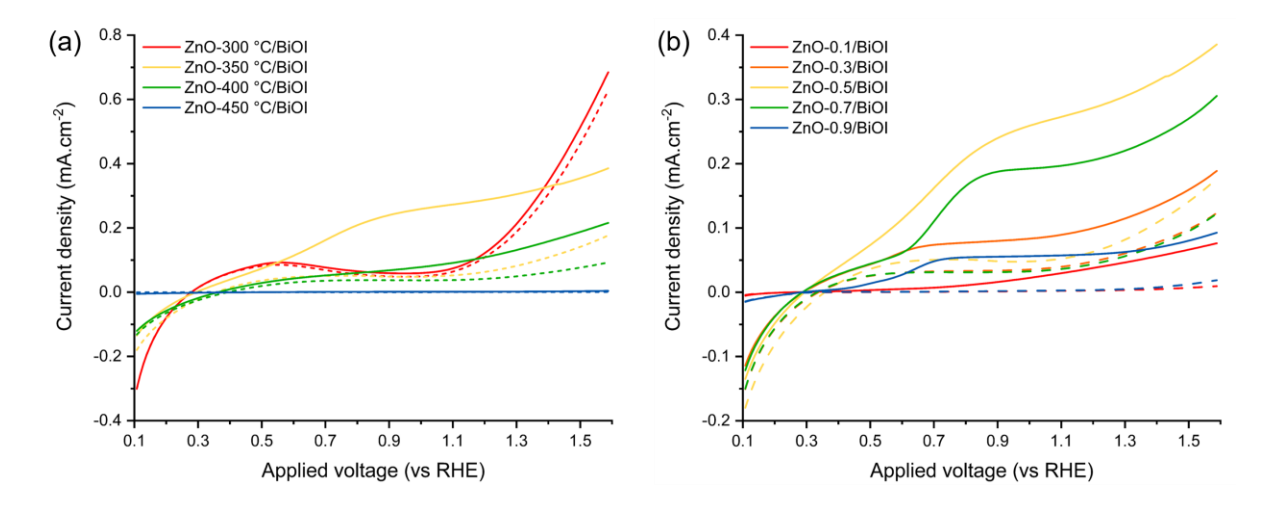


Figure 3-21. JV curves of ZnO/BiOI films in the dark (dashed lines) and under the action of light (350 nm, 2.58 mW·cm<sup>-2</sup>) (solid lines), (a) with ZnO deposited from 0.5 g Zn(OAc)<sub>2</sub>·2H<sub>2</sub>O at 300, 350, 400 and 450 °C; (b) with ZnO deposited from 0.1, 0.3, 0.5, 0.7 and 0.9 g Zn(OAc)<sub>2</sub>·2H<sub>2</sub>O at 350 °C. Samples were irradiated at the semiconductor–electrolyte interface. The voltage was swept from 0.10 V<sub>RHE</sub> to 1.60 V<sub>RHE</sub> at a rate of 10 mV·s<sup>-1</sup>.

In summary, the ZnO/BiOI heterojunction with the ZnO film deposited from 0.5 g  $Zn(OAc)_2 \cdot 2H_2O$  at 350 °C showed the best performance in the PEC water oxidation.

Therefore, more PEC measurements were obtained on it for a more comprehensive understanding. The applied bias photo-to-current efficiency (ABPE) is useful in quantifying the photoresponse efficiency of photoanodes under an applied voltage. In this work, ABPE was determined for the ZnO/BiOI heterojunction and parent materials under 1 sun illumination from equation (4), and the calculated ABPE was plotted against the applied potential (vs. RHE) (Figure 3-22). The ABPE of ZnO is maximized at 0.55 VRHE with the value of 2.59%, while the maximum ABPE of BiOI was ultralow (0.03% at 1.02 VRHE). The maximum efficiency of the ZnO/BiOI heterojunction was 3.49% at 0.78 VRHE, which was almost 1.5 and 100 folds higher than that of ZnO and BiOI respectively. Thus, the enhanced PEC performance of the ZnO/BiOI heterojunction was elucidated further.

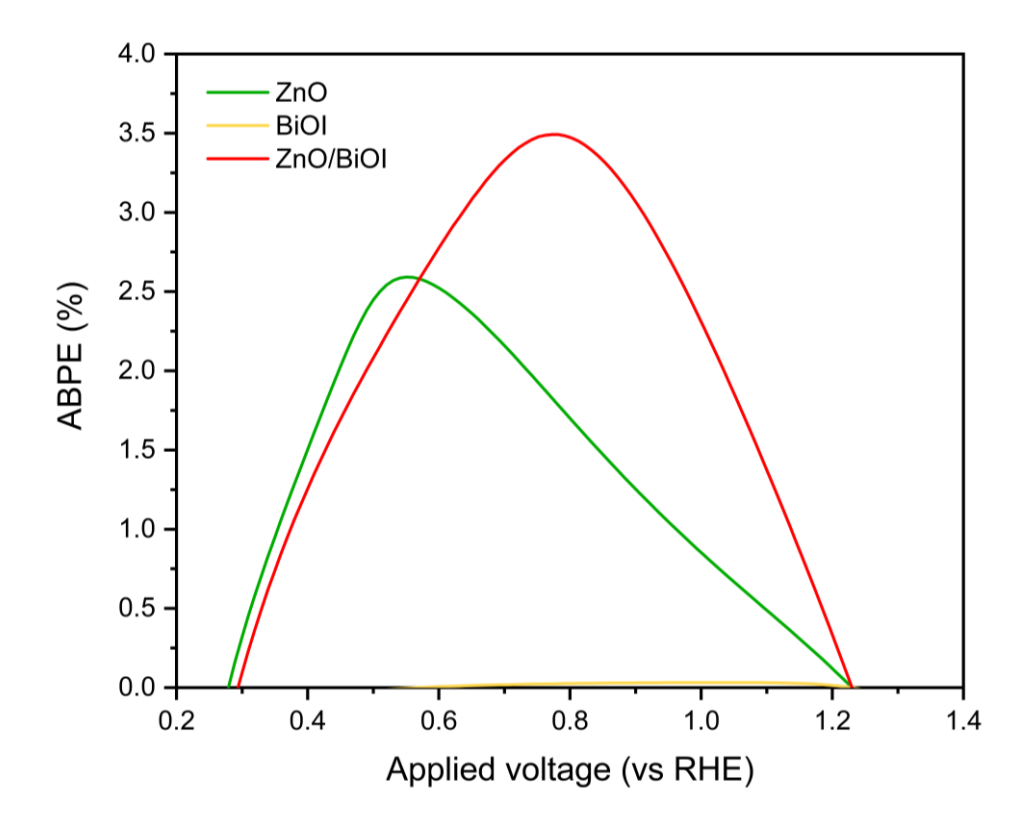


Figure 3-22. ABPE curves of ZnO, BiOI, and ZnO/BiOI under the action of light (1 sun illumination), with all ZnO layers grown from 0.5 g Zn(OAc)<sub>2</sub>-2H<sub>2</sub>O at 350 °C.

For the quantification of the photoelectric conversion efficiency under irradiation with diverse wavelengths, the incident photon-to-current efficiency (IPCE) was measured for the ZnO/BiOI heterojunction and parent materials, ZnO and BiOI, with the applied voltage on photoanodes held at 1.23  $V_{RHE}$ . All tested films were irradiated by the monochromatic light from the front. It can be seen from Figure 3-23 that the IPCE of

the ZnO/BiOI heterojunction was larger than both parent materials in the whole wavelength range from 250 nm to 650 nm, where ZnO/BiOI exhibited a quantum efficiency of 10.2–33.5% in UV region and processed a higher level of visible light activity (IPCE of ~0.1 to ~3%). Hence, the utilization of the visible light in ZnO/BiOI was improved significantly during the PEC water oxidation process. In addition, the IPCE of ZnO/BiOI was higher than the calculated sum of two parent materials as well, proving that this enhancement was from the synergetic effect of the built heterojunction but not the simple sum of two kinds of materials.

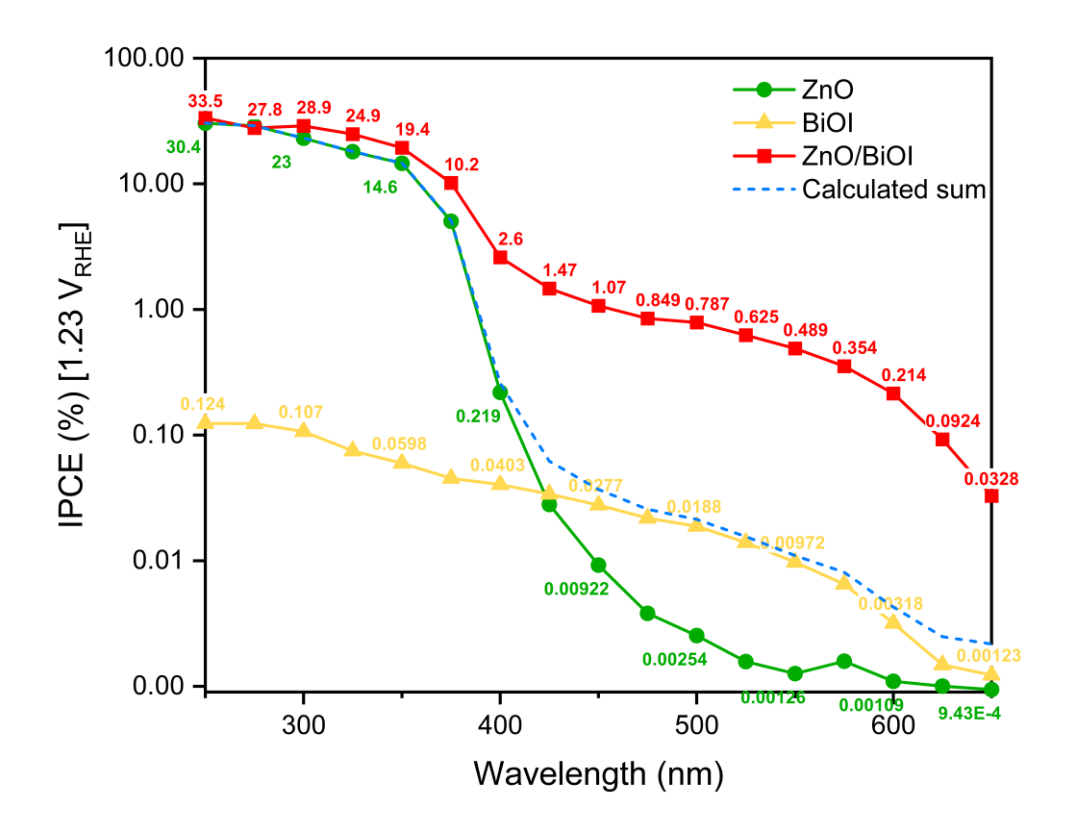


Figure 3-23. IPCE of ZnO, BiOI, and ZnO/BiOI films, with all ZnO layers grown from 0.5 g Zn(OAc)<sub>2</sub>·2H<sub>2</sub>O at 350 °C.

After the functional optimization of the ZnO/BiOI heterojunction and the determination of its PEC performance in the lab scale, the performance of the as-fabricated films in practical applications for solar water splitting was predicted by multiplying IPCE with AM 1.5 spectrum, where theoretical solar photocurrents (TSPs) were obtained.<sup>59</sup> Diagrams of the calculation process are shown in Figure 3-24. The single-layer BiOI, ZnO films and the ZnO/BiOI heterojunction exhibited TSPs of ~0.0028 mA·cm<sup>-2</sup>, ~0.12 mA·cm<sup>-2</sup> and ~0.27 mA·cm<sup>-2</sup> individually. The TSP of the ZnO/BiOI heterojunction was increased a lot compared with both parent materials, and even more than twice higher

than the sum of TSPs of the BiOI and ZnO films, which demonstrated again the improved PEC water oxidation activity of the heterojunction. It could be seen clearly that under real sunlight irradiation, almost all incident photons in the visible range were wasted by the single-layer ZnO film (Figure 3-24a). However, the solar light absorption limitation of ZnO was largely reduced in the ZnO/BiOI heterojunction due to the existence of BiOI with a smaller bandgap (Figure 3-24c). Because there is much more visible light (44%) than UV light (4%) in the solar spectrum, over twice enhanced solar activity of the ZnO/BiOI heterojunction was obtained.

A table including the PEC performance of ZnO, BiOI and ZnO/BiOI photoelectrodes is provided for comparison among the fabricated films herein and materials reported by other groups on PEC water oxidation (Table 3-2). The compared materials had similar structures or were prepared from similar film deposition methods. It can be seen in the table that the ZnO/BiOI heterojunction in this work presented a better performance (0.27 mA·cm<sup>-2</sup> at 1.23 V<sub>RHE</sub> with the onset potential of 0.3 V<sub>RHE</sub>) than reported work. Furthermore, the film deposition method used herein, AACVD, is cheaper and easier to achieve the large-scale production than others such as the solvothermal method. However, there is still a gap of PEC performance between this ZnO/BiOI heterojunction and state-of-the-art photoanodes. For example, the photoanodes of WO<sub>3</sub> with controlled structures exhibited a photocurrent density of 3.16 mA·cm<sup>-2</sup> at 1.23 V<sub>RHE</sub>, while with an onset potential of 0.6 V<sub>RHE</sub>.<sup>64</sup>

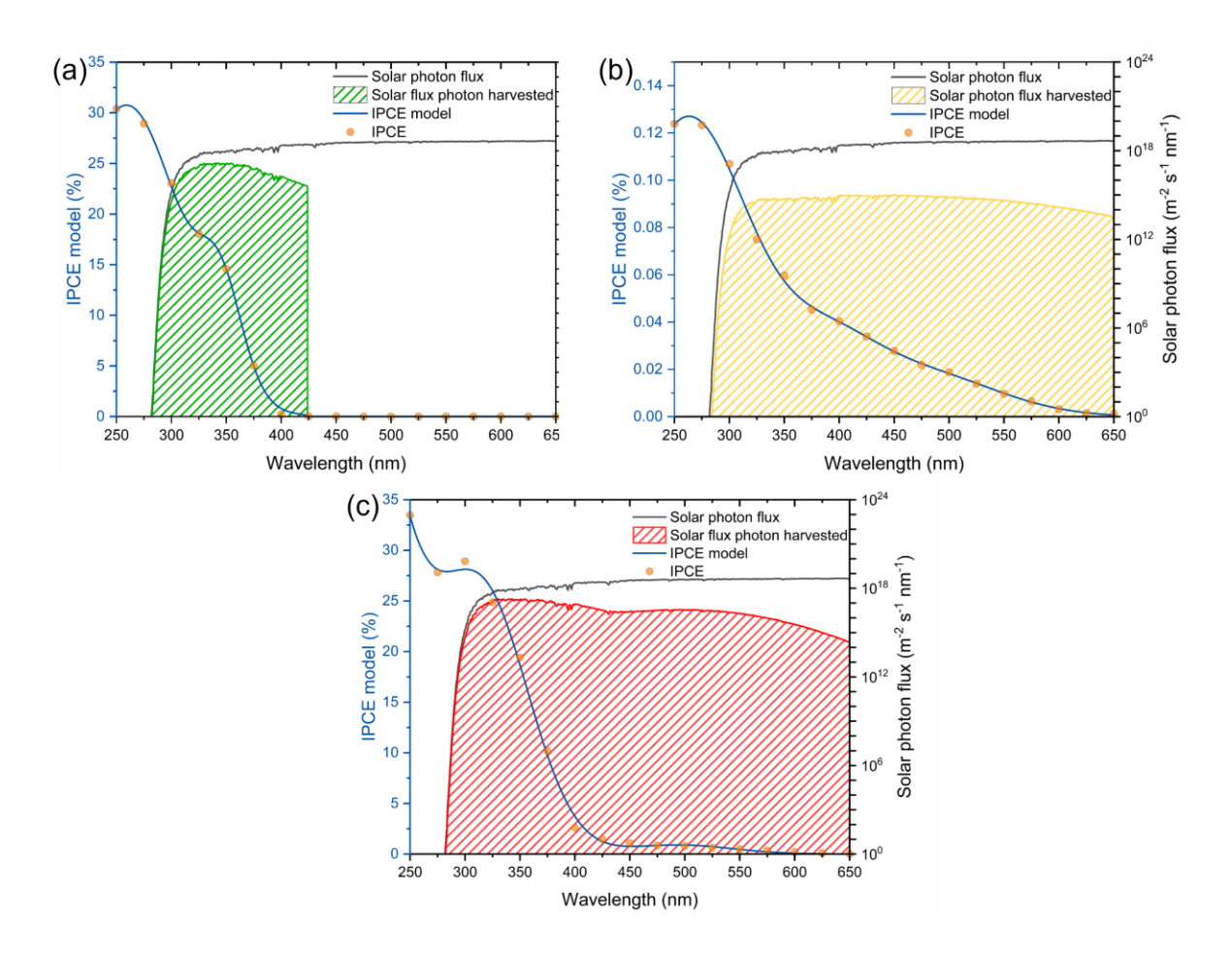


Figure 3-24. TSPs of (a) BiOI, (b) ZnO and (c) ZnO/BiOI under AM 1.5 solar spectrum when the applied voltage was held at 1.23  $V_{RHE}$ , with all ZnO layers grown from 0.5 g  $Zn(OAc)_2 \cdot 2H_2O$  at 350 °C.

Table 3-2. A summary of the PEC water oxidation performance of selected studies using ZnO, BiOI and ZnO/BiOI.

Material	Film fabrication method	Photocurrent density	Onset potential	Testing condition	Light source	Reference
ZnO	AACVD	0.12 mA·cm·² at 1.23 V (vs. RHE)	0.3 V (vs. RHE)	0.5 M Na₂SO₄	AM1.5	This work
ZnO	AACVD	80 μA·cm <sup>-2</sup> at 0.5 V (vs. Ag/AgCl)	-0.32 V (vs. Ag/AgCI)	1 M Na <sub>2</sub> SO <sub>4</sub>	AM 1.5 simulator	65
ZnO	Glancing-angle deposition	142 μA·cm <sup>-2</sup> at 1.0 V	0.2 V (vs. Ag/AgCl)	0.5M NaClO₄	AM 1.5 simulator	66
ZnO	CVD	0.45 mA·cm <sup>-2</sup> at 0.6 V (vs. Ag/AgCl)	-0.31 V (vs. Ag/AgCl)	0.5 M Na <sub>2</sub> SO <sub>4</sub>	365 nm UV illumination	67
BiOI	AACVD	2.8 µA·cm⁻² at 1.23 V (vs. RHE)	0.6 V (vs. RHE)	0.5 M Na <sub>2</sub> SO <sub>4</sub>	AM1.5	This work
BiOI	Spray coating	~0.2 mA·cm <sup>-2</sup> at 1.23 V (vs. RHE)	0.63 V (vs. RHE)	1 M Na₂SO₄	AM 1.5 simulator	11
BiOI	Dip coating	~2 µA·cm <sup>-2</sup> at 0 V (vs. SCE)	ns	0.5 M Na <sub>2</sub> SO <sub>4</sub>	500 W Xe lamp with a cut-off filter (420 nm)	12
BiOI	Electrophoretic deposition	6.56 µA·cm⁻² at 1.23 V (vs. RHE)	ns	0.5 M Na₂SO₄	Solar light simulator with a cut-off filter (420 nm)	68
BiOI	AACVD	0.15 mA⋅cm <sup>-2</sup> at 1 V vs. Ag/AgCI	0 V vs. Ag/AgCl	0.5 M Na <sub>2</sub> SO <sub>4</sub>	AM 1.5 simulator	7
ZnO/BiOI	AACVD	0.27 mA⋅cm <sup>-2</sup> at 1.23 V (vs. RHE)	0.3 V (vs. RHE)	0.5 M Na <sub>2</sub> SO <sub>4</sub>	AM1.5	This work
ZnO/BiOI	Solvothermal method	0.2 mA·cm <sup>-2</sup> at 1.2 V (vs. Ag/AgCl)	ns	0.5 M Na <sub>2</sub> SO <sub>4</sub>	300 W Xe lamp with a cut-off filter (420 nm)	30

ns means not stated

# 3.3.6 Surface roughness

The significant improvement in the PEC performance of the ZnO/BiOI heterojunction has been shown in detail. In this section, the reasons accounting for this improvement were investigated. First, AFM was used to study the surface roughness of the asfabricated films. Because the water oxidation reaction takes place on the surface of

the photoelectrodes, the surface properties might have some impact on the final performance of the films. The roughness factors of the ZnO, BiOI and ZnO/BiOI films were ~1.04, ~1.76 and ~1.14 respectively (project areas are all  $5 \times 5 \ \mu m^2$ ), as determined from AFM (Figure 3-25). Normally, a rougher surface of the material is likely to influence its PEC performance positively. However, in this work, the BiOI film had the poorest activity but the roughest film surface. In addition, even if the ZnO/BiOI heterojunction had a similar surface roughness to the single-layer ZnO film, it showed a more than double improvement in the solar activity. This indicates that the difference in surface roughness cannot account for the improved PEC performance of films deposited in this work.

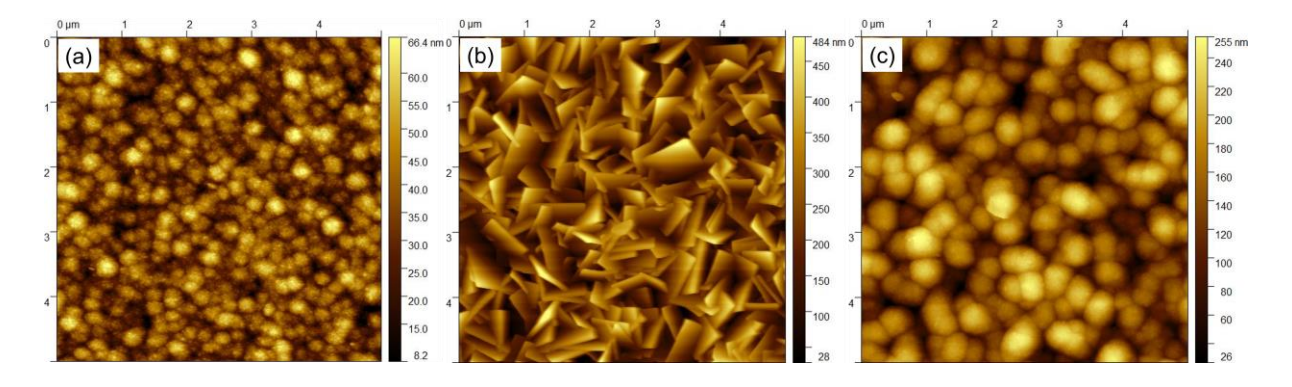


Figure 3-25. AFM images of ZnO, BiOI, and ZnO/BiOI films deposited on FTO, with all ZnO layers grown from 0.5 g Zn(OAc)<sub>2</sub>·2H<sub>2</sub>O at 350 °C.

# 3.3.7 Photoluminescence spectroscopy and transient absorption spectroscopy

PL spectroscopy was used to assess the recombination rate of photogenerated charge carriers, which is an important factor influencing the PEC properties of semiconductors. A higher PL peak intensity generally means a higher charge recombination rate. Under the excitation wavelength of 325 nm, the PL spectra of the ZnO/BiOI heterojunction and parent materials were collected at room temperature and shown in Figure 3-26. High PL emission intensity was observed for the ZnO film, with two peaks at ~400 nm and ~570 nm respectively. Similar PL spectra have also been reported in other literature. The peak at ~400 nm was due to the recombination of near-band-edge excitons, while the other peak originated from the defects in the ZnO film, such as oxygen and zinc vacancies. Compared with ZnO, the BiOI film showed negligible PL

peak intensity, which was reasonable due to the indirect band gap nature of BiOI. A similar observation has been reported as well.<sup>71</sup>

In addition, the steady-state PL signals of the ZnO/BiOI heterojunction were lower than the single-layer ZnO film under the same excitation condition, which indicated a reduced electron-hole recombination rate and was in line with the results in JV curves. Because BiOI showed extreme low fluorescent, and the ZnO layer of the ZnO/BiOI heterojunction absorbed all light with 325 nm wavelength, which could be seen in the transmittance spectra (Figure 3-16a), the PL spectrum of the ZnO/BiOI heterojunction only showed features from ZnO. The weaker PL signal of the ZnO/BiOI heterojunction than that of pure ZnO was clear evidence for the reduced recombination of photogenerated electrons and holes in the heterojunction due to the charge transfer between layers, which also backed our assumption that the improved PEC activity of the ZnO/BiOI heterojunction was because of the spatial separation of photogenerated charge carriers across the layers of the material and the increased charge carrier lifetime.

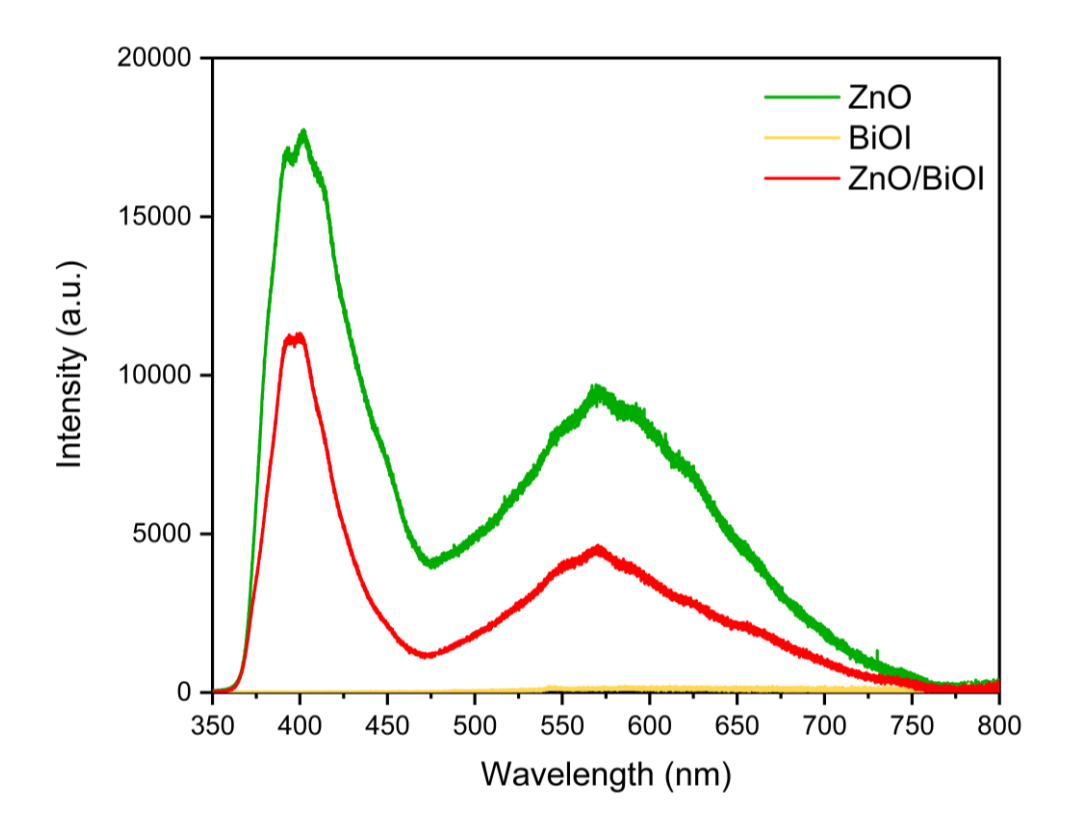


Figure 3-26. PL spectra of ZnO, BiOI, and ZnO/BiOI, with all ZnO layers grown from 0.5 g Zn(OAc)<sub>2</sub>-2H<sub>2</sub>O at 350 °C. The excitation wavelength was 325 nm.

Transient absorption spectroscopy (TAS) measurements were carried out to study the charge carrier dynamics in the ZnO, BiOI and ZnO/BiOI films, the "temporal" and "spectral" behavior of photogenerated charge carriers in the heterojunction could be analyzed. The temporal features, the decay kinetics, observed in the TAS measurements provide information about the lifetimes and recombination processes of photogenerated charge carriers. In addition, the spectral characterizations are influenced by the population or depopulation of photogenerated charge carriers, so contributing to the understanding of the charge separation processes in the heterojunction.<sup>72</sup>

First, the transient absorption decay kinetics from 10 µs to 1 s are shown in Figure 3-27. In the electromagnetic spectrum of the ZnO film, there was almost no signals in the blue region (the probe wavelength of 550 nm), but bleach signals with long lifetime were seen in the red region (the probe wavelength of 1100 nm) (Figure 3-27a). The loss in ground state absorption could lead to the stronger bleach signals.<sup>72</sup> These weak bleach signals (maximum at around -0.01 mΔO.D.) declined to half of the initial intensity in ~200 ms (t<sub>50%</sub>). These observations were comparable with TAS studies of ZnO thin films reported previously.<sup>73</sup> For the BiOI film, stronger transient absorption was observed in the blue region (maximum at around 0.13 mΔO.D.) than in the red region (maximum at around 0.02 mΔO.D.) (Figure 3-27b). Different from the ZnO film, there was no bleach signals in the BiOI film. In addition, the decay of signals from BiOI showed the power law behaviour, indicating the appearance of the recombination mediated by traps in BiOI.74 The t<sub>50%</sub> of these signals was ~60 µs. Little transient absorption studies of BiOI in long timescale has been reported, but most attention were paid to the behaviour of BiOI in ultrafast timescale (fs to ns).<sup>75–77</sup> However, slow timescale studies were carried out where the p-type BiOI was as the photocathode.<sup>78</sup> The bleach signals of the p-type BiOI were collected through the visible region, being strongest in the blue region and decaying with a t<sub>50%</sub> of ~20 µs. In another report, a significantly faster decay in BiOI powders was found in the sulfite solution, with a t<sub>50%</sub> of around 0.5 µs.<sup>79</sup> Interestingly, a composite behavior between that of ZnO and BiOI was observed in the ZnO/BiOI heterojunction (Figure 3-27c). Like the single-layer BiOI film, a strong absorption was observed in the blue region (maximum at around 0.12 m $\Delta$ O.D in ZnO/BiOI, and the signals decayed with a close  $t_{50\%}$  (~40  $\mu$ s). On the

contrary, bleach signals with long lifetime ( $t_{50\%} = \sim 300$  ms) were showed in the red region, which was like the single-layer ZnO film.

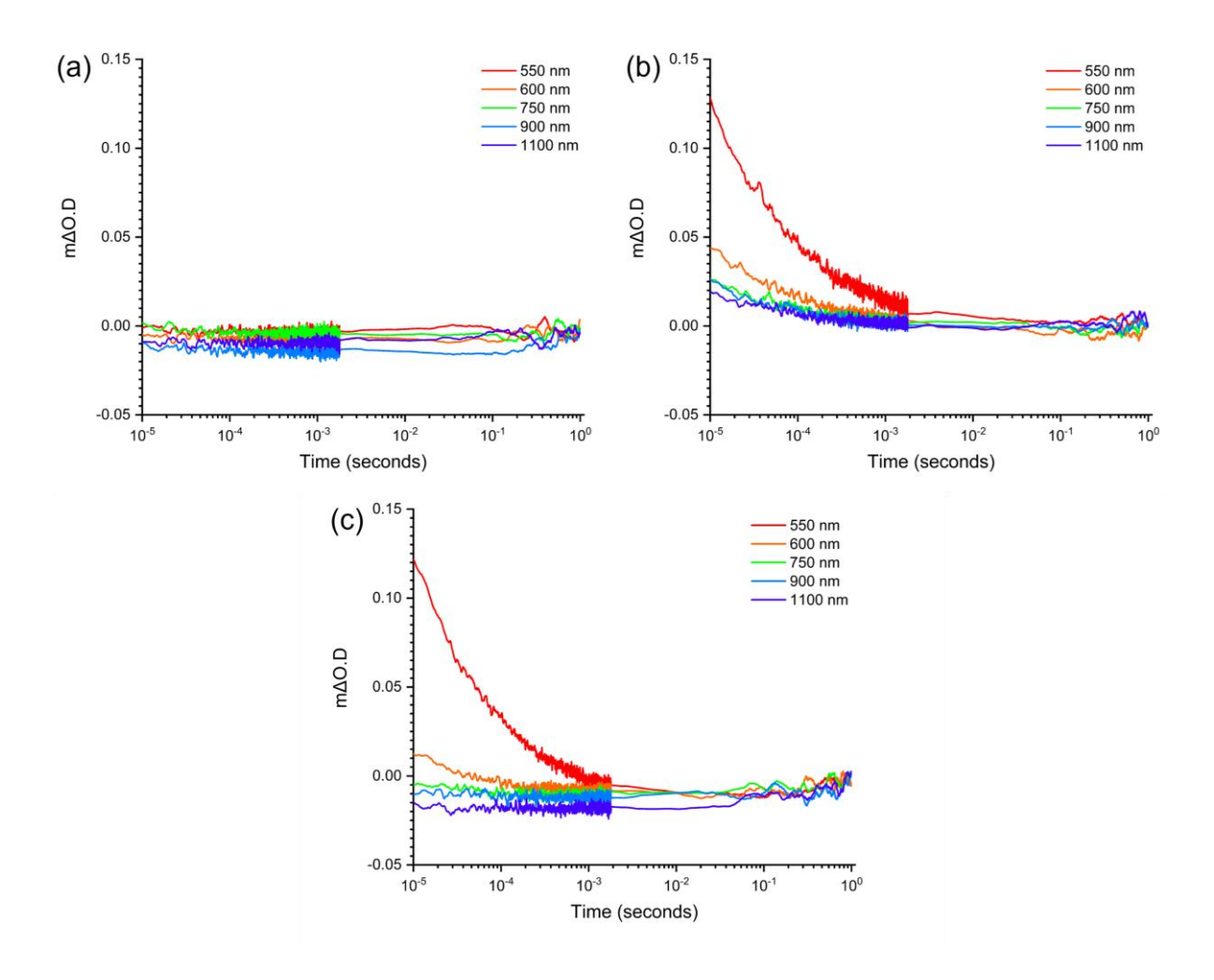


Figure 3-27: Transient absorption decay kinetics of (a) ZnO, (b) BiOI and (c) ZnO/BiOI films deposited on FTO from 10 μs after the laser pulse until 1 s, measured at select probe wavelengths from 550 to 1100 nm. The excitation wavelength was 355 nm. The pulse width was ~6 ns. All ZnO layers were grown from 0.5 g Zn(OAc)<sub>2</sub>·2H<sub>2</sub>O at 350 °C.

The transient absorption spectra for the ZnO, BiOI and ZnO/BiOI films are shown in Figure 3-28. The single-layer ZnO film exhibited weak and broad bleach signals within the visible region as previously mentioned, with the strongest signal at ~900 nm (Figure 3-28a). Strong and positive transient absorption signals were seen in the blue region for the BiOI film, while the signal became weaker in the red region (Figure 3-28b). Furthermore, there was a hybrid spectrum of ZnO and BiOI observed for the

ZnO/BiOI heterojunction at early timescales (10–100 µs), but the transient absorption signals bleached totally by 10 ms (Figure 3-28c).

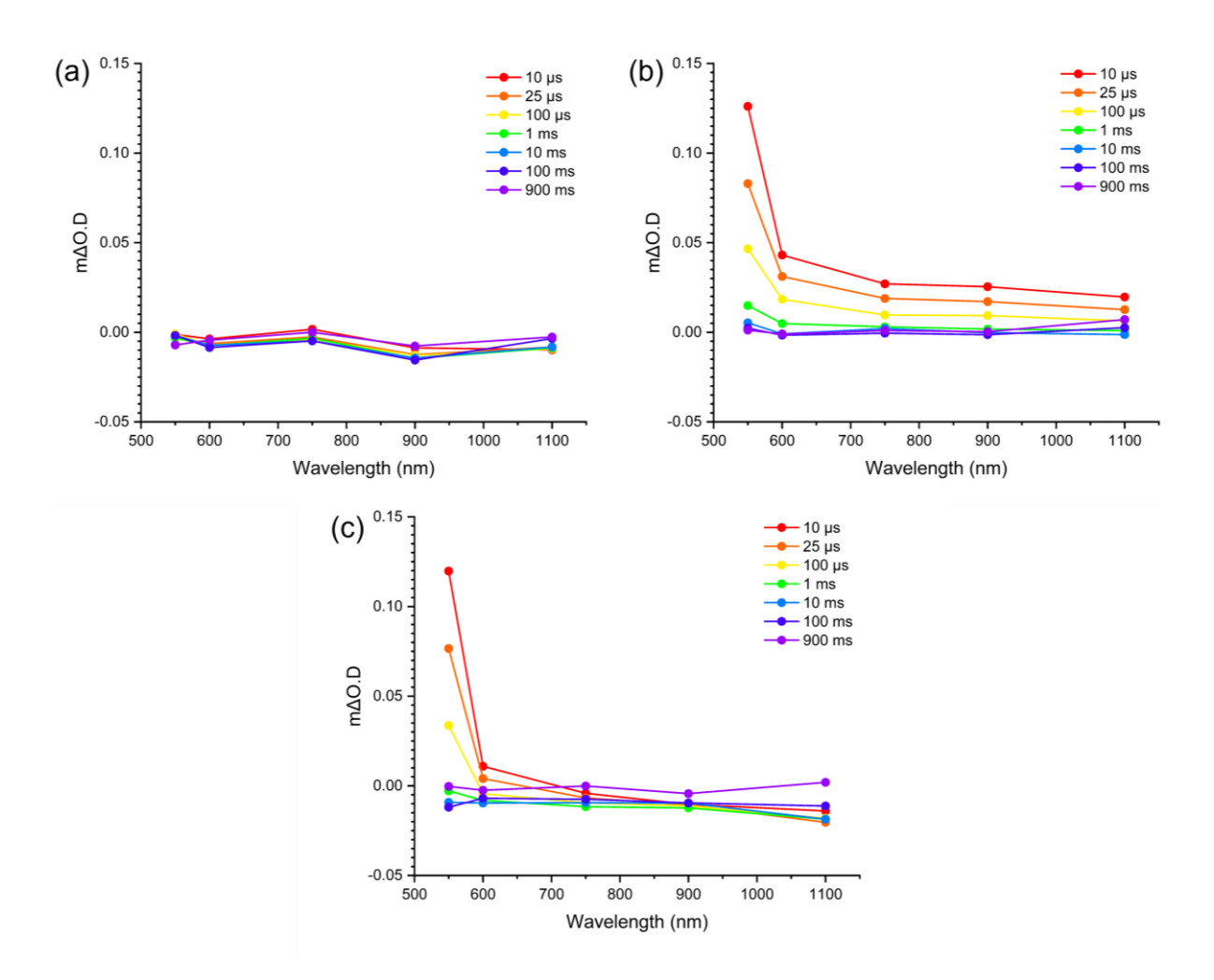


Figure 3-28: Transient absorption spectra of (a) ZnO, (b) BiOI and (c) ZnO/BiOI films deposited on FTO at select times from 10 μs after the laser pulse until 900 ms, measured at select probe wavelengths from 550 to 1100 nm. The excitation wavelength was 355 nm. The pulse width was ~6 ns. All ZnO layers were grown from 0.5 g Zn(OAc)<sub>2</sub>·2H<sub>2</sub>O at 350 °C.

The comparison of transient absorption decay kinetics with the probe wavelengths of 550 nm and 1100 nm are shown in Figure 3-29. It should be noted that only around 50% pump excitation could be used in the TAS measurement due to absorbance by the ZnO film, but 100% pump excitation was able to be utilized by the BiOI film based on the analysis of the UV-Vis transmission spectra (Figure 3-16a). This meant that the same quantity of light was absorbed by the single-layer ZnO film and the top ZnO layer

of the heterojunction. However, compared with the single-layer BiOI film, only half amount of the light was absorbed by the bottom BiOI layer of the heterojunction. At the probe wavelength of 550 nm, strong positive signals were seen at early timescales (~10 μs) in both BiOI and ZnO/BiOI (Figure 3-29a), where around 50% less pump excitation arrived at the bottom BiOI layer in the heterojunction than the single-layer BiOI film. In addition, at the probe wavelength of 1100 nm, nearly double intensity of bleach signals were seen at early timescales (~10 μs) in ZnO/BiOI compared with ZnO (Figure 3-29b). To sum up, the above observations indicated that the populations of charge carriers in the ZnO/BiOI heterojunction were approximately twice larger than parent materials at early timescales, considering their differences in the pump light absorption. It was demonstrated that the separation of charge carriers in the ZnO/BiOI heterojunction was improved. Whereas similar decay behaviors in the heterojunction and parent materials indicated that recombination kinetics of charge carriers in the respective layers of the heterojunction were almost unchanged compared with parent materials.

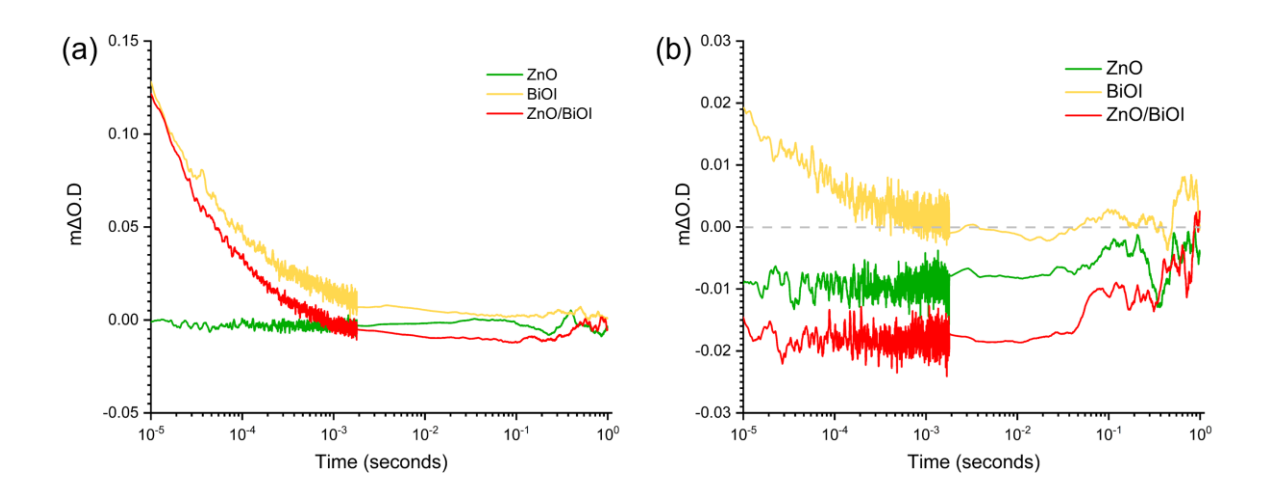


Figure 3-29: Transient absorption decay kinetics for the ZnO, BiOI and ZnO/BiOI films deposited on FTO, measured at the probe wavelengths (a) 550 nm and (b) 1100 nm from 10 μs after the laser pulse until 1 s. The excitation wavelength was 355 nm. The pulse width was ~6 ns. All ZnO layers were grown from 0.5 g Zn(OAc)<sub>2</sub>·2H<sub>2</sub>O at 350 °C.

## 3.3.8 Stability test

The stability of photoanodes is important in their practical PEC applications. Therefore, the stability of the ZnO/BiOI heterojunction and parent materials was measured for 1.5

hours in the 0.5M Na<sub>2</sub>SO<sub>4</sub> aqueous solution with the applied voltage of 1.23 V<sub>RHE</sub> (Figure 3-30). The BiOI film showed the worst stability among all tested samples. The photocurrent density of BiOI dropped dramatically in first 100 s, and at the end of the test, the photocurrent density reduced by ~90%. This poor stability was expected and in accordance with other literatures because of the serious photocorrosion of BiOI.<sup>7,11</sup> Furthermore, it was observed that the ZnO/BiOI heterojunction had a similar stability compared with the single ZnO film, where the photocurrent density of both samples presented a rapid decline in first 800 s. After 1.5 hours, the photocurrent density of ZnO/BiOI and ZnO dropped to ~18% and ~13% respectively.

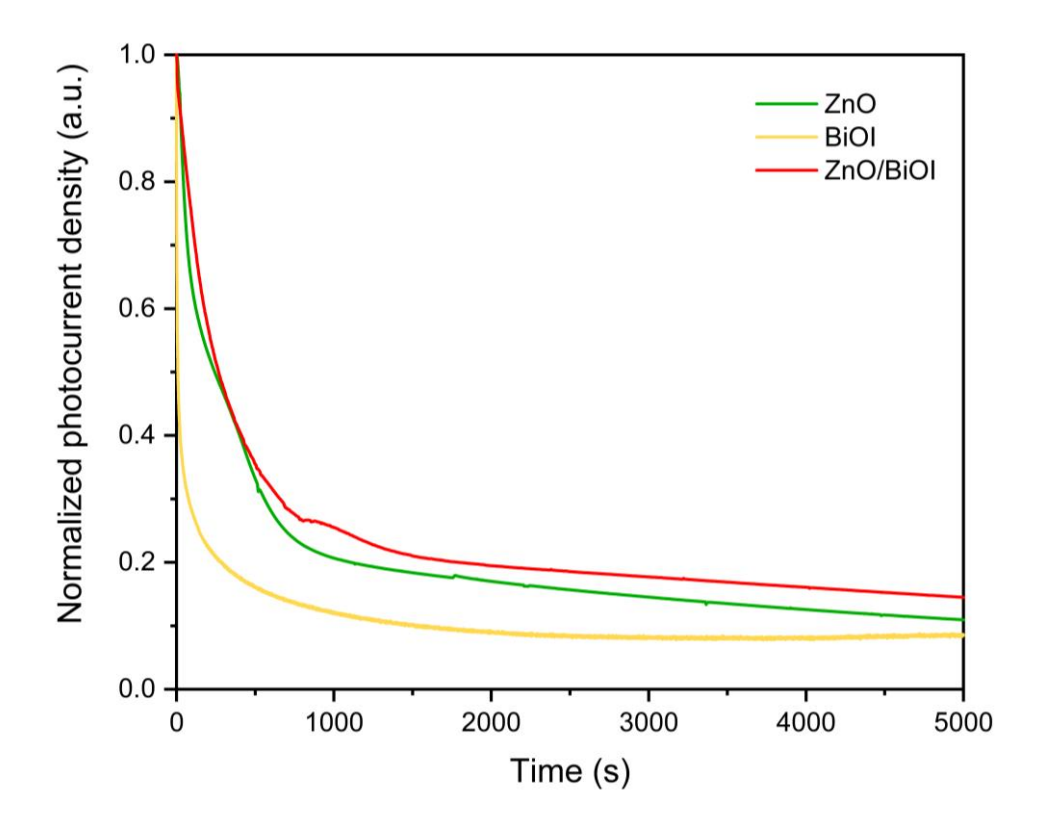


Figure 3-30. Stability of ZnO, BiOI, and ZnO/BiOI photoanodes at 1.23 V<sub>RHE</sub>, under the action of light (350 nm, 2.58 mW·cm<sup>-2</sup>).

JV curves (Figure 3-31) were measured before and after the 1.5-hour stability test to study the stability of samples further. In Figure 3-31, it can be observed that the photocurrent density of ZnO/BiOI and parent materials all decreased a lot after the1.5-hour stability test, which was consistent with the results in the stability test. Under the action of light, the photocurrent density of ZnO, BiOI and ZnO/BiOI dropped from 0.390 mA·cm<sup>-2</sup> to 0.165 mA·cm<sup>-2</sup>, from 0.035 mA·cm<sup>-2</sup> to 0.026 mA·cm<sup>-2</sup>, and from 1.441

mA·cm<sup>-2</sup> to 0.723 mA·cm<sup>-2</sup> individually at the applied voltage of 1.23 V<sub>RHE</sub>, while the onset potentials kept unchanged.

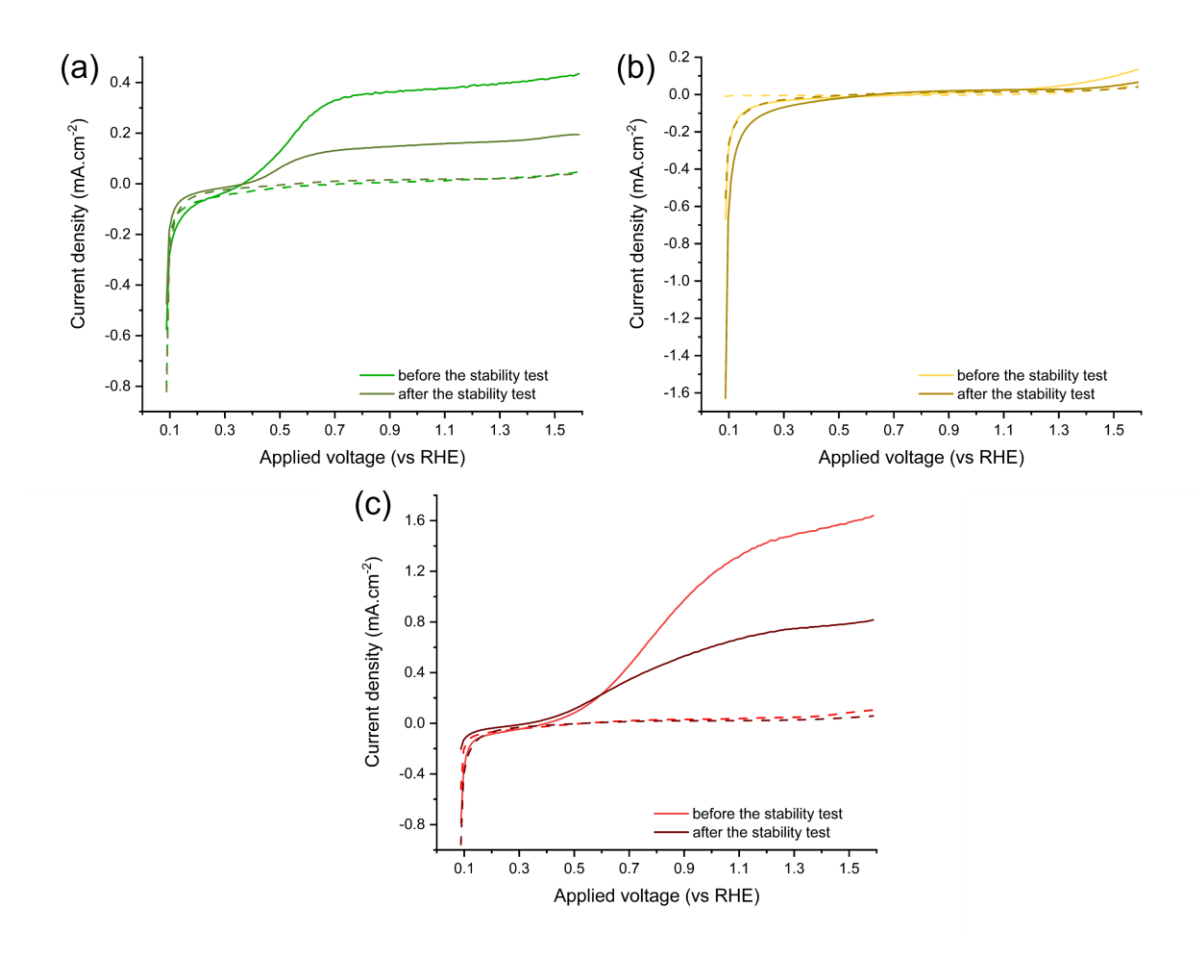


Figure 3-31. JV curves of (a) ZnO, (b) BiOI and (c) ZnO/BiOI films deposited on FTO were measured in the dark (dashed lines) and under the action of light (1 sun illumination, solid lines) before and after the 1.5-hour stability test. The voltage was swept from 0.10 V<sub>RHE</sub> to 1.60 V<sub>RHE</sub> at a rate of 10 mV·s<sup>-1</sup>.

In addition, the pre- and post-stability test GIXRD patterns were obtained to investigate the variation in film composition (Figure 3-32). It was shown that the relative peak intensity between the ZnO phase and FTO substrate decreased after the stability test (Figure 3-32a), indicating that ZnO was dissolved in the electrolyte. However, in Figure 3-32b, there was no visible change in the relative peak intensity for the single-layer BiOI film. In the ZnO/BiOI heterojunction, the relative peak intensity from ZnO was weaker and peaks from BiOI slightly changed (Figure 3-32c).

Both ZnO and BiOI suffered from the hole-induced photocorrosion in aqueous electrolytes. 11,80 There are two possible decomposition ways for ZnO in PEC water splitting, which restricts the stability of ZnO severely. Firstly, ZnO would dissolve with the pH of the electrolyte decreased. As water oxidized in the photo-electrocatalytic process, the local pH at the photoanode will become slightly acidic. This will dissolve ZnO by corrosion, where the reaction is

$$ZnO + 2H^+ \rightarrow Zn^{2+} + H_2O$$
 (1)

In addition, it has been reported that ZnO suffers from photoinduced dissolution. Photocorrosion will occur when ZnO is photoexcited, where the photogenerated holes could lead to the structural collapse of ZnO.<sup>80,81</sup> The overall reaction can be described as

$$2ZnO + h^+ \rightarrow 2Zn^{2+} + O_2$$
 (2)

As a result, in the photocorrosion process of ZnO, only soluble Zn<sup>2+</sup> will be generated, which explains why the peak intensity in GIXRD patterns was reduced but no extra peaks were observed. In addition, it has been reported that for BiOI, a surface layer of bismuth hydroxide might form on the film surface when BiOI is exposed to aqueous electrolytes, which could act as an insulating layer, leading to the inhibited transfer of charge carriers. However, this compositional change was invisible in XRD patterns.<sup>11</sup> In the heterojunction structure, ZnO was deposited on top of the BiOI layer. Therefore, the stability of the ZnO/BiOI heterojunction is mainly determined by the top ZnO layer.

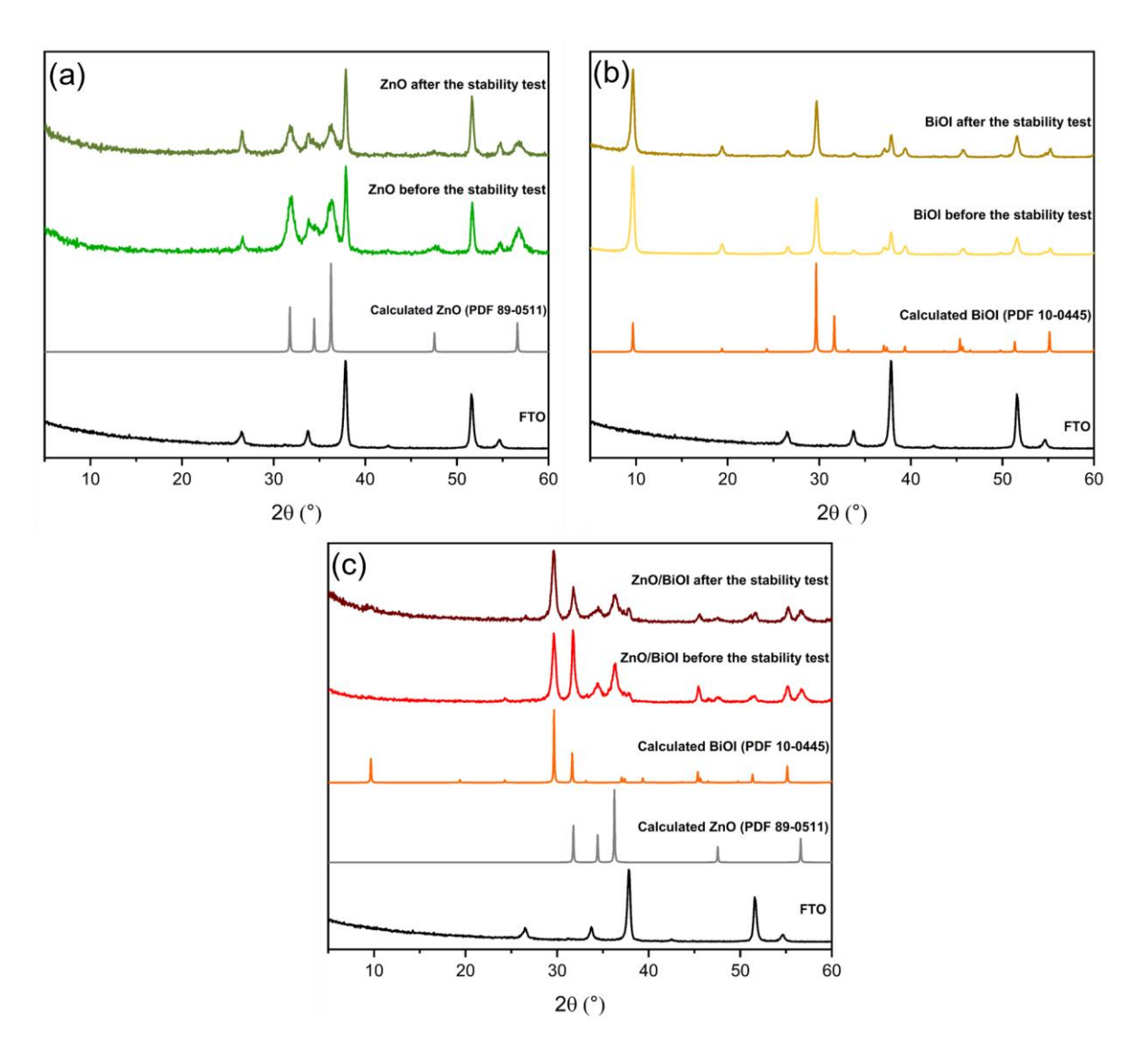


Figure 3-32. GIXRD patterns of (a) ZnO, (b) BiOI and (c) ZnO/BiOI deposited on FTO before and after the 1.5-hour stability test.

## 3.3.9 Faradaic efficiency measurements

The faradaic efficiency (FE) of ZnO/BiOI and ZnO in the process of PEC water oxidation was measured (Figure 3-33 and Figure 3-34). However, the poor intrinsic stability of ZnO and BiOI did not allow us to carry out these measurements before the materials corroded. It is extremely challenging to measure O<sub>2</sub> evolution rates for photoanodes of limited stability as materials often degrade before significant volumes of this gas can be evolved. Moreover, as can be seen from reaction (2), adventitious gases (O<sub>2</sub>) can also be produced from the decomposition of the photoelectrode itself.<sup>80,81</sup> During measurements, relatively low light intensity (4 mW) was chosen to minimise the rate of photocorrosion. Despite the low photocurrent produced in Figure

3-33a, the photocurrent decayed rapidly within 1h. Integrating the photocurrent and converting the charge to a predicted volume of O<sub>2</sub> assuming 100% FE gave a total of ~6 μL of O<sub>2</sub> (Figure 3-33b). By injecting a known amount of O<sub>2</sub> into the sample headspace, the voltage response was able to be converted into a volume of O<sub>2</sub> (Figure 3-33c). The result is shown in Figure 3-33d, indicating that much more O<sub>2</sub> was produced than could be accounted for by the photocurrent. The overproduction of O<sub>2</sub> was attributed to the photocorrosion of ZnO in the ZnO/BiOI heterojunction during the measurement. This hypothesis was confirmed further by measuring anomalous O<sub>2</sub> generation from the ZnO film, as shown in Figure 3-34. Consequently, it was not possible to calculate FE for the samples studied herein until stability issues are solved.

The stability of ZnO strongly depends on the pH of the electrolyte. <sup>82</sup> Due to the serious photocorrosion of ZnO in neutral electrolytes, such as Na<sub>2</sub>SO<sub>4</sub>, this challenge in the FE measurement was also met by others in the literature, <sup>83–85</sup> where the mass corrosion of ZnO was observed in 60 mins or less. The FE of ZnO for PEC water splitting has been reported by others, <sup>86–88</sup> where alkaline electrolytes were used in all cases. However, also suffering from a degree of instability in the alkaline electrolyte, the FE of ZnO was seen to decrease from 85% to 45% during the 150 min measurement process. <sup>86</sup>

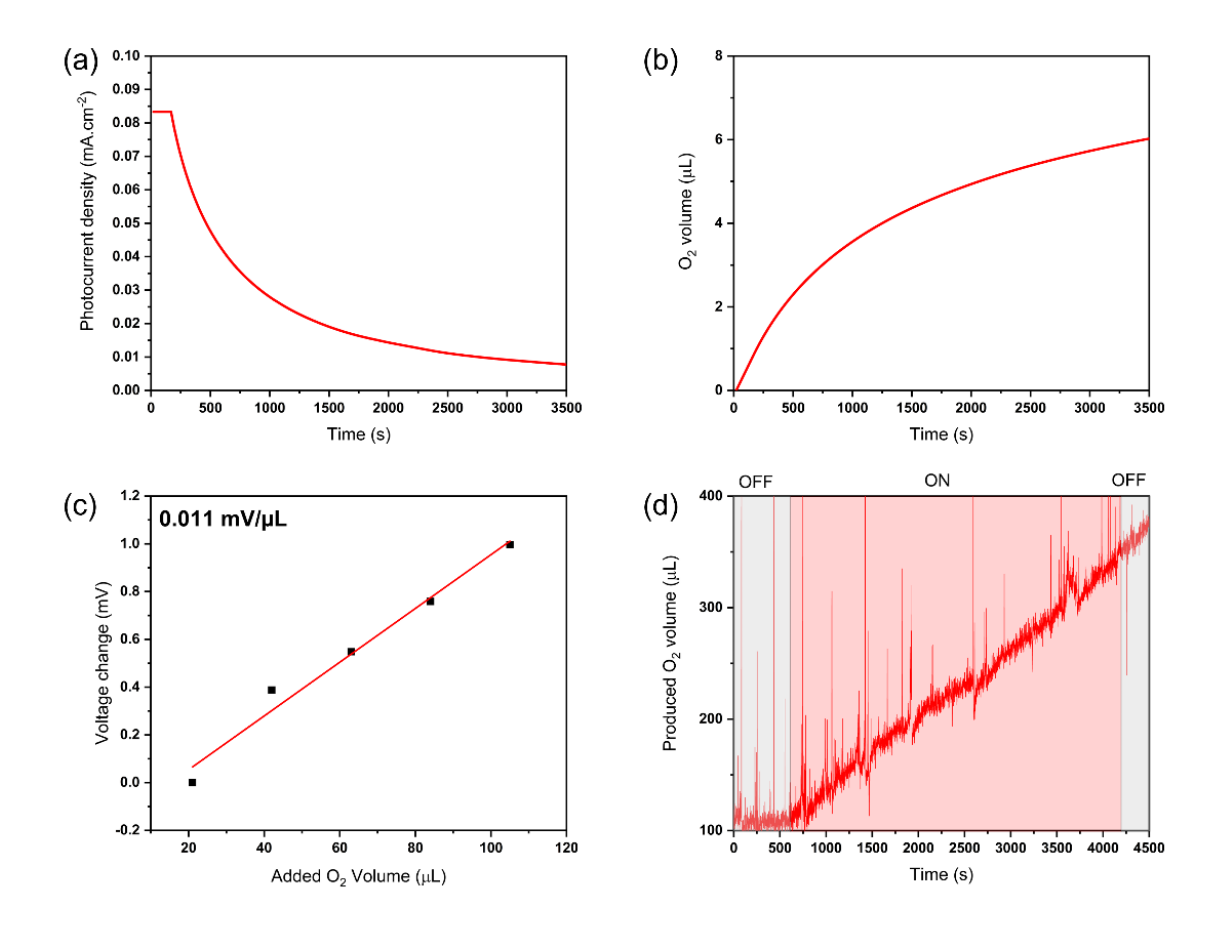


Figure 3-33. (a) Photocurrent vs. time plots of the ZnO/BiOI photoanode at a constant potential of 1.0 V vs. Ag/AgCI. (b) Theoretical O<sub>2</sub> yield calculated from photocurrent. (c) Liner calibration of voltage vs. O<sub>2</sub> volume. (d) Experimental O<sub>2</sub> yield of ZnO/BiOI. Grey and red areas correspond to irradiation light off and on respectively.

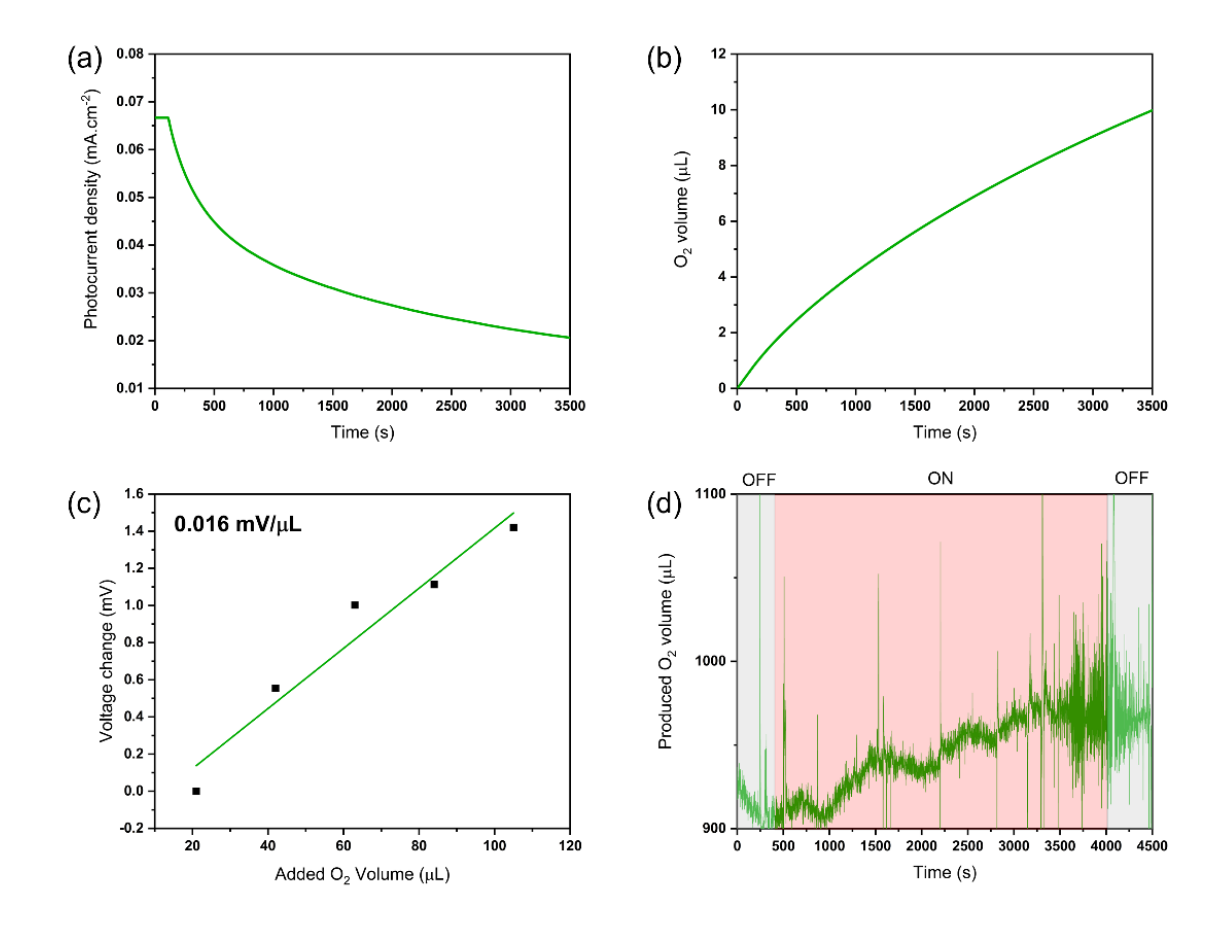


Figure 3-34. (a) Photocurrent vs. time plots of the ZnO photoanode at a constant potential of 1.0 V vs. Ag/AgCl. (b) Theoretical O<sub>2</sub> yield calculated from photocurrent. (c) Liner calibration of voltage vs. O<sub>2</sub> volume. (d) Experimental O<sub>2</sub> yield of ZnO. Grey and red areas correspond to irradiation light off and on respectively.

#### 3.3.10 TiO<sub>2</sub>/BiOI heterostructure

In addition to ZnO, another kind of semiconductor with a wide band gap, namely TiO<sub>2</sub>, was also attempted to be combined with BiOI to build up a heterojunction, where BiOI was at the bottom while TiO<sub>2</sub> was on the top. In the GIXRD patterns of single-layer TiO<sub>2</sub> and BiOI films on FTO, only peaks from tetragonal anatase phase (*PDF 21-1272*) and tetragonal BiOI phase (*PDF 10-0445*) were exhibited respectively (Figure 3-35). In addition, strong and sharp peaks from TiO<sub>2</sub> were observed in the TiO<sub>2</sub>/BiOI heterojunction, and a small peak from BiOI at 29.6° could be seen as well. Therefore, it can be determined from GIXRD patterns that both BiOI and TiO<sub>2</sub> were deposited successfully in the form of single layers and the heterojunction *via* AACVD.

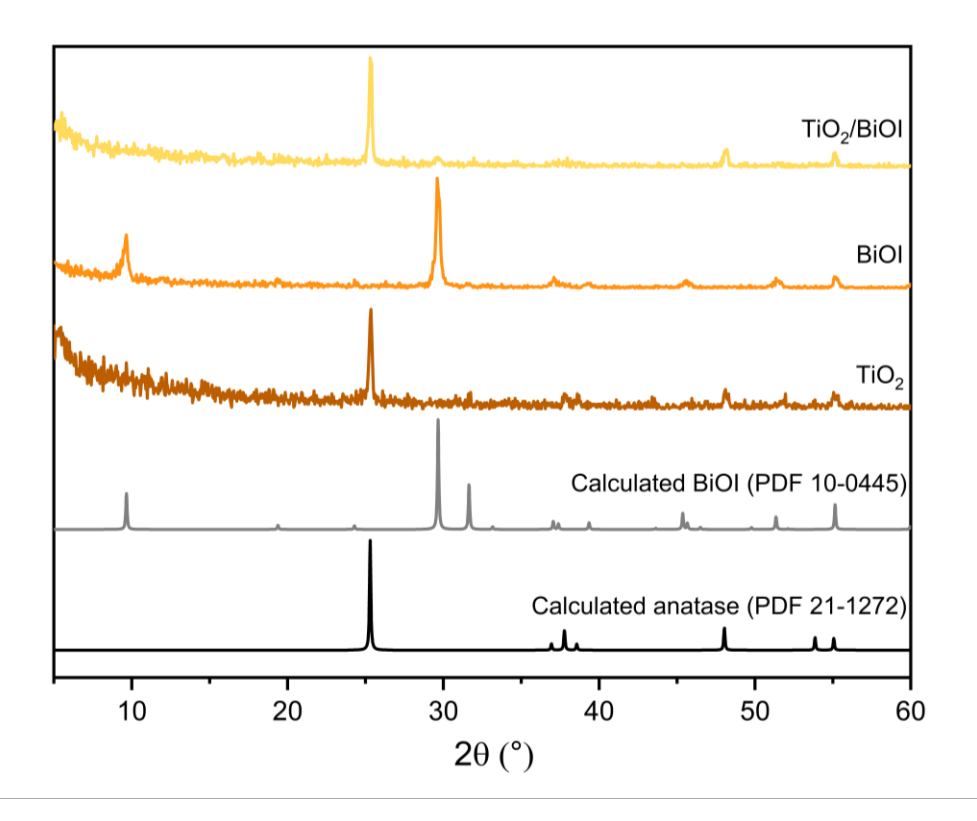


Figure 3-35. GIXRD patterns of TiO<sub>2</sub>, BiOI and TiO<sub>2</sub>/BiOI films deposited on FTO.

The PEC activities of obtained TiO<sub>2</sub>, BiOI and TiO<sub>2</sub>/BiOI films as photoanodes were investigated firstly by *JV* curves (Figure 3-36), where *JV* curves were measured in the dark and under the action of light with sweeping the applied voltage 0.10 V<sub>RHE</sub> to 1.60 V<sub>RHE</sub>. Under 1 sun irradiation, as discussed above, BiOI still showed a low photocurrent of 0.02 mA·cm<sup>-2</sup> at 1.10 V<sub>RHE</sub>, with the onset potential of 0.60 V<sub>RHE</sub>. For the TiO<sub>2</sub> film, the onset potential was around 0.32 V<sub>RHE</sub>, and the photocurrent density reached to 0.15 mA·cm<sup>-2</sup> at 1.10 V<sub>RHE</sub>. With the same onset potential with the single-layer TiO<sub>2</sub>, the TiO<sub>2</sub>/BiOI heterojunction exhibited a photocurrent density of 0.21 mA·cm<sup>-2</sup> at 1.10 V<sub>RHE</sub>. Unlike the significant improvement observed in the ZnO/BiOI heterojunction and parent materials, the PEC water oxidation activity of the TiO<sub>2</sub>/BiOI heterojunction was only enhanced 1.4 times compared with intrinsic TiO<sub>2</sub>.

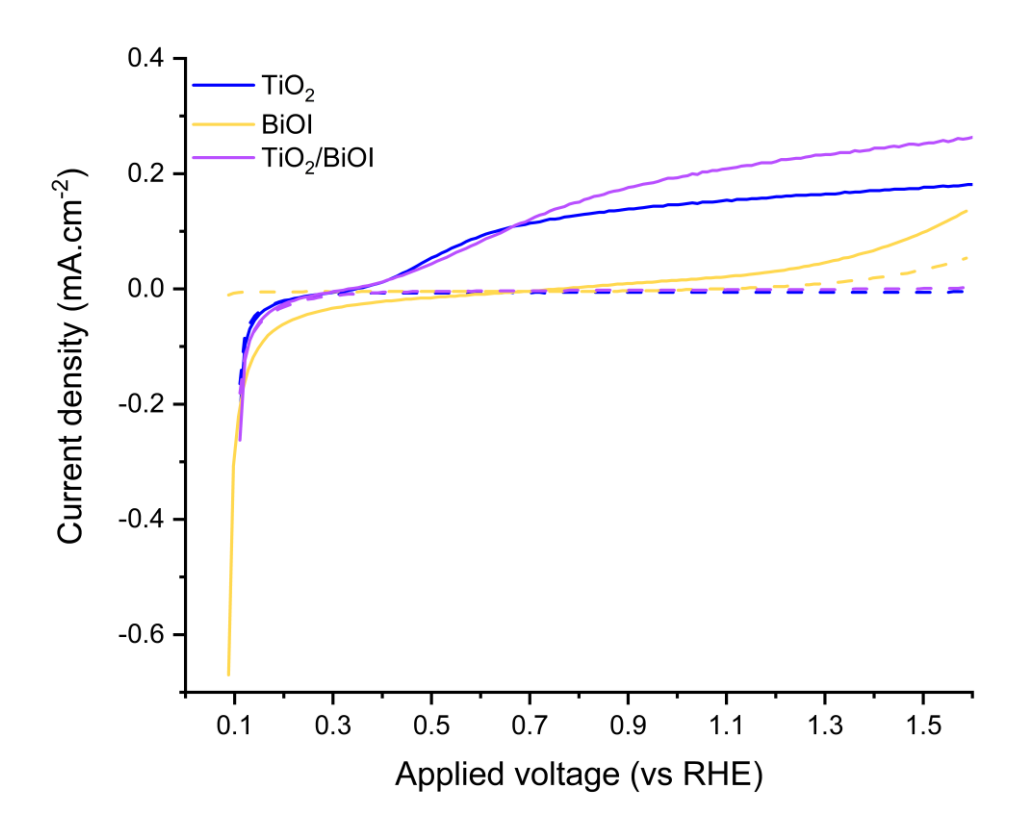


Figure 3-36. JV curves of TiO<sub>2</sub>, BiOI and TiO<sub>2</sub>/BiOI films deposited on FTO were measured in the dark (dashed lines) and under the action of light (1 sun illumination, solid lines). The voltage was swept from 0.10 V<sub>RHE</sub> to 1.60 V<sub>RHE</sub> at a rate of 10 mV·s<sup>-1</sup>.

Furthermore, IPCE measurements were processed for TiO<sub>2</sub>, BiOI and TiO<sub>2</sub>/BiOI films (Figure 3-37). Compared with the single-layer TiO<sub>2</sub>, a slight improved efficiency was observed for the TiO<sub>2</sub>/BiOI heterojunction in the UV range. Although the IPCE of the TiO<sub>2</sub>/BiOI showed a visible increase in the visible range, it was still far less than that of the ZnO/BiOI heterojunction. Therefore, based on this less impressive PEC performance, there were no more detailed characterizations on the TiO<sub>2</sub>/BiOI heterojunction.

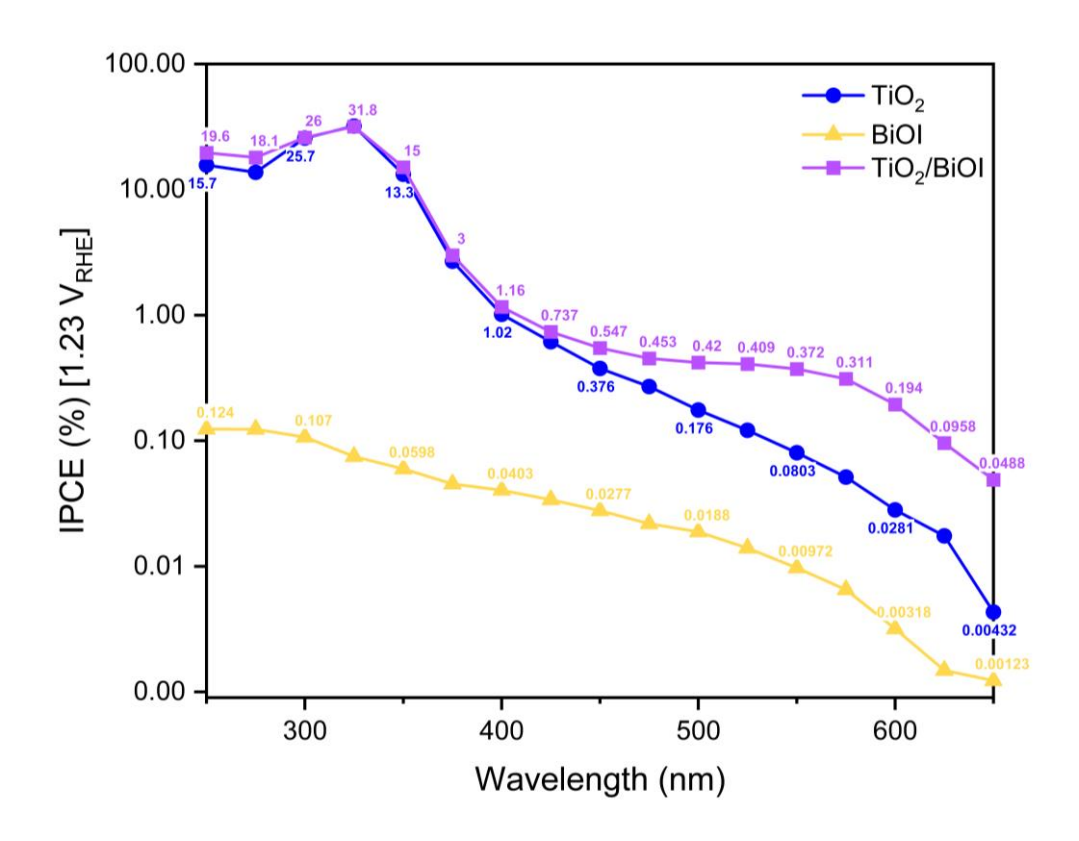


Figure 3-37. IPCE for TiO<sub>2</sub>, BiOI, and TiO<sub>2</sub>/BiOI films deposited on FTO.

Several reasons could explain why no ideal improvement in the PEC activity occurred when combining TiO<sub>2</sub> and BiOI to build a heterojunction. Firstly, energy band alignment is an important factor, which needs to be considered in the heterojunction construction. As determined in the GIXRD patterns (Figure 3-35), TiO<sub>2</sub> deposited in this work was in the anatase phase, so its VBM and CBM is 2.60 eV and -0.60 eV.89 As shown in Figure 3-2, the CBMs of BiOI and ZnO were 0.60 eV and -0.21 eV, respectively. In addition, the VBMs of BiOI and ZnO were 2.39 eV and 3.11 eV, respectively. It has been reported that under visible light irradiation with energy less than 2.95 eV, electrons in the VB of BiOI could be excited to -0.56 eV, which was more negative than the potential of the original CBM.90 In this situation, stagger VB and CB positions could be formed between BiOI and ZnO. Therefore, in the ZnO/BiOI heterojunction, photogenerated electrons in the CB of BiOI could easily transfer to the CB of ZnO and holes would be left in the VB, which would be able to effectively separate the photogenerated electrons and holes, leading to the dramatically improved PEC performance. However, due to the more negative CBM of TiO<sub>2</sub> than BiOI, the stagger band alignment would not appear in the TiO<sub>2</sub>/BiOI heterojunction.

Secondly, it has been previously reported that, compared with 350 °C, TiO<sub>2</sub> thin films deposited at 400 °C showed a better performance in PEC applications. <sup>91</sup> Nevertheless, the deposition temperature below 400 °C had to be used in this work to avoid the decomposition of BiOI. Therefore, the optimized PEC activity might not be able to be obtained for the TiO<sub>2</sub>/BiOI heterojunction. Furthermore, the single-layer TiO<sub>2</sub> film was less active in PEC measurements than the single-layer ZnO film deposited at the same temperature *via* AACVD, meaning that ZnO was more suitable in the heterojunction construction with BiOI for the improved performance in PEC applications.

## 3.4 Summary

In conclusion, films of ZnO, BiOI and TiO2, and heterojunctions formed by their combinations, BiOI/ZnO, ZnO/BiOI and TiO2/BiOI were successfully prepared by AACVD. Compared with TiO<sub>2</sub>, ZnO showed more potential in the heterojunction construction with BiOI. For the constituted BiOI/ZnO and ZnO/BiOI heterojunctions, their composition, clear bilayer structures and optical properties were characterized by GIXRD, XPS, SEM and UV-Vis spectroscopy. Although the BiOI/ZnO structure was far less active, the ZnO/BiOI heterojunction showed a dramatically improved activity in the PEC water oxidation compared with parent materials. Through investigating the influence of deposition temperatures and film thickness, the ZnO/BiOI heterojunction composed of 390 nm thick BiOI film deposited at 300 °C and 120 nm thick ZnO film deposited at 350 °C was found to have the optimized PEC performance. The TSP of the ZnO/BiOI heterojunction was 0.271 mA·cm<sup>-2</sup>, which was around 100 and 2.2 times higher than that of intrinsic BiOI (0.0028 mA·cm<sup>-2</sup>) and ZnO (0.121 mA·cm<sup>-2</sup>), respectively. Based on the overall analysis of transmission spectroscopy, PL and TAS, it was shown that the improved PEC performance observed in the ZnO/BiOI heterojunction contributed to the synergetic effect of enhanced solar absorption in visible range and spatial separation of photogenerated charge carriers between BiOI and ZnO layers in the heterojunction. However, the ZnO/BiOI showed a poor stability in the neutral aqueous electrolyte due to serious photocorrosion, so the deposition of a protective layer on top is possible to make the heterojunction more stable in practical PEC applications.

#### 3.5 Reference

- (1) Moss, B.; Babacan, O.; Kafizas, A.; Hankin, A. A Review of Inorganic Photoelectrode Developments and Reactor Scale-Up Challenges for Solar Hydrogen Production. *Adv Energy Mater* **2021**, *11* (13), 2003286. https://doi.org/10.1002/aenm.202003286.
- (2) Finegold, L.; Cude, J. L. Biological Sciences: One and Two-Dimensional Structure of Alpha-Helix and Beta-Sheet Forms of Poly(L-Alanine) Shown by Specific Heat Measurements at Low Temperatures (1.5-20 K). *Nature* **1972**, *238* (5358), 38–40. https://doi.org/10.1038/238038a0.
- (3) Kafizas, A.; Godin, R.; Durrant, J. R. Charge Carrier Dynamics in Metal Oxide Photoelectrodes for Water Oxidation. In *Semiconductors and Semimetals*; Elsevier, 2017; Vol. 97, pp 3–46. https://doi.org/10.1016/bs.semsem.2017.02.002.
- (4) Bannister, F. A. The Crystal-Structure of the Bismuth Oxyhalides. *Mineral Mag J Mineral Soc* **1935**, 24 (149), 49–58. https://doi.org/10.1180/minmag.1935.024.149.01.
- (5) Mi, Y.; Zhou, M.; Wen, L.; Zhao, H.; Lei, Y. A Highly Efficient Visible-Light Driven Photocatalyst: Two Dimensional Square-like Bismuth Oxylodine Nanosheets. *Dalt Trans* **2014**, *43* (25), 9549–9556. https://doi.org/10.1039/c4dt00798k.
- (6) An, H.; Du, Y.; Wang, T.; Wang, C.; Hao, W.; Zhang, J. Photocatalytic Properties of BiOX (X = Cl, Br, and I). *Rare Metals* **2008**, *27* (3), 243–250. https://doi.org/10.1016/S1001-0521(08)60123-0.
- (7) Bhachu, D. S.; Moniz, S. J. A.; Sathasivam, S.; Scanlon, D. O.; Walsh, A.; Bawaked, S. M.; Mokhtar, M.; Obaid, A. Y.; Parkin, I. P.; Tang, J.; Carmalt, C. J. Bismuth Oxyhalides: Synthesis, Structure and Photoelectrochemical Activity. *Chem Sci* **2016**, *7* (8), 4832–4841. https://doi.org/10.1039/C6SC00389C.
- (8) Zhang, K. L.; Liu, C. M.; Huang, F. Q.; Zheng, C.; Wang, W. D. Study of the Electronic Structure and Photocatalytic Activity of the BiOCl Photocatalyst. *Appl Catal B* **2006**, *68* (3–4), 125–129. https://doi.org/10.1016/J.APCATB.2006.08.002.

- (9) Huang, W. L.; Zhu, Q. Electronic Structures of Relaxed BiOX (X = F, Cl, Br, I) Photocatalysts. *Comput Mater Sci* **2008**, *4*3 (4), 1101–1108. https://doi.org/10.1016/j.commatsci.2008.03.005.
- (10) Kwolek, P.; Szaciłowski, K. Photoelectrochemistry of N-Type Bismuth Oxyiodide. *Electrochim Acta* **2013**, *104*, 448–453. https://doi.org/10.1016/j.electacta.2012.10.001.
- (11) Hahn, N. T.; Hoang, S.; Self, J. L.; Mullins, C. B. Spray Pyrolysis Deposition and Photoelectrochemical Properties of N-Type BiOI Nanoplatelet Thin Films. *ACS Nano* **2012**, *6* (9), 7712–7722. https://doi.org/10.1021/nn3031063.
- Wang, H.; Liang, Y.; Liu, L.; Hu, J.; Wu, P.; Cui, W. (12)Enriched Degradation and Photoelectric Photoelectrocatalytic Performance of BiOI Photoelectrode by Coupling RGO. Appl Catal B **2017**, 208. 22-34. https://doi.org/10.1016/j.apcatb.2017.02.055.
- (13) Jia, H.; He, W.; Zhang, B.; Yao, L.; Yang, X.; Zheng, Z. Facile Synthesis of Bismuth Oxyhalide Nanosheet Films with Distinct Conduction Type and Photo-Induced Charge Carrier Behavior. *Appl Surf Sci* **2018**, *441*, 832–840. https://doi.org/10.1016/j.apsusc.2018.02.030.
- (14) Hu, J.; Weng, S.; Zheng, Z.; Pei, Z.; Huang, M.; Liu, P. Solvents Mediated-Synthesis of BiOI Photocatalysts with Tunable Morphologies and Their Visible-Light Driven Photocatalytic Performances in Removing of Arsenic from Water. *J Hazard Mater* **2014**, *264*, 293–302. https://doi.org/10.1016/j.jhazmat.2013.11.027.
- (15) Babu, V. J.; Bhavatharini, R. S. R.; Ramakrishna, S. Electrospun BiOl Nano/Microtectonic Plate-like Structure Synthesis and UV-Light Assisted Photodegradation of ARS Dye. *RSC Adv* **2014**, *4* (37), 19251–19256. https://doi.org/10.1039/c4ra00579a.
- (16) Huang, H.; Xiao, K.; Zhang, T.; Dong, F.; Zhang, Y. Rational Design on 3D Hierarchical Bismuth Oxylodides via in Situ Self-Template Phase Transformation and Phase-Junction Construction for Optimizing Photocatalysis against Diverse Contaminants. *Appl Catal B* **2017**, *203*, 879–888. https://doi.org/10.1016/j.apcatb.2016.10.082.

- (17) Dandapat, A.; Horovitz, I.; Gnayem, H.; Sasson, Y.; Avisar, D.; Luxbacher, T.; Mamane, H. Solar Photocatalytic Degradation of Trace Organic Pollutants in Water by Bi(0)-Doped Bismuth Oxyhalide Thin Films. *ACS Omega* **2018**, *3* (9), 10858–10865. https://doi.org/10.1021/acsomega.8b00759.
- (18) Poznyak, S. K.; Kulak, A. I. Photoelectrochemical Properties of Bismuth Oxyhalide Films. *Electrochim Acta* **1990**, 35 (11–12), 1941–1947. https://doi.org/10.1016/0013-4686(90)87103-9.
- (19) Zhang, X.; Yang, H.; Zhang, B.; Shen, Y.; Wang, M. BiOI-TiO<sub>2</sub> Nanocomposites for Photoelectrochemical Water Splitting. *Adv Mater Interfaces* **2016**, 3 (1). https://doi.org/10.1002/admi.201500273.
- (20) Putri, A. A.; Kato, S.; Kishi, N.; Soga, T. Relevance of Precursor Molarity in the Prepared Bismuth Oxylodide Films by Successive Ionic Layer Adsorption and Reaction for Solar Cell Application. *J Sci Adv Mater Devices* **2019**, *4* (1), 116–124. https://doi.org/10.1016/J.JSAMD.2019.01.007.
- (21) Ye, L.; Chen, J.; Tian, L.; Liu, J.; Peng, T.; Deng, K.; Zan, L. BiOl Thin Film via Chemical Vapor Transport: Photocatalytic Activity, Durability, Selectivity and Mechanism. *Appl Catal B* **2013**, *130–131*, 1–7. https://doi.org/10.1016/j.apcatb.2012.10.011.
- (22) Sun, Z.; Oka, D.; Fukumura, T. Epitaxial Growth of Bismuth Oxyhalide Thin Films Using Mist CVD at Atmospheric Pressure. *Chemical Communications* **2020**, *56* (66), 9481–9484. https://doi.org/10.1039/D0CC03431B.
- (23) Li, H.; Yang, Z.; Zhang, J.; Huang, Y.; Ji, H.; Tong, Y. Indium Doped BiOl Nanosheets: Preparation, Characterization and Photocatalytic Degradation Activity. *Appl Surf Sci* **2017**, *423*, 1188–1197. https://doi.org/10.1016/J.APSUSC.2017.06.301.
- (24) Talreja, N.; Afreen, S.; Ashfaq, M.; Chauhan, D.; Mera, A. C.; Rodríguez, C. A.; Mangalaraja, R. V. Bimetal (Fe/Zn) Doped BiOl Photocatalyst: An Effective Photodegradation of Tetracycline and Bacteria. *Chemosphere* **2021**, *280*, 130803. https://doi.org/10.1016/j.chemosphere.2021.130803.
- (25) Talreja, N.; Ashfaq, M.; Chauhan, D.; Mera, A. C.; Rodríguez, C. A. Strategic Doping Approach of the Fe-BiOI Microstructure: An Improved Photodegradation

- Efficiency of Tetracycline. *ACS Omega* **2021**, *6* (2), 1575–1583. https://doi.org/10.1021/acsomega.0c05398.
- (26) Wang, Z.; Chen, M.; Huang, D.; Zeng, G.; Xu, P.; Zhou, C.; Lai, C.; Wang, H.; Cheng, M.; Wang, W. Multiply Structural Optimized Strategies for Bismuth Oxyhalide Photocatalysis and Their Environmental Application. *Chem Eng J* **2019**, *374*, 1025–1045. https://doi.org/10.1016/j.cej.2019.06.018.
- (27) Vinoth, S.; Rajaitha, P. M.; Pandikumar, A. Modulating Photoelectrochemical Water Splitting Performance by Constructing a Type-II Heterojunction between g-C<sub>3</sub>N<sub>4</sub> and BiOI. *New J Chem* **2021**, *45* (4), 2010–2018. https://doi.org/10.1039/D0NJ05384H.
- (28) Dai, G.; Yu, J.; Liu, G. Synthesis and Enhanced Visible-Light Photoelectrocatalytic Activity of P-n Junction BiOI/TiO<sub>2</sub> Nanotube Arrays. *J Phys Chem C* **2011**, *115* (15), 7339–7346. https://doi.org/10.1021/jp200788n.
- (29) Wang, L.; Daoud, W. A. BiOI/TiO2-Nanorod Array Heterojunction Solar Cell: Growth, Charge Transport Kinetics and Photoelectrochemical Properties. *Appl Surf Sci* **2015**, *324*, 532–537. https://doi.org/10.1016/J.APSUSC.2014.10.110.
- (30) Kuang, P.-Y.; Ran, J.-R.; Liu, Z.-Q.; Wang, H.-J.; Li, N.; Su, Y.-Z.; Jin, Y.-G.; Qiao, S.-Z. Enhanced Photoelectrocatalytic Activity of BiOl Nanoplate–Zinc Oxide Nanorod p–n Heterojunction. *Chem A Eur J* **2015**, *21* (43), 15360–15368. https://doi.org/10.1002/chem.201501183.
- (31) Chang, C.; Yang, H.-C.; Gao, N.; Lu, S.-Y. Core/Shell p-BiOl/n-β-Bi<sub>2</sub>O<sub>3</sub> Heterojunction Array with Significantly Enhanced Photoelectrochemical Water Splitting Efficiency. *J Alloys Compd* **2018**, *738*, 138–144. https://doi.org/10.1016/j.jallcom.2017.12.145.
- (32) Ye, K.-H.; Chai, Z.; Gu, J.; Yu, X.; Zhao, C.; Zhang, Y.; Mai, W. BiOl–BiVO<sub>4</sub> Photoanodes with Significantly Improved Solar Water Splitting Capability: P–n Junction to Expand Solar Adsorption Range and Facilitate Charge Carrier Dynamics. *Nano Energy* **2015**, *18*, 222–231. https://doi.org/10.1016/j.nanoen.2015.10.018.
- (33) Kegel, J.; Povey, I. M.; Pemble, M. E. Zinc Oxide for Solar Water Splitting: A Brief Review of the Material's Challenges and Associated Opportunities. *Nano Energy* **2018**, *54*, 409–428. https://doi.org/10.1016/j.nanoen.2018.10.043.

- (34) Wang, K.; Sun, N.; Li, X.; Zhang, R.; Zu, G.; Wang, J.; Pei, R. A Hemin Binding G-Quadruplex/Pb<sup>2+</sup> Complex to Construct a Visible Light Activated Photoelectrochemical Sensor on a ZnO/BiOI Heterostructure. *Anal Methods* **2015**, *7* (21), 9340–9346. https://doi.org/10.1039/c5ay02197a.
- (35) Ma, M.; Huang, Y.; Liu, J.; Liu, K.; Wang, Z.; Zhao, C.; Qu, S.; Wang, Z. Engineering the Photoelectrochemical Behaviors of ZnO for Efficient Solar Water Splitting. *J Semicond* **2020**, *41* (9), 091702. https://doi.org/10.1088/1674-4926/41/9/091702.
- (36) Liu, J.; Zou, S.; Lou, B.; Chen, C.; Xiao, L.; Fan, J. Interfacial Electronic Interaction Induced Engineering of ZnO-BiOI Heterostructures for Efficient Visible-Light Photocatalysis. *Inorg Chem* **2019**, *58* (13), 8525–8532. https://doi.org/10.1021/acs.inorgchem.9b00834.
- (37) Tang, J.; Xue, Y.; Ma, C.; Zhang, S.; Li, Q. Facile Preparation of BiOI/T-ZnOw p—n Heterojunction Photocatalysts with Enhanced Removal Efficiency for Rhodamine B and Oxytetracycline. *New J Chem* **2022**, *46* (27), 13010–13020. https://doi.org/10.1039/D2NJ01609E.
- (38) Jiang, J.; Zhang, X.; Sun, P.; Zhang, L. ZnO/BiOI Heterostructures: Photoinduced Charge-Transfer Property and Enhanced Visible-Light Photocatalytic Activity. *J Phys Chem C* **2011**, *115* (42), 20555–20564. https://doi.org/10.1021/jp205925z.
- (39) Zeng, P.; Yu, H.; Chen, M.; Xiao, W.; Li, Y.; Liu, H.; Luo, J.; Peng, J.; Shao, D.; Zhou, Z.; Luo, Z.; Wang, Y.; Chang, B.; Wang, X. Flower-like ZnO Modified with BiOI Nanoparticles as Adsorption/Catalytic Bifunctional Hosts for Lithium–Sulfur Batteries. *J Energy Chem* **2020**, *51*, 21–29. https://doi.org/10.1016/J.JECHEM.2020.03.040.
- (40) Hisatomi, T.; Kubota, J.; Domen, K. Recent Advances in Semiconductors for Photocatalytic and Photoelectrochemical Water Splitting. *Chem Soc Rev* **2014**, *43* (22), 7520–7535. https://doi.org/10.1039/C3CS60378D.
- (41) Zhao, L.; Qin, X. J.; Shao, G. J.; Wang, N. The Influence of H<sub>2</sub>O Content in Solvents {water + Carbinol} and {water + Ethanol} on the Deposition Mechanism of

- AZO Films Synthesized by Cold-Wall AACVD. *Chem Vap Depos* **2012**, *18* (7–9), 256–262. https://doi.org/10.1002/cvde.201206981.
- (42) Pan, M.; Zhang, H.; Gao, G.; Liu, L.; Chen, W. Facet-Dependent Catalytic Activity of Nanosheet-Assembled Bismuth Oxylodide Microspheres in Degradation of Bisphenol A. *Environ Sci Technol* **2015**, *49* (10), 6240–6248. https://doi.org/10.1021/acs.est.5b00626.
- (43) Sun, J.; Wen, J.; Wu, G.; Zhang, Z.; Chen, X.; Wang, G.; Liu, M. Harmonizing the Electronic Structures on BiOI with Active Oxygen Vacancies toward Facet-Dependent Antibacterial Photodynamic Therapy. *Adv Funct Mater* **2020**, *30* (42). https://doi.org/10.1002/adfm.202004108.
- (44) Jagt, R. A.; Huq, T. N.; Börsig, K. M.; Sauven, D.; Lee, L. C.; Macmanus-Driscoll, J. L.; Hoye, R. L. Z. Controlling the Preferred Orientation of Layered BiOl Solar Absorbers. *J Mater Chem C* **2020**, *8* (31), 10791–10797. https://doi.org/10.1039/d0tc02076a.
- (45) Andrei, V.; Jagt, R. A.; Rahaman, M.; Lari, L.; Lazarov, V. K.; MacManus-Driscoll, J. L.; Hoye, R. L. Z.; Reisner, E. Long-Term Solar Water and CO<sub>2</sub> Splitting with Photoelectrochemical BiOl–BiVO<sub>4</sub> Tandems. *Nat Mater* **2022**, *21* (8), 864–868. https://doi.org/10.1038/s41563-022-01262-w.
- (46) Teng, Q.; Zhou, X.; Jin, B.; Luo, J.; Xu, X.; Guan, H.; Wang, W.; Yang, F. Synthesis and Enhanced Photocatalytic Activity of a BiOI/TiO<sub>2</sub> Nanobelt Array for Methyl Orange Degradation under Visible Light Irradiation. *RSC Adv* **2016**, *6* (43), 36881–36887. https://doi.org/10.1039/C6RA01707J.
- (47) Yan, T.; Liu, H.; Gao, P.; Sun, M.; Wei, Q.; Xu, W.; Wang, X.; Du, B. Facile Synthesized Highly Active BiOI/Zn<sub>2</sub>GeO<sub>4</sub> Composites for the Elimination of Endocrine Disrupter BPA under Visible Light Irradiation. *New J Chem***2015**, *39* (5), 3964–3972. https://doi.org/10.1039/C4NJ02360A.
- (48) Ma, F. Q.; Yao, J. W.; Zhang, Y. F.; Wei, Y. Unique Band Structure Enhanced Visible Light Photocatalytic Activity of Phosphorus-Doped BiOl Hierarchical Microspheres. *RSC Adv* **2017**, *7* (58), 36288–36296. https://doi.org/10.1039/c7ra06261c.

- (49) Cai, L.; Yao, J.; Li, J.; Zhang, Y.; Wei, Y. Sonochemical Synthesis of BiOI-TiO<sub>2</sub> heterojunction with Enhanced Visible-Light-Driven Photocatalytic Activity. *J Alloys Compd* **2019**, 783, 300–309. https://doi.org/10.1016/j.jallcom.2018.12.387.
- (50) Yi, S.; Zhao, F.; Yue, X.; Wang, D.; Lin, Y. Enhanced Solar Light-Driven Photocatalytic Activity of BiOBr-ZnO Heterojunctions with Effective Separation and Transfer Properties of Photo-Generated Chargers. *New J Chem* **2015**, *39* (8), 6659–6666. https://doi.org/10.1039/c5nj00707k.
- (51) Haber, J.; Stoch, J.; Ungier, L. X-Ray Photoelectron Spectra of Oxygen in Oxides of Co, Ni, Fe and Zn. *J Electron Spectros Relat Phenomena* **1976**, *9* (5), 459–467. https://doi.org/10.1016/0368-2048(76)80064-3.
- (52) Hou, D.; Hu, X.; Hu, P.; Zhang, W.; Zhang, M.; Huang, Y. Bi<sub>4</sub>Ti<sub>3</sub>O<sub>12</sub> Nanofibers–BiOI Nanosheets p–n Junction: Facile Synthesis and Enhanced Visible-Light Photocatalytic Activity. *Nanoscale* **2013**, *5* (20), 9764. https://doi.org/10.1039/c3nr02458j.
- (53) Zuarez-Chamba, M.; Tuba-Guamán, D.; Quishpe, M.; Vizuete, K.; Debut, A.; Herrera-Robledo, M. Photocatalytic Degradation of Bisphenol A on BiOl Nanostructured Films under Visible LED Light Irradiation. *J Photochem Photobiol A Chem* **2022**, *431*, 114021. https://doi.org/10.1016/j.jphotochem.2022.114021.
- (54) Hassan, I. A.; Sathasivam, S.; Nair, S. P.; Carmalt, C. J. Antimicrobial Properties of Copper-Doped ZnO Coatings under Darkness and White Light Illumination. *ACS Omega* **2017**, 2 (8), 4556–4562. https://doi.org/10.1021/acsomega.7b00759.
- (55) Ponja, S. D.; Sathasivam, S.; Parkin, I. P.; Carmalt, C. J. Highly Conductive and Transparent Gallium Doped Zinc Oxide Thin Films via Chemical Vapor Deposition. *Sci Rep* **2020**, *10* (1), 638. https://doi.org/10.1038/s41598-020-57532-7.
- (56) Promdet, P.; Quesada-Cabrera, R.; Sathasivam, S.; Li, J.; Jiamprasertboon, A.; Guo, J.; Taylor, A.; Carmalt, C. J.; Parkin, I. P. High Defect Nanoscale ZnO Films with Polar Facets for Enhanced Photocatalytic Performance. *ACS Appl Nano Mater* **2019**, 2 (5), 2881–2889. https://doi.org/10.1021/acsanm.9b00326.

- (57) Viezbicke, B. D.; Patel, S.; Davis, B. E.; Birnie, D. P. Evaluation of the Tauc Method for Optical Absorption Edge Determination: ZnO Thin Films as a Model System. *Phys Status Solidi B Basic Res* **2015**, *252* (8), 1700–1710. https://doi.org/10.1002/pssb.201552007.
- (58) Shinde, S. S.; Shinde, P. S.; Sapkal, R. T.; Oh, Y. W.; Haranath, D.; Bhosale, C. H.; Rajpure, K. Y. Photoelectrocatalytic Degradation of Oxalic Acid by Spray Deposited Nanocrystalline Zinc Oxide Thin Films. *J Alloys Compd* **2012**, *538*, 237–243. https://doi.org/10.1016/j.jallcom.2012.05.124.
- (59) Kafizas, A.; Francàs, L.; Sotelo-Vazquez, C.; Ling, M.; Li, Y.; Glover, E.; McCafferty, L.; Blackman, C.; Darr, J.; Parkin, I. Optimizing the Activity of Nanoneedle Structured WO<sub>3</sub> Photoanodes for Solar Water Splitting: Direct Synthesis via Chemical Vapor Deposition. *J Physl Chem C* **2017**, *121* (11), 5983–5993. https://doi.org/10.1021/acs.jpcc.7b00533.
- (60) Di, J.; Xia, J.; Yin, S.; Xu, H.; Xu, L.; Xu, Y.; He, M.; Li, H. Preparation of Sphere-like g-C<sub>3</sub>N<sub>4</sub>/BiOI Photocatalysts via a Reactable Ionic Liquid for Visible-Light-Driven Photocatalytic Degradation of Pollutants. *J Mater Chem A* **2014**, *2* (15), 5340–5351. https://doi.org/10.1039/c3ta14617k.
- (61) Ahn, K. S.; Yan, Y.; Shet, S.; Deutsch, T.; Turner, J.; Al-Jassim, M. Enhanced Photoelectrochemical Responses of ZnO Films through Ga and N Codoping. *Appl Phys Lett* **2007**, *91* (23). https://doi.org/10.1063/1.2822440.
- (62) Li, M.; Tu, X.; Wang, Y.; Su, Y.; Hu, J.; Cai, B.; Lu, J.; Yang, Z.; Zhang, Y. Highly Enhanced Visible-Light-Driven Photoelectrochemical Performance of ZnO-Modified In<sub>2</sub>S<sub>3</sub> Nanosheet Arrays by Atomic Layer Deposition. *Nanomicro Lett* **2018**, *10* (3), 45. https://doi.org/10.1007/s40820-018-0199-z.
- (63) Sharma, D.; Upadhyay, S.; Satsangi, V. R.; Shrivastav, R.; Waghmare, U. V; Dass, S. Improved Photoelectrochemical Water Splitting Performance of Cu<sub>2</sub>O/SrTiO<sub>3</sub> Heterojunction Photoelectrode. *J Phys Chem C* **2014**, *118* (44), 25320–25329. https://doi.org/10.1021/jp507039n.
- (64) Zheng, G.; Wang, J.; Zu, G.; Che, H.; Lai, C.; Li, H.; Murugadoss, V.; Yan, C.; Fan, J.; Guo, Z. Sandwich Structured WO3 Nanoplatelets for Highly Efficient

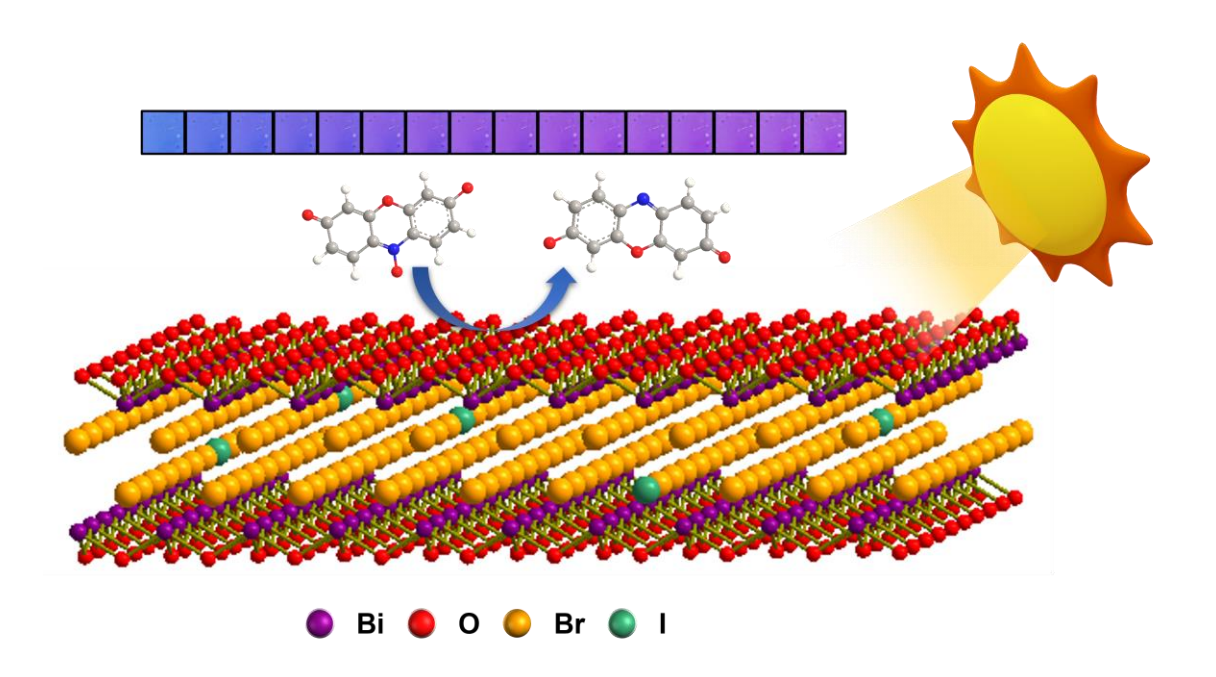
- Photoelectrochemical Water Splitting. *J Mater Chem A* **2019**, 7 (45), 26077–26088. https://doi.org/10.1039/c9ta09188b.
- (65) Guo, Y.; Shi, W.; Zhu, Y.; Xu, Y.; Cui, F. Enhanced Photoactivity and Oxidizing Ability Simultaneously via Internal Electric Field and Valence Band Position by Crystal Structure of Bismuth Oxyiodide. *Appl Catal B* **2020**, *262*, 118262. https://doi.org/10.1016/J.APCATB.2019.118262.
- (66) Jiang, Z.; Liang, X.; Liu, Y.; Jing, T.; Wang, Z.; Zhang, X.; Qin, X.; Dai, Y.; Huang, B. Enhancing Visible Light Photocatalytic Degradation Performance and Bactericidal Activity of BiOI via Ultrathin-Layer Structure. *Appl Catal B* **2017**, *211*, 252–257. https://doi.org/10.1016/j.apcatb.2017.03.072.
- (67) Lim, T.; Mirabedini, P. S.; Jung, K.; Alex Greaney, P.; Martinez-Morales, A. A. High-Index Crystal Plane of ZnO Nanopyramidal Structures: Stabilization, Growth, and Improved Photocatalytic Performance. *Appl Surf Sci* **2021**, *536*, 147326. https://doi.org/10.1016/j.apsusc.2020.147326.
- (68) Shan, L. W.; He, L. Q.; Suriyaprakash, J.; Yang, L. X. Photoelectrochemical (PEC) Water Splitting of BiOI{001} Nanosheets Synthesized by a Simple Chemical Transformation. *J Alloys Compd* **2016**, 665, 158–164. https://doi.org/10.1016/J.JALLCOM.2016.01.008.
- (69) Lin, B.; Fu, Z.; Jia, Y. Green Luminescent Center in Undoped Zinc Oxide Films Deposited on Silicon Substrates. *Appl Phys Lett* **2001**, 79 (7), 943–945. https://doi.org/10.1063/1.1394173.
- (70) Musa, I.; Qamhieh, N.; Mahmoud, S. T. Synthesis and Length Dependent Photoluminescence Property of Zinc Oxide Nanorods. *Results Phys* **2017**, *7*, 3552–3556. https://doi.org/10.1016/J.RINP.2017.09.035.
- (71) Li, Y.; Li, Z.; Gao, L. Construction of Z-Scheme BiOI/g-C<sub>3</sub>N<sub>4</sub> Heterojunction with Enhanced Photocatalytic Activity and Stability under Visible Light. *J Mater Sci Mater Electron* **2019**, *30* (13), 12769–12782. https://doi.org/10.1007/s10854-019-01642-0.
- (72) Iqbal, A.; Kafizas, A.; Sotelo-Vazquez, C.; Wilson, R.; Ling, M.; Taylor, A.; Blackman, C.; Bevan, K.; Parkin, I.; Quesada-Cabrera, R. Charge Transport Phenomena in Heterojunction Photocatalysts: The WO<sub>3</sub>/TiO<sub>2</sub> System as an

- Archetypical Model. *ACS Appl Mater Interfaces* **2021**, *13* (8), 9781–9793. https://doi.org/10.1021/acsami.0c19692.
- (73) Jiamprasertboon, A.; Kafizas, A.; Sachs, M.; Ling, M.; Alotaibi, A. M.; Lu, Y.; Siritanon, T.; Parkin, I. P.; Carmalt, C. J. Heterojunction A-Fe<sub>2</sub>O<sub>3</sub>/ZnO Films with Enhanced Photocatalytic Properties Grown by Aerosol-Assisted Chemical Vapour Deposition. *Chem A Eur J* **2019**, *25* (48), 11337–11345. https://doi.org/10.1002/chem.201902175.
- (74) Moss, B.; Lim, K. K.; Beltram, A.; Moniz, S.; Tang, J.; Fornasiero, P.; Barnes, P.; Durrant, J.; Kafizas, A. Comparing Photoelectrochemical Water Oxidation, Recombination Kinetics and Charge Trapping in the Three Polymorphs of TiO<sub>2</sub>. *Sci Rep* **2017**, *7* (1), 2938. https://doi.org/10.1038/s41598-017-03065-5.
- (75) Bhosale, A. H.; Narra, S.; Bhosale, S. S.; Diau, E. W. Interface-Enhanced Charge Recombination in the Heterojunction between Perovskite Nanocrystals and BiOI Nanosheets Serves as an S-Scheme Photocatalyst for CO<sub>2</sub> Reduction. *J Phys Chem Lett* **2022**, *13*, 7987–7993. https://doi.org/10.1021/acs.jpclett.2c02153.
- (76) Rieger, S.; Fürmann, T.; Stolarczyk, J. K.; Feldmann, J. Optically Induced Coherent Phonons in Bismuth Oxylodide (BiOI) Nanoplatelets. *Nano Lett* **2021**, *21* (18), 7887–7893. https://doi.org/10.1021/acs.nanolett.1c00530.
- (77) Huq, T. N.; Lee, L. C.; Eyre, L.; Li, W.; Jagt, R. A.; Kim, C.; Fearn, S.; Pecunia, V.; Deschler, F.; MacManus-Driscoll, J. L.; Hoye, R. L. Z. Electronic Structure and Optoelectronic Properties of Bismuth Oxyiodide Robust against Percent-Level Iodine-, Oxygen-, and Bismuth-Related Surface Defects. *Adv Funct Mater* **2020**, *30* (13). https://doi.org/10.1002/adfm.201909983.
- (78) Chang, A.-M.; Chen, Y.-H.; Lai, C.-C.; Pu, Y.-C. Synergistic Effects of Surface Passivation and Charge Separation to Improve Photo-Electrochemical Performance of BiOI Nanoflakes by Au Nanoparticle Decoration. *ACS Appl Mater Interfaces* **2021**, *13* (4), 5721–5730. https://doi.org/10.1021/acsami.0c18430.
- (79) Li, K.; Gong, K.; Liu, J.; Yang, Y.; Nabi, I.; Bacha, A.-U.-R.; Cheng, H.; Han, J.; Zhang, L. New Insights into the Role of Sulfite in BiOX Photocatalytic Pollutants

- Elimination: In-Operando Generation of Plasmonic Bi Metal and Oxygen Vacancies. *J Hazard Mater* **2021**, *418*, 126207. https://doi.org/10.1016/j.jhazmat.2021.126207.
- (80) Rudd, A. L.; Breslin, C. B. Photo-Induced Dissolution of Zinc in Alkaline Solutions. *Electrochim Acta* **2000**, *45* (10), 1571–1579. https://doi.org/10.1016/S0013-4686(99)00322-9.
- (81) Han, J.; Qiu, W.; Gao, W. Potential Dissolution and Photo-Dissolution of ZnO Thin Films. *J Hazard Mater* **2010**, *178* (1–3), 115–122. https://doi.org/10.1016/J.JHAZMAT.2010.01.050.
- (82) Govatsi, K.; Seferlis, A.; Neophytides, S. G.; Yannopoulos, S. N. Influence of the Morphology of ZnO Nanowires on the Photoelectrochemical Water Splitting Efficiency. *Int J Hydrogen Energy* **2018**, *43* (10), 4866–4879. https://doi.org/10.1016/j.ijhydene.2018.01.087.
- (83) Pawar, A. U.; Kim, C. W.; Kang, M. J.; Kang, Y. S. Crystal Facet Engineering of ZnO Photoanode for the Higher Water Splitting Efficiency with Proton Transferable Nafion Film. *Nano Energy* **2016**, *20*, 156–167. https://doi.org/10.1016/J.NANOEN.2015.11.035.
- (84) Long, X.; Gao, L.; Li, F.; Hu, Y.; Wei, S.; Wang, C.; Wang, T.; Jin, J.; Ma, J. Bamboo Shoots Shaped FeVO<sub>4</sub> Passivated ZnO Nanorods Photoanode for Improved Charge Separation/Transfer Process towards Efficient Solar Water Splitting. *Appl Catal B* **2019**, *257*, 117813. https://doi.org/10.1016/J.APCATB.2019.117813.
- (85) Yang, T.; Xue, J.; Tan, H.; Xie, A.; Li, S.; Yan, W.; Shen, Y. Highly Ordered ZnO/ZnFe<sub>2</sub>O<sub>4</sub> Inverse Opals with Binder-Free Heterojunction Interfaces for High-Performance Photoelectrochemical Water Splitting. *J Mater Chem A* **2018**, *6* (3), 1210–1218. https://doi.org/10.1039/C7TA07798J.
- (86) Zeng, Y.; Yang, T.; Li, C.; Xie, A.; Li, S.; Zhang, M.; Shen, Y. Zn<sub>x</sub>Cd<sub>1-x</sub>Se Nanoparticles Decorated Ordered Mesoporous ZnO Inverse Opal with Binder-Free Heterojunction Interfaces for Highly Efficient Photoelectrochemical Water Splitting. *Appl Catal B* **2019**, *245*, 469–476. https://doi.org/10.1016/j.apcatb.2019.01.011.

- (87) Govatsi, K.; Seferlis, A.; Yannopoulos, S. N.; Neophytides, S. G. The Photo-Electrokinetics of the O<sub>2</sub> Evolution Reaction on ZnO Nanorods. *Electrochim Acta* **2019**, 298, 587–598. https://doi.org/10.1016/J.ELECTACTA.2018.12.082.
- (88) Asha, K.; Banerjee, A.; Saxena, S.; Khan, S. A.; Sulaniya, I.; Satsangi, V. R.; Shrivastav, R.; Kant, R.; Dass, S. Morphological Influence of Electrode/Electrolyte Interface towards Augmenting the Efficiency of Photoelectrochemical Water Splitting A Case Study on ZnO. *J Power Sources* **2019**, *432*, 38–47. https://doi.org/10.1016/j.jpowsour.2019.05.068.
- (89) Bledowski, M.; Wang, L.; Ramakrishnan, A.; Khavryuchenko, O. V.; Khavryuchenko, V. D.; Ricci, P. C.; Strunk, J.; Cremer, T.; Kolbeck, C.; Beranek, R. Visible-Light Photocurrent Response of TiO2-Polyheptazine Hybrids: Evidence for Interfacial Charge-Transfer Absorption. *Phys Chem Chem Phys* **2011**, *13* (48), 21511–21519. https://doi.org/10.1039/c1cp22861g.
- (90) Zhang, X.; Zhang, L.; Xie, T.; Wang, D. Low-Temperature Synthesis and High Visible-Light-Induced Photocatalytic Activity of BiOI/TiO<sub>2</sub> Heterostructures. *J Phys Chem C* **2009**, *113* (17), 7371–7378. https://doi.org/10.1021/jp900812d.
- (91) Tahir, A. A.; Peiris, T. A. N.; Wijayantha, K. G. U. Enhancement of Photoelectrochemical Performance of AACVD-Produced TiO<sub>2</sub> Electrodes by Microwave Irradiation While Preserving the Nanostructure. *Chem Vap Depos* **2012**, *18* (4–6), 107–111. https://doi.org/10.1002/cvde.201106974.

Chapter 4: lodide-doped BiOBr films with enhanced photocatalytic activity under visible-light irradiation



# 4.1 Background

Semiconductors with photocatalytic activity have come into focus since the first report of photocatalytic water splitting on  $TiO_2$ .<sup>1</sup> In a photocatalytic process, the unlimited solar energy can be utilized to drive the decomposition of harmful pollutants or produce green energy such as hydrogen, which shows huge potential in solving worldwide-concerned problems about environmental pollution and energy depletion. However, the wide bandgap of  $TiO_2$  ( $\geq 3.0$  eV) seriously hinders its practical applications because only UV radiation (~4% of sunlight) can be harvested by  $TiO_2$ .

As one of the alternatives to the traditional TiO<sub>2</sub> photocatalyst, bismuth oxyhalides, BiOX (X= CI, Br and I), have received much attention in the photocatalytic field. The Bi<sub>2</sub>O<sub>2</sub>X<sub>2</sub> sandwiched structure of BiOX can generate an internal electric field.<sup>2</sup> The existence of this internal electric field is thought to favour the decrease of the charge carrier recombination that is detrimental to photocatalytic performance.<sup>3</sup> Furthermore, BiOX with indirect band gaps are beneficial to the separation of photogenerated charge carriers thus further reducing recombinative losses.<sup>4</sup> Among three kinds of bismuth oxyhalides, BiOCI shows no photocatalytic capacity under visible light due to the widest band gap of 3.5 eV. BiOI has the narrowest band gap (1.8 eV) leading to

the rapid recombination rate of photogenerated electron-hole pairs.<sup>5</sup> BiOBr has been investigated widely and shows excellent photocatalytic activity.<sup>5–7</sup> However, the wide optical band gap (2.7 eV) limits its visible-light activity and photocatalytic applications in real life.<sup>8</sup> Therefore, it is vital to search for BiOBr relative materials with a higher photocatalytic activity within the visible-light range of the solar spectrum.

Until now, diverse studies have been implemented to improve the visible-light activity of BiOBr. For instance, controlling the growth of BiOBr with specific morphologies or facets, 9-11 building a heterojunction with other semiconductors such as AgBr, C<sub>3</sub>N<sub>4</sub> and CdS, 12-14 and the synthesis of solid solutions including BiOCl<sub>x</sub>Br<sub>1-x</sub> and BiOBr<sub>x</sub>l<sub>1-x</sub>. 15-18 Wherein, one of the most promising approaches for the enhanced photocatalytic activity is to dope BiOBr with other halogens. Considering similar crystal structures and compositions of BiOX and close ionic radii of two neighboring halides (Cl<sup>-</sup> = 1.67 Å, Br<sup>-</sup> = 1.82 Å and l<sup>-</sup> = 2.06 Å), 19 halogen ions can substitute each other and then dope into the lattice easily, combined with the formation of favorable crystal defects and the continuous adjustment of band gaps. 20 Different from pure BiOX, solid solutions based on BiOX are composed of two or more types of halides, which is able to combine the individual advantages of each BiOX through adjusting the position of the valence band maximum (VBM) and conduction band minimum (CBM) in solid solutions, so that the visible-light harvesting and the redox capabilities of intrinsic materials as photocatalysts can be improved. 21

Compared with other BiOX based solid solutions, BiOBr<sub>x</sub>I<sub>1-x</sub> showed some unique advantages. Firstly, due to narrow band gaps, BiOBr<sub>x</sub>I<sub>1-x</sub> can utilize the sunlight more efficiently. In addition, the formation energies of BiOBr<sub>x</sub>I<sub>1-x</sub> are low due to similar ionic radii and electronegativities of Br and I (2.96 for Br and 2.66 for I). The great miscibility of Br and I also benefits the continuous modification of the band structures in BiOBr<sub>x</sub>I<sub>1-x</sub>, and thus band gaps and redox potentials of BiOBr<sub>x</sub>I<sub>1-x</sub> are easy to be tuned.<sup>22</sup> Furthermore, it has been reported that for BiOBr<sub>x</sub>I<sub>1-x</sub>, the mobility of photogenerated holes can be decreased while that of electrons barely changes, limiting the recombination rate of photogenerated charge carriers.<sup>4</sup>

Nanostructured materials are attractive as photocatalysts in environmental applications because they process short diffusion distance for the separation of charge carriers and large surface areas. To date, various research on Cl<sup>-</sup>/l<sup>-</sup> doped BiOBr in

the powder form has been reported where the hydro/solvothermal method is the most common preparation method, 16,23,24 and the excellent photocatalytic performance has been shown in organic pollutant decomposition, 25 PEC biosensors and CO2 reduction. However, these nano-powders are easy to agglomerate because of high surface energies, reducing active sites in photocatalysis. In solution-based photocatalytic processes, it is hard to separate these materials with tiny sizes by sedimentation for recycling. In addition, the preparation methods adopted in these studies are difficult to achieve large-scale production which is necessary for industrialization.

Compared with powders, materials in the immobilized form, such as films and coatings, are more desirable in practical photocatalytic applications because less amount of photocatalysts would be required.<sup>28</sup> Furthermore, films can maximize the light absorption, and benefit the reclamation and long-term utilization of photocatalysts due to the elimination of complicated separation processes. Especially for pollutant removal in wastewater, the photocatalyst-free water can be obtained directly after treatment. However, there is little work reported for the thin film fabrication of doped BiOX.<sup>8,25,28,29</sup>

In this work, without extra steps to deposit powder samples into films, iodide-doped BiOBr thin films were grown directly using AACVD, which is a feasible, scalable and cheap method for thin-film deposition. Iodide-doped BiOBr with various dopant amounts were deposited on both FTO and glass. The influence of I<sup>-</sup> concentration on the crystal structure, compositions, morphologies and optical properties of deposited films were characterised in detail, and the photocatalytic performance of AACVD-films on FTO was investigated with the *smart resazurin* (*Rz*) ink under both UV and visible light, where the iodide-doped BiOBr films exhibited a significant improvement in the visible-light photocatalytic activity compared with both pure BiOBr and BiOI. Furthermore, the PL spectroscopy and PEC measurements were carried out to investigate possible accounts for this great improvement. To the best of our knowledge, it is the first time to fabricate iodide-doped BiOBr thin films by AACVD, and the *smart Rz* ink is also first used in the photocatalytic test of colourful iodide-doped BiOBr films under visible-light irradiation.

## 4.2 Experimental

## 4.2.1 Film deposition

**lodide-doped BiOBr thin films** *via* **AACVD.** All chemicals were used without further purification. Stoichiometric amounts of BiBr<sub>3</sub> (Alfa Aesar) and Bil<sub>3</sub> (Sigma-Aldrich) with total of 1 mmol were dissolved in 25 mL anhydrous dimethylformamide (DMF, Thermos Fisher) with varying the molar ratio from 9:1, 8:2, 7:3, 6:4, 5:5, 4:6, 3:7, 2:8 to 1:9. The precursor solution was ultrasonicated for 10 mins. Compressed air (flow rate: 1.0 L·min<sup>-1</sup>) was used as the carrier gas. lodide-doped BiOBr films were grown on glass or FTO glass (NSG TEC 15) substrates (15 cm × 4.5 cm) at 300 °C. For the next PEC measurements, one side of the substrate was covered when films were deposited on FTO. The duration of the deposition was 60 mins. Substrates were cooled naturally to room temperature under the air flow. The samples obtained from precursor solutions with the molar ratio (BiBr<sub>3</sub>:Bil<sub>3</sub>) of 9:1, 8:2, 7:3, 6:4, 5:5, 4:6, 3:7, 2:8 and 1:9 will be denoted as **I-BB S1**, **I-BB S2**, **I-BB S3**, **I-BB S4**, **I-BB S5**, **I-BB S6**, **I-BB S7**, **I-BB S8** and **I-BB S9** respectively, where S means sample.

**BiOBr and BiOI thin films** *via* **AACVD.** For comparison, pure BiOBr and BiOI films were deposited as well. BiBr<sub>3</sub> (0.4487 g, 1 mmol) and BiI<sub>3</sub> (0.5897 g, 1 mmol) in anhydrous DMF (25 mL) was ultrasonicated for 10 mins to form the precursor solution, respectively. All parameters used in the AACVD process are the same with those used for iodide-doped BiOBr thin films.

#### 4.2.2 Smart Rz ink preparation

The *Rz* ink was prepared according to the reported literature.<sup>30</sup> 1.5g Hydroxyethylcellulose was dissolved in 98.5 mL distilled water after stirring for 8 hours. 0.1333 g resazurin sodium salt and 13.3333 g glycerol were added to the aqueous polymer, and then stirred overnight. The prepared ink was stored in the fridge and stirred for 5 mins before use every time for fully mixing.

#### 4.2.3 Physical characterization

Grazing-incident X-ray diffraction (GIXRD) patterns were measured from  $5^{\circ}$ – $60^{\circ}$  (0.05° steps and 1.5 seconds/step) using a Panalytical Empyrean diffractometer. X ray source was Cu K $\alpha$  ( $\lambda$  = 1.5406 Å) at 40 kV with 40 mA emission current. The angle of

the incident beam was 1°. The film morphology was studied by a JEOL JSM-7600 field emission scanning electron microscope (SEM) and energy dispersive spectroscopy (EDS). X-ray fluorescence (XRF) was used to study the film composition by a Panalytical Epsilon Energy-Dispersive XRF spectrometer. UV-Vis-NIR transmission spectra was measured by a Shimadzu UV-3600i Plus spectrometer between 300-1100 nm. X-ray photoelectron spectroscopy (XPS) was undertaken on a Thermo Scientific K-alpha spectrometer (monochromated Al K<sub>α1</sub> radiation (8.3418 Å)). A dual beam system was employed for charge compensation. Survey scans (0-1200 eV) at 50 eV pass energy. Depth profiling XPS using an Ar<sup>+</sup> ion beam to etch the surface. All peak positions were calibrated to adventitious carbon (284.8 eV) using CasaXPS®. Photoluminescence (PL) spectra were obtained at room temperature by a PL spectroscopy (Renishaw 1000) with an excitation wavelength of 325 nm. Atomic force microscopy (AFM) was performed by a Keysight 5500 scanning probe atomic force microscope. Images over a projected area of 5 µm × 5 µm were recorded in tapping mode using Si cantilevers with a resonant frequency of ~ 70 kHz and a ~ 2 N m<sup>-1</sup> spring constant (NuNano SCOUT-70). The roughness factor was obtained through dividing the measured surface area by the projected area.

# 4.2.4 Photocatalytic test

The prepared *smart Rz* ink was coated on the film through spin coating with 6000 rpm for 10 s. Afterwards, films were irradiated top-down with the 365 nm (2.87 mW·cm<sup>-2</sup>), 450 nm (2.01 mW·cm<sup>-2</sup>) or 627 nm (1.32 mW·cm<sup>-2</sup>) light from a multiple wavelength LED board at a fixed distance of 11 cm from the light source to the sample, and the emission spectra of the LED light source are shown in Figure 4-1. Digital images were taken at specific intervals using the phone camera. The average RGB values across the film area were acquired from digital images using *ImageJ* software, as a function of irradiation time, where the red component was used to monitor the colour change in the *Rz* ink.<sup>31</sup> The normalized value of the red component, Rt, were calculated using the equation (1):

$$R_t = \frac{RGB_{R,t}}{RGB_{R,t} + RGB_{G,t} + RGB_{B,t}}$$
(1)

where the  $RGB_{R,t}$ ,  $RGB_{G,t}$  and  $RGB_{B,t}$  values are the red, green and blue components of photographs at irradiation time t.

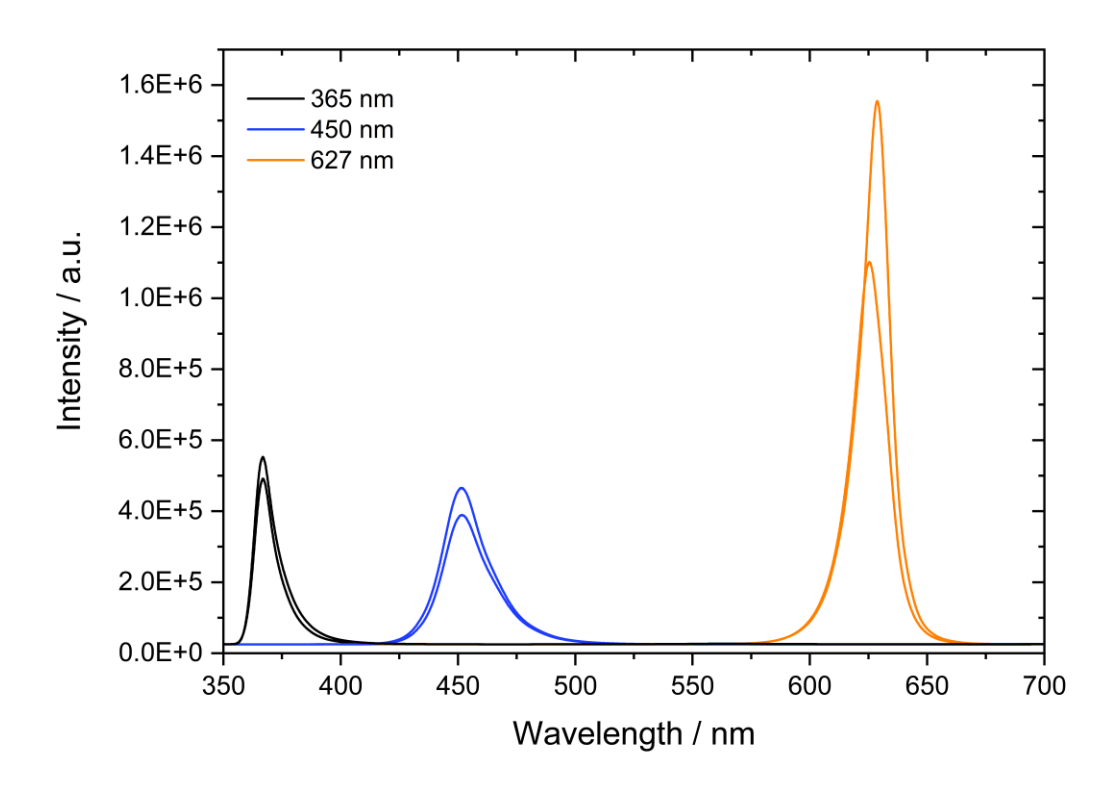


Figure 4-1. The emission spectra of the 365 nm, 450 nm and 627 nm LED.

### 4.2.5 Photoelectrochemical measurements

A 220 W Xe lamp with a 420 nm cutoff filter was used as the light source. All tests were carried out under ambient environment. With the constant voltage of 1.0 V<sub>RHE</sub>, transient photocurrent was collected in a three-electrode configuration through controlling the cycle irradiation on and off. The electrolyte was Na<sub>2</sub>SO<sub>4</sub> aqueous solution (0.5 M) with pH of 6.6. The as-fabricated film, Ag/AgCl/3M-KCl and Pt mesh were used as the working electrode, reference electrode and counter electrode, respectively. A *Compactstat.h* electrochemical workstation (*IVIUMSTAT*, *Netherland*) was implemented to apply voltages and measure currents. In the same system, *JV* curves were collected through sweeping the voltage from 0.10 V<sub>RHE</sub> to 1.60 V<sub>RHE</sub> at a rate of 10 mV·s<sup>-1</sup>, under both dark and irradiation conditions.

The applied voltage in our JV curves were reported against  $V_{RHE}$ , converted by the equation (1) mentioned in **Chapter 3**.

#### 4.3 Results and discussions

#### 4.3.1 GIXRD characterization

The composition and crystallographic structures of the deposited bismuth oxyhalide films were determined first by GIXRD (Figure 4-2). Sharp peaks from all samples showed their good crystallinity. Both undoped films on FTO only showed pure tetragonal phases of BiOBr and BiOI, respectively, corresponding to standard *PDF-78-0348* and *10-0445* (Figure 4-2a). Furthermore, in their enlarged patterns (30.5° – 33.0°), the evolution of the strongest (102) peak is shown (Figure 4-2b). Successive peak shifts were observed to smaller angles with the increased concentration of doped I<sup>-</sup> because of the larger ion radius of I<sup>-</sup> (2.20 Å) than that of Br<sup>-</sup> (1.96 Å). If was observed that in I-BB from S1 to S7, due to the low I<sup>-</sup> concentration, all doped samples exhibited the same tetragonal phase to BiOBr but not BiOI. However, with the increased amount of doped I<sup>-</sup>, the peak position and shape of I-BB S8 and S9 varied dramatically and became similar to that of BiOI. This gradual shift and the sharp shape of the XRD peaks also indicated that I-BB films with pure phases but not simple mixtures of BiOBr and BiOI were deposited on FTO *via* AACVD.

In addition, different from reported similar materials in powders,<sup>32</sup> films deposited by AACVD displayed a preferential growth in the (102) lattice plane, where the lattice substitution of Br with I did not change this growth trend and even caused the (102) peak to become sharper and more intense. It has been reported that for BiOBr, (102) facets have a narrower band gap, stronger oxidation capacity of holes, more efficient electron injection and more active sites, likely resulting in the better sunlight utilization and higher photocatalytic activity. <sup>10,33</sup> In addition, BiOI films with dominant (102) facets also showed efficient transfer and separation of photogenerated charge carriers. <sup>34</sup> Unit cell parameters and average crystallite size of deposited films were determined from the GIXRD data (

Table 2-1). It can be seen that compared with the almost constant a value in **I-BB** samples (**S1** – **S7**) within a relative low range of the dopant concentration, the c value increased more significantly with the increased concentration of dopants, and thus leading to the cell expansion. This indicated that the halide anion in c-lattice axis had a stronger influence than that in a or b lattice axis. However, due to the dramatic

increase in the I<sup>-</sup> concentration, the unit cell parameters of **I-BB S8** and **S9** enlarged unusually and did not follow the above variation trend. Furthermore, the increase trend of calculated *c* values showed a deviation from Vegard's law (Figure 4-3). The variation of lattice constants, especially *c*, is caused by both the intrinsic difference in halide anionic radii and the weak van de Waals force between adjacent layers.<sup>36</sup> The regular change in unit cell parameters further proved the successful deposition of **I-BB** films. This change could influence the visible-light absorption and photogenerated charge conversion efficiency of semiconductors as well.<sup>37</sup>

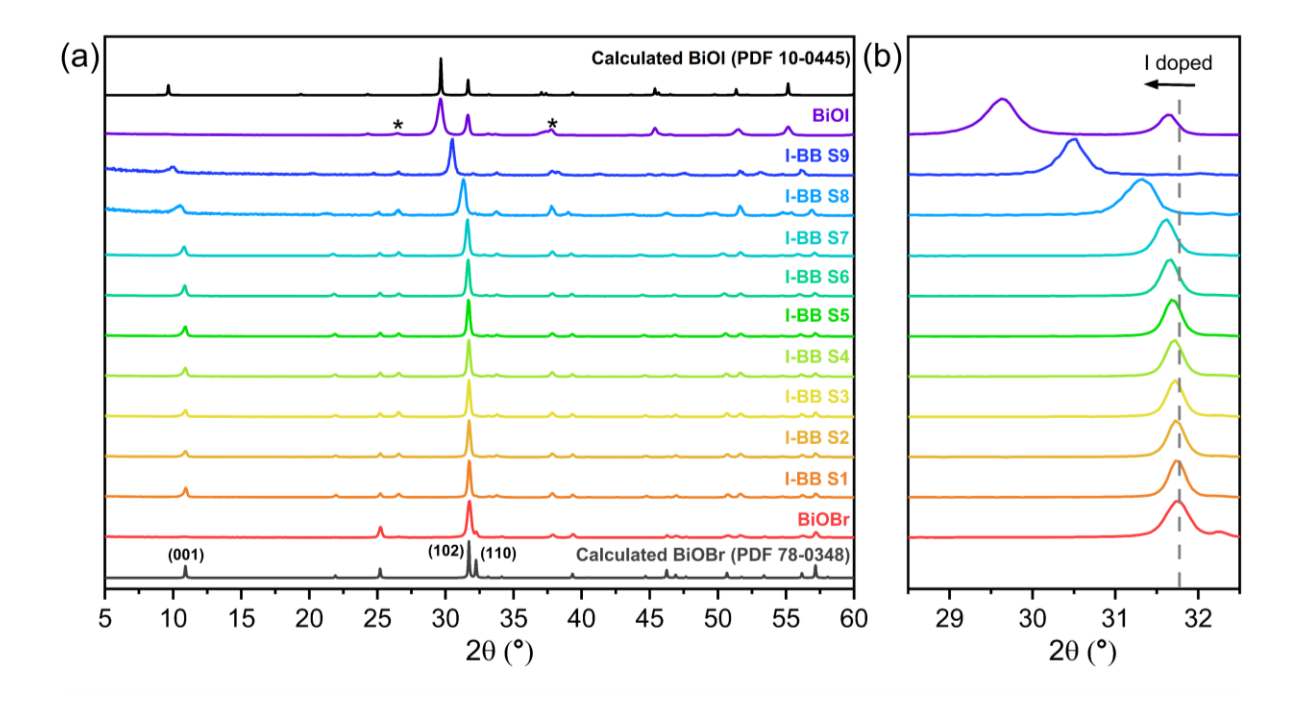


Figure 4-2. (a) GIXRD patterns and (b) enlarged patterns of BiOBr, BiOI and **I-BB** films deposited on FTO. The asterisked peaks indicate positions of reflections from the FTO substrate.

Table 4-1. Unit cell parameters (a, c), cell volume (V) and average crystallite size of BiOBr, BiOI and **I-BB** films.

Films	Molar ratio (Br:I) in precursors	a [Å]	c [Å]	V [ų]	Average crystallite size (Å)
BiOBr standard		3.923	8.105	124.75	-
BiOI standard		3.994	9.149	145.9	-
BiOBr		3.923 (0)	8.095 (1)	124.60 (2)	249 (4)
I-BB S1	9:1	3.924 (0)	8.100 (1)	124.71 (2)	310 (7)
I-BB S2	8:2	3.925 (0)	8.104 (1)	124.82 (2)	319 (7)
I-BB S3	7:3	3.925 (0)	8.112 (0)	124.94 (0)	313 (8)
I-BB S4	6:4	3.926 (1)	8.117 (3)	125.09 (6)	337 (10)
I-BB S5	5:5	3.924 (0)	8.129 (7)	125.18 (11)	293 (5)
I-BB S6	4:6	3.925 (1)	8.144 (2)	125.44 (5)	293 (4)
I-BB S7	3:7	3.926 (1)	8.167 (2)	125.86 (5)	274 (7)
I-BB S8	2:8	3.926 (1)	8.320 (3)	128.21 (7)	159 (5)
I-BB S9	1:9	3.999 (3)	9.083 (5)	145.32 (17)	157 (10)
BiOI		3.996 (1)	9.148 (8)	146.10 (14)	178 (4)

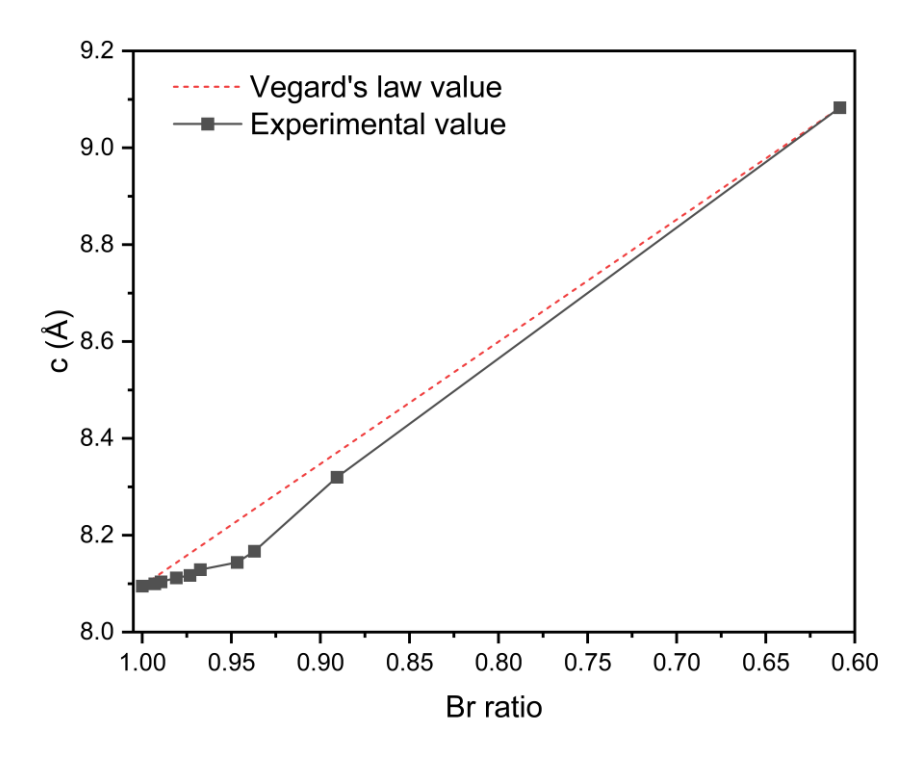


Figure 4-3. Comparison of *c* values of **I-BB** samples calculated from GIXRD patterns and from the Vegard's law.

Besides crystalline FTO, amorphous glass was used as the substrate for the film deposition as well. Significantly different from that of FTO, **I-BB** films grown on glass showed the preferential growth orientation in the (001) direction (Figure 4-4a). However, the gradual peak shift towards lower angles was observed in these films with the increased dopant amount (Figure 4-4b), which is similar to samples on FTO. It was also demonstrated that iodide-doped BiOBr films were successfully deposited on glass *via* AACVD, further proving the feasibility of the **I-BB** film deposition on various substrates. In addition, the preferential growth orientation of films could be controlled by using different substrates.

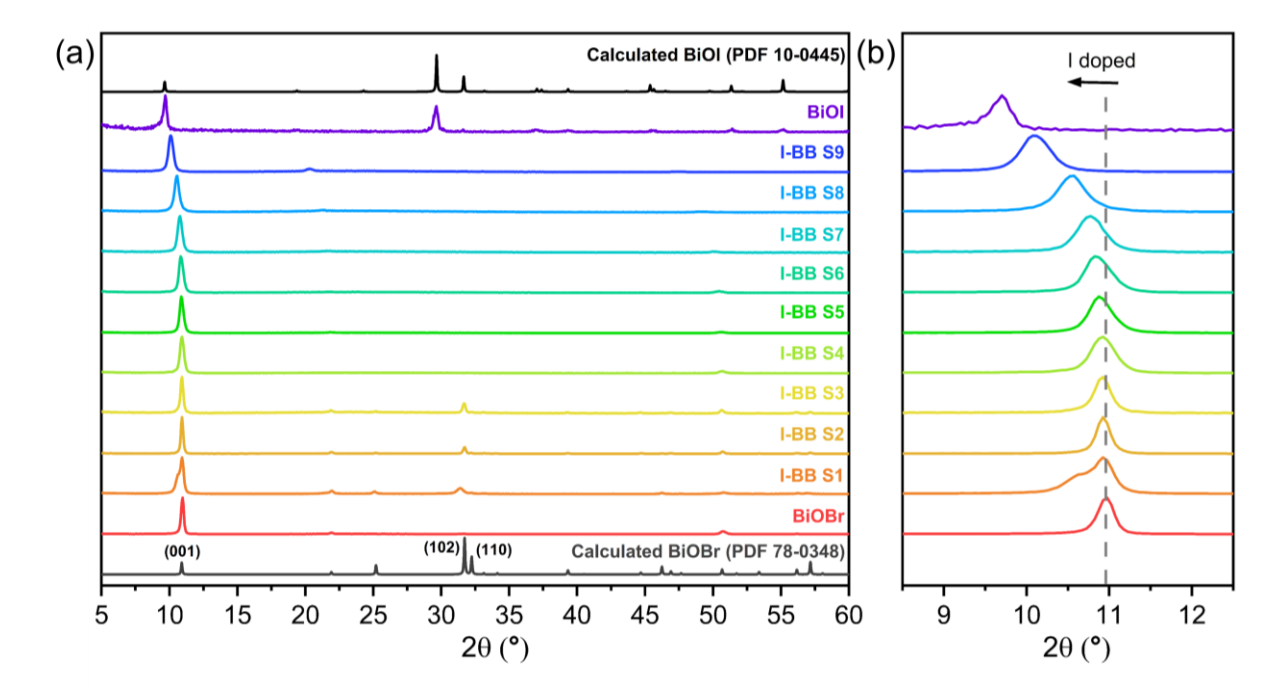


Figure 4-4. (a) GIXRD patterns and (b) enlarged patterns of BiOBr, BiOI and **I-BB** films deposited on glass.

The bulk composition of prepared samples was attempted to be determined by EDS and XRF. Unfortunately, due to peaks from Sn in the substrate overlapping significantly with the peaks from I in the film, it was inaccurate and difficult to acquire the bulk composition in EDS and XRF characterizations. Therefore, in this work, only high resolution XPS was utilized to study the surface composition of samples and the bulk composition was analyzed quantitatively through depth profile.

## 4.3.2 XPS analysis

The surface composition and elemental valence states of films were investigated using high resolution XPS. Firstly, films of parent materials, BiOBr and BiOI, were characterized. In Figure 4-5a, the peaks at 159.9 and 165.2 eV were assigned to the Bi  $4f_{7/2}$  and Bi  $4f_{5/2}$  spin-orbital splitting photoelectrons, respectively. The splitting between these bands was about 5.3 eV, indicating that bismuth was present in its normal Bi<sup>3+</sup> state.<sup>38</sup> In Figure 4-6a, peaks from Bi<sup>3+</sup> are at 159.3 eV and 164.6 eV for BiOI. In addition, secondary Bi  $4f_{7/2}$  peaks centred at 158.5 ( $\pm$  0.3) eV in BiOBr and BiOI originated from the existence of metallic bismuth, which is often observed in XPS due to the photoreduction of BiOX under incident X-rays.<sup>7,39</sup> The O 1s spectra of both pure films could be fitted into two peaks. The peak at 530.4 eV and 529.7 eV belongs to Bi-O bonds in the [Bi<sub>2</sub>O<sub>2</sub>]<sup>2+</sup> layer of BiOBr and BiOI respectively.<sup>40,41</sup> The other peaks at 531.3 eV for BiOBr and 531.7 eV for BiOI could be attributed to oxygen adhered on the surface.<sup>42,43</sup> Besides Bi and O elements presenting in both films, Br and I elements were observed in pure BiOBr and BiOI films separately, with peak positions comparable to previous reports.<sup>7,44</sup>

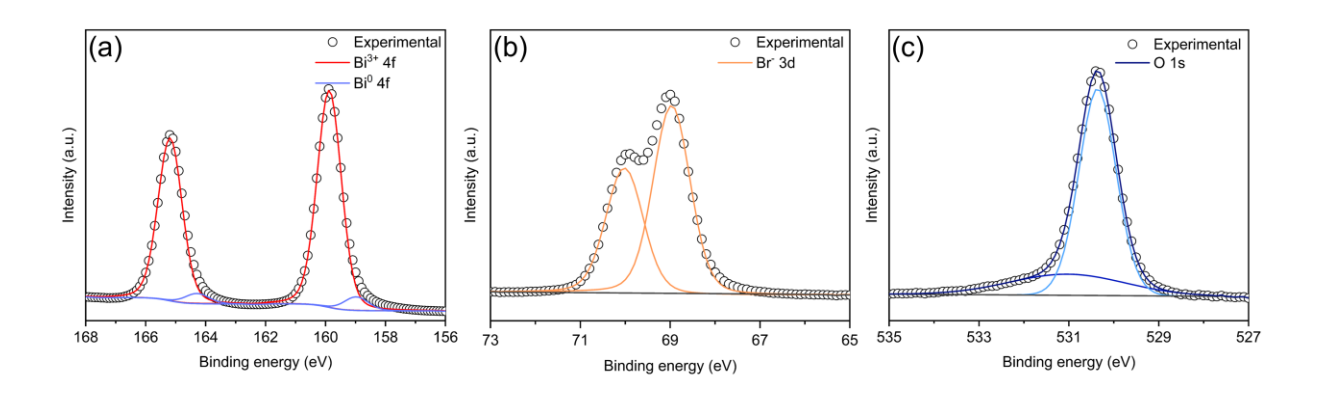


Figure 4-5. High resolution XPS spectra of the (a) Br 3d and (b) O 1s peaks from the BiOBr film on FTO.

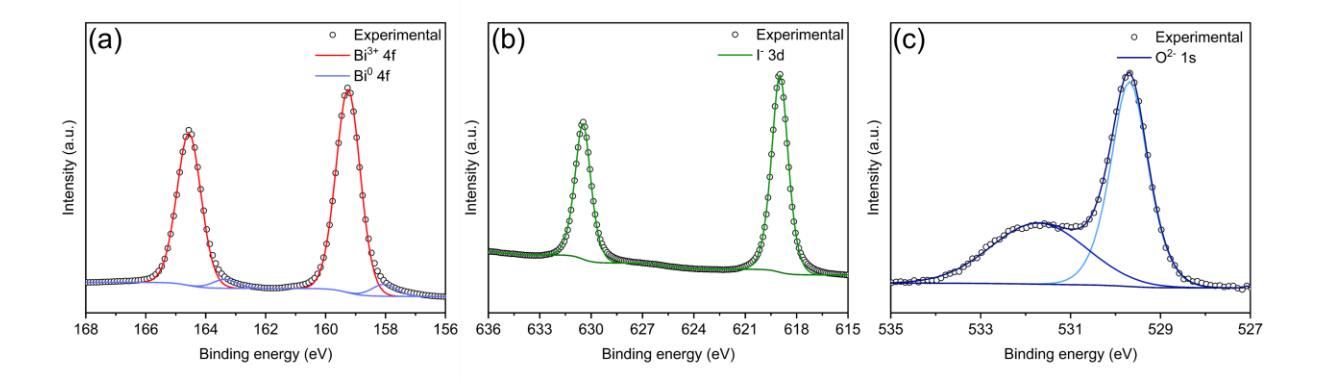


Figure 4-6. High resolution XPS spectra of the (a) Bi 4f, (b) I 3d and (c) O 1s peaks from the BiOI film on FTO.

Furthermore, the composition of all doped samples was characterized by XPS, where Bi, Br, O and I elements coexisted. Atomic ratios of Br and I in the I-BB films were calculated from high resolution XPS spectra of Br 3d and I 3d, and then summarized in Table 4-2. For the high resolution XPS spectra of I 3d (Figure 4-7), the signal produced I 3d<sub>5/2</sub> and I 3d<sub>3/2</sub> peaks centered at 619.0 eV and 630.5 eV respectively, indicating the existence of I- in all films. 7,45 In addition, obvious enhancement of the peak intensity of I 3d illustrated the increased dopant amount in I-BB films. During the formation of solid solutions, iodide was more difficult to be doped into the lattice structure compared with other halides, such as CI and Br, due to its large radius. 17 Meanwhile, in the AACVD process, heavier Bil<sub>3</sub> was harder to form the mist than BiBr<sub>3</sub>, leading to the loss of iodide source. Therefore, the dopant concentration in the deposited films was significantly lower than that in the precursor solutions. XPS depth profiling was carried out as well and showed that the peak intensity from I 3d decreased dramatically with the increased etching time, demonstrating that most of the iodide was distributed on the film surface (Figure 4-8). This surface accumulation of dopants might be favorable to improve the film performance in the heterogeneous photocatalysis which is a surface-based process.

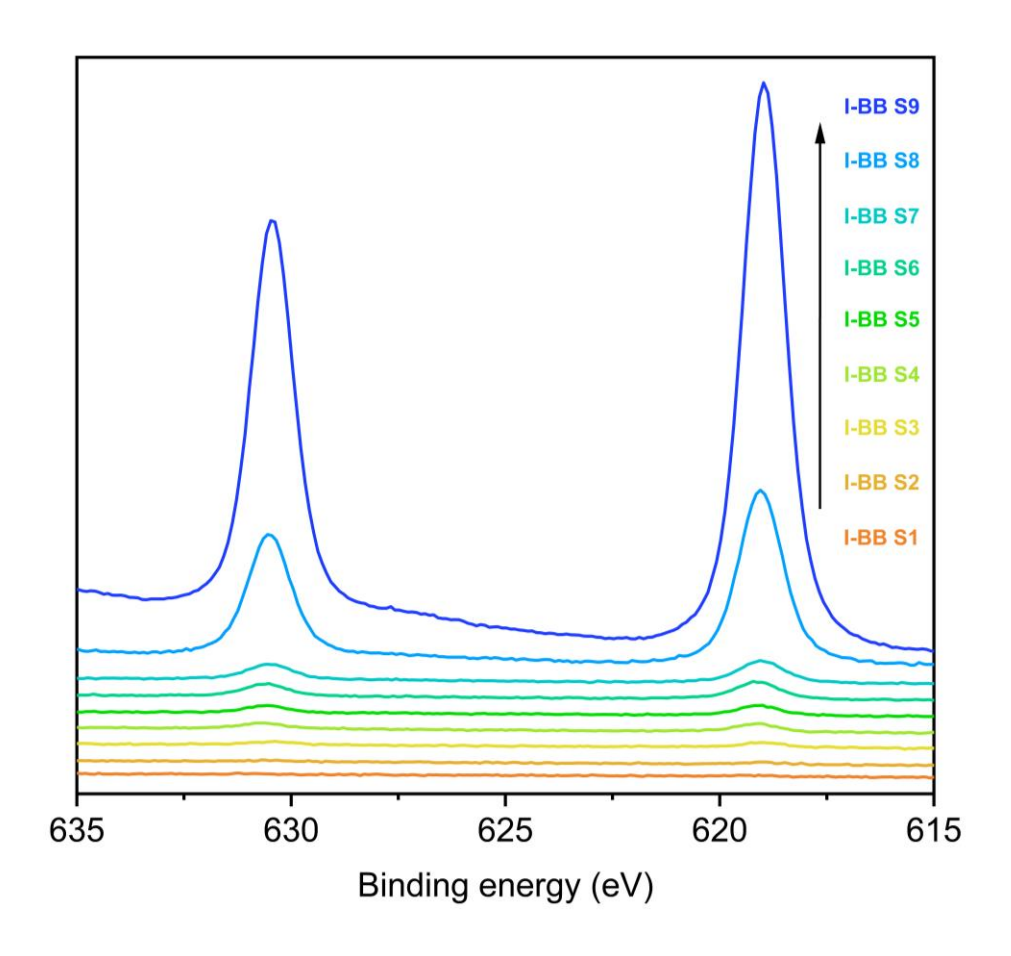


Figure 4-7. High resolution XPS spectra of I 3d of all I-BB samples on FTO.

Table 4-2. Atomic concentration of as-fabricated I-BB films on FTO.

	I-BB S1	I-BB S2	I-BB S3	I-BB S4	I-BB S5	I-BB S6	I-BB S7	I-BB S8	I-BB S9
Br	99.3%	99.0%	98.1%	97.3%	96.7%	94.7%	93.7%	89.1%	60.8%
I	0.7%	1.0%	1.9%	2.7%	3.3%	5.3%	6.3%	10.9%	39.2%

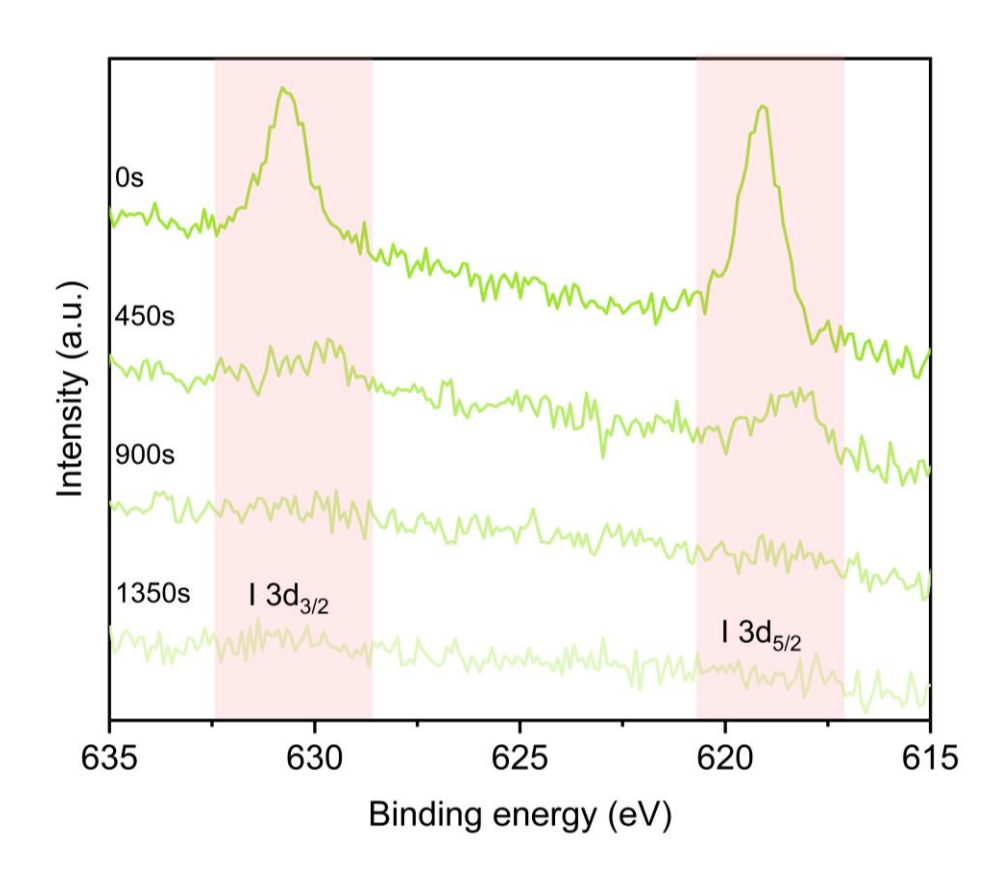


Figure 4-8. XPS depth profile analysis of I 3d from the I-BB S4 on FTO.

Using **I-BB S4** as a representative, XPS spectra of the doped samples were analysed in more details. Two peaks of Bi<sup>3+</sup> 4f centred at 159.7 eV and 165.0 eV could be assigned to the Bi  $4f_{7/2}$  and Bi  $4f_{5/2}$  respectively.<sup>39</sup> Similar to pure BiOBr and BiOI films, XPS peaks from Bi<sup>0</sup> were observed in the doped samples as well (Figure 4-9a). In addition, the Br 3d spectra were best fitted using two peaks corresponding to Br (Br  $3d_{5/2} = 68.7$  eV and Br  $3d_{3/2} = 69.8$  eV) (Figure 4-9b).

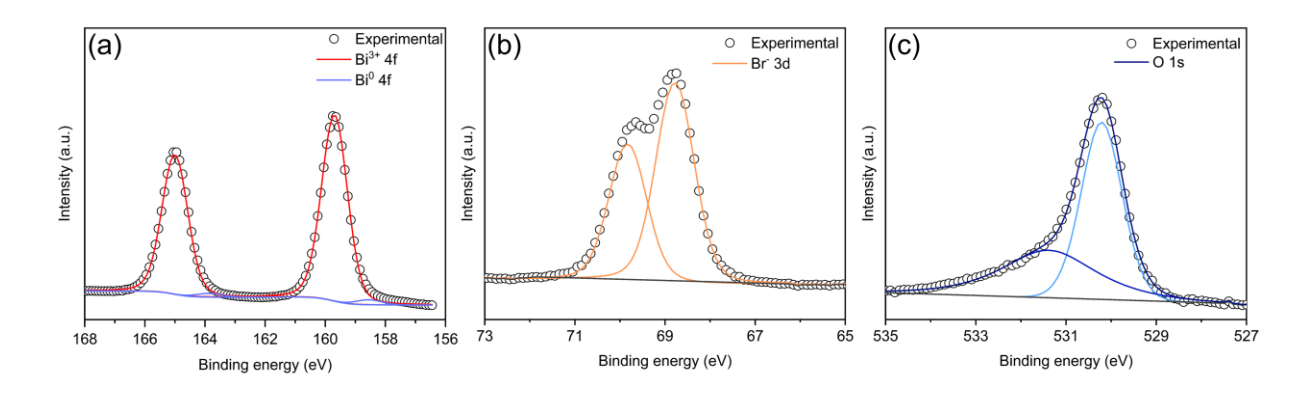


Figure 4-9. High resolution XPS spectra of (a) Bi 4f, (b) Br 3d and (c) O 1s from **the I-BB S4** film grown on FTO.

It was worth mentioning that, in Figure 4-10, peaks from Bi 4f in **I-BB** films, where **I-BB S4** acted as a representative, showed a shift to lower binding energy than those of pure BiOBr, indicating the existence of bismuth elements with lower valence states (Bi<sup>(3-x)+</sup>).<sup>44,46</sup> Bi<sup>(3-x)+</sup> is able to act as electron traps, benefiting the separation of the photogenerated charge carriers in the photocatalytic reaction.<sup>44</sup> In addition, it has been reported that oxygen vacancies (OVs) could be formed from the dangling bonds in [Bi<sub>2</sub>O<sub>2</sub>]<sup>2+</sup> layers caused by Bi<sup>(3-x)+</sup>.<sup>47</sup> The presence of OVs was further proved by the XPS spectra of O 1s (Figure 4-9c). As discussed above, the peak at 530.4 eV belonged to lattice O<sup>2-</sup>, and the other at 531.3 eV could be attributed to oxygen adsorbed at OV sites.<sup>47</sup> Furthermore, a significant enhancement of the O 1s signal at 531.3 eV was observed in **I-BB** films compared with that in pure BiOBr, indicating the greater concentration of OVs in **I-BB** samples.

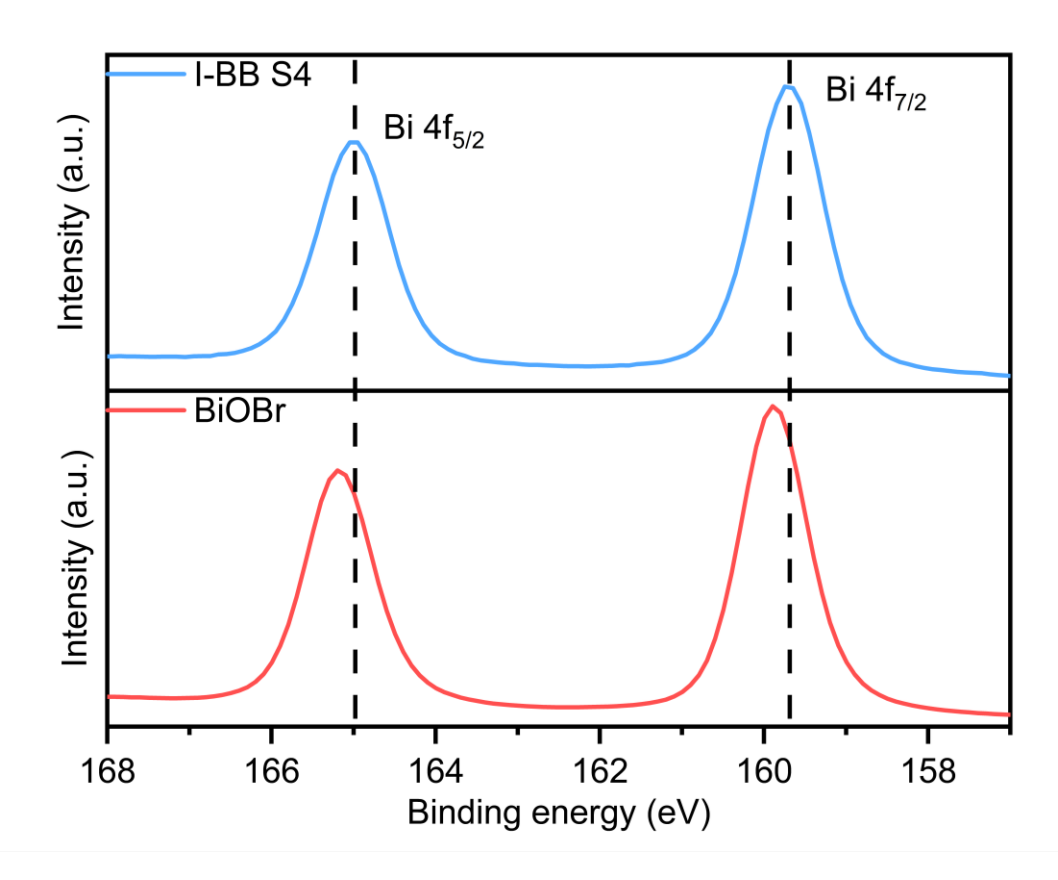


Figure 4-10. High resolution XPS spectra of Bi 4f from I-BB S4 and BiOBr on FTO.

In addition, the high resolution XPS of **I-BB** films deposited on glass was also performed to characterize the surface composition. XPS peaks of Bi 4f and Br 3d with comparable positions to those of the films on FTO were presented for the film on glass, with **I-BB S4** as the representative (Figure 4-11a, b). Besides the peak assigned to

the lattice oxygen anion (529.7 eV), a peak at 532.4 eV was observed in the O 1s spectra of the **I-BB S4** film on glass, which was not seen in any films on FTO (Figure 4-11c). This peak corresponded to hydroxyl groups absorbed on the film surface.<sup>48</sup> Therefore, different from FTO, there was no OVs formed in the film deposition process when the amorphous glass was used as the substrate.

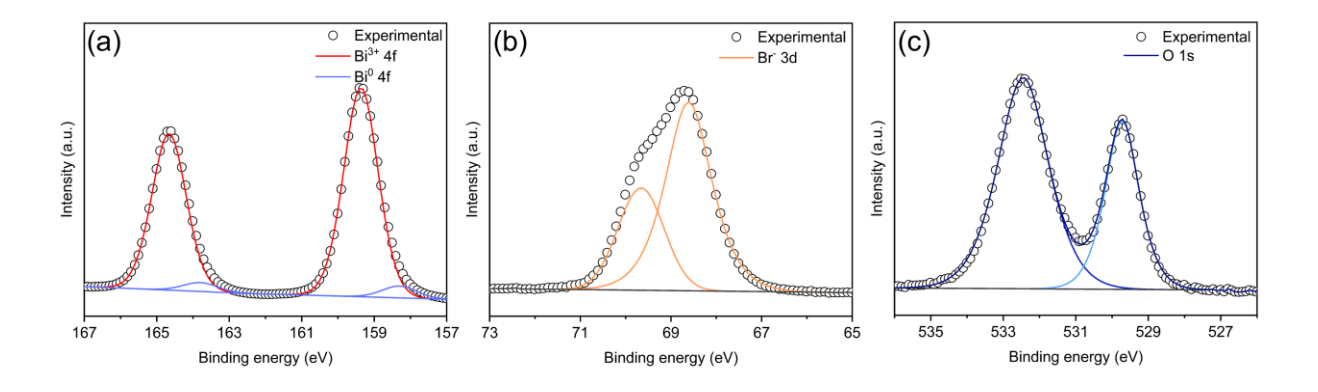


Figure 4-11. High resolution XPS spectra of (a) Bi 4f, (b) Br 3d and (c) O 1s from the **I-BB S4** film grown on glass.

Similar to the films on FTO, two I 3d peaks positioned at 618.9 eV and 630.4 eV were observed in the XPS spectra of films on glass and did not show any shift, demonstrating that iodide-doped BiOBr films were deposited successfully on glass (Figure 4-12). The gradually stronger peak intensity also proved that there was an increased dopant concentration in the deposited films with increasing the amount of Bil<sub>3</sub> in precursor solutions. Atomic ratios of Br and I in I-BB films on glass were calculated from XPS spectra as well, and then summarized in Table 4-3. However, through comparing the results calculated from XPS spectra of I-BB films on FTO and glass, it was found that the surface atomic concentration of iodide varied a lot in the deposited film even though the precursor solution with the same ratio of BiBr<sub>3</sub> and Bil<sub>3</sub> was used in the AACVD process. This variation was not unexpected because it was hard to control the dopant concentration in the final film. Any small difference in the fabrication process is possible to have a dramatic influence on the film composition.

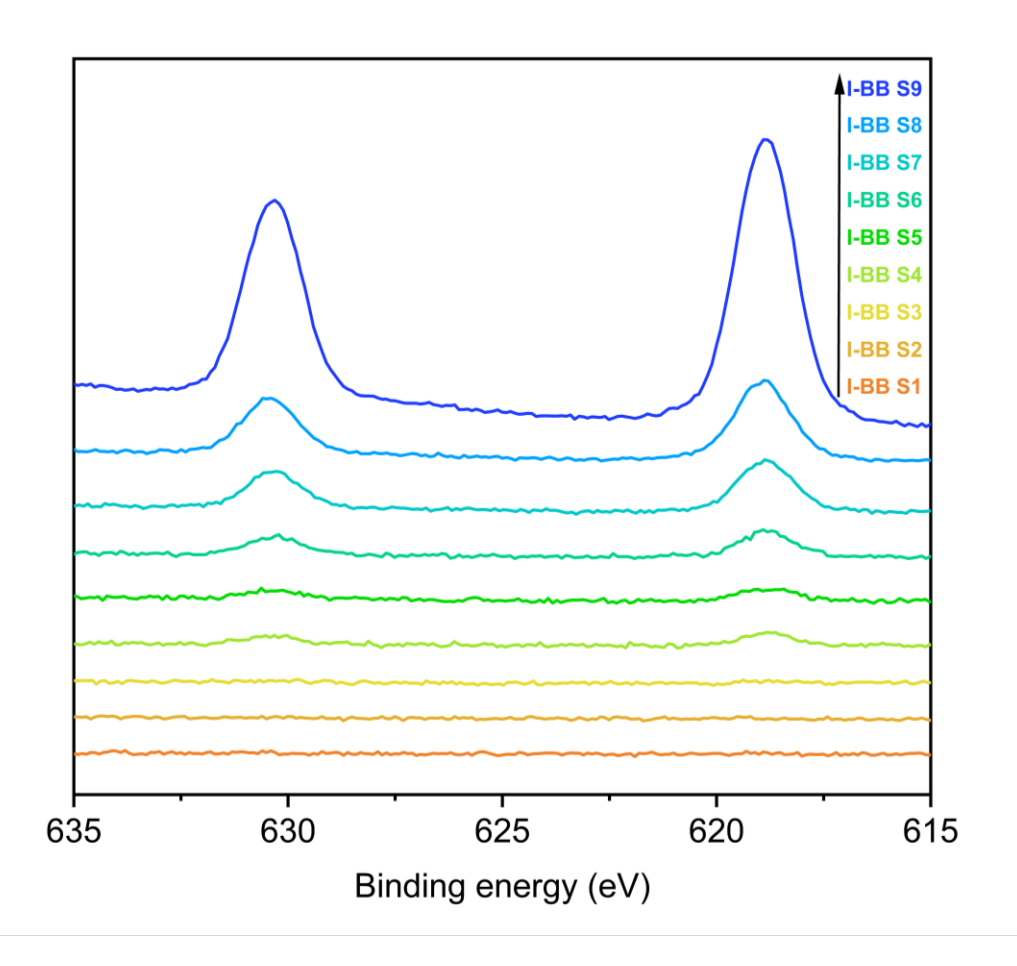


Figure 4-12. High resolution XPS spectra of I 3d of all I-BB samples on glass.

Table 4-3. Atomic concentration of as-fabricated **I-BB** films on glass.

	I-BB S1	I-BB S2	I-BB S3	I-BB S4	I-BB S5	I-BB S6	I-BB S7	I-BB S8	I-BB S9
Br	~100%	~100%	99.1%	97.2%	95.7%	90.4%	82.2%	64.1%	33.3%
ı	_	-	0.9%	2.8%	4.3%	9.6%	17.8%	35.9%	66.7%

# 4.3.3 Film morphology

Top-down and cross-sectional SEM was used to study the surface morphology and the thickness of films deposited on FTO respectively (Figure 4-13 and Figure 4-14). Firstly, for both parent materials and doped ones, all films deposited on FTO featured compact and uniform plate-shape grains. These square nanoplatelets are typical for BiOX because their structures are composed of [Bi<sub>2</sub>O<sub>2</sub>]<sup>2+</sup> and halide slabs.<sup>49</sup> Considering the smaller calculated average crystallite size from GIXRD patterns (

Table 2-1), the particle size observed in top-down SEM images indicated that nanograins in the as-fabricated films were constituted by multiple crystallites. Significant morphological differences in film surfaces were observed among BiOBr, BiOI and I-BB samples. Varied from the original morphology of BiOBr, the grain edges observed in doped films became sharper with the increased amount of doped iodide. In addition, the grain size of films decreased from ~1.3 μm to ~0.5 μm. Until the concentration of I⁻ in the film increased to 39.2 at%, which was observed in I-BB S9, the surface morphology was closer to BiOI rather than BiOBr. A similar trend was also reported in other iodide-doped BiOX.<sup>17</sup> Furthermore, the slightly variation in the film thickness was found in the cross-sectional images of all samples, where the film thickness was around 400 nm. It was determined that the dopant amount did not have an effect on the thickness of the deposited films, and thus in the next measurements of the light absorption and photocatalytic performance, the influence from the film thickness could be excluded.

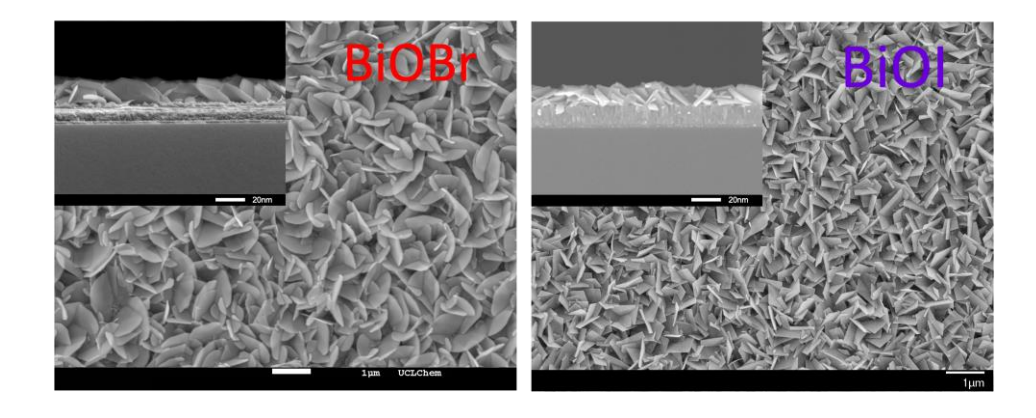


Figure 4-13. Top-view SEM and inserted side-view SEM images of BiOBr and BiOI on FTO.

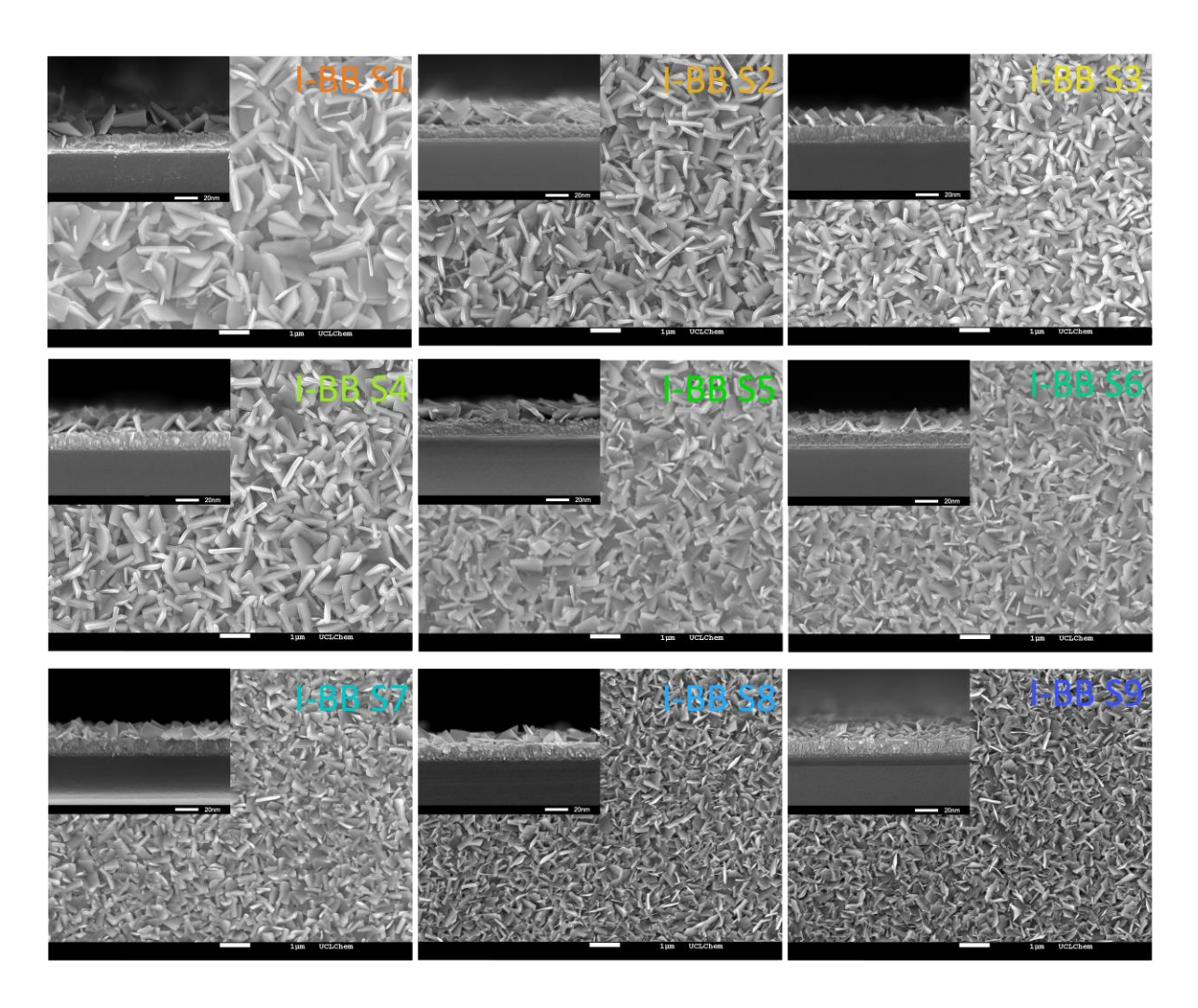


Figure 4-14. Top-view SEM and inserted side-view SEM images of I-BB S1, I-BB S2, I-BB S3, I-BB S4, I-BB S5, I-BB S6, I-BB S7, I-BB S8 and I-BB S9 on FTO.

However, dramatically different from films deposited on FTO, the surface morphology of films deposited on glass, especially doped samples, exhibited poor coverage and limited grain growth (Figure 4-15 and Figure 4-16). As determined from XPS results, the dopant concentration of the deposited films on glass was much lower than that of the film on FTO. For **I-BB S1** on glass, its surface morphology is almost the same with that of undoped BiOBr due to the extremely low dopant concentration. In addition, it could be seen from top-view SEM images that the surface morphology became patchier with more iodide doped into the film. The grain shape in films on glass also varied a lot from those on FTO. This difference could be contributed to the different preferential growth orientation observed in the GIXRD patterns (Figure 4-2 and Figure 4-4). Compared with films on FTO, films grown on glass showed dominantly exposed (001) facets, leading to the formation of sharper and thinner particles.<sup>11</sup>

Furthermore, the poor coverage of iodide-doped BiOBr films on glass is likely resulted from the poorer precursor solution droplet attachability on the amorphous glass substrate than crystalline FTO, which was shown in **Chapter 2** with the contact angle of DMF on glass (45.8°) being much larger than that on FTO (12.9°). Considering the poor coverage of films on glass, no side-view SEM images were collected. In addition, the further measurements on surface roughness, optical properties, and photocatalytic activities only focused on the superior films deposited on FTO and not glass.

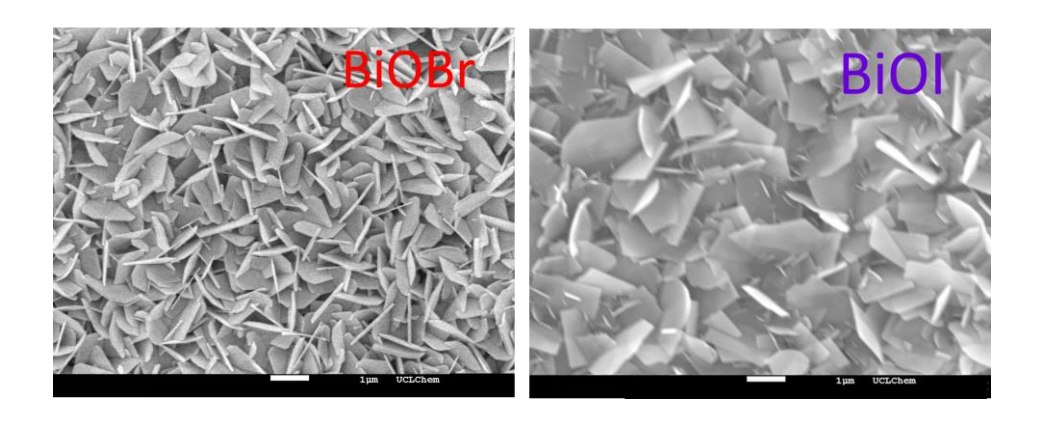


Figure 4-15. Top-view SEM images of BiOBr and BiOI on glass.

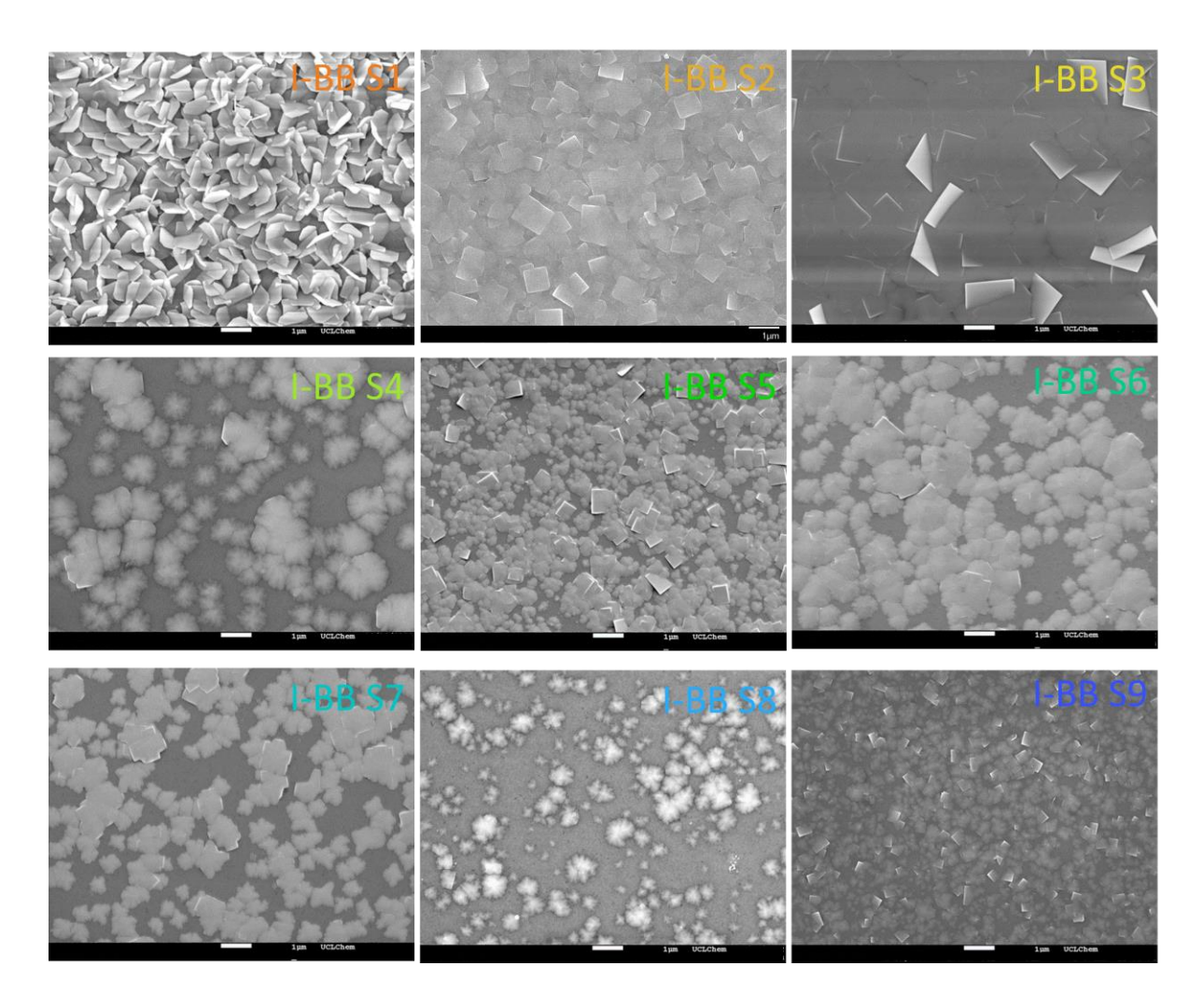


Figure 4-16. Top-view SEM images of I-BB S1, I-BB S2, I-BB S3, I-BB S4, I-BB S5, I-BB S6, I-BB S7, I-BB S8 and I-BB S9 on glass.

## 4.3.4 Surface roughness

The surface roughness of films is one of the important influence factors in heterogeneous photocatalytic processes.<sup>50</sup> As a result, the surface roughness of the parent materials and all doped films deposited on FTO were studied herein by AFM (Figure 4-17 and Figure 4-18), and the calculated roughness factors are summarized in Table 4-4. It was found that the surface roughness decreased slightly with increased dopant amount. This mild decrease is likely resulted from the more compact and dense film growth induced by smaller grains in the doped films, which was shown in SEM images as well.

It has been reported that powder BiOBr<sub>x</sub>I<sub>1-x</sub> solid solutions with larger specific surface areas showed better photocatalytic efficiency due to richer reactive sites.<sup>51</sup> However,

in this work, the roughest BiOBr film, whose roughness factor was 2.03, did not show the highest activity in visible-light photocatalysis. In addition, which would be discussed in the following part, the change trend of photocatalytic activities no matter under UV or visible light was not in accordance with that of roughness factors. Therefore, this indicated that the dramatic difference in UV-light or visible-light photocatalytic activities could not be attributed to the marginal difference in specific surface areas of samples. This observation contrary to the previous research is possibly because of the difference in sample forms, where the effect of the specific surface area on the photocatalytic performance in films is weaker than in powders.

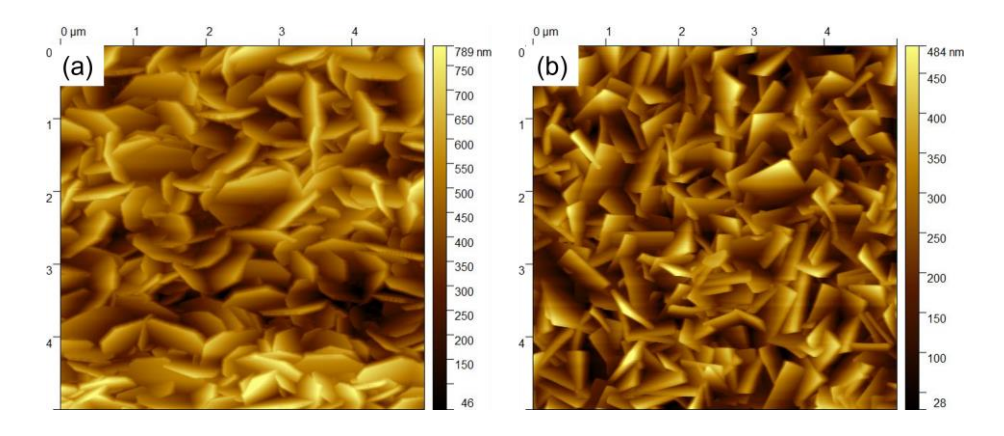


Figure 4-17. AFM images of (a) BiOBr and (b) BiOI films. Both images were of a 5 x 5 µm square area.

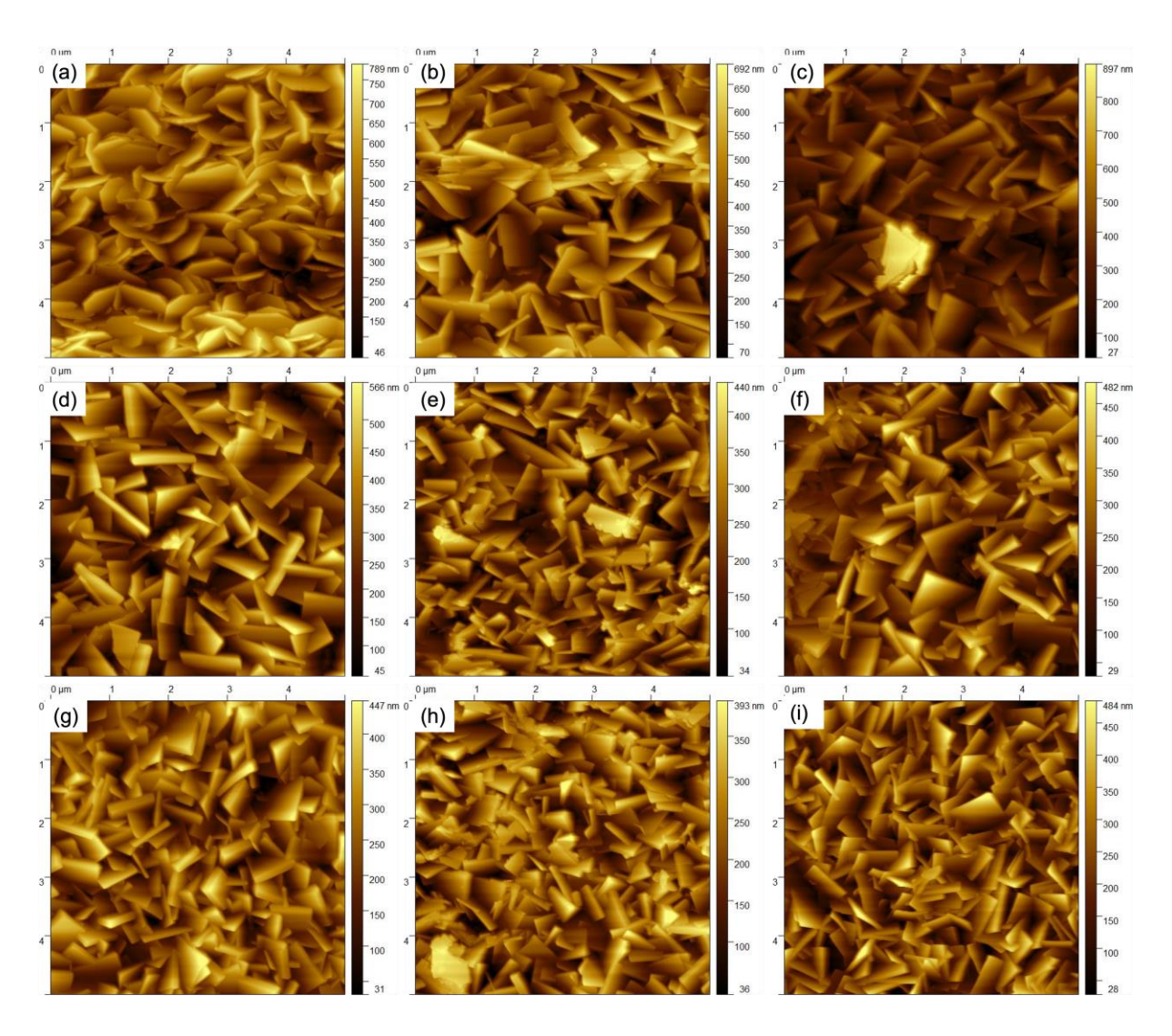


Figure 4-18. AFM images of (a) **I-BB S1**, (b) **I-BB S2**, (c) **I-BB S3**, (d) **I-BB S4**, (e) **I-BB S5**, (f) **I-BB S6**, (g) **I-BB S7**, (h) **I-BB S8** and (i) **I-BB S9** on FTO. All images were of a 5 x 5  $\mu$ m square area.

Table 4-4. Roughness factors of films on FTO calculated from AFM images.

	BiOBr	I-BB S1	I-BB S2	I-BB S3	I-BB S4	I-BB S5	I-BB S6	I-BB S7	I-BB S8	I-BB S9	BiOI
Roughness factor	2.03	1.87	1.83	1.70	1.67	1.54	1.48	1.52	1.54	1.59	1.76

# 4.3.5 Optical properties and band gap calculations

The optical properties of BiOBr, BiOI and doped samples deposited on FTO were investigated using UV-Vis transmittance spectroscopy (Figure 4-19). The BiOBr film

had a high transmission degree of visible light, with a band edge at ~400 nm. This poor visible-light harvesting is one drawback limiting BiOBr in practical photocatalytic applications. However, successive redshifts of the absorption edges from 400 nm to 550 nm were observed for films with increased concentration of I<sup>-</sup> dopants which is gradually closer to that of BiOI (~600 nm). This edge shift is also in accordance with the colour variation of iodide-doped BiOBr films from white to yellow then to orange. This indicated that, while not as good as BiOI, these iodide-doped BiOBr films processed a wider absorption range in visible light, and the visible-light (>400 nm) absorption ability was reinforced as well. Therefore, compared with pure BiOBr, a larger part of solar light could be utilized by **I-BB** films in the photocatalytic process.

In addition to the position of band edges, the band edge shapes of **I-BB** films and parent materials also showed some differences. The sharp edges at 400 nm and 600 nm were observed for BiOBr and BiOI respectively, which could be attributed to the intrinsic transition from the valence band (VB) to the conduction band (CB).<sup>52</sup> However, the **I-BB** films showed absorption edges with long tails, which is a characteristic of doped semiconductors.<sup>32,53</sup> This indicated that the impurity level was formed in the forbidden band through I<sup>-</sup> doping. These tails could be attributed to the transition between the I *5p* level above the original VB and CB.<sup>54</sup>

Furthermore, optical band gaps of as-deposited films were calculated through the Tauc plot method which was mentioned in **Chapter 2** (Figure 4-20), considering that BiOBr, BiOI and doped ones are indirect semiconductors (n=1/2), and summarized in Table 4-5.<sup>4,16</sup> The experimental band gaps of BiOBr and BiOI were 2.72 eV and 1.79 eV respectively, which was consistent with the reported values.<sup>7</sup> Compared with undoped BiOBr, a small amount of I<sup>-</sup> dopant was able to cause the redshift of the optical band gaps. The band gap started to decrease to 2.61 eV with only 0.7 at% I<sup>-</sup> in the film of I-BB S1, and then to 2.44 eV for I-BB S4 with 2.7 at% dopant, finally to 2.01 eV for I-BB S9 with the dopant concentration of 39.2 at%. This decline trend determined that the optical band gaps of deposited films could be tailored through adjusting the doping amount of I<sup>-</sup> in BiOBr. At the same time, this trend also proved that the continuous iodide-doped BiOBr films were deposited successfully *via* AACVD.

Computational work of BiOX has been reported that the valence band maximum (VBM) is largely composed of X np states, and the condition band minimum (CBM) is

mainly contributed by the Bi 6p state.<sup>4,35,54</sup> Therefore, while the CBM would not change a lot, even a trace amount of doped I<sup>-</sup> with the lower electronegativity could make the VBM position of BiOBr shift up sensitively, leading to the reduced band gap.<sup>55</sup> In addition, the existence of OVs, which was determined by XPS, could narrow the band gap as well.<sup>56</sup>

In BiOBr<sub>x</sub>I<sub>1-x</sub> solid solutions, the VB edge potential ( $E_{VB}$ ) can be estimated by the following empirical equation:

$$E_{VB} = \chi - E_e + 0.5E_g \tag{2}$$

where  $\chi$  is the absolute electronegativity which is the geometric mean of the electronegativity of atoms constituting the semiconductor,  $E_e$  is the free-electron energy on the hydrogen scale (~4.5 eV), and  $E_g$  is the experimental band gap of the semiconductor.

The narrower band gap is able to broaden the visible-light absorption scale, which could make electrons easier to be photoexcited. Therefore, more charge carriers could be generated, favouring the enhancement of photocatalytic activity. However, based on the above equation,  $E_{VB}$  of the semiconductor would decrease with smaller  $E_g$ , leading to the weakened redox ability of photogenerated electrons and holes. In addition, a narrowed band gap also benefits the recombination of electron-hole pairs. The competition among these factors results in the nonlinear variation of the photocatalytic activity under both UV- and visible-light with the increased I concentration in **I-BB** films, which will be discussed further in the next part.

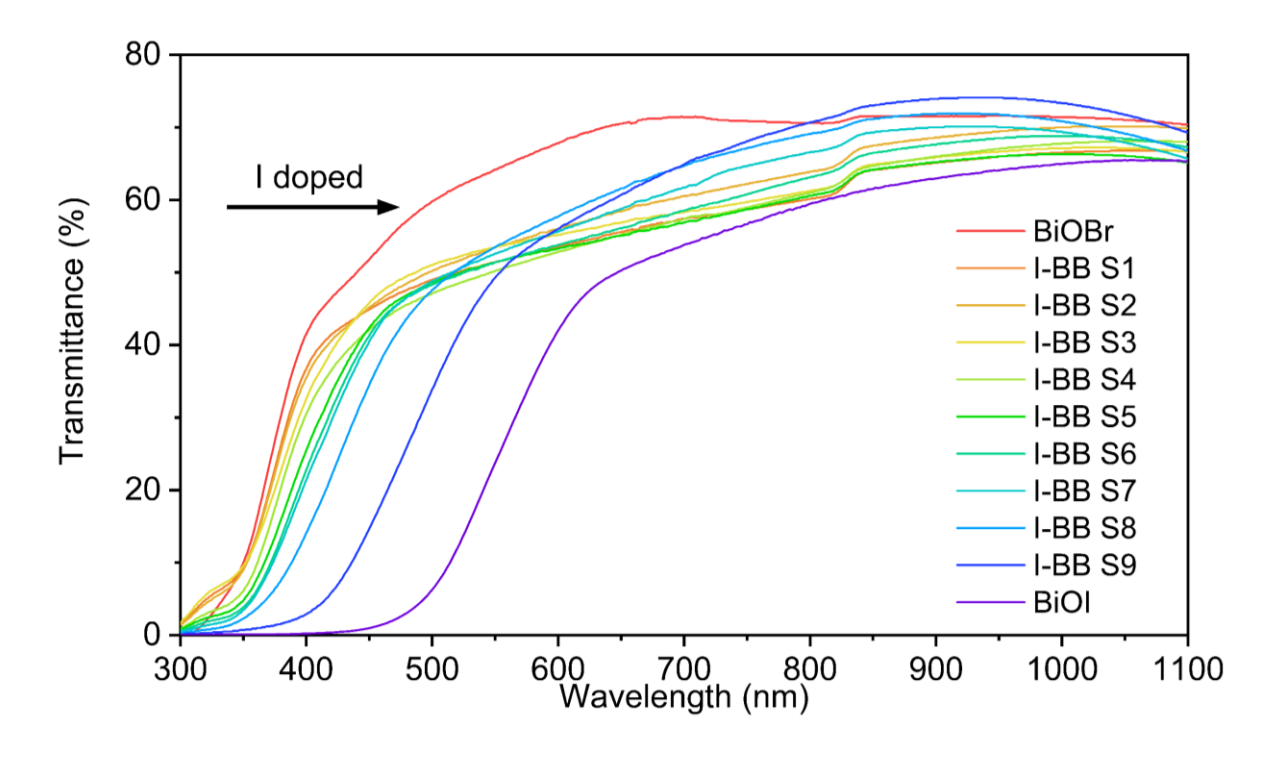


Figure 4-19. UV-Vis transmittance spectra of BiOBr, BiOI and **I-BB** films deposited on FTO.

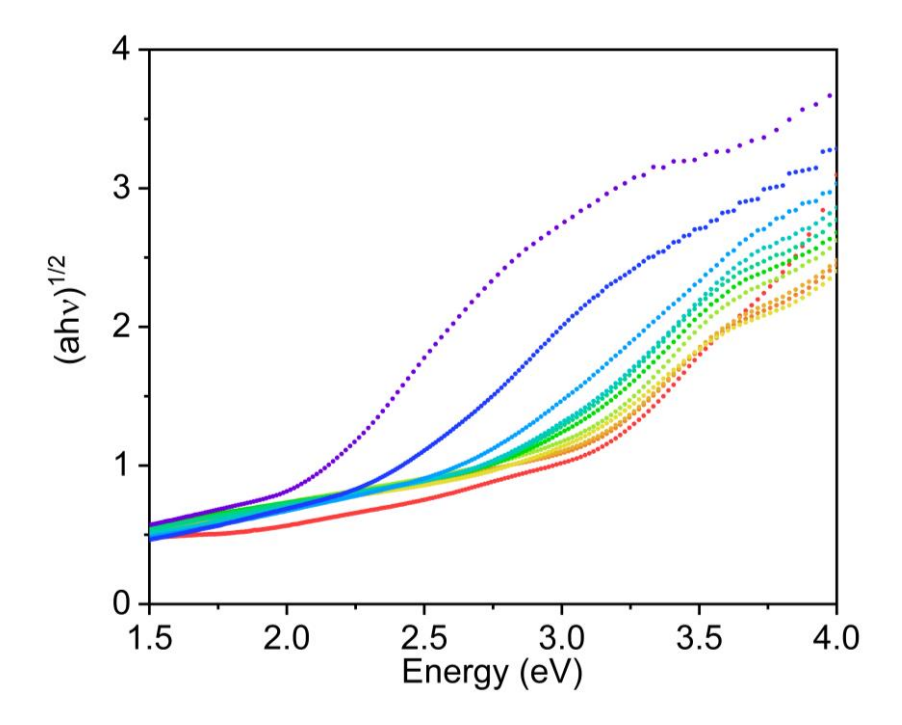


Figure 4-20. Optical band gaps were calculated through the Tauc plot method.

Table 4-5. Optical band gaps of BiOBr, BiOI and I-BB films deposited on FTO.

	BiOBr	I-BB S1	I-BB S2	I-BB S3	I-BB S4	I-BB S5	I-BB S6	I-BB S7	I-BB S8	I-BB S9	BiOI
Bandgap (eV)	2.72	2.61	2.59	2.46	2.44	2.42	2.40	2.34	2.19	2.01	1.79

### 4.3.6 Photocatalysis test

The photocatalytic performance of the as-prepared **I-BB** films and parent materials were investigated by the *smart Rz* ink under visible light (450 nm and 627 nm LED irradiation). The photocatalytic reaction was monitored through the digital photographic method. Digital images of the *Rz* ink coated on films were recorded as a function of irradiation time ranging from 0 to 990 s with the interval of 30 s.

In the degradation process of a dye, the following steps are possibly involved: (1) photocatalytic degradation, (2) dye photolysis<sup>58</sup> and (3) dye-photosensitization<sup>59–61</sup>. However, dye photolysis and dye-photosensitization are non-photocatalytic processes and lead to the dye-bleaching. These would happen if the dye was irradiated with a light source comprising a remarkable level of photons with wavelengths which can be strongly absorbed by the dye. In the dye-photosensitization process by a light with sufficient energy, *hv*, the electronic excitation of the dye, D, is normally involved, and then the electron would be injected into the CB of the semiconductor, SC. The electron finally reacts with the oxidizing agent, Ox, in the system, such as O<sub>2</sub> and H<sub>2</sub>O<sub>2</sub>. The whole process could be expressed:

$$D \xrightarrow{hv} D^* \xrightarrow{SC} D^{+*} + SC(e^-) \xrightarrow{Ox} D^{+*} + Ox^-$$

where D<sup>++</sup> is the oxidized radical of the dye which is unstable and could react to produce colourless products further.<sup>62</sup>

Firstly, the test under 627 nm irradiation (1.32 mW·cm<sup>-2</sup>) was carried out. It was observed that the dye was slowly bleached on both blank FTO substrate and **I-BB S5** film, and no pink *resorufin (Rf)*, which is the reduced form of *Rz*, was generated (Figure 4-21). In addition, the bleaching rate was largely independent of the type of underneath

semiconductors. Furthermore, there was a significant sacrificial electron donor, glycerol, in the prepared *smart Rz* ink, which inhibits a dye-photosensitization process. As a result, it was determined that this dye bleaching under 627 nm irradiation was caused *via* dye photolysis rather than dye-photosensitization.<sup>62</sup>

Besides 627 nm, the photocatalytic performance of samples was measured under 450 nm irradiation (2.01 mW·cm<sup>-2</sup>) as well. Figure 4-23 showed a set of recorded images for blank FTO, BiOBr, **I-BB** samples and BiOI in first 450 s. No colour change was observed for the ink on FTO, but **I-BB** samples on FTO, especially **I-BB S4**, coated with the ink demonstrated a smooth colour change from royal blue to pink over the entire area. This indicated that, under 450 nm illumination, the *Rz* ink was stable and the FTO substrate had no photocatalytic activity for this ink. The different behaviors of the *Rz* ink under two kinds of light could be explained through comparing the emission spectra of 450 nm and 627 nm LED and the absorption spectrum of the blank FTO with ink coating, where a significantly larger amount of 627 nm light could be absorbed by the coating than the 450 nm light (Figure 4-22). This meant that dye photolysis is unlikely to happen under 450 nm irradiation. Therefore, the colour change of the ink observed in this situation was only due to the photocatalytic degradation induced by underneath semiconducting films.

Derived from the below recorded images, a series of R<sub>t</sub> values *vs.* the irradiation time t, could be obtained, and the plots of all measured films are illustrated in Figure 4-24. It was found that among all samples, **I-BB S4** with 2.7 at% I<sup>-</sup> doping reached the plateau of the plot first and showed the highest photocatalytic activity. At 300 s, the plot of **I-BB S4** showed a clear peak where the film colour stopped changing, indicating the blue *Rz* dye was completely reduced to pink *Rf*, corresponding to what is shown in Figure 4-23. In addition, this also demonstrated that, compared with the plots of both parent materials, doping I<sup>-</sup> within a specific percentage range into BiOBr was able to improve the visible-light photocatalytic performance of materials effectively.

In order to compare the ink degradation rate of all samples intuitively and quantitively, the formal quantum efficiency (FQE) was calculated as well from the R<sub>t</sub> vs. t plots. With the increased I<sup>-</sup> amount, the FQEs improved first and then declined gradually, where **I-BB S4** with the optimal performance was able to degrade the Rz dye at a rate of  $1.09 \times 10^{-19}$  photons<sup>-1</sup>·cm<sup>2</sup>·s, compared to  $1.60 \times 10^{-20}$ ,  $5.29 \times 10^{-20}$ ,  $5.42 \times 10^{-20}$ ,

 $6.64 \times 10^{-20}$ ,  $5.01 \times 10^{-20}$ ,  $3.34 \times 10^{-20}$ ,  $6.33 \times 10^{-21}$  and  $2.37 \times 10^{-21}$  photons<sup>-1</sup>·cm<sup>2</sup>·s for **I-BB S1**, **I-BB S2**, **I-BB S3**, **I-BB S4**, **I-BB S5**, **I-BB S6**, **I-BB S7**, **I-BB S8** and **I-BB S9** respectively. The pure BiOBr  $(1.14 \times 10^{-20} \text{ photons}^{-1} \cdot \text{cm}^2 \cdot \text{s})$  and BiOI  $(2.17 \times 10^{-20} \text{ photons}^{-1} \cdot \text{cm}^2 \cdot \text{s})$  was almost one and three orders of magnitude lower respectively in FQEs than **I-BB S4**. One of the reasons for the poor photocatalytic activity of BiOBr herein was its low absorption capacity of the visible-light illumination with 450 nm wavelength, which was shown in Figure 4-19. Differently, the degradation rate of BiOI was inappreciable over the investigated time limits, which was possible due to the ultra-rapid recombination of photogenerated charge carriers in BiOI induced by its narrow bang gap.<sup>63</sup>



Figure 4-21. Images of the Rz ink coating on I-BB S5 (upper) and FTO (lower).

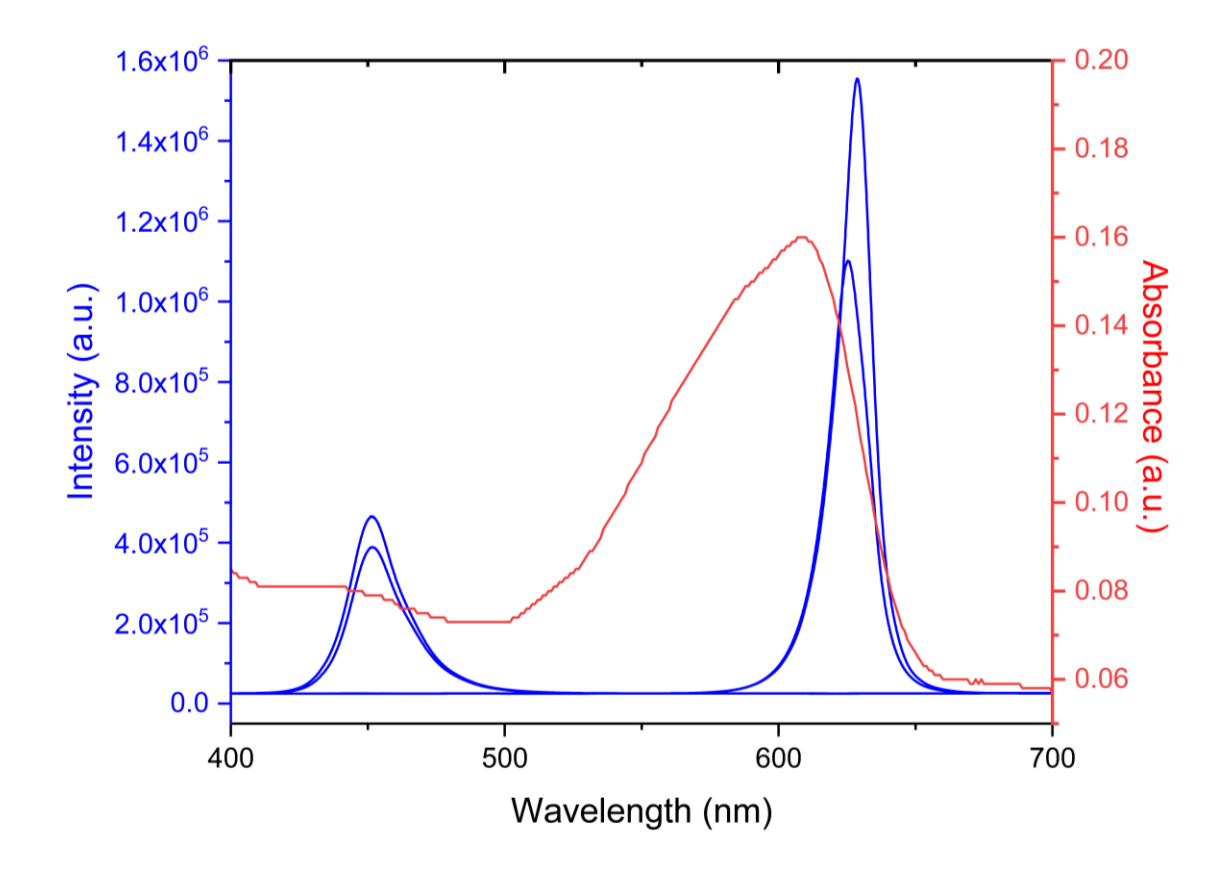


Figure 4-22. The absorption spectrum (red) of the *smart Rz* ink coated on blank FTO. The blue lines illustrate the emission spectra of the 450 nm and 627 nm LED.

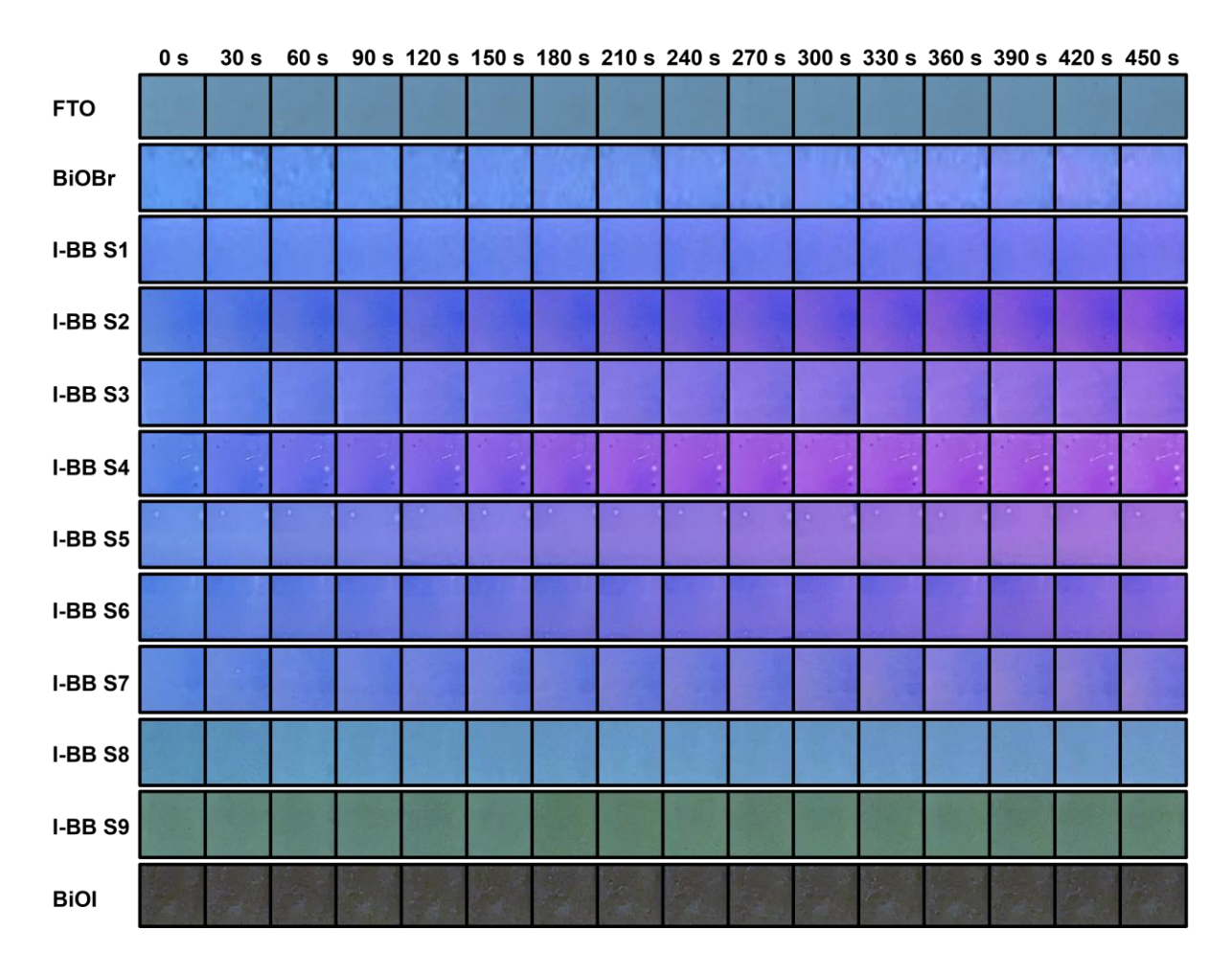


Figure 4-23. Images of the *Rz* ink coating on FTO, BiOBr, **I-BB** samples and BiOI under 450 nm LED irradiation.

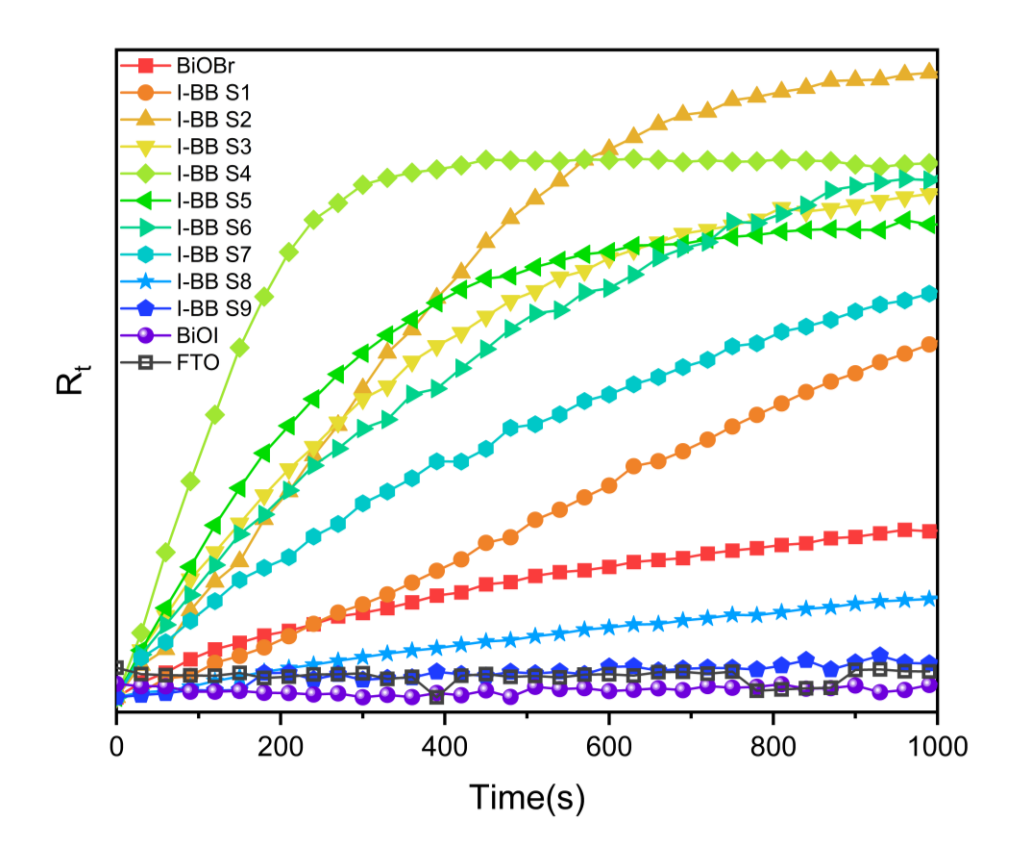


Figure 4-24.  $R_t$  vs. t plots of the Rz intelligence ink on BiOBr, BiOI and **I-BB** films deposited on FTO under 450 nm LED irradiation.

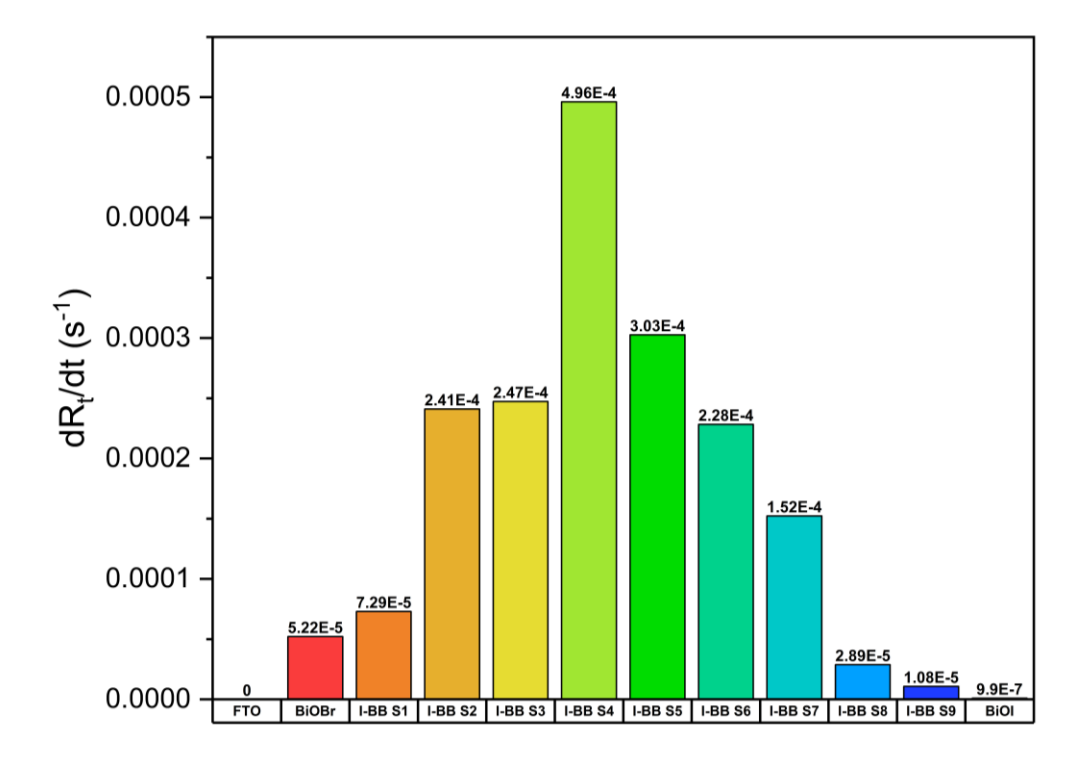


Figure 4-25. Rates of *Rz* conversion (dR<sub>t</sub>/dt) of FTO, BiOBr, **I-BB** and BiOI films deposited on FTO under 450 nm LED irradiation.

For the purpose of the comprehensive investigation of the photocatalytic activity of samples, the UV light source (365 nm LED irradiation, 2.87 mW·cm<sup>-2</sup>) was utilized in the photocatalysis measurements as well. The colour change under 365 nm LED irradiation was much faster than that of 450 nm LED due to the stronger input power of the light source and the higher absorption capacity of tested samples at the wavelength of 365 nm. Therefore, in the UV-light photocatalysis test, digital images of the *Rz* ink on BiOBr and **I-BB S1-S7** films were recorded from 0 to 720 s with the interval of 10 s in first 240 s, then changed with the interval of 30 s (Figure 4-26). However, for less active samples, such as **I-BB S8**, **I-BB S9** and BiOI, the interval of the taken images was kept at 30 s.

The colour change of all samples in the first 150 s is shown in Figure 4-26. Similar to the 450 nm irradiation, there was no decomposition of Rz on FTO under 365 nm illumination, so the dye photolysis was negligible. However, the variation trend of the colour change rate among samples was dramatically different from the result obtained from 450 nm irradiation, where the pure BiOBr exhibited the fastest colour change rather than **I-BB S4**. Furthermore, due to the high photocatalytic activity of BiOBr, not only from blue Rz to pink Rf, the colour change from pink Rf to colourless dihydroresorufin (HRf), the further reduced form, was also observed.

R<sub>t</sub> vs. t plots under 365 nm LED irradiation was generated from relative images as well and shown in Figure 4-27. Like observed in the images, at 30 s, BiOBr was the first to reach the plateau of the plot followed by other **I-BB** samples, showing the completed conversion of *Rz* to *Rf*. After that, the R<sub>t</sub> value started to decrease, indicating the formation of colourless *HRf*.

Whereas, due to the extremely close slopes of plots, it was difficult to compare the photocatalytic performance of all samples accurately. Therefore, FQEs of BiOBr, **I-BB** and BiOI films was also calculated from Rt vs. t plots under 365 nm LED irradiation, where BiOBr processing the highest FQE of  $8.86 \times 10^{-18}$  photons<sup>-1</sup>·cm<sup>2</sup>·s (Figure 4-28). The FQEs of **I-BB S1-S3** decreased gradually from  $7.39 \times 10^{-18}$  photons<sup>-1</sup>·cm<sup>2</sup>·s to  $4.62 \times 10^{-18}$  photons<sup>-1</sup>·cm<sup>2</sup>·s. However, not keeping the monotonical decrease with the increased iodide dopant concentration, an increase in the FQE (6.71  $\times 10^{-18}$  photons<sup>-1</sup>·cm<sup>2</sup>·s) was observed for **I-BB S4**. Afterwards, the decline trend of FQEs existed again for **I-BB S5-S9**, from  $3.87 \times 10^{-18}$  photons<sup>-1</sup>·cm<sup>2</sup>·s to  $4.35 \times 10^{-21}$ 

photons<sup>-1</sup>·cm<sup>2</sup>·s. BiOI still showed the lowest FQE under 365 nm irradiation, because the recombination rate of charge carriers was independent of the excitation wavelength. <sup>64</sup>

As determined in UV-Vis transmittance spectra (Figure 4-19), all samples could strongly absorb 365nm light and then be excited to generate charge carriers with the incident energy (3.40 eV) higher than their bandgap energies. Therefore, BiOBr with the most positive VB edge potential would show the best photocatalytic activity due to the strongest oxidation ability.<sup>54</sup> Interestingly, although the VBM rises as I concentration increasing, the photocatalytic activity did not deteriorate monotonically for **I-BB** films in this work, but **I-BB S4** showed an abnormal improvement.

As mentioned before, the VBM position of BiOBr<sub>x</sub>I<sub>1-x</sub> is sensitive to the I<sup>-</sup> concentration. With the relatively stable CBM position, the uplift of VB edge position through doing I<sup>-</sup> in BiOBr could narrow the band gap to enhance the ability of visible-light harvesting, but at the expense of the oxidation ability of holes in VB. Therefore, two competitive factors did not induce the visible-light photocatalytic performance of **I-BB** samples to improve monotonically with the increase of the dopant amount but to reach a maximum at **I-BB S4** with the iodide concentration of 2.7 at%. <sup>65</sup> However, for the photocatalytic test under UV illumination, when all samples can utilize the incident light, the rate of the *Rz* ink decomposition did not decrease with the upshifting VB edge potential, but suddenly increased for **I-BB S4**, suggesting that apart from the edge position of VB, there were some other factors influencing the photocatalytic activity of iodide-doped BiOBr.

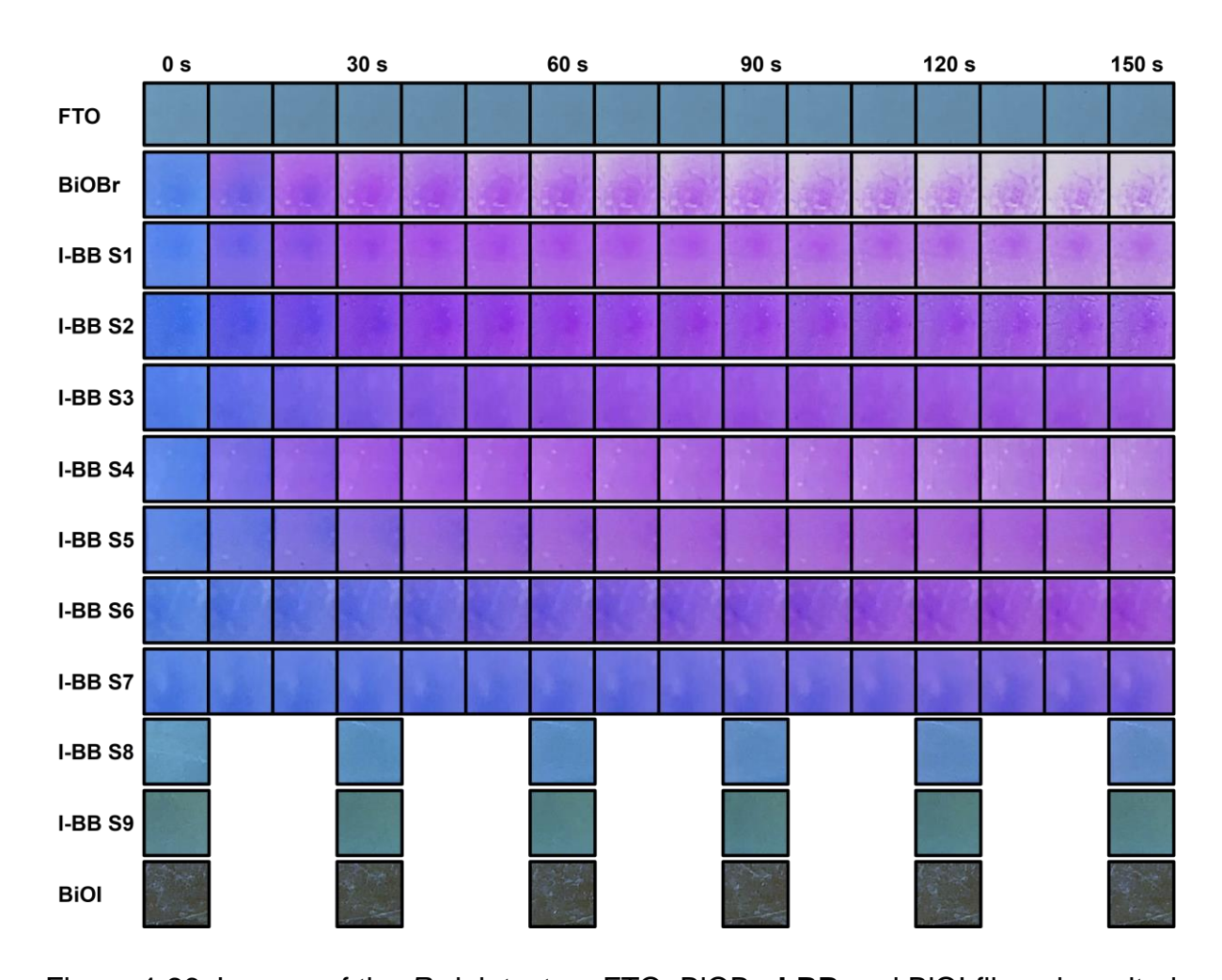


Figure 4-26. Images of the *Rz* ink test on FTO, BiOBr, **I-BB** and BiOI films deposited on FTO under 365 nm LED irradiation.

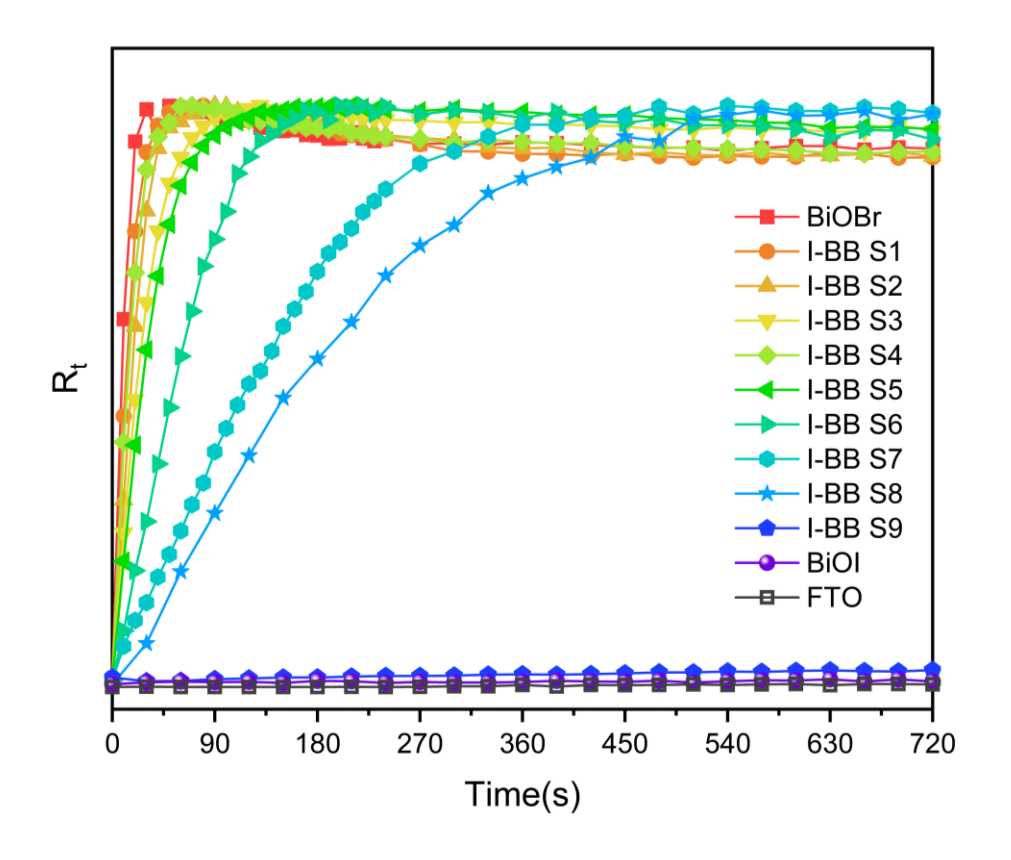


Figure 4-27.  $R_t$  vs. t plots of the Rz ink test on FTO, BiOBr, **I-BB** and BiOI films deposited on FTO under 365 nm LED irradiation.

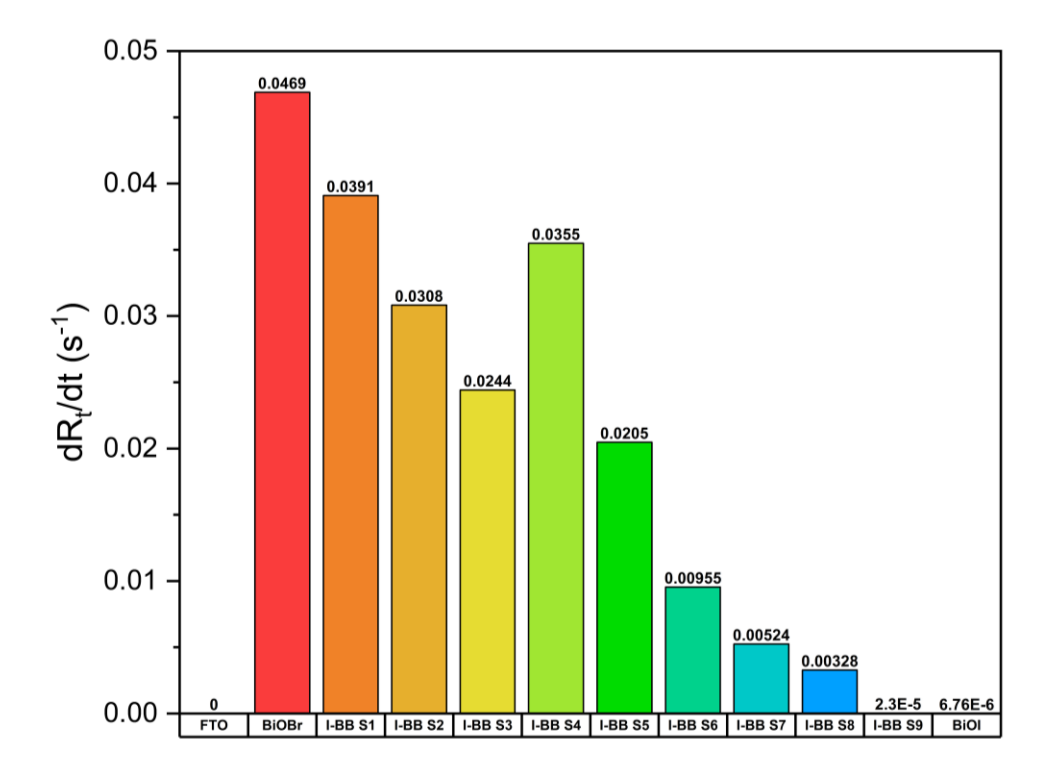


Figure 4-28. Rates of *Rz* conversion (dR<sub>t</sub>/dt) of FTO, BiOBr, **I-BB** and BiOI films deposited on FTO under 365 nm LED irradiation.

### 4.3.7 Photoluminescence spectroscopy

PL spectroscopy was used to gain a deeper insight into the improved photocatalytic performance of **I-BB** films. Electrons would be excited from VB to CB with a higher energy level when semiconductors are irradiated by the light with the energy larger than their bandgap energy, leaving holes in VB. However, these photogenerated electrons are unstable in the excited state, and tend to recombine with holes after jumping back to the ground state, which can produce PL emissions. As a result, the weaker PL emission intensity indicates less recombination and better separation efficiency of photogenerated electron-hole pairs.<sup>66</sup>

In Figure 4-29, both pure BiOBr and BiOI did not show PL emission, demonstrating that there was no radiative recombination of photogenerated charge carriers in BiOBr and BiOI due to their indirect band features. Similar observations have also been reported in other works. 47,67-70 On the contrary, for **I-BB** samples, due to impurity states generated by I dopant, intense fluorescence peaks were observed. In Figure 4-29, **I-BB S1** exhibited the strongest PL emission. With I<sup>-</sup> concentration increasing, the peak intensity declined and reached the lowest for I-BB S4. However, as the amount of I<sup>-</sup> exceeding 2.7 at%, the PL emission strengthen again. This suggested that **I-BB S4** processed the least recombination of photogenerated charge carriers. This trend is consistent with the results in the above photocatalytic tests. However, when the I<sup>-</sup> concentration increased above 10.9 at% (I-BB S8), the PL peak did not keep being more intense. There was even no PL emission observed for I-BB S9 with 39.2 at% I<sup>-</sup>, similar to BiOI. This decrease in PL emission showed that nonradiative recombination tended to dominate in I-BB S8 and I-BB S9 with the excess of dopant sites.<sup>71</sup> These nonradiative transitions could reduce the lifetime of excited charge carriers, leading to poor photocatalytic activities of I-BB S8 and I-BB S9 shown in smart ink measurements under both visible and UV light (Figure 4-24 and Figure 4-27).<sup>72</sup> In addition, the PL peaks of **I-BB** samples red-shifted gradually with the increased I dopant concentration, showing that the transition band gap was narrowed, which was conducive to the absorption of photons with longer wavelength. This observation also corresponded to the variation in optical band gaps of **I-BB** samples shown in Figure 4-20. It is worth mentioning that all peaks exhibited in the PL emission spectra were centered at 600-625 nm but not 450-500 nm which were more often reported. 56,73,74 The reason of this difference is that these peaks at 600-625 nm were

characteristic emissions from the OVs-induced defect states in BiOBr,<sup>11,47</sup> which further gave evidence of the existence of OVs in **I-BB** samples discussed in the XPS part.

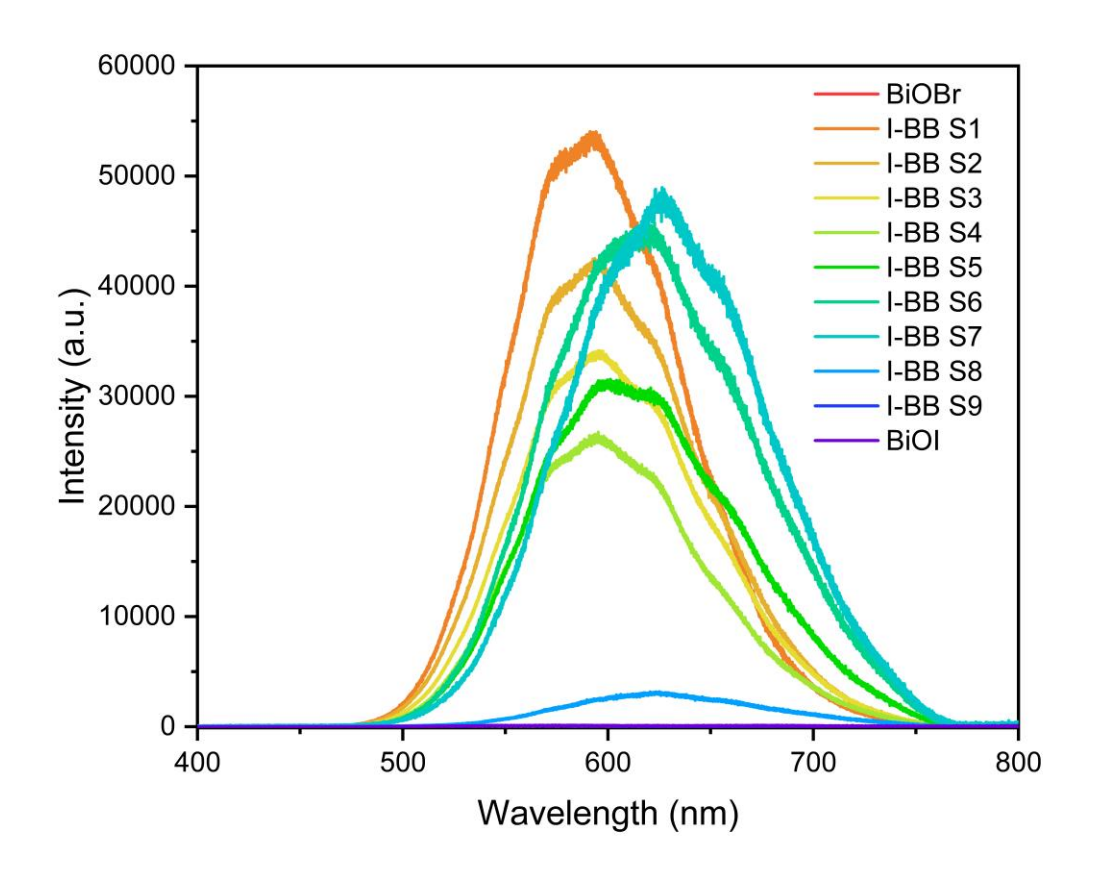


Figure 4-29. Photoluminescence spectra excited at 325 nm of BiOBr, BiOI and **I-BB** films deposited on FTO.

#### 4.3.8 Photoelectrochemical measurements

Besides PL spectra, PEC measurements were carried out for BiOBr, **I-BB** and BiOI films as well because the PEC performance of semiconductors could reveal the separation efficiency of the photogenerated charge carriers.<sup>75</sup> In Figure 4-30, as photoanodes, all of the films deposited on FTO displayed a reversible and positive transient photocurrent response with different intensities during three on/off intermittent visible-light irradiation cycles. It was demonstrated that the transfer of photogenerated charge carriers and electron collection were achieved for these samples within the PEC cell.<sup>24</sup> In addition, photocurrents of all films changed slightly

in the three cycles, indicating their great photo-response stability. Among all **I-BB** samples, **I-BB S2-S6** generated higher photocurrent intensities than both pure BiOBr and BiOI, and **I-BB S4** showed the strongest photocurrent signal. It was proved that through doping I<sup>-</sup> into BiOBr within a specific concentration range, the PEC activity of the materials could be improved. In addition, the variation trend of transient photocurrents was in accordance with that of photocatalytic performance (Figure 4-25). The strongest transient photocurrent intensity of **I-BB S4** indicated the dramatically strengthened separation efficiency and extended lifetime of photogenerated charge carriers in **I-BB S4**, and thus the optimized activity was obtained in the photocatalytic decomposition of the *Rz* ink. <sup>76,77</sup> Furthermore, the better visible-light harvesting ability of **I-BB** films than pure BiOBr, which was shown in Figure 4-19, was favorable to increase the quantity of photogenerated charge carriers, which was also one of reasons for the more intense photocurrent response.

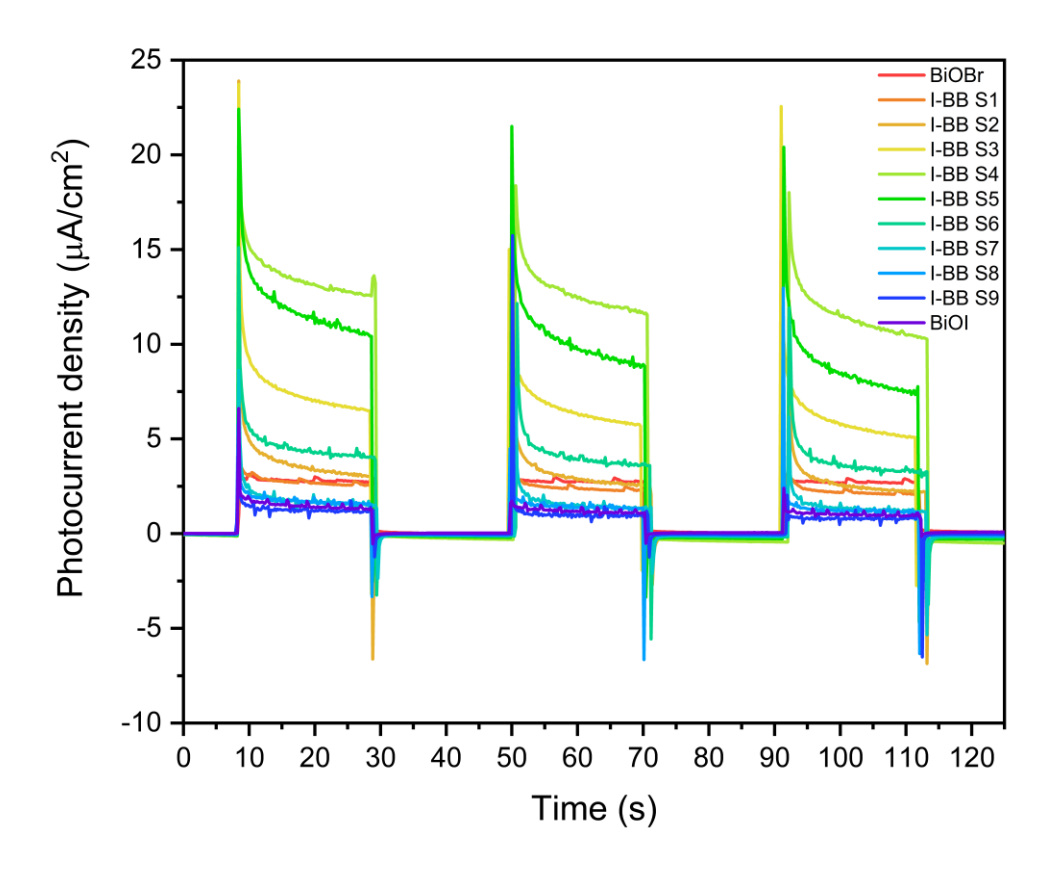


Figure 4-30. Transient photocurrent response of BiOBr, BiOI and **I-BB** films deposited on FTO.

JV curves were collected for BiOBr, BiOI and **I-BB** samples under on/off illumination with the voltage swept from 0.11 V<sub>RHE</sub> to 1.10 V<sub>RHE</sub>, where the photocurrent density

increased steadily with the increased voltage (Figure 4-31 and Figure 4-32). BiOBr showed the photoanode current of 4.9 nA·cm<sup>-2</sup> at 1.0 V<sub>RHE</sub> with the onset potentials of ~0.33 V<sub>RHE</sub> due to the poor absorption of visible light. Starting from **I-BB S1** with 0.7 at% I<sup>-</sup>, the photocurrent density increased gradually, and the onset potential shifted negatively with the increased dopant concentration. Until the I<sup>-</sup> concentration up to 2.7 at% (**I-BB S4**), the lowest onset potential was observed at ~0.25 V<sub>RHE</sub>, and the photocurrent density increased by almost 10 times (46.5 nA·cm<sup>-2</sup> at 1.0 V<sub>RHE</sub>) compared to undoped BiOBr, which attributed to the faster separation and better transfer capacity of charges. Then, the PEC performance of **I-BB S5-S9** declined and became closer to that of BiOI. BiOI showed an extra low photoanode current (2.6 nA·cm<sup>-2</sup> at 1.0 V<sub>RHE</sub>) with the onset potential of ~0.81 V<sub>RHE</sub>, which was resulted from the serious charge recombination.

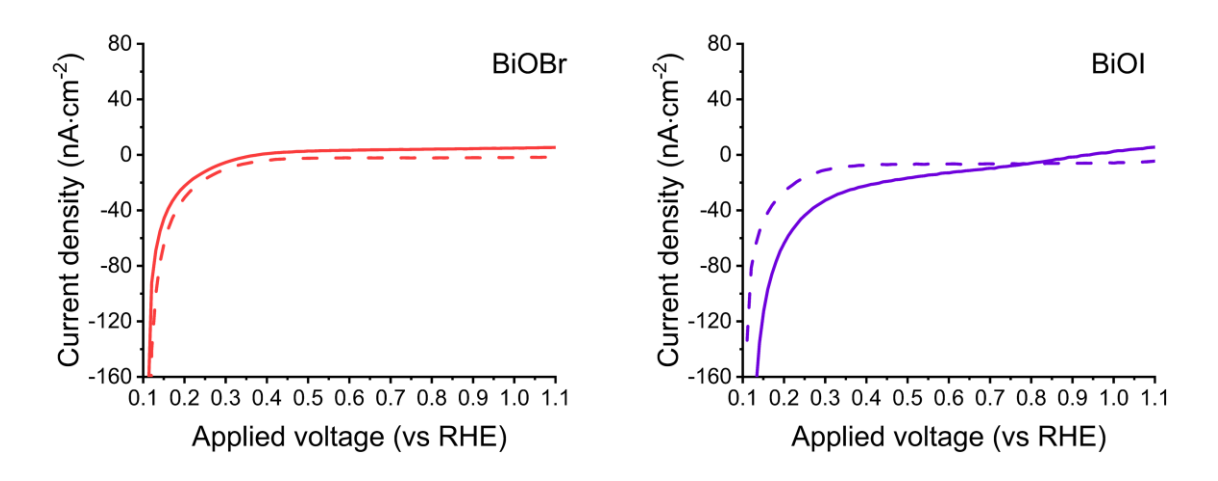


Figure 4-31. JV curves of BiOBr and BiOI films on FTO were measured with front-side illumination (1 sun illumination, solid lines) and in the dark (dashed lines). The voltage was swept from 0.11  $V_{RHE}$  to 1.10  $V_{RHE}$  at a rate of 10 mV·s<sup>-1</sup>.

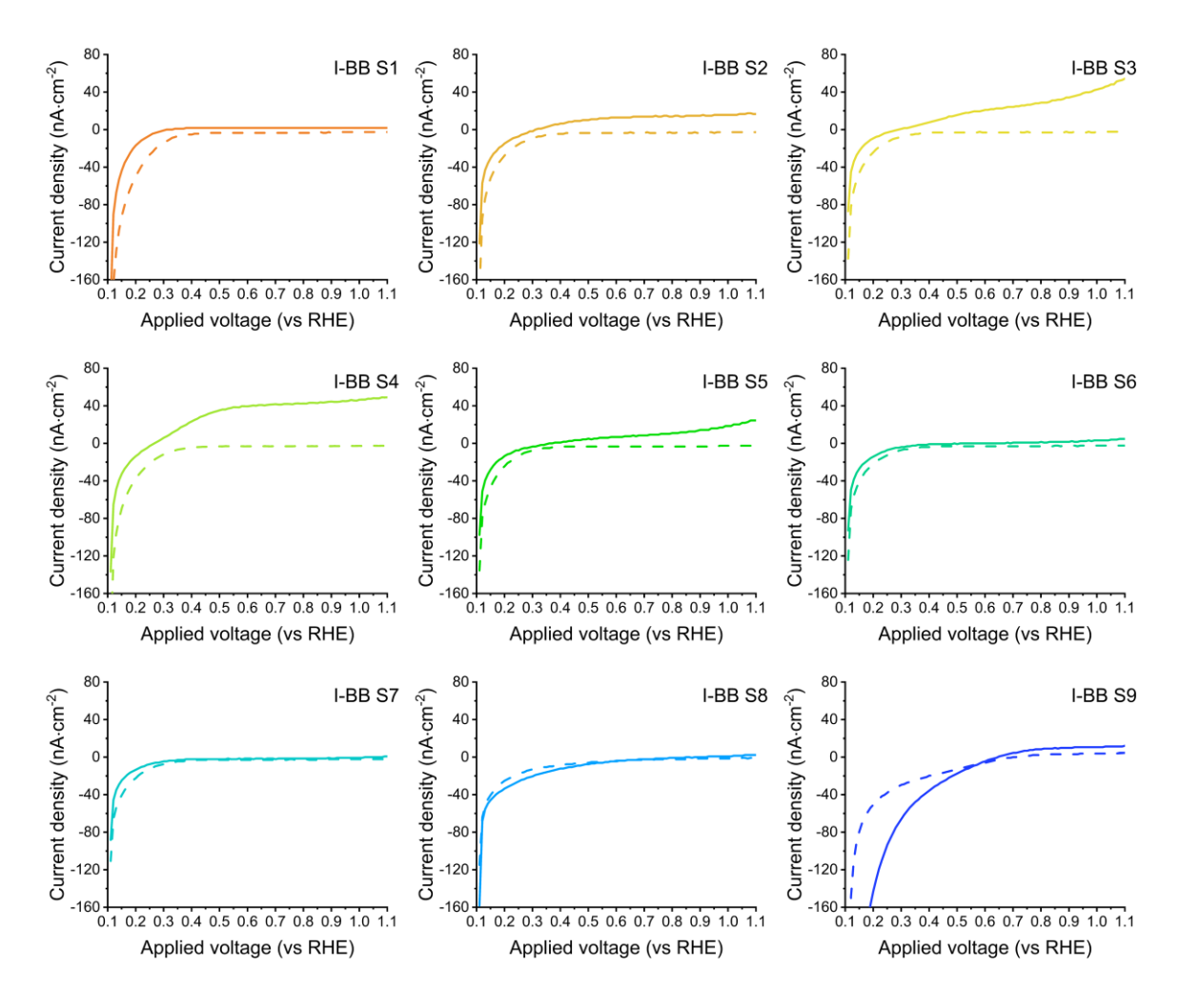


Figure 4-32. *JV* curves of **I-BB** films on FTO were measured with front-side illumination (1 sun illumination, solid lines) and in the dark (dashed lines). The voltage was swept from 0.11 V<sub>RHE</sub> to 1.10 V<sub>RHE</sub> at a rate of 10 mV·s<sup>-1</sup>.

Based on the above analysis of both PL and PEC measurements, the improved separation and transfer behaviors of the photogenerated charge carriers in **I-BB** samples, especially **I-BB S4**, were highlighted. Meanwhile, the reasons behind the variation trend of the photocatalytic performance of samples were revealed as well. It has been reported that, through doping I<sup>-</sup> into BiOBr, the hybridization of Br 4p and I 5p orbitals could reduce the mobility of photoinduced holes significantly, while have little impact on the mobility of electrons. <sup>56,78</sup> In addition, impurity defects generated from the disorders in the crystal structure were able to be as trap centers for charge carriers. <sup>79</sup> All of these effects were able to facilitate the charge carrier separation. Furthermore, the presence of OVs in the as-fabricated **I-BB** films could influence the charge separation efficiency as well. In the photocatalytic process, OVs could act as

electron acceptors, leading to the prolonged lifetime and promoted interfacial transfer of photogenerated electrons and holes.<sup>11</sup>

However, the optimal concentration of the iodide dopant should exist because excess dopants could act as recombination centers and weakened the separation of photoinduced electron-hole pairs, leading to an impaired photocatalytic activity.<sup>32</sup> Furthermore, due to the intrinsic layer structure of BiOX, an internal electric filed could be formed. As obtained from GIXRD results (

Table 2-1), *c* values grew with more I<sup>-</sup> doped into BiOBr, indicating the enlarged interlayer space. Therefore, the distance for the transportation of photogenerated charge carriers driven by the internal electric field would become longer, against the efficient separation of charge carriers.<sup>80</sup> Consequently, through doping I<sup>-</sup> into BiOBr, the transfer and separation efficiency of photogenerated electrons and holes was improved, and finally maximized when the I<sup>-</sup> concentration reached to 2.7 at%, contributing to the optimized visible-light photocatalytic performance in the *Rz* ink decomposition.

# 4.4 Summary

In this work, thin films of iodide-doped BiOBr films were deposited on both glass and FTO successfully using AACVD. The surface and bulk composition of as-fabricated films were identified by GIXRD and XPS. In addition, the influence of the dopant amount on the surface morphology of films was studied through SEM and AFM imaging. While less UV-light active than BiOBr, in the smart Rz ink test, I-BB samples showed significant enhancement in the photocatalytic activity under visible-light irradiation. The greatest performance was observed for the 2.7 at% I-BB film through minimizing the contradictory between the narrowed band gap and the decreased redox potential of the photocatalyst, where the complete degradation of Rz was observed in 300 s. Such a remarkable photocatalytic activity of the 2.7 at% I-BB film is much better than that of traditional photocatalysts (TiO<sub>2</sub>, C<sub>3</sub>N<sub>4</sub> and WO<sub>3</sub>) which require over 10 mins to degrade Rz ink completely. Furthermore, the 2.7 at% I-BB coating in the smart ink test showed a comparable performance to state-of-the-art materials, such as CdS and BiOCI/Plaster of Paris, and the light source utilized in this work even has a longer wavelength and weaker power.<sup>62,81</sup> UV-Vis spectroscopy, PL and PEC measurements showed that the improved photocatalytic performance of I-BB films could be attributed

to the stronger visible-light absorbance, generated OVs, and increased separation and transfer efficiency of charge carriers. In summary, a scalable thin-film deposition method for the iodide-doped BiOBr with the remarkable visible-light photocatalytic activity was developed. Furthermore, this route is likely to be viable to produce other highly active and user-friendly photocatalytic films.

#### 4.5 Reference

- (1) Fujishima, A.; Honda, K. Electrochemical Photolysis of Water at a Semiconductor Electrode. *Nature* **1972**, *238* (5358), 37–38. https://doi.org/10.1038/238037a0.
- (2) Bannister, F. A. The Crystal-Structure of the Bismuth Oxyhalides. *Mineral Mag J Mineral Soc* **1935**, 24 (149), 49–58. https://doi.org/10.1180/minmag.1935.024.149.01.
- (3) Mi, Y.; Zhou, M.; Wen, L.; Zhao, H.; Lei, Y. A Highly Efficient Visible-Light Driven Photocatalyst: Two Dimensional Square-like Bismuth Oxylodine Nanosheets. *Dalt Trans* **2014**, *43* (25), 9549–9556. https://doi.org/10.1039/c4dt00798k.
- (4) Zhang, H.; Liu, L.; Zhou, Z. Towards Better Photocatalysts: First-Principles Studies of the Alloying Effects on the Photocatalytic Activities of Bismuth Oxyhalides under Visible Light. *Phys Chem Chem Phys* **2012**, *14* (3), 1286–1292. https://doi.org/10.1039/C1CP23516H.
- (5) An, H.; Du, Y.; Wang, T.; Wang, C.; Hao, W.; Zhang, J. Photocatalytic Properties of BiOX (X = Cl, Br, and I). *Rare Metals* **2008**, *27* (3), 243–250. https://doi.org/10.1016/S1001-0521(08)60123-0.
- (6) Chen, L.; Huang, R.; Xiong, M.; Yuan, Q.; He, J.; Jia, J.; Yao, M.; Luo, S.; Au, C.; Yin, S. Room-Temperature Synthesis of Flower-Like BiOX (X=Cl, Br, I) Hierarchical Structures and Their Visible-Light Photocatalytic Activity. *Inorg Chem* **2013**, *52* (19), 11118–11125. https://doi.org/10.1021/ic401349j.
- (7) Bhachu, D. S.; Moniz, S. J. A.; Sathasivam, S.; Scanlon, D. O.; Walsh, A.; Bawaked, S. M.; Mokhtar, M.; Obaid, A. Y.; Parkin, I. P.; Tang, J.; Carmalt, C. J. Bismuth Oxyhalides: Synthesis, Structure and Photoelectrochemical Activity. *Chem Sci* **2016**, *7* (8), 4832–4841. https://doi.org/10.1039/C6SC00389C.

- (8) Cheng, H.; Huang, B.; Dai, Y. Engineering BiOX (X = Cl, Br, I) Nanostructures for Highly Efficient Photocatalytic Applications. *Nanoscale* **2014**, *6* (4), 2009. https://doi.org/10.1039/c3nr05529a.
- (9) Zhang, J.; Shi, F.; Lin, J.; Chen, D.; Gao, J.; Huang, Z.; Ding, X.; Tang, C. Self-Assembled 3-D Architectures of BiOBr as a Visible Light-Driven Photocatalyst. *Chem Mater* **2008**, *20* (9), 2937–2941. https://doi.org/10.1021/cm7031898.
- (10) Zhang, H.; Yang, Y.; Zhou, Z.; Zhao, Y.; Liu, L. Enhanced Photocatalytic Properties in BiOBr Nanosheets with Dominantly Exposed (102) Facets. *J Phys Chem C* **2014**, *118* (26), 14662–14669. https://doi.org/10.1021/jp5035079.
- (11) Li, H.; Shang, J.; Ai, Z.; Zhang, L. Efficient Visible Light Nitrogen Fixation with BiOBr Nanosheets of Oxygen Vacancies on the Exposed {001} Facets. *J Am Chem Soc* **2015**, *137* (19), 6393–6399. https://doi.org/10.1021/jacs.5b03105.
- (12) Kong, L.; Jiang, Z.; Lai, H. H.; Nicholls, R. J.; Xiao, T.; Jones, M. O.; Edwards, P. P. Unusual Reactivity of Visible-Light-Responsive AgBr–BiOBr Heterojunction Photocatalysts. *J Catal* **2012**, 293, 116–125. https://doi.org/10.1016/J.JCAT.2012.06.011.
- (13) Fu, J.; Tian, Y.; Chang, B.; Xi, F.; Dong, X. BiOBr-Carbon Nitride Heterojunctions: Synthesis, Enhanced Activity and Photocatalytic Mechanism. *J Mater Chem* **2012**, *22* (39), 21159–21166. https://doi.org/10.1039/c2jm34778d.
- (14) Cui, B.; An, W.; Liu, L.; Hu, J.; Liang, Y. Synthesis of CdS/BiOBr Composite and Its Enhanced Photocatalytic Degradation for Rhodamine B. *Appl Surf Sci* **2014**, *319* (1), 298–305. https://doi.org/10.1016/J.APSUSC.2014.05.179.
- (15) Liu, Y.; Son, W.-J.; Lu, J.; Huang, B.; Dai, Y.; Whangbo, M.-H. Composition Dependence of the Photocatalytic Activities of BiOCl 1- x Br x Solid Solutions under Visible Light. *Chem A Eur J* **2011**, *17* (34), 9342–9349. https://doi.org/10.1002/chem.201100952.
- (16) Jia, Z.; Wang, F.; Xin, F.; Zhang, B. Simple Solvothermal Routes to Synthesize 3D BiOBr<sub>x</sub>I<sub>1-x</sub> Microspheres and Their Visible-Light-Induced Photocatalytic Properties. *Ind Eng Chem Res* **2011**, *50* (11), 6688–6694. https://doi.org/10.1021/ie102310a.

- (17) Zhang, B.; Ji, G.; Liu, Y.; Gondal, M. A.; Chang, X. Efficient Adsorption and Photocatalytic Pceerformance of Flower-like Three-Dimensional (3D) I-Doped BiOCIBr Photocatalyst. *Catal Commun* **2013**, *36*, 25–30. https://doi.org/10.1016/j.catcom.2013.02.021.
- (18) Wang, Y.; Zhang, S.; Yan, Y.; Ren, H.; Chen, J.; Liu, L.; Wu, X. Multi-Anions-Coupled Electronic States in Cl<sup>-</sup>-Doped BiOBr Induce Highly Efficient Decomposition of Tetracycline Hydrochloride. *Mater Res Bull* **2023**, *158*, 112045. https://doi.org/10.1016/j.materresbull.2022.112045.
- (19) Shannon, R. D. Revised Effective Ionic Radii and Systematic Studies of Interatomic Distances in Halides and Chalcogenides. *Acta Crystallographica Section A* **1976**, *32* (5), 751–767. https://doi.org/10.1107/S0567739476001551.
- (20) Qi, L.; Yang, Y.; Zhang, P.; Le, Y.; Wang, C.; Wu, T. Hierarchical Flower-like BiOl<sub>x</sub>Br<sub>(1-x)</sub> Solid Solution Spheres with Enhanced Visible-Light Photocatalytic Activity. *Appl Surf Sci* **2019**, *467–468*, 792–801. https://doi.org/10.1016/j.apsusc.2018.10.184.
- (21) Shao, Y.; Ji, M.; Zhang, Y.; Zhao, J.; Liu, Z.; Li, H.; Li, H.; Yin, S.; Xia, J. Integration of Double Halogen Atoms in Atomically Thin Bismuth Bromide: Mutative Electronic Structure Steering Charge Carrier Migration Boosted Broad-Spectrum Photocatalysis. *Appl Surf Sci* **2021**, *541*, 148477. https://doi.org/10.1016/j.apsusc.2020.148477.
- (22) Liu, S.; Liang, P.; Liu, J.; Xin, J.; Li, X.; Shao, C.; Li, X.; Liu, Y. Anchoring Bismuth Oxybromo-lodide Solid Solutions on Flexible Electrospun Polyacrylonitrile Nanofiber Mats for Floating Photocatalysis. *J Colloid Interface Sci* **2022**, *608*, 3178–3191. https://doi.org/10.1016/j.jcis.2021.11.046.
- (23) Deng, F.; Luo, Y.; Li, H.; Xia, B.; Luo, X.; Luo, S.; Dionysiou, D. D. Efficient Toxicity Elimination of Aqueous Cr(VI) by Positively-Charged BiOCl<sub>x</sub>I<sub>1-x</sub>, BiOBr<sub>x</sub>I<sub>1-x</sub> and BiOCl<sub>x</sub>Br<sub>1-x</sub> Solid Solution with Internal Hole-Scavenging Capacity via the Synergy of Adsorption and Photocatalytic Reduction. *J Hazard Mater* **2020**, 383, 121127. https://doi.org/10.1016/j.jhazmat.2019.121127.

- (24) Qin, Q.; Guo, Y.; Zhou, D.; Yang, Y.; Guo, Y. Facile Growth and Composition-Dependent Photocatalytic Activity of Flowerlike BiOCI<sub>1-x</sub>Br<sub>x</sub> Hierarchical Microspheres. *Appl Surf Sci* **2016**, *390*, 765–777. https://doi.org/10.1016/j.apsusc.2016.08.134.
- (25) Dandapat, A.; Horovitz, I.; Gnayem, H.; Sasson, Y.; Avisar, D.; Luxbacher, T.; Mamane, H. Solar Photocatalytic Degradation of Trace Organic Pollutants in Water by Bi(0)-Doped Bismuth Oxyhalide Thin Films. *ACS Omega* **2018**, *3* (9), 10858–10865. https://doi.org/10.1021/acsomega.8b00759.
- (26) Feng, J.; Li, N.; Du, Y.; Ren, X.; Wang, X.; Liu, X.; Ma, H.; Wei, Q. Ultrasensitive Double-Channel Microfluidic Biosensor-Based Cathodic Photo-Electrochemical Analysis via Signal Amplification of SOD-Au@PANI for Cardiac Troponin i Detection. *Anal Chem* **2021**, 93 (42), 14196–14203. https://doi.org/10.1021/acs.analchem.1c02922.
- (27) Yin, H. Y.; Zheng, Y. F.; Song, X. C. Synthesis and Enhanced Visible Light Photocatalytic CO<sub>2</sub> Reduction of BiPO<sub>4</sub>–BiOBr<sub>x</sub>I<sub>1-x</sub> p–n Heterojunctions with Adjustable Energy Band. *RSC Adv* **2019**, *9* (20), 11005–11012. https://doi.org/10.1039/C9RA01416K.
- (28) Alansi, A. M.; Qahtan, T. F.; Saleh, T. A. Solar-Driven Fixation of Bismuth Oxyhalides on Reduced Graphene Oxide for Efficient Sunlight-Responsive Immobilized Photocatalytic Systems. *Adv Mater Interfaces* **2021**, *8* (3), 2001463. https://doi.org/10.1002/admi.202001463.
- (29) Jia, H.; Li, Y.; Mao, Y.; Yu, D.; He, W.; Zheng, Z. Room Temperature Synthesis of BiOBr<sub>1-x</sub>I<sub>x</sub> Thin Films with Tunable Structure and Conductivity Type for Enhanced Photoelectric Performance. *RSC Adv* **2020**, *10* (68), 41755–41763. https://doi.org/10.1039/D0RA08211B.
- (30) Mills, A.; Wells, N.; O'Rourke, C. Correlation between ΔAbs, ΔRGB (Red) and Stearic Acid Destruction Rates Using Commercial Self-Cleaning Glass as the Photocatalyst. *Catal Today* **2014**, *230*, 245–249. https://doi.org/10.1016/J.CATTOD.2013.11.023.

- (31) Mills, A.; O'Rourke, C.; Wells, N. A Smart Ink for the Assessment of Low Activity Photocatalytic Surfaces. *Analyst* **2014**, *139* (21), 5409–5414. https://doi.org/10.1039/c4an01375a.
- (32) Lin, H.; Li, X.; Cao, J.; Chen, S.; Chen, Y. Novel I<sup>-</sup>-Doped BiOBr Composites: Modulated Valence Bands and Largely Enhanced Visible Light Phtotocatalytic Activities. *Catal Commun* **2014**, *49*, 87–91. https://doi.org/10.1016/j.catcom.2014.02.010.
- (33) Wu, Y.; Ji, H.; Liu, Q.; Sun, Z.; Li, P.; Ding, P.; Guo, M.; Yi, X.; Xu, W.; Wang, C. C.; Gao, S.; Wang, Q.; Liu, W.; Chen, S. Visible Light Photocatalytic Degradation of Sulfanilamide Enhanced by Mo Doping of BiOBr Nanoflowers. *J Hazard Mater* **2022**, *424*, 127563. https://doi.org/10.1016/J.JHAZMAT.2021.127563.
- (34) Sun, Z.; Zhang, H.; Mei, B. Enhanced Charge Separation and Transfer Efficiency of BiOI with the Dominantly Exposed (102) Facet for Sensitive Photoelectrochemical Photodetection. *Inorg Chem* **2023**, *62* (14), 5512–5519. https://doi.org/10.1021/acs.inorgchem.2c04523.
- (35) Liu, G.; Wang, T.; Ouyang, S.; Liu, L.; Jiang, H.; Yu, Q.; Kako, T.; Ye, J. Band-Structure-Controlled BiO(ClBr)<sub>(1-x)</sub>/2I<sub>x</sub> Solid Solutions for Visible-Light Photocatalysis. *J Mater Chem A* **2015**, 3 (15), 8123–8132. https://doi.org/10.1039/c4ta07128j.
- (36) Keller, E.; Krämer, V. A Strong Deviation from Vegard's Rule: X-Ray Powder Investigations of the Three Quasi-Binary Phase Systems BiOX–BiOY (X, Y = Cl, Br, I). *Zeitschrift für Naturforsch B* **2005**, *60* (12), 1255–1263. https://doi.org/10.1515/znb-2005-1207.
- (37) Huo, W.; Xu, W.; Guo, Z.; Zhang, Y.; Dong, F. Motivated Surface Reaction Thermodynamics on the Bismuth Oxyhalides with Lattice Strain for Enhanced Photocatalytic NO Oxidation. *Appl Catal B* **2021**, *284*, 119694. https://doi.org/10.1016/J.APCATB.2020.119694.
- (38) Zhang, Y.; Park, M.; Kim, H. Y.; Ding, B.; Park, S. J. In-Situ Synthesis of Nanofibers with Various Ratios of BiOCl<sub>x</sub>/BiOBr<sub>y</sub>/BiOl<sub>z</sub> for Effective Trichloroethylene Photocatalytic Degradation. *Appl Surf Sci* **2016**, *384*, 192–199. https://doi.org/10.1016/j.apsusc.2016.05.039.

- (39) Jia, X.; Cao, J.; Lin, H.; Zhang, M.; Guo, X.; Chen, S. Transforming Type-I to Type-II Heterostructure Photocatalyst via Energy Band Engineering: A Case Study of I-BiOCl/I-BiOBr. *Appl Catal B* **2017**, *204*, 505–514. https://doi.org/10.1016/j.apcatb.2016.11.061.
- (40) Li, X.; Chen, T.; Lin, H.; Cao, J.; Huang, H.; Chen, S. Intensive Photocatalytic Activity Enhancement of Bi<sub>5</sub>O<sub>7</sub>I via Coupling with Band Structure and Content Adjustable BiOBr<sub>x</sub>I<sub>1-x</sub>. *Sci Bull (Beijing)* **2018**, *63* (4), 219–227. https://doi.org/10.1016/j.scib.2017.12.016.
- (41) Ye, L.; Tian, L.; Peng, T.; Zan, L. Synthesis of Highly Symmetrical BiOI Single-Crystal Nanosheets and Their {001} Facet-Dependent Photoactivity. *J Mater Chem* **2011**, *21* (33), 12479–12484. https://doi.org/10.1039/c1jm11005e.
- (42) Liu, H.; Su, Y.; Chen, Z.; Jin, Z.; Wang, Y. Novel 3D Flowerlike Au/BiOBr0.2I0.8 Composites with Highly Enhanced Visible-Light Photocatalytic Performances. *Sep Purif Technol* **2014**, *133*, 343–350. https://doi.org/10.1016/j.seppur.2014.07.020.
- (43) Wang, X.; Hu, X.; Yang, W.; Wang, F.; Liu, M.; Zhu, X.; Zhang, Y.; Yao, S. Exploitation of a Turn-on Photoelectrochemical Sensing Platform Based on Au/BiOI for Determination of Copper(II) Ions in Food Samples. *J Electroanal Chem* **2021**, *895*, 115536. https://doi.org/10.1016/J.JELECHEM.2021.115536.
- (44) Cai, L.; Zhang, G.; Zhang, Y.; Wei, Y. Mediation of Band Structure for BiOBr<sub>x</sub>I<sub>1-x</sub> Hierarchical Microspheres of Multiple Defects with Enhanced Visible-Light Photocatalytic Activity. *CrystEngComm* **2018**, *20* (26), 3647–3656. https://doi.org/10.1039/C8CE00700D.
- (45) Jia, X.; Cao, J.; Lin, H.; Zhang, M.; Guo, X.; Chen, S. Novel I-BiOBr/BiPO<sub>4</sub> Heterostructure: Synergetic Effects of I<sup>-</sup> Ion Doping and the Electron Trapping Role of Wide-Band-Gap BiPO<sub>4</sub> Nanorods. *RSC Adv* **2016**, *6* (61), 55755–55763. https://doi.org/10.1039/C6RA06330F.
- (46) Zhang, G.; Zhang, L.; Liu, Y.; Liu, L.; Huang, C.-P.; Liu, H.; Li, J. Substitution Boosts Charge Separation for High Solar-Driven Photocatalytic Performance. *ACS Appl Mater Interfaces* **2016**, *8* (40), 26783–26793. https://doi.org/10.1021/acsami.6b08676.

- (47) Wang, H.; Yong, D.; Chen, S.; Jiang, S.; Zhang, X.; Shao, W.; Zhang, Q.; Yan, W.; Pan, B.; Xie, Y. Oxygen-Vacancy-Mediated Exciton Dissociation in BiOBr for Boosting Charge-Carrier-Involved Molecular Oxygen Activation. *J Am Chem Soc* **2018**, *140* (5), 1760–1766. https://doi.org/10.1021/jacs.7b10997.
- (48) Yu, Z.; Yang, H.; Soin, N.; Chen, L.; Black, N.; Xu, K.; Sharma, P. K.; Tsonos, C.; Kumar, A.; Luo, J. Bismuth Oxyhalide Based Photo-Enhanced Triboelectric Nanogenerators. *Nano Energy* **2021**, *89*, 106419. https://doi.org/10.1016/J.NANOEN.2021.106419.
- (49) Lei, Y.; Wang, G.; Guo, P.; Song, H. The Ag–BiOBr<sub>x</sub>I<sub>1-x</sub> Composite Photocatalyst: Preparation, Characterization and Their Novel Pollutants Removal Property. *Appl Surf Sci* **2013**, *279*, 374–379. https://doi.org/10.1016/j.apsusc.2013.04.118.
- (50) Wang, Z.; Chen, M.; Huang, D.; Zeng, G.; Xu, P.; Zhou, C.; Lai, C.; Wang, H.; Cheng, M.; Wang, W. Multiply Structural Optimized Strategies for Bismuth Oxyhalide Photocatalysis and Their Environmental Application. *Chem Eng J* **2019**, *374*, 1025–1045. https://doi.org/10.1016/j.cej.2019.06.018.
- (51) Liu, Q. Y.; Han, G.; Zheng, Y. F.; Song, X. C. Synthesis of BiOBr<sub>x</sub>I<sub>1-x</sub> Solid Solutions with Dominant Exposed {0 0 1} and {1 1 0} Facets and Their Visible-Light-Induced Photocatalytic Properties. *Sep Purif Technol* **2018**, *203*, 75–83. https://doi.org/10.1016/j.seppur.2018.04.011.
- (52) Wang, W.; Huang, F.; Lin, X.; Yang, J. Visible-Light-Responsive Photocatalysts XBiOBr–(1–x)BiOI. *Catal Commun* **2008**, *9* (1), 8–12. https://doi.org/10.1016/j.catcom.2007.05.014.
- (53) Shen, S.; Zhao, L.; Zhou, Z.; Guo, L. Enhanced Photocatalytic Hydrogen Evolution over Cu-Doped ZnIn<sub>2</sub>S<sub>4</sub> under Visible Light Irradiation. *J Phys Chem C* **2008**, *112* (41), 16148–16155. https://doi.org/10.1021/jp804525q.
- (54) Huo, X.; Huang, L.-F. Physical Spread and Technical Upshift in the Band Gaps of Visible-Light Photocatalytic Bismuth Oxyhalide Solid Solutions. *Comput Mater Sci* **2020**, *184*, 109870. https://doi.org/10.1016/j.commatsci.2020.109870.

- (55) Kong, L.; Guo, J.; Makepeace, J. W.; Xiao, T.; Greer, H. F.; Zhou, W.; Jiang, Z.; Edwards, P. P. Rapid Synthesis of BiOBr<sub>x</sub>I<sub>1-x</sub> Photocatalysts: Insights to the Visible-Light Photocatalytic Activity and Strong Deviation from Vegard's Law. *Catal Today* **2019**, 335, 477–484. https://doi.org/10.1016/j.cattod.2019.02.013.
- (56) Wang, Q.; Liu, Z.; Liu, D.; Liu, G.; Yang, M.; Cui, F.; Wang, W. Ultrathin Two-Dimensional BiOBr<sub>x</sub>I<sub>1-x</sub> Solid Solution with Rich Oxygen Vacancies for Enhanced Visible-Light-Driven Photoactivity in Environmental Remediation. *Appl Catal B* **2018**, 236, 222–232. https://doi.org/10.1016/j.apcatb.2018.05.029.
- (57) Zhao, R.; Jia, Z.; Li, T.; Liu, J.; Li, R.; Wang, Y.; Wang, Y.; Zhang, X.; Fan, C. Concise Fabrication of 3D Rose-like BiOBrxI1–x with Exceptional Wide Spectrum Visible-Light Photocatalytic Activity. *Inorg Chem Commun* **2019**, *101*, 150–159. https://doi.org/10.1016/j.inoche.2019.01.021.
- (58) Cardoso, J. C.; Bessegato, G. G.; Boldrin Zanoni, M. V. Efficiency Comparison of Ozonation, Photolysis, Photocatalysis and Photoelectrocatalysis Methods in Real Textile Wastewater Decolorization. *Water Res* **2016**, *98*, 39–46. https://doi.org/10.1016/J.WATRES.2016.04.004.
- (59) Wu, T.; Liu, G.; Zhao, J.; Hidaka, H.; Serpone, N. Photoassisted Degradation of Dye Pollutants. V. Self-Photosensitized Oxidative Transformation of Rhodamine B under Visible Light Irradiation in Aqueous TiO 2 Dispersions. *J Phys Chem B* **1998**, *102* (30), 5845–5851. https://doi.org/10.1021/jp980922c.
- (60) Rochkind, M.; Pasternak, S.; Paz, Y. Using Dyes for Evaluating Photocatalytic Properties: A Critical Review. *Molecules* **2015**, *20* (1), 88–110. https://doi.org/10.3390/molecules20010088.
- (61) Rajeshwar, K.; Osugi, M. E.; Chanmanee, W.; Chenthamarakshan, C. R.; Zanoni, M. V. B.; Kajitvichyanukul, P.; Krishnan-Ayer, R. Heterogeneous Photocatalytic Treatment of Organic Dyes in Air and Aqueous Media. *J Photochem Photobiol C Photochem Rev* **2008**, 9 (4), 171–192. https://doi.org/10.1016/j.jphotochemrev.2008.09.001.
- (62) Mills, A.; Wells, N.; O'Rourke, C. Probing the Activities of UV and Visible-Light Absorbing Photocatalyst Powders Using a Resazurin-Based Photocatalyst Activity

- Indicator Ink (Rz Paii ). *J Photochem Photobiol A Chem* **2017**, 338, 123–133. https://doi.org/10.1016/j.jphotochem.2017.01.030.
- (63) Zhang, X.; Zhang, L.; Xie, T.; Wang, D. Low-Temperature Synthesis and High Visible-Light-Induced Photocatalytic Activity of BiOI/TiO<sub>2</sub> Heterostructures. *J Phys Chem C* **2009**, *113* (17), 7371–7378. https://doi.org/10.1021/jp900812d.
- (64) Johnston, M. B.; Herz, L. M. Hybrid Perovskites for Photovoltaics: Charge-Carrier Recombination, Diffusion, and Radiative Efficiencies. *Acc Chem Res* **2016**, *49* (1), 146–154. https://doi.org/10.1021/acs.accounts.5b00411.
- (65) Zhang, J.; Han, Q.; Zhu, J.; Wang, X. A Facile and Rapid Room-Temperature Route to Hierarchical Bismuth Oxyhalide Solid Solutions with Composition-Dependent Photocatalytic Activity. *J Colloid Interface Sci* **2016**, *477*, 25–33. https://doi.org/10.1016/j.jcis.2016.05.027.
- (66) Tebyetekerwa, M.; Zhang, J.; Xu, Z.; Truong, T. N.; Yin, Z.; Lu, Y.; Ramakrishna, S.; Macdonald, D.; Nguyen, H. T. Mechanisms and Applications of Steady-State Photoluminescence Spectroscopy in Two-Dimensional Transition-Metal Dichalcogenides. *ACS Nano* **2020**, *14* (11), 14579–14604. https://doi.org/10.1021/acsnano.0c08668.
- (67) Wu, J.; Xie, Y.; Ling, Y.; Dong, Y.; Li, J.; Li, S.; Zhao, J. Synthesis of Flower-Like g-C<sub>3</sub>N<sub>4</sub>/BiOBr and Enhancement of the Activity for the Degradation of Bisphenol A Under Visible Light Irradiation. *Front Chem* **2019**, *7*, 649. https://doi.org/10.3389/fchem.2019.00649.
- (68) Li, J.; Zhou, Q.; Yang, F.; Wu, L.; Li, W.; Ren, R.; Lv, Y. Uniform Flower-like BiOBr/BiOI Prepared by a New Method: Visible-Light Photocatalytic Degradation, Influencing Factors and Degradation Mechanism. *New J Chem* **2019**, *43* (37), 14829–14840. https://doi.org/10.1039/c9nj03038g.
- (69) Li, Y.; Li, Z.; Gao, L. Construction of Z-Scheme BiOI/g-C<sub>3</sub>N<sub>4</sub> Heterojunction with Enhanced Photocatalytic Activity and Stability under Visible Light. *J Mater Sci Mater Electron* **2019**, *30* (13), 12769–12782. https://doi.org/10.1007/s10854-019-01642-0.
- (70) Sun, Y.; Zhang, W.; Xiong, T.; Zhao, Z.; Dong, F.; Wang, R.; Ho, W.-K. Growth of BiOBr Nanosheets on C<sub>3</sub>N<sub>4</sub> Nanosheets to Construct Two-Dimensional

- Nanojunctions with Enhanced Photoreactivity for NO Removal. *J Colloid Interface Sci* **2014**, *418*, 317–323. https://doi.org/10.1016/j.jcis.2013.12.037.
- (71) Gfroerer, T. H. Photoluminescence in Analysis of Surfaces and Interfaces. *Encycl Anal Chem* **2006**. https://doi.org/10.1002/9780470027318.A2510.
- (72) Stoneham, A. M. Non-Radiative Transitions in Semiconductors. *Reports Prog Phys* **1981**, *44* (12), 1251–1295. https://doi.org/10.1088/0034-4885/44/12/001.
- (73) Zhang, H.; Tee, J. C. L.; Jaenicke, S.; Gondal, M. A.; Dastageer, M. A.; Basheer, C.; Chuah, G.-K. BiOBr<sub>n</sub>I<sub>1-n</sub> Solid Solutions as Versatile Photooxidation Catalysts for Phenolics and Endocrine Disrupting Chemicals. *Catal Today* **2021**, *375*, 547–557. https://doi.org/10.1016/j.cattod.2020.01.009.
- (74) Liu, T.; Wang, Y. Synergistic Effect of Iodine Doping and Platinum Loading on Boosting the Visible Light Photocatalytic Activity of BiOBr. *Inorg Chem Commun* **2020**, *114*, 107846. https://doi.org/10.1016/j.inoche.2020.107846.
- (75) Jia, X.; Cao, J.; Lin, H.; Chen, Y.; Fu, W.; Chen, S. One-Pot Synthesis of Novel Flower-like BiOBr<sub>0.9</sub>I<sub>0.1</sub>/BiOI Heterojunction with Largely Enhanced Electron-Hole Separation Efficiency and Photocatalytic Performances. *J Mol Catal A Chem* **2015**, 409, 94–101. https://doi.org/10.1016/j.molcata.2015.08.008.
- (76) Bi, C.; Cao, J.; Lin, H.; Wang, Y.; Chen, S. Tunable Photocatalytic and Photoelectric Properties of I<sup>-</sup>-Doped BiOBr Photocatalyst: Dramatic PH Effect. *RSC Adv* **2016**, *6* (19), 15525–15534. https://doi.org/10.1039/C5RA22943J.
- (77) Fung, C. S. L.; Khan, M.; Kumar, A.; Lo, I. M. C. Visible-Light-Driven Photocatalytic Removal of PPCPs Using Magnetically Separable Bismuth Oxybromolodide Solid Solutions: Mechanisms, Pathways, and Reusability in Real Sewage. *Sep Purif Technol* **2019**, *216*, 102–114. https://doi.org/10.1016/j.seppur.2019.01.077.
- (78) Bian, Y.; Gu, Y.; Zhang, X.; Chen, H.; Li, Z. Engineering BiOBr<sub>x</sub>I<sub>1-x</sub> Solid Solutions with Enhanced Singlet Oxygen Production for Photocatalytic Benzylic C H Bond Activation Mediated by N-Hydroxyl Compounds. *Chinese Chem Lett* **2021**, *32* (9), 2837–2840. https://doi.org/10.1016/j.cclet.2021.02.006.

- (79) Ren, K.; Liu, J.; Liang, J.; Zhang, K.; Zheng, X.; Luo, H.; Huang, Y.; Liu, P.; Yu, X. Synthesis of the Bismuth Oxyhalide Solid Solutions with Tunable Band Gap and Photocatalytic Activities. *Dalt Trans* **2013**, *42* (26), 9706. https://doi.org/10.1039/c3dt50498k.
- (80) Xu, H.-Y.; Han, X.; Tan, Q.; He, X.-L.; Qi, S.-Y. Structure-Dependent Photocatalytic Performance of BiOBr<sub>x</sub>I<sub>1-x</sub> Nanoplate Solid Solutions. *Catalysts* **2017**, 7 (5), 153. https://doi.org/10.3390/catal7050153.
- (81) Singh, V. P.; Mishra, D.; Kabachkov, E. N.; Shul'ga, Yu. M.; Vaish, R. The Characteristics of BiOCl/Plaster of Paris Composites and Their Photocatalytic Performance under Visible Light Illumination for Self-Cleaning. *Mater Sci Energy Technol* **2020**, *3*, 299–307. https://doi.org/10.1016/j.mset.2019.12.001.

### **Chapter 5: Conclusions and future work**

Experiments accomplished in this thesis were composed of three parts: (1) phenethylammonium bismuth iodide ([PEA]<sub>3</sub>[Bi<sub>2</sub>I<sub>9</sub>]) film deposition, (2) ZnO/BiOI heterojunction construction and (3) iodide-doped BiOBr.

In Chapter 2, single crystals of [PEA] $_3$ [Bi $_2$ I $_9$ ] were prepared through the solvothermal synthesis, and [PEA] $_3$ [Bi $_2$ I $_9$ ] films were deposited successfully *via* AACVD on three kinds of substrates, including glass, TiO $_2$ /glass and FTO/glass. Deposition parameters including temperatures and the concentration of precursor solutions were optimized in the AACVD processes. In addition, the annealing conditions were studied in order to remove co-crystallized DMF in the films and retain the film morphologies. It was found that the type of substrate was able to influence the preferential orientation, morphologies and optoelectrical properties of films. Only powdery materials were obtained on amorphous glass, but crystallized films with (10 $\overline{1}$ ) preferential orientation and uniform and compact morphologies were deposited on crystalline substrates including TiO $_2$ /glass and FTO/glass. Furthermore, band bending occurred between semiconducting [PEA] $_3$ [Bi $_2$ I $_9$ ] films and substrates due to the formation of heterojunctions. [PEA] $_3$ [Bi $_2$ I $_9$ ] films were investigated in various applications, and possible reasons for their failures were also discussed.

In Chapter 3, in order to improve the performance in PEC water oxidation under sunlight, double-layer heterojunctions combining ZnO and BiOI were constructed by AACVD. The structure of the heterojunctions had a great influence on the final PEC performance, where the ZnO/BiOI heterojunction (the ZnO film on top and the BiOI film at bottom) showed a significant improvement in PEC performance while no improvement was observed in the reversed structure (BiOI/ZnO). Such a difference resulted from the different incident light harvesting and film morphologies. The influence of deposition temperatures and thickness of the ZnO film in the heterojunctions was also investigated, and the ZnO/BiOI heterojunction with 390 nm thick BiOI film deposited at 300 °C and 120 nm thick ZnO film deposited at 350 °C showed the best PEC performance. ZnO/BiOI had a theoretical solar photocurrent of 0.271 mA·cm<sup>-2</sup>, which was much better than the parent materials, BiOI (0.0028 mA·cm<sup>-2</sup>) and ZnO (0.121 mA·cm<sup>-2</sup>). This improved activity in PEC water oxidation could be explained by the enhanced visible-light harvesting, effective charge transfer and

separation, and reduced recombination of photogenerated charge carriers in the ZnO/BiOI heterojunction, which was characterized by PL spectroscopy and TAS.

lodide-doped BiOBr films were investigated in the Chapter 4. Due to doping I<sup>-</sup>, the crystal structures and film morphologies were changed. In addition, optical band gaps could be tuned through controlling the dopant concentration. In the *smart* ink test, it was found that compared with parent materials, iodide-doped BiOBr films showed a dramatic improvement in photocatalysis under visible-light illumination, and the highest activity was observed for the 2.7 at% iodide-doped BiOBr. Based on the analysis of transmittance and PL spectra and PEC measurements, it was determined that the narrowed band gap, generated OVs, and increased separation and transfer efficiency of photogenerated electrons and holes all contributed to the improved visible-light photocatalytic activity of 2.7 at% iodide-doped BiOBr. This work also proved that iodide-doped BiOBr coatings fabricated by AACVD showed potential to be utilized in the sustainable construction.

As a scalable method to fabricate functional films, AACVD has the potential to become economically viable. However, the study about mechanisms during the AACVD process is limited and mechanisms vary a lot for different precursors and target materials. In addition, there are numerous parameters influencing the deposited films for AACVD, such as the type of carrier gas, solvents, precursors and substrates, temperatures, flow rate and so on. As a result, future investigations should focus on investigating the reaction mechanisms for the preparation of precursor solutions and film deposition, as well as the further optimization of the above functional films in practical applications.

For the work about [PEA]<sub>3</sub>[Bi<sub>2</sub>I<sub>9</sub>], the single crystal and the precursor solution used in AACVD should be investigated in more details. The interaction between precursors, PEAI and BiI<sub>3</sub>, and the solvent, DMF, needs to be revealed to understand mechanisms of the single crystal growth and film deposition. In addition, it is also worthy to utilize other solvents, such as dimethylsulphoxide, to study the effect of the kind of solvents on the physical and chemical properties of deposited films. Furthermore, [PEA]<sub>3</sub>[Bi<sub>2</sub>I<sub>9</sub>] films with less pinholes and cracks need to be fabricated for their utilization in perovskite solar cells. Less thick films are possible to be obtained through using less precursor solutions and increased flow rate. Some complexing agents, such

as ethylenediaminetetraacetic acid, can attempt to be added into the precursor solution to improve the quality of deposited films through adjusting the film growth rate in the AACVD process.

In the work about the ZnO/BiOI heterojunction, because the heterojunction showed poor stability in PEC water oxidation caused by serious photocorrosion of ZnO and BiOI, a protective layer could be deposited on the heterojunction to improve the stability and retain the high PEC activity of the heterojunction. For example, an extra thin layer of TiO<sub>2</sub> could be deposited on top of the heterojunction through atmospheric pressure chemical vapour deposition, so that the stability of the photoanode is likely to be improved with the transfer of photogenerated charge carriers unaffected. In addition, different heterojunction structures with the bottom BiOI layer replaced by other BiOX materials, such as BiOCI and BiOBr, could attempt to be constructed to investigate whether this method is universal to improve the PEC performance of BiOXs.

Finally, about the study of iodide-doped BiOBr, except XPS, other widely used characterization methods, such as EDS and XRF, were not able to determine the film composition due to the disturbance of the FTO substrate. Therefore, more work needs to be done to measure the dopant concentration in films accurately. Furthermore, the photocatalytic mechanism of iodide-doped BiOBr under both UV and visible light irradiation need to be investigated through radical trapping experiments, which is also helpful to understand the influence of doping on the band structure of BiOBr. In addition, in this thesis, the photocatalytic performance of deposited films was only tested by *Rz* ink, so the development of iodide-BiOBr coatings fabricated by AACVD should incorporate the photocatalytic application in real life, such as the degradation of pollutants in air.

### **Publications**

- (1) Wang, M.; Quesada-Cabrera, R.; Sathasivam, S.; Blunt, M. O.; Borowiec, J.; Carmalt, C. J. Visible-Light-Active Iodide-Doped BiOBr Coatings for Sustainable Infrastructure. *ACS Appl Mater Interfaces* **2023**. https://doi.org/10.1021/acsami.3c11525.
- (2) Wang, M.; Kafizas, A.; Sathasivam, S.; Blunt, M. O.; Moss, B.; Gonzalez-Carrero, S.; Carmalt, C. J. ZnO/BiOI Heterojunction Photoanodes with Enhanced Photoelectrochemical Water Oxidation Activity. *Appl Catal B* **2023**, *331*, 122657. https://doi.org/10.1016/j.apcatb.2023.122657.
- (3) Zhao, D.; Sathasivam, S.; Wang, M.; Carmalt, C. J. Transparent and Conducting Boron Doped ZnO Thin Films Grown by Aerosol Assisted Chemical Vapor Deposition. *RSC Adv* **2022**, *12* (51), 33049–33055. https://doi.org/10.1039/D2RA05895B.
- (4) Wang, M.; Carmalt, C. J. Film Fabrication of Perovskites and Their Derivatives for Photovoltaic Applications via Chemical Vapor Deposition. *ACS Appl Energy Mater* **2022**, *5* (5), 5434–5448. https://doi.org/10.1021/acsaem.1c02612.
- (5) Wang, M.; Sanchez Perez, C.; Habib, F.; Blunt, Mattew. O.; Carmalt, C. J. Scalable Production of Ambient Stable Hybrid Bismuth Based Materials: AACVD of Phenethylammonium Bismuth Iodide Films\*\*. *Chem A Eur J* **2021**, *27* (36), 9406 9413. https://doi.org/10.1002/chem.202100774.
- (6) Daskalakis, S.; Wang, M.; Carmalt, C. J.; Vernardou, D. Electrochemical Investigation of Phenethylammonium Bismuth Iodide as Anode in Aqueous Zn<sup>2+</sup> Electrolytes. *Nanomaterials* **2021**, *11* (3), 1–8. https://doi.org/10.3390/nano11030656.